Development of a Hybrid Microwave-Optical System to Monitor Human Thermoregulation

Allann Al-Armaghany

A thesis submitted for the degree of

Doctor of Philosophy

of

University College London

Sensors, Systems and Circuits Group

Department of Electronic and Electrical Engineering

University College London

February 2015

I, Allann Al-Armaghany, confirm that the work presented in this thesis is my own. Where information has been derived from other sources, I confirm that this has been indicated in the thesis.

16/02/2015

Abstract

Warming of human tissue causes vasodilation and therefore, increase in blood volume. Such thermal responses allow the assessment of hemodynamics in the tissue, providing physiological and clinically important information of the diagnosed subject. Local warming is often accomplished on the skin because of its accessibility and simplicity. To allow the investigation into deeper tissue such as the muscle, an innovative hybrid microwave-optical system has been developed. This comprises of a microwave system, an optical monitoring and cooling system. The tissue warming is induced by a novel microwave applicator, which was based on microstrip patch design operating at 2.45 GHz with a superstrate interface layer to improve the coupling of electromagnetic (EM) waves into the skin. The active cooling was introduced to reduce skin heating. While the optical sensors based on Near-Infrared Spectroscopy (NIRS), was used to measure the changes in tissue oxygenation including the muscle. This thesis demonstrates the development procedure, covering the design and operation of the entire system. Moreover, the majority of the work is based on the four developed applicators, where each design was evaluated using EM and thermal simulation based on numerical phantoms. The study evaluates the distribution of absorbed EM energy in the tissue known as the specific absorption rate (SAR). The applicators are developed in the following order: (i) Applicator I was fabricated for preliminary study for general tissue heating with the integrated optical probes. This early study provided an insight to the importance of superstrate thickness and material. (ii) Applicator II, which introduces a new approach to skin cooling based on Thermoelectric Coolers (TEC) and high thermal conductive superstrate. This design could cool the skin and monitor tissue oxygenation, skin perfusion and temperature. (iii) Applicator III was an updated model of the predecessor, resolving cooling configuration and the discrepancy in operating frequency, and was capable of minimising skin heating effectively (iv) Circularly polarized (CP) Applica-

tor aimed at reduction of the SAR in the superficial layer, and hence skin heating.

The simulated thermal study of all developed applicators was validated with *ex-vivo* (mimicked phantom) and *in-vivo* experimental trials. The measurements and the simulation model were in agreement, apart from the CP applicator due to the complexity of measurement. The results from the phantom and human calf indicated superficial heating was reduced by about 5.0-6.0 °C when skin cooling was applied, while the temperature change in muscle was not significantly affected. The measurement with mimicked tissue showed the applicator was capable of elevating muscle temperature by approximately 3.0-4.0 °C. This is a sufficient increase to cause tissue dilation, and therefore, change in the thermal response. The hybrid microwave-optical system has been developed and examined on three human calves during *in-vivo* physiological study. The results using Applicator II illustrated that the device can successfully stimulate and measure thermal responses in terms of oxy/deoxy/total haemoglobin concentrations changes (ΔHbO_2/ΔHHb/ΔHbT). The slope (rate of change) of ΔHbT curve during microwave exposure is defined as the thermal response. This parameter is essential in studying physiological responses between different subject, particularly in vascular diseases, transplanted free flaps and other conditions, including chronic spinal cord injury. Subjects with such conditions will have a distinguishable response to tissue heating than a healthy subject. The monitored haemodynamic signals of Applicator II are primarily based on superficial responses. However, measurements with Applicator III showed the potential of the applicator. The measured thermal response was 0.83×10^{-3} μ M/s without skin cooling, which was dedicated by skin heating. The introduced cooling system has reduced the skin temperature and maintained the local skin micro-circulation, which was monitored with the secondary optical system based on Laser Doppler Flowmetry (LDF). This probe measures blood flow at superficial depth, and consequently, was used as a validation tool to demonstrate the cooling efficiency. The measured thermal response with skin over-cooling was -0.08×10^{-3} μ M/s. The negative response indicates arterial constriction, and therefore, the skin heat was eliminated while the simulations study to indicate the muscle temperature was elevated by 3 °C. However, the response was dominant by the superficial response. Obtaining a response from muscle only was challenging and currently being solved in numerous applicator and cooling technique, which have been presented in the thesis.

Acknowledgements

I would like to take this opportunity to express my sincere gratitude to my supervisor, Dr Kenneth Tong, for his patient advice and indispensable encouragement throughout this work. Equally I would like thank my second supervisor, Dr Terence Leung for his helpful guidance and encouragement. I'm fortunate to have been supervised by both of them.

My thanks to David Highton for his guidance in the physiological evaluation of the results and his input toward the future clinical application of the project. Special thanks to Ralph Benjamin for his technical guidance throughout the research work.

I would like to thank Tom Hamer for fabricating the applicator casing, Piotr Kostecki for PCB fabrication, Andrew Moss for milling machine training and also big thanks to IT staff.

I wish to express my special thanks to Jianling Chen, for her assistance in fabrication the tissue mimicked phantom. Also would like to thank Amin Amiri for his time to assist me in measuring the dielectric properties of the phantom. Thanks to Shashi Halai who participated in many discussions on various ideas.

I wish to express my sincere thanks to my parents Mohammed and Nasreen for their daily support and also to my sister Aveen who always stood by me.

My deepest appreciation to my uncles H.Bamarni and G.Armaghany for providing me with the necessary fund through out my PhD.

Finally I would like to thank all my colleagues in the Radar group for making work life enjoyable and entertaining including.

Publications

A. Al-Armaghany, K. Tong; T. Leung, "Microwave Applicator for Deep Tissue Warming and its Application in Thermoregulation Monitoring," *Biomedical Engineering, IEEE Transactions 2014* (In progress for submission)

A. Al-Armaghany, K. Tong; T. Leung, "Development of a Hybrid Microwave-Optical Deep Muscle Warming Monitor," *Microwave Workshop Series on RF and Wireless Technologies for Biomedical and Healthcare Applications (IMWS-BIO), 2014 IEEE MTT-S International* (Accepted, In proceeding)

A. Al-Armaghany, K. Tong, D. Highton and T. Leung, "Validation of a Hybrid Microwave-Optical Monitor to investigate Thermal Provocation in Microvasculature," *in Advances in Experimental Medicine and Biology, Springer New York,* 2015, pp. (Accepted, In proceeding)

A. Al-Armaghany, K. Tong, and T. Leung, "Development of a Hybrid Microwave-Optical Thermoregulation Monitor for the Muscle," *in Advances in Experimental Medicine and Biology, Springer New York*, 2014, pp. (Award winning paper, 'The Duane F. Bruley Travel Award')

Al-Armaghany, A. Tong, K.; Leung, T.S., "Superficial heat reduction technique for a hybrid microwave-optical device," *Engineering in Medicine and Biology Society (EMBC), 2013 35th Annual International Conference of the IEEE*, vol., no., pp.3749,3752, 3-7 July 2013

A. Al-Armaghany, K. Tong, and T. Leung, "Development of a Hybrid Microwave-Optical Tissue Oxygenation Probe to Measure Thermal Response in the Deep Tissue," *in Advances in Experimental Medicine and Biology, vol. 789, Springer New York*, 2013, pp. 371,377. (Award winning paper, 'The Duane F. Bruley Travel Award')

Al-Armaghany, A. Bo Yu; Mak, T.; Kin-Fai Tong; Yihe Sun, "Feasibility study for future implantable neural-silicon interface devices," *Engineering in Medicine and Biology Society,EMBC, 2011 Annual International Conference of the IEEE*, vol., no., pp.3009,3015, Aug. 30 2011-Sept. 3 2011

Jianling Chen; Junhong Wang; Kin-Fai Tong; Al-Armaghany, A., "A GPS/Wi-Fi dual-band arc-shaped slot patch antenna for UAV application," *Antennas and Propagation Conference (LAPC), 2013 Loughborough*, vol., no., pp.490,493, 11-12 Nov. 2013

K. Tong; Hong-Jun Tang;A. Al-Armaghany.; Wei Hong, "Low-Profile Orthogonally Tripolarized Antennas," *Antennas and Wireless Propagation Letters, IEEE* , vol.12, no., pp.876,879, 2013

Balleri, Alessio; Al-Armaghany, Allann; Griffiths, Hugh; Tong, Kinfai; Matsuura, Takashi; Karasudani, Takashi; Ohya, Yuji: "Measurements and analysis of the radar signature of a new wind turbine design at X-band," *IET Radar, Sonar & Navigation*, 7, (2), p. 170-177,

Balleri, Alessio; Al-Armaghany, Allann; Griffiths, Hugh; Tong, Kenneth; Matsuura, Takashi, "The radar signature of the Wind Lens: A less disruptive wind turbine?," *Radar Systems (Radar 2012), IET International Conference on* , vol., no., pp.1,5, 22-25 Oct. 2012

Research Contribution

This corresponds to the novelty aspects of the work and general contribution to today's technology development of biomedical devices.

- The developed hybrid system is a novel diagnostic technique to assess blood volume change in superficial and deep tissue. Current non-invasive devices are limited to skin assessment, and therefore, measuring muscle responses is not achievable. The system uses microwave to induce heat and causes blood volume to increase. The applicator accommodates for the integrated NIRS probes to monitor the blood volume alterations. This approach has not been previously investigated.

- The applicator design was centred on thermal characteristics, where a high thermal conductive (HTC) substrate and superstrate were used. This was specially designed to consider active cooling, optical and temperature monitoring. Moreover, a superstrate material acting as a matching medium and isolation of radiating element to tissue was first time used with microwave patch antenna for inducing heat to tissue and the same time optimised for skin cooling efficiency. The presented work in this thesis shows results in EM and thermal point of view.

- One of the distinguished design feature is the considered skin cooling approach with use of peltier coolers. This is a novel approach which have not been employed by other therapeutic applicators, where water cooling is typically used. The cooling mechanism coincides with the applicator design and the optimised thermal material for increase cooling efficiency.

- The microwave system used is based on solid-state frequency synthesizer controlled by an Arduino microcontroller, which allows for greater flexibility, ad-

vanced monitoring and safety mechanism. The system introduces a sweeping function which allows for direct and self calibration of optimal operating frequency before every experiment. This feature is essential for applicators operating in close proximity to tissue (reactive near-field regions). This microwave system is integrated with cooling system for real time monitoring and control of exposure and temperature levels.

- This research work also explores circularly polarised applicators, which have not been previously investigated in greater depth, particularly with the current advancement in computation technology to solve complex EM problems. The presented work (simulation and validation) shows a virtually important characteristics, where the peak superficial tissue absorption of EM energy was significantly reduced while maintaining the muscle absorption. This investigation allows for future development of CP applicators for improved deep tissue warming with reduced superficial hot spots to the linearly polarised applicators.

Contents

List of Figures

List of Tables

Acronyms

ADC Analogue to Digital Converter

CW Continuous Wave

CP Circularly Polarised

DAC Digital to Analogue Converter

DAQ Digital Acquisition

DSA Digital Step Attenuator

DPF Differential Pathlength Fctor

EM Electromagnetic Wave

E-field Electric field

FFT Fast Fourier Transform

FM Frequency Modulated

HbO_2 oxy-hameoglobin concentration in micro molar per second

Hbb deoxy-hameoglobin concentration in micro molar per second

HbT Total hameoglobin concentration in micro molar per second

HPA High Power Amplifier

HTC High Thermal Conductive

LDF Laser Doppler Flowmetry

LDO	Low-dropout Regulator
LED	Light Emitting Diode
LP	Linearly Polarised
LHCP	Left Hand Circularly Polarised
LO	Local Oscillator
MBL	Modified Beer Lambert
H-field	Magnetic field
NIRS	Near-Infrared Spectroscopy
NTC	Negative Temperature Coefficient
NC	No Cooling
nTHI	normalised Tissue Haemoglobin Index
PCB	Printed Circuit Board
PTC	Positive Temperature Coefficient
PLL	Phase Locked Loop
PWM	Pulse Width Modulation
RP	Reflected Power
RF	Radio Frequency
RHCP	Right Hand Circularly Polarised
SAR	Specific Absorption Rate
SPI	Serial Peripheral Interface
SC	Skin Cooling
SRS	Spatially Resolved Spectroscopy

TMp Tissue Mimicked Phantom

TP Transmitted Power

TEC Thermoelectric cooling, TE module, Peltier cooler

TOI Tissue Oxygenation Index %

TM Transverse Mode

VCO Voltage Controlled Oscillator

VNA Vector Network Analyser

VSWR Voltage Standing Wave Ratio

Chapter 1

Introduction

1.1 Overview

Inducing local heating into biological tissue will increase the metabolic rate, which elevates the intermediate product known as metabolites. This process is responsible for causing vasodilation in the nearby vessels, which increase blood flow to regulate the excess of heat. Evaluation of the human thermoregulation system during an induced heating may provide further information to psychophysiology of various diseases or injuries. Currently, studies on thermoregulation have been limited to skin surface monitoring. It is easily to diagnose superficial tissue with the use of direct-contact resistive heating element integrated with skin perfusion meter to dilate and monitor the skin microcirculation. The monitoring technique is based on laser doppler flowmetry, which is commercially available.

Thermal responses can also occur in the muscle as it was indicated in the literature [1, 2]. In another study, it was demonstrated the muscle blood flow was increased by four times during warming [3]. Deep tissue such as muscle cannot be accessed. Invasive approach was employed to measure blood flow using radioactive tracer washout [2, 3]. This method was limited by the regulated usage of radioactive material, which restricted the study. The motivation of this work is the development of the device that is capable of monitoring deep tissue thermal responses. A hybrid microwave-optical probe is introduced in this thesis to provide a new non-invasive modality that can cause dilation in the muscle while monitoring the thermoregulation response of the tissue from the skin surface. This is based on the employed microwave applicator (therapeutic antenna) to induced EM energy muscle warming at a depth of 12.0-16.0 mm from the skin surface. The developed Near Infrared Spectroscopy (NIRS) system utilises optical probes to detect changes in blood volume and therefore tissue oxygenation in deep tissue. The configuration and the basic operation of the proposed hybrid probe in this thesis are illustrated in Figure 1.1. An LDF monitor was also integrated as a comparison tool for skin and muscle responses. The device integrates a cooling system, to reduce skin perfusion caused by superficial warming of interacting EM energy.

The growth of biomedical engineering is led by the collaboration between engineering and medical sciences. The diagnosis and treatment techniques for complicated medicinal problems have been leaping forward. The continuous developments in health care have significantly improved the quality of life, and overall increase in the survival

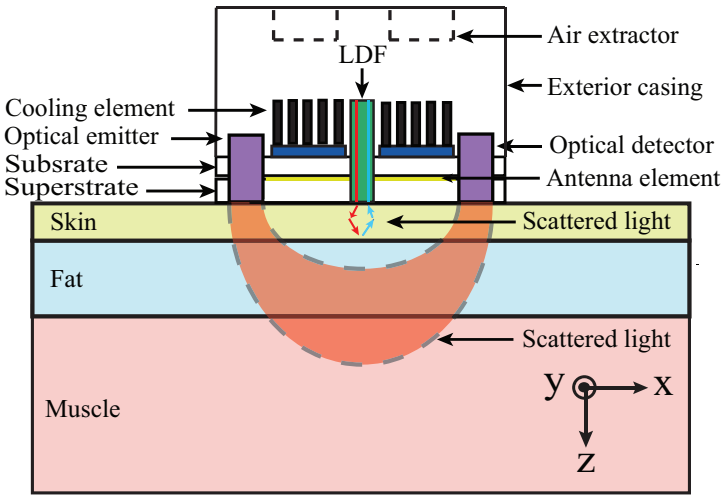

Figure 1.1: Hybrid probe concept model.

rate. Microwaves and Radio frequency (RF) devices are employed in medical application, including, implants telemetry, diagnosis, imaging and thermal therapy [4–6]. Radio frequency range between 300MHz-300GHz are known as microwave radiation [7], which are commonly used in daily devices. Microwave radiation also categorized as a non-ionising radiation for its insufficient energy to damage biological cells, unless significant power is applied to deliberately overheat the tissue for therapeutic applications [4, 8].

The interaction between Electromagnetic (EM) fields and biological tissue is known as bioelectromagentics, the biological tissue absorbs the EM energy, and in turn it is converted it into heat. In microwave radio frequency range, EM field currently is used in non-invasive thermal physiotherapy treatments, with typical applicators such as cavity backed dipole antenna for an external treatment [9]. One of the main disadvantages of such system is the poor efficiency in which the field aims at depositing into the tissue for deep heating treatment, always overheating the skin surface especially when driven by higher power source.

Biological tissues are complex media to investigate due to the numerous water compositions at different parts of a human body. Consequently, the tissue is a lossy dielectric medium, which absorbs the EM energy, and generates heat by the inter molecular vibration. This outcome causes the propagating microwave to attenuate inside the tissue. This is the fundamental reason why the non-invasive antenna arrangements must be efficiently coupled to the skin surface to deposit EM field to achieve greater pene-

tration depth. This work investigates the characteristics of biological tissue in relation to the performance of the radiated EM field.

1.2 Research Objectives

The general aim of this work is to develop a non-invasive device that is capable of warming and monitoring the tissue (muscle) while reducing superficial heating to provide a new insight of human physiology in deeper tissue. This involves the development and validation process of the hybrid system, which is based on microwave applicator for inducing heat and NIRS to monitor thermoregulation in tissue. To achieve this, the work is divided into smaller tasks.

- To develop an applicator that is capable of elevating muscle temperature by about 3.0-4.0 °C. The design needs to be directly contact to tissue to reduce leakage to the surrounding. The applicator design should be well coupled to tissue, reducing skin absorption and maximising EM energy into deeper tissue. The applicator must also be specifically designed to include the optical probes in the appropriate geometry. This part of work is largely reliant on EM simulation package.

- Integrate a cooling system to the applicator for mitigating the superficial hot spot produced by the absorbed microwave. With cooling element in mind, the design of the applicator must be carefully considered for efficient EM coupling and skin cooling simultaneously.

- In vivo, measurements will be the essential step in this project, by evaluating the physiological response introduced by the microwave warming on to human subjects. To achieve this safely, the fabricated applicator must be validated on tissue equivalent phantoms. This also needs to be fabricated with dielectric properties identical to biological tissue at the desired operating frequency. The simulation study can then be contrasted with the measured thermal distribution.

- Microwave source is required to induce microwave to the radiating element. The aim of this study to design a microwave system that is capable of supplying desired RF power with integrated power meter for safety features.

1.3 Thesis Outline

The achieved work during this PhD period is presented in this thesis

Chapter 2 provides general literature review corresponding to the investigation. This includes previous studies of therapeutic applicators and other employed techniques of inducing heat to the tissue. Moreover, this chapter also explores the current modalities of measuring change of blood volume and perfusion introduced by external heating. A comparison of methods has been outlined, highlighting the advantage of the hybrid system when considering deep tissue monitoring. The literature review is also expanded specifically within each chapter.

Chapter 3 introduces the general background theory, including interaction of EM energy into biological tissue. This is an essential chapter in understanding the behaviour of the absorbed EM field in a lossy dielectric medium. This includes early-stage study of SAR and evaluation of the biological heat generated by the deposited microwave energy. This chapter includes human physiological effect introduced by tissue heating.

Chapter 4 briefly describes the current *ex-vivo* techniques of evaluating applicators on tissue mimicked phantoms. Then one of the reviewed phantom recipes was used to develop multi-layered tissue. The dielectric property of each fabricated layer was measured and compared with the corresponding actual tissue properties. This part of the PhD was essential for validation of the developed applicators.

Chapter 5 shows the development procedure of the hybrid system. This includes specific background review, characterising microwave components and finally the combined operation. Detailed control system is presented with the integration of cooling element. This chapter ends with a brief discussion and operation of the used optical system.

With the system and the phantom being developed to allow for early stage study. The focus was shifted toward the core topic of this thesis, which was the linear polarised applicator design presented in chapter 6. This chapter introduces microstrip antenna theory, and the modelling techniques used for simulation study of each applicator. Three applicator designs were introduced in this chapter, and all were validated using thermal imaging of either on phantom or on human calf. The study conducted to evaluate performance of the applicator at different conditions, including composition of

tissue, proximity of applicator (superstrate thickness) cooling configurations and more.

Chapter 7 expands the applicator study into the excitation of circular polarisation, with detailed evaluation of feeding techniques. The antenna was modelled for SAR comparisons with the previous linear polarised design. The CP applicator was then developed and validated via thermographic imaging.

Chapter 8 presents the experimental protocol, safety precautions, tissue thickness measurement and finally the *in-vivo* haemoglobin concentration results for Applicator I & II. The chapter highlights the main goal of the hybrid system, by effectively measuring thermal response induced by the microwave applicator.

Chapter 9 this chapter concludes the work in this thesis and highlights the outcome of the results. This chapter ends with the future development of segment of the hybrid monitor.

Chapter 2

Literature Review

The literature review of general work in this thesis is presented. This investigates the heating technique conducted by other studies. Detailed literature on the RF applicators is presented, including therapeutic devices for cancer treatment or sport injury recovery of diathermy.

2.1 Induced Heating in Bioloigcal Tissue

The use of heat in medical applications dates back to approximately (2500 B.C.) in Egypt [10], and Rome in (200 A.D), where a hot iron used to provide superficial heating to tumour for pain relief, and in 1989 the use of hot-water circulation cisterns resulting in palliative effect for different tumours. Recently, microwave antenna and high intensity focused ultrasound (HIFU) are common applicators for hyperthermia treatment with various benefits and drawbacks. Hyperthermia induced by microwave is commonly used for superficial heating, caused by the attenuation in biological tissue, Microwave diathermy operating at 2.45 GHz is an example of superficial heating for physiotherapy treatments. Recent study suggests a non-invasive microwave applicator for superficial heating have an average depth of 10 to 40 mm depending on the operating frequency and water contents of tissue [11]. Microwave applicator also used to assist in cancer treatment in conjunction with radio and chemotherapy [12, 13]. Current research studies show the use of an antenna array for focused cancer hyperthermia treatments to achieve uniform regional heating [14]. HIFU provides a non-invasive local hyperthermia treatment for cancer at greater depth up to 60 mm in the tissue (operating between 1.0-3.0 MHz)[15], since ultrasound waves are less vulnerable to attenuation in the medium particularly in the fat layer. However, one of the limitations of HIFU is the obstruction of bone that can absorb or reflect the beam, and therefore introducing undesirable effects. Radio frequency applicators are considered for regional warming, simple to design and implement. However, the downside is fat burns caused by the E-field components which cannot be controlled [16]. This method is limited to superficial layer only. Th methods are listed and compare in Table 2.1

2.2 Electromagnetic Field in Therapy

The interaction of EM field with biological tissue dates back to the discovery of electromagnetic, in 1791 Galvni and Volts experimented the EM field effect on frog legs.

Table 2.1: Tissue warming techniques.

Technique	Advantage	Disadvantage	Comments
Ultrasound	50-100 mm depth, no hot spot in fat layer, no interference with temperature sensors	Localised heating, Require to be coupled to tissue, problematic if bone is present	Used for cancer treatment typically head and neck.
RF	Regional warming and simple to implement	Limited to tissue with thin fat thickness, E-field components cannot be controlled	Used for superficial cancer treatment
Microwave	can be miniaturised, hot spots can be mitigated	Limited penetration depth 10-40 mm, shielding is required particularly lower bands.	used in conjunction with chemotherapy for superficial cancer treatment

Not until 1927 when high-frequency currents were used by *d'Arsonval, Tesla*, at that point it was realized the potential of EM in localized hyperthermia [17], during same year diathermy was named, which had a meaning of "deep heating" and spread of EM. Recently, hyperthermia has been investigated not only for cancer treatment but also into physiological effect and for tissue muscle recovery and joint healing [1, 18]. On the other hand, EM applicators proved to be used for obtaining valuable information of biological tissues such as imaging, cancer diagnosis and implant communication [19]. Large amount of literature established on the antenna array for breast cancer diagnosis and imaging with use of radar techniques. [20, 21], while another literature shows the use of the antenna array for a non-invasive microwave hyperthermia, primarily for cancer treatment [22, 23].

2.2.1 Applicator Placement

Antennas and other electromagnetic devices are clinically used for therapeutic applications. Microwave hyperthermia can be achieved with use of invasive or non-invasive techniques as demonstrated in Figure 2.1 [7]. Figure 2.1a show an example of a non-

contact applicator, this approach typically has greater leakage to the surrounding environment, where treatment has to be implemented in a special isolated room [24]. A non-contact applicator will be of larger applicator size as it is not loaded to a high dielectric material, and therefore, heating area is also larger depending on the spacing of the applicator to the tissue (regional warming). Figure 2.1b is a typical microwave applicator operating in direct contact separated by a coupling medium, which is often a water bolus for skin cooling. This approach offer reduced microwave leakage, localised-regional warming, skin cooling and miniaturised applicator geometry[25, 26] This is approach was adopted for the Hybrid probe for ease of integration with optical probes. However, excluding the water bolus, where other means of cooling are explored in this work. Figure 2.1c is an interstitial probe for superficial confined heating area. This device is minor invasive (not required to penetrate the muscle), which is capable of raising local temperature by over 50 °C to effectively kill the tumour cells in a short exposure duration of 1-3 minutes. The main advantage of this approach is the heating directly localized to the area of interest. Figure 2.1d is also an interstitial probe for deep tissue, which is completely invasive. This is typically used for deep tissue ablation [27, 28].

The electric field produces heat in tissue when a capacitor plate applicator is used with typical operating frequency of 27.12MHz within ISM band. Capacitive heating is a simple method. However, the problem is the overheating of fat tissue caused by the large dielectric mismatch between fat and muscle layer that reflects and discontinues the perpendicular E-field components which is the most significant [29]. At low RF

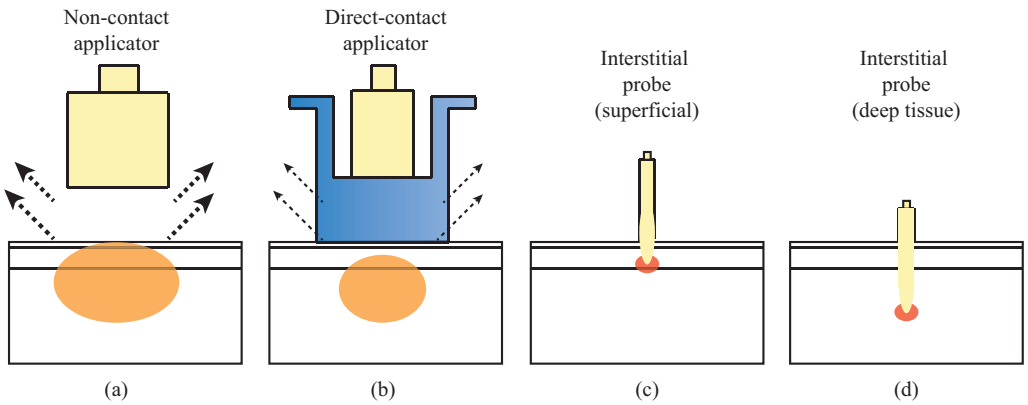

Figure 2.1: Microwave applicators in therapy. a) non-contact applicator, (b)non-invasive direct contact applicator, c) superficial microwave ablation, d) deep tissue microwave ablation

band the quasi-static condition is applied to solve Maxwell's equations. This is due to the fact the biological tissue becomes an electrically small object in comparison to a significantly large wavelength.

An alternative method for low frequency operation is by inductive heating, which is magnetically induced hyperthermia. A typical H-field applicator consists of a solenoid current loop or coaxial loop [30], where eddy current is induced in the tissue with the E-field is tangential to the skin interface, which minimises the overheating problem in the fat layer and thus increases penetration depth. Magnetic-field applicator typically operates at RF band such as 13.56, 27.12 and 40 MHz [19]. A noticeable problem with H-field applicator is the heating pattern, due to the fact the shape of the coil which produces a null or low temperature at the centre of the coil [31].

The final investigated tissue warming method is the radiative heating, which is the considered method for this project typically operating in the microwave frequency band. Unlike the low frequency RF applicators mentioned above where the quasi-static approximation is needed to be considered for the significantly large wavelength in comparison to the object dimension [32]. In the microwave radiative applicator, coupling of EM power into tissue have been achieved with the use of waveguides, dipoles and microstrip patch antennas [19, 33]. Microwave's applicators are generally more compact in size in comparison to RF applicators because of the shorter wavelength requirement, which also provide a selective focused heating in local area rather than regional. In addition further control can be achieved with microwave applicator with use of match loading or coupling medium to minimise skin warming and to provide uniform deposited energy in the tissue [9].

2.2.2 Microwave Applicators

Microwave hyperthermia currently investigated in frequency range of 433, 900 MHz and 2450 MHz. Therapeutic applicators with microwaves allow for non-invasive hyperthermia and microwave diathermy treatment, particularly used for superficial heating, due to the high absorption caused by the high-water contents of muscle tissue. Moreover, recent research has been encouraging in overcoming the problems of penetration depth by implementing beam forming antenna array, thus by focusing energy on the tumour site where all the energies are coherently added [23, 34]. Despite the penetration

depth limits for a single element applicator, microwave diathermy remains to be used clinically for superficial heating without causing heating or burns to the skin, a complete non-invasive method. Biological Tissue in the microwave operating region can absorb energy 7000 times more effectively than shortwave radio frequency [35], this is caused by the interaction of microwave with lossy and high-water content medium. The average depth of interest in microwave diathermy for rehabilitation is between 10 and 40 mm as a function of frequency [11]. Microwave diathermies have an advantage over ultrasound in superficial heating, particularly on the anatomical sites where the bones are present, whereas microwave can penetrate through [36].

2.3 Clinical Application

EM and thermal simulation were employed to study the heating pattern of a generic direct contact microwave applicator at 2.45 GHz, compared against a resistive heater. Both methods are based on an anatomical model, which includes all the necessary electrical and thermal properties as discussed in Chapter 3 and 6. The cross section thermal distribution results are presented in Figure 2.2. It can be seen with a resistive heater Figure 2.2a uniform peak surface temperature is achieved at approximately 42.6 °C. However, the peak temperature in the muscle is 38.7 °C, that is only elevated by 1.7 °C. In contrast; the thermal distribution with microwave warming in Figure 2.2b shows a superficial warming peaking at about 41.5°C and muscle warming approximately 41.5 °C. This is an increase of about 5 °C from original temperature of 37.0 °C. This basic study illustrates the difference between current clinical studies of superficial tissue warming using a resistive heater with LDF monitor in contrast to the hybrid system, which utilises microwave warming the muscle combined with NIRS, which measures blood volume in deep tissue.

Currently measuring thermal responses provide useful information on pathophysiology. The use of LDF with resistive skin heating element, is already established in many applications. In most cases, where local warming is induced to dilate the superficial tissue and measure the blood flow. Typical Applications, including assessment of amputation level [37], predicting outcome of burn wounds [37], human chronic spinal cord injury and free flap monitoring [38–40]. The main limitation of this modality, is measuring thermal response on superficial layer up to 2.0 mm. Therefore, measuring

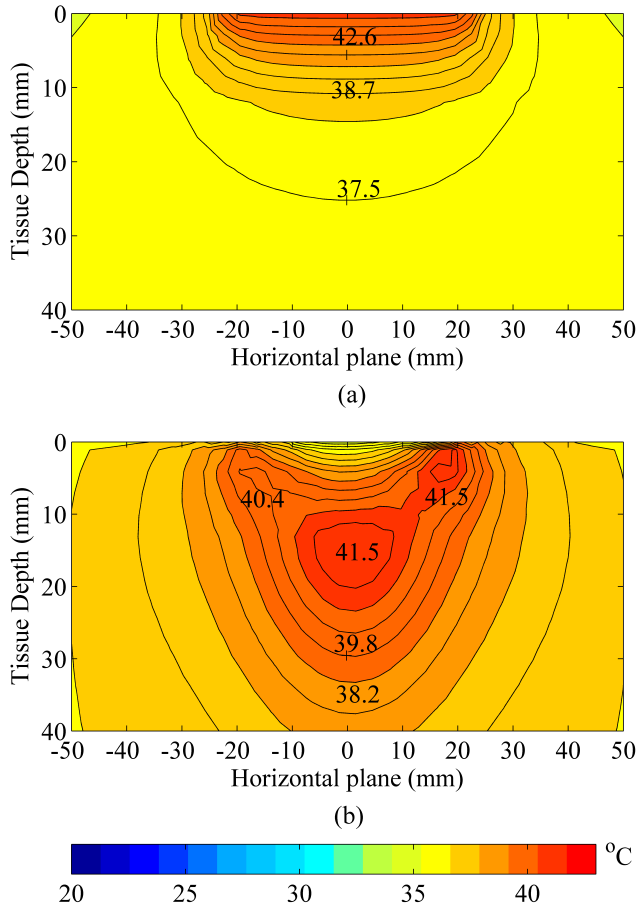

Figure 2.2: Cross sectional cut of thermal distribution for simulated direct contact Applicator against resistive heater: (a) resistive heating (b) microwave warming .

deep tissue thermal response may provide beneficial physiological information about a disease or tissue injury. Some work has been established on measuring muscle thermoregulation. This was achieved by immersing an animal in a hot-water bath [2], which is not sufficient for the limited penetration of the heat as shown in the thermal simulation. However, microwave applicators have been employed on human subject in many various therapeutic applications involving to heat up the muscle [1][3]. Those works were aimed at treatment, and there was no actual measurement or integration of the optical system to study blood flow in the muscle. This is where the hybrid microwave-optical probe is aimed to achieve. Starting a new modality technique, which can aid the physiotherapist in comprehensive evaluation of the already established application but with muscle responses. Table2.2 compares the current commercial available approach against the hybrid system.

Table 2.2: Comparisions of hybrid system with commercial aviliable devices

	Existing Approach	**Hybrid System**
Target warming	Skin warming	Deep tissue (muscle)
Warming technique	Resistive Coil superficial warming	Microwave deep and superficial warming
Thermal response measurement	Skin blood flow / perfusion (Superficial)	Blood volume and oxygenation changes
Measurement technique	Laser Doppler flowmetry	Near infrared spectroscopy
Remarks	Commercially available probe: Skin heating and LDF monitoring Probes:VHP1/2/3 (Moor Instruments)	Skin cooling is required to minimise microwave hot spot in the skin and fat layer

Chapter 3

Theory

This chapter covers the background theory of the propagating EM field in biological tissue. The EM interaction with a lossy dielectric medium such as organic tissue is a frequency-dependent problem. Moreover, the loss factor in the medium is directly related to the to absorption, which leads to tissue heating. The generated heat induces thermoregulation and physiological changes of the living biological medium. Therefore, the amount of heating required is defined to the particular application which must be identified before proceeding to any numerical or experimental study.

3.1 Electromagnetic Interaction in Biological Tissue

Electromagnetic (EM) field arises from electrically charged objects, excited by the fundamental force known as electromagnetism. The EM field is a force field with energy that capable of causing an act over a remote distance. This work focuses on EM field in microwave operating frequency, since the lower frequency region will have different characteristics when interacted with organic tissue. Electromagnetic device in medical application is a well-established field, with common known applications such as hyperthermia for therapy and radiometry for diagnosis on human subjects [23, 41]. However, other studies shown greater interest on EM field absorption in a biological body, and particularly on head models for mobile phone dosimetry [42]. Other studies looked into further details such as the interaction with biological membrane [43], with nervous system [44], and into molecular effects [45, 7].

The interface of EM waves in a biological system is vital for establishing the field behavior in the tissue. The interaction not only depends on the exposure of EM field but depends on the reaction of the organic tissue. The biological system is capable of neutralizing to external influences, especially of EM sources [7]. The compensation can be pathological, which imposes structural alteration, particularly with high power. Living system also exerts physiological effects to the elevated temperature inside the tissue, further detail in Section 3.2.

Organic tissue composites of water and ion content, therefore, human tissues are lossy dielectric medium, which can attenuate and absorb the propagating EM waves. The rate of deposited power per mass of tissue is known as specific absorption rate (SAR) [35]. The water content in the medium varies from one organ to another, yielding a complex non-homogenous medium that exerts additional complication to the prop-

agating microwave radiation. Furthermore, understanding the interaction and the behavior of EM field in biological tissue, it is essential to study the physics behind it by reviewing Maxwell's equations in a dielectric and dispersive medium. The study of EM exposure to biological media assists the development of biological antenna for deep tissue heating.

3.1.1 Wave Propagation in Lossy Dielectric Medium

The behavior of electromagnetic field propagating in biological media is determined by the dielectric properties of the tissue, since the human body is inhomogeneous in both physical and electrical properties. Every organic material in the body has its own relative permittivity, and each can vary in dielectric properties between healthy and deceased state. The electromagnetic field is often viewed as the combination of electric (E-field) and magnetic field (H-field). The E-field is derived from coulomb's law and expresses the interaction between two electric point charges, resulting in a vector field with unit of volts per meter (V/m). The movement of charges exerts another force between the charges, which is the magnetic field with units of Amps per meter (A/m). The magnetic flux density relationship is similar to the electric flux density but with use of permeability, however, biological tissues at high frequencies are non-magnetic and therefore assumed as unity value. When a material is subjected to an EM field, the charged particles of the material produce current and alter the wave propagation compared to in free space. In a homogeneous and linear medium, the dielectric constant is static. However, this is not the case in biological tissue a better approximation would be considered as a an anisotropic medium. The dielectric properties of the organic medium have dependence on frequency, temperature, polarization and location [46, 47]. In this situation the analysis of dielectric constant must be treated as complex permittivity with magnitude and phase, this is expressed with use Maxwell constitutive relations [7].

$$\overline{D} = \hat{\varepsilon}\overline{E} + \overline{P} \tag{3.1.1}$$

$$\overline{J} = \sigma\overline{E} \tag{3.1.2}$$

Where $\overline{D}$ is the electric flux density (C/m^2), which has proportional characteristics to the electric field $\overline{E}$ (V/m) in the dielectric medium. The complex permittivity $\hat{\varepsilon}$

(F/m) is the essential property that describes the interaction of E-field with material. The induced current density given in Equation 3.1.2 is defined as $\overline{J}$ (A/m^2), whereas σ is the electrical conductivity of the medium (S/m), like the permittivity both parameters are a function of field strength in a particular position inside the medium. In addition $\overline{P}$ is the polarization density or charge density, were applied E-field becomes polarized in a lossy dielectric material, due to the change or the addition in electric dipoles that corresponds to dielectric properties of the medium. The electric dipole moment is the measure of the overall polarity that is defined by the separation between positive and negative charges. The dielectric property of a medium is a function of frequency known as dielectric spectroscopy as shown in dielectric spectroscopy Figure 3.1.

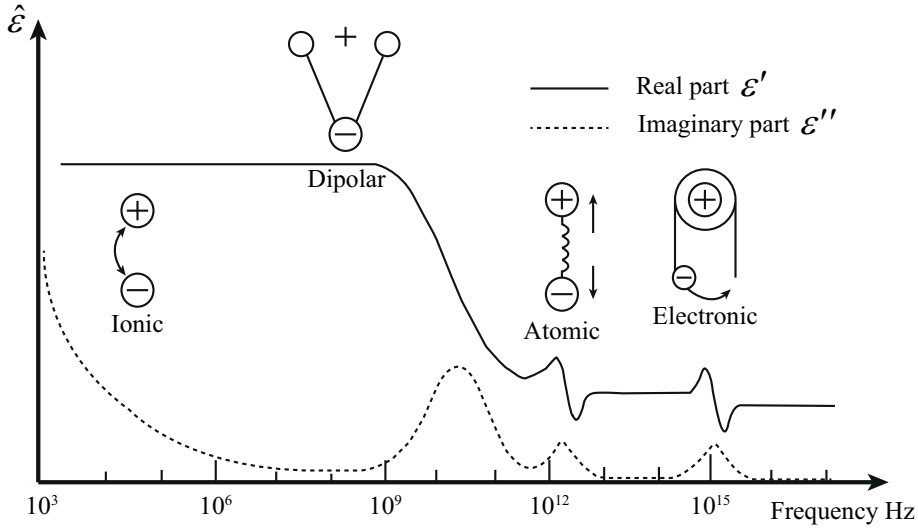

Figure 3.1: Dielectric spectroscopy [48].

The dielectric spectroscopy is a measure of dielectric properties as a function of frequency as shown in Figure 3.1. The frequency of EM field reflects to the material polarization. Moreover, the change in dipole polarization is not instantaneous to the applied EM field. The phase difference represents the response of the medium to an applied field, and hence the requirement of complex permittivity. In the microwave operating region, the interaction of E-field in a dielectric medium causes the electric dipole in the medium to change orientation and thus polarization, which can be expressed in detail with dielectric relaxation theory described by the Debye model in Equation 3.1.3.

3.1.2 Complex Permittivity

The exposures of EM field to biological tissue are generally characterized in a complex form with respect to relative permittivity, conductivity and angular frequency. The permittivity of a material are often normalized to the constant permittivity of free space $\varepsilon_o = 8.85 \times 10^{-12}$. The complex permittivity definition is defined by $\hat{\varepsilon}$:

$$\hat{\varepsilon} = \varepsilon_o(\varepsilon' - j\varepsilon'') \tag{3.1.3}$$

Where ε' the real part of the permittivity , while ε'' is the imaginary part of the permittivity, which is defined as out of phase loss factor that can be further elaborated into:

$$\varepsilon'' = \frac{\sigma}{\omega\varepsilon_o} \tag{3.1.4}$$

By substitution the previous equations, the complex relative permittivity of a lossy media is given by

$$\hat{\varepsilon} = \varepsilon_o\left(\varepsilon' - j\varepsilon''\right) = \varepsilon_o\left(\varepsilon_r + \frac{\sigma}{j\omega\varepsilon_o}\right) \tag{3.1.5}$$

From Equation 3.1.5 the real part of complex permittivity is also represented by to the relative permittivity of the medium $\varepsilon_r' = \varepsilon_r$. The imaginary part of the complex permittivity is related to the conductivity of the medium with respect to the angular frequency. The real part of the permittivity ε' is a measure of how much energy from an external electric field is stored in a material. The Imaginary part of the permittivity ε'', is the loss factor and it is a measure of how dissipative or lossy a material is to an external electric field. These values are used to describe the characteristics at single frequency as the value may change with frequency. The real part of the permittivity decreases with increasing frequency, whereas the conductivity increases with frequency. The relation between the imaginary and the real part complex permittivity defined as the loss tangent or the dissipation factor as shown in Equation 3.1.6

$$\tan\delta_e = \left(\frac{\varepsilon''}{\varepsilon'}\right) \tag{3.1.6}$$

The complex permittivity vector diagram, indicates the relative permittivity and the loss factor are 90 °out of phase. The loss tangent is the resultant angle which explains the ratio of the lost to the stored energy. The propagation of EM field in a medium induces current density from the moving charges of the free electrons. For a good a conducting material Maxwell's diffusion equation is used to demonstrate the exponential field

decay known as the skin depth δ_s in meters, given in Equation 3.1.7.

$$\delta = \frac{1}{\sqrt{\pi \mu f \sigma}} \tag{3.1.7}$$

] kin depth is an important parameter that can be beneficial, where it describes the penetration depth of propagating field with respect to conductivity and frequency. However, the biological medium not considered as a good conductors, where the current displacement current is a function of frequency. Consequently, significant attenuation is expected to the propagating wave. A general equation was found as shown below in Equation 3.1.8 [7].

$$\delta = \left(\frac{1}{\omega}\right)\left\{\left(\frac{\mu\varepsilon}{2}\right)\left[\left(1+\rho^2\right)^{\frac{1}{2}} - 1\right]\right\}^{\frac{1}{2}} \tag{3.1.8}$$

Where the resistivity $\rho = \frac{\sigma}{\omega\varepsilon}$, and $\mu = \mu_o$ for biological media. Skin depth is essential for frequency selection for particular application and medium.

3.1.3 Dielectric Relaxation

The EM dispersion in biological tissue can be characterised by the relaxation theory, which defines the time required for dipoles to be oriented or polarized when exposed to electric field. In 1957 Schwan provided significant enhancement in interpretations of different relaxation mechanism [49], and then introduced three types of relaxation regions $(\alpha_i, \beta_i, \gamma_i)$ to characterise the electric properties of biological tissue over a wide range of frequency. The γ dispersion operating in gigahertz region is induced by the polarization with water molecules. Whereas β_i dispersion operating at around hundreds of kilohertz is due to the polarization of the cell membranes and for even lower frequency α_1 dispersion occurs due to the ionic diffusion process. Each of these relaxation regions is characterised by a time constant τ, which is taken for the reorientation of the molecular dipoles, this can take as short as pico-second [47].

From Figure 3.1 dipolar relaxation occurs in the biological mediums at microwave radiation. The movement of dipoles and electric charges occurs due to the applied EM field, where the interaction is a function of frequency. The Debye relaxation model is often used to approximate the dielectric properties of material based on time constant τ [50], the relaxation mechanisms are not instantaneous. Debye model was derived from the frequency response of the first-order system, with complex permittivity in a

frequency domain as shown below considered for a single relaxation time.

$$\hat{\varepsilon} = \varepsilon_\infty + \frac{\varepsilon_s - \varepsilon_\infty}{1 + j\omega\tau} \tag{3.1.9}$$

Where ε_s is the static permittivity for lower frequency range at $\omega\tau \ll 1$, while ε_∞ is the infinite permittivity at high frequencies were $\omega\tau \gg 1$, and τ is the relaxation time constant recognized as the time constant of molecular polarization, as $f_c = \frac{1}{2\pi\tau}$, where f_c is the centre frequency. The Debye model [51] modified to account for the electrical conductivity is,

$$\hat{\varepsilon} = \varepsilon_\infty + \frac{\varepsilon_s - \varepsilon_\infty}{1 + j\omega\tau} - \frac{j\sigma_s}{\omega\varepsilon_o} = \varepsilon' - j\varepsilon'' \tag{3.1.10}$$

Where σ_s is the static ionic conductivity, this extension allows for approximation of losses in biological tissue caused by the conduction current of free ions. However, the derived Debye model so far only characterise for a single relaxation, and can be modified for multi dispersion or multi-poles for characterising the material over the wider frequency band. Moreover, the second-order Debye model was characterised for accurate approximations, particularly in a vast complicated mediums, give by:

$$\hat{\varepsilon} = \varepsilon_\infty + \frac{\varepsilon_{s1} - \varepsilon_\infty}{1 + j\omega\tau_1} + \frac{\varepsilon_{s2} - \varepsilon_\infty}{1 + j\omega\tau_2} \tag{3.1.11}$$

Biological tissue can impose further complication due to its composition, the Debye theory can account for multi dispersions regions as discussed, however it does not account for the broadening of the dispersion that caused by the composition of tissue. The was resolved by the introduction of the distribution parameter α_n to the Debye model, this solution is known as Cole-Cole equation given below, where $\Delta\varepsilon_n = \varepsilon_s - \varepsilon_\infty$ [52]:

$$\hat{\varepsilon}(\omega) = \varepsilon_\infty + \sum_n \frac{\Delta\varepsilon_n}{1 + (j\omega\tau_n)^{(1-\alpha_n)}} + \frac{\sigma_s}{j\omega\varepsilon_o} \tag{3.1.12}$$

To summarise, the electrical properties of biological tissue over wide-band frequency can be approximated with use of Debye or Cole-Cole models based on relaxation theory. This theory is vital for numerical calculation with accurate approximation of dielectric properties of a large bandwidth analysis such as the case with Gaussian pulse. Moreover, the Cole-Cole dielectric relaxation was applied to the simulation model in this thesis (CST microwave studio) producing best-fit tissue electrical properties as a function of frequency.

3.1.4 Dielectric Properties of Biological Tissue

The electrical properties of biological tissue are previously measured by *Gabriel et al*, which is available in the literature [53, 54]. The frequency range of the measurement was between 10 Hz to 20 GHz with the use of the open-ended coaxial probe for impedance measurements. A parametric model was later developed based on Debye and Cole-Cole model to describe the changes in dielectric properties as a function of frequency [52]. The model can function from 10Hz up to 10 0GHz with a large database of biological tissue samples. However, for this thesis only the primary tissue layers are required and used for the numerical study. Table 3.1 shows the extracted electrical properties (Cole-Cole model) of the primary tissue layers at a single frequency of 2.45 GHz . The data shows clearly the muscle has significantly greater relative permittivity (about 10 times) and electrical conductivity in comparison to the fat layer. The loss factor in the muscle indicates large attenuation in muscle, which causes an increase in E-field absorption in the tissue. The skin layer also considered as a lossy medium after the muscle. Based on the Cole-Cole model it was possible to plot conductivity of the primary used tissue as a function of frequency as shown in Figure 3.2. It can be observed, the conductivity increases with the frequency caused by the interaction with water molecules, which acts as a short circuits at the upper frequency range [51]. In Figure 3.3 the relative permittivity decreases with increasing frequency, and the change is unnoticeable for fat tissue over frequency range.

Figure 3.4, shows the penetration depth dependency with frequency for the selected biological tissue. The penetration depth also known as the skin depth (previously discussed), which is defined at the propagating field reduces by approximately

Table 3.1: Properties of biological tissue at 2.45 GHz [52].

Tissue	Relative permittivity	Conductivity (S/m)	Penetration depth (mm)	Density (kg/m^3)
Skin	38	1.46	11.07	1100
Fat	5.33	0.10	52.06	910
Muscle	52.86	1.71	9.88	1041
Bone	11.38	0.39	9.88	1850

36.8% of its original value [51]. The penetration depth decreases exponentially with the increasing frequency. This shows an inverse relationship with the previous figure of the conductivity. Fat tissue has the greatest penetration depth because of the low conductivity.

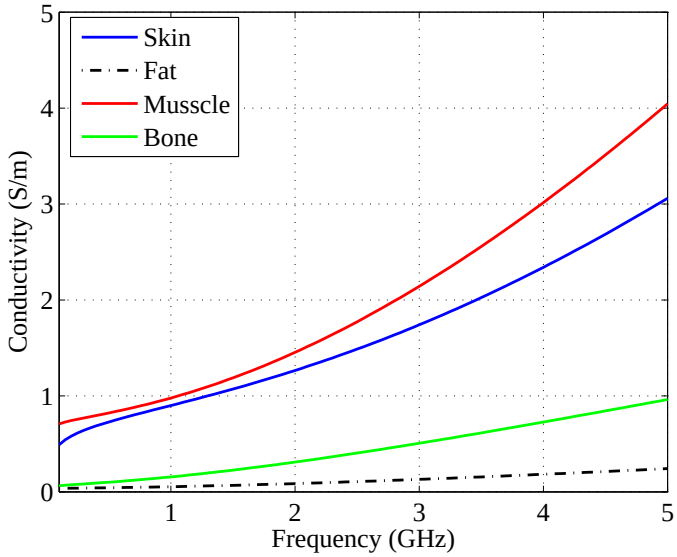

Figure 3.2: Conductivity of biological tissue as a function of frequency.

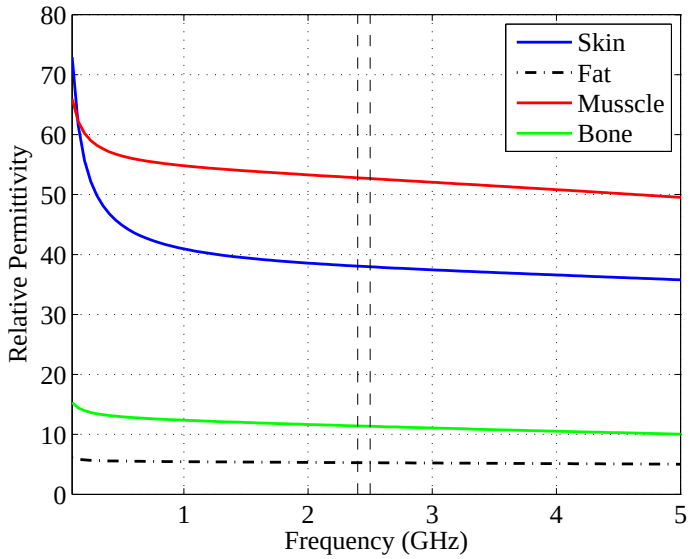

Figure 3.3: Relative permittivity of biological tissue as a function of frequency.

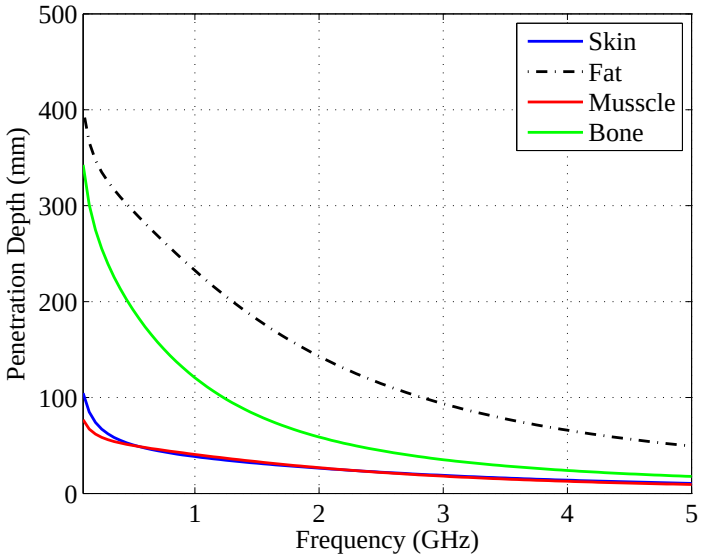

Figure 3.4: Penetration depth of biological materials as a function of frequency.

3.1.5 EM Interaction Between Two Dielectric Medium

So far, the interaction and the characteristic of propagating EM energy was considered in an isotropic medium as a function complex permittivity. In reality, biological medium is inhomogeneous and consists of numerous layers with different dielectric properties. For simplicity, the propagation of EM wave can be considered as optical propagation. This study introduces the wave impedance (η), reflection (Γ) and transmission coefficientsT_in. Figure 3.5 illustrates a schematic of propagating propagation EM wave in medium-1 with a particular wave impedance of (η_1) incident on the tissue boundary of medium-2 with a new-wave impedance of (η_2)[51]. Assuming medium-1 is air and medium-2 is biological tissue, where $\eta = 120\pi$ in free space. The incident perpendicular field component (P_i) will partially reflect from the surface of the second medium (P_r) caused by the difference of electrical properties. The transmitted field (P_t) will experience slower velocity and shorter wavelength as demonstrated in Figure 3.5. This is a similar process to the tangential fields, where E_i corresponds to the incident electric field, E_r is the reflected and E_t is the transmitted field.

The reflected field can be characterised by the reflection coefficient, that is defined as the ratio of reflected field intensity to the incident field, as demonstrated in Equation 3.1.13. The expression for the transmission coefficient is the ratio of transmitted field

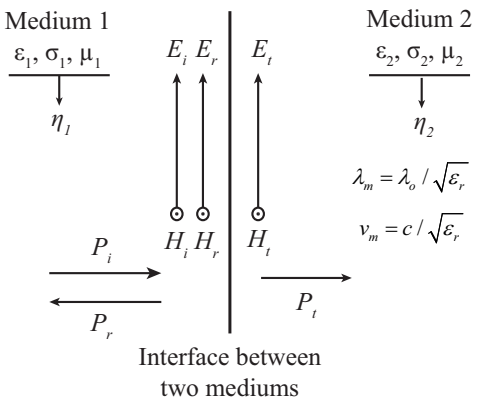

Figure 3.5: General EM field transmission and reflection at different medium.

to the incidence given in Equation 3.1.14.

$$\Gamma = \frac{E_r}{E_i} pp \tag{3.1.13}$$

$$T_p = \frac{Et}{E_i} \tag{3.1.14}$$

Where $E_i = \eta_1 H_i$, $E_r = -\eta_i H_r$ and $E_t = \eta_2 H_2$. The expressions are expanded in terms of wave impedance shown below in Equation 3.1.15 and 3.1.16

$$\Gamma = \frac{\eta_2 - \eta_1}{\eta_2 + \eta_1} \tag{3.1.15}$$

$$T_p = \frac{2\eta_2}{\eta_2 + \eta_1} \tag{3.1.16}$$

The general wave impedance can be estimated from the ratio of the electric to the magnetic field of the propagating wave in the particular medium shown in Equation 3.1.17[55].

$$\eta = \sqrt{\frac{j\omega\mu}{\sigma + j\omega\varepsilon'}} \tag{3.1.17}$$

The reflection and transmission coefficient are derived further to evaluate for perpendicular and tangential components. Furthermore, the equation solves for different angle of incident generalized from Snell's law [51].

3.1.6 Dosimetry

The propagating EM waves are absorbed by the biological medium, the rate of energy absorbed is associated with the loss factor of the tissue. The standard measure

of dosimetry is the rate of energy absorbed per unit mass, and hence the specific absorption rate. The SAR is a time derivative of the applied energy (dW) absorbed by the mass derivative (dm) in a volume (dV) with a given mass density (ρ_i) as shown in Equation 3.1.18 [7].

$$SAR = \frac{d}{dt}\left(\frac{dW}{dm}\right) = \frac{d}{dt}\left(\frac{dW}{\rho_i(dV)}\right) \tag{3.1.18}$$

The expression can then be evaluated to describe the EM field energy inside the biological tissue with respect to the electrical properties. The energy absorbed by unit mass is relative to the electric conductivity and density of the medium. This is shown below in the general SAR equation.

$$SAR(x, y, z) = \frac{\sigma}{2\rho_i}|E(x, y, z)|^2 \tag{3.1.19}$$

Where σ is the electrical conductivity of the medium, and E is the propagating electric field components in the x, y, z direction. The SAR is in W/kg and is based on the listed parameters for 2.45 GHz (for this work) in Table3.1 The SAR is classified into whole-body average and local peak average. The whole-body average SAR estimates the elevation of core body temperature. When the tissue absorption increases it means the temperature has elevated, which, therefore, could lead to tissue damage if the absorption requirement was exceeded [56]. While local SAR is applied for a confined region, for example, mobile phones RF exposure to human head [57].

There are two local SAR limits that must be adopted for commercial devices such as mobile phone operating in near-field to the human brain. The ANS/IEEE C95.1 applied for United States, with an exposure limit of 1.6 W/kg for a $1g$ of cubic average [58] The ICNIRP in European union developed an exposure limit of 2 W/kg [59]. While the whole-body exposure for both standards is 0.08 W/kg. However, for medical purposes, the limit is significantly higher, such as in therapeutic devices, where the tissue temperature is elevated to 42-45 °C. To achieve such temperature, the SAR must be approximately 235 W/kg and the power delivered to the applicator was 27.3 Watts [60]. In the hybrid applicator the delivered power is only 3 Watts RMS. The study SAR for applicator development is a significant step to a safe exposure of microwave. The SAR is sensitive to many characteristics of the applicator, including operating frequency, polarisation and proximity.

In the early stages of this work, the SAR as a function of frequency was studied in a simple EM simulation. The investigation was based on a plane-wave EM boundary condition and biological medium model, which consisted of skin, fat and muscle. The detail of simulation method will be discussed in Chapter6 Section 6.4.1. The numerical results are presented in Figure 3.6, which are normalised SAR. In the first scenario, where the skin thickness was 2.0 mm, and fat was 10.0 mm. The SAR was based on 1g of tissue averaging. The skin absorption for 2450 MHz was 50 % higher than operating at 915 MHz and a 310% increase from 450 MHz. The SAR in the muscle is dominated by the lower frequency bands of 915 MHz and 434 MHz. Operating at 434 MHz the loss factor is inferior to the other operating frequencies. Consequently, higher power is required to achieve the required SAR. Figure 3.6b shows the normalised SAR for 1.0 mm skin and 7.0 mm fat layer. By inspection, the absorption at 2450 MHz is significantly high at the skin surface than the previous study. In contrast, operating at 915 MHz and 434 MHz presents no significant change when the tissue thickness was varied. This study indicates operation at higher frequency is a function of skin and fat thickness because of the short wavelength. This is vital to study with the actual applicator, as the result indicated the tissue warming can be significantly different with respect to tissue thickness.

The specific absorption rate can be directly related to temperature as shown in Equation 3.1.20. The SAR can be determined by measuring the E-field at a desired

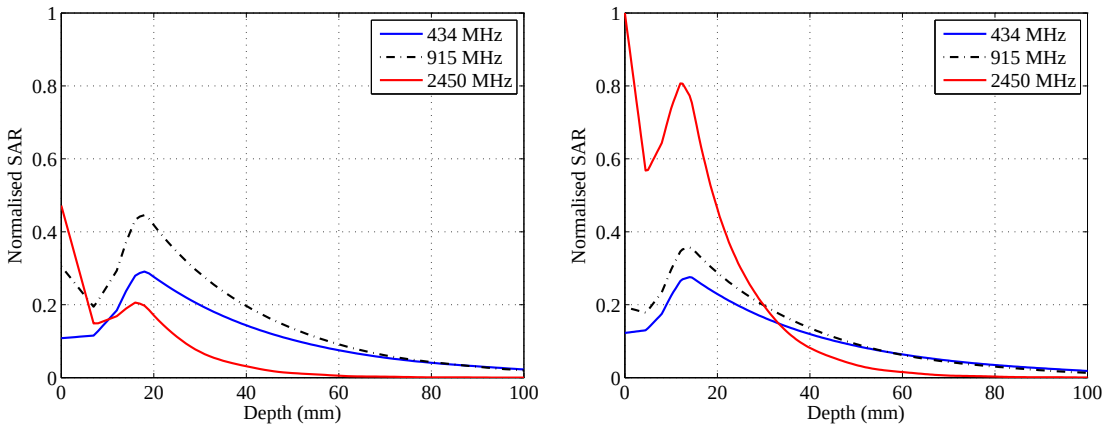

(a) (b)

Figure 3.6: Simulated SAR as a function of frequency in the multi-layered biological medium with the skin, fat and muscle thickness of (a) 2.0,10 and 200 mm, (b) 1.0,7.0 and 200 mm

location or point, these measurements can be implemented for phantoms study, typically with mobile phones with head models. Where C is the specific heat capacity of the tissue exposed to E-field $(J/kg\,^{\circ}C)$, ΔT is the temperature difference between the elevated temperature and the core temperature of the tissue before exposure $(\,^{\circ}C)$. Whereas Δt is time duration of the exposure.

$$SAR = C\Delta T/\Delta t \tag{3.1.20}$$

Moreover, for enhanced estimation of the elevated temperature the expression is expanded to account for cooling mechanisms of the biological tissue. This is based on the following Equation 3.1.21 found in literature study[13]. Where P_m is the metabolic heating rate, P_c and P_b are the dissipated power by thermal conduction and blood flow per unit volume respectively.

$$\frac{\Delta T}{\Delta t} = \frac{(SAR + P_m - P_c - P_b)}{C} \tag{3.1.21}$$

Figure 3.7 demonstrates a typical diathermy transient temperature change in tissue with and without blood flow [13]. This schematic are typically used to estimate SAR with the use of Equation 3.1.20 and 3.1.21. Consequently, the rate of tissue absorption can be estimated from the linear slope in the first 3-minutes of exposure. After 10-minute of microwave exposure the temperature difference ΔT is large enough to start the vasodilation process, which acts to dissipate the applied heat away with the aid of thermal conduction. In contrast, tissue without blood flow the temperature continues to elevate until it reaches the steady state. At this point, equilibrium is met and therefore, $SAR = P_c$. In the scenario with the dilated tissue, the heat dissipation increases with the blood flow, which halts the temperature curve from further elevation and forces early steady state at lower temperature level (SAR=$P_c + P_b$). The figure clearly indicates the significance of ensuring a safe level of deposited energy by taking into the consideration if the subject or the diagnosed site is poorly dilated. Therefore, temperature is increased beyond the safety level, caused by the poor blood flow and therefore, heat dissipation. This study can be also used in the same manner to the approximation of blood flow rate (m_{bf}) in the muscle by estimating the slope decline produced by the vasodilation with the use of following Equation 3.1.22[13].

$$m_{bf} = p_b/k_2 C_b \Delta T' \tag{3.1.22}$$

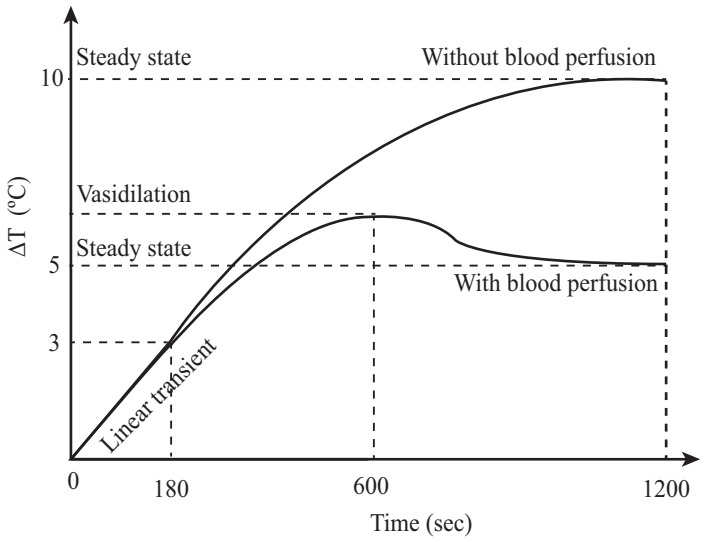

Figure 3.7: Schematic of transient exposure against the temperature change in a human tissue with and without blood flow [13].

Where p_b is the density of blood, $k_2 = 0.698$ is a constant, C_b is the specific heat capacity of blood. For therapeutic such as hyperthermia, the exposure power must be increased sufficiently to override the blood flow cooling effect. In contrast, for hybrid system, the induced cooling mechanism is the sole purpose of this PhD work. The intended power is low and just sufficient to dilate the tissue for monitoring the thermoregulation process.

3.2 Thermal Therapy

Tissue warming such as hyperthermia is a general physical therapy in which temperature raised between $41°C$ to $45°C$ while maintained over time period [9]. Temperature elevation in biological tissue for any therapeutic application is determined but the energy deposited in the tissue and the physiological response of the human body. The amount of heat produced is defined by joule's law, specifying the produced heat is directly proportional to the square of the field intensity, the resistance of the media and duration of the exposure [61].

The deposited energy via microwave and other EM applicators has further complications with dependency to operating frequency, input power, polarizations of the field and tissue electrical properties. In addition, these factors determine the penetration depth at which EM can propagate through the medium. With heat is generated

due to the absorbed EM energy, human body responds to the change in temperature with the increase in blood flow caused by the dilated blood vessels to diminish the excess of heat from warm to normal regions. The physiological responses can increase the healing rate in diseased or damaged tissue due to the increase in white blood cells and antibodies while the increase in transport taking away the toxin and debris away from the treated area. In addition, the heating provides decreased muscle spasm and promotes pain relief and relaxation [9, 61].

3.2.1 Bioheat Transfer

The temperature elevation inside the human body is determined by absorption and transfer of energy or heat, where the absorbed energy is proportional to the operating frequency and electrical properties of the tissue. The energy transfer is due to the metabolic rate and the generated blood flow in the biological tissue. The human thermoregulatory system maintained body temperature of about 37 °C at a wide range of environmental conditions. The blood flow in the body varies depending on three factors [62]:

- Body metabolisms, where the blood transport oxygen to entire body and takes away carbon dioxide from cells.
- Heat transferee for system thermoregulation, where the blood can have dual influence to increase or decrease in temperatures, it can act as a heat sink to cool down the local tissue, or it can be as a thermal source.
- Vascular system is essential in regulation of blood pressure to allow alteration of blood flow distribution leading an increase the cardiac output to maintain blood flow in a thermal stress region.

From the discussed three factors, it can be drawn that the blood flow serves its function as to remove or release heat. Penne's in 1948 [63] introduced the bioheat equation, which considers the effect of blood in tissue modelled as a heat source or sink. this was modified to include external heat sourcee such as EM exposure (defined by SAR) as shown in Equation 3.2.1. The equation is used in the simulation model to study the thermal distribution by the induced EM power of the applicator.

$$\rho_i C \frac{\partial T_t}{\partial t} = k\frac{\partial^2 T_t}{dx^2} + k\frac{\partial^2 T_t}{dy^2} + k\frac{\partial^2 T_t}{dz^2} + \omega_b C_b (T_a - T_t) + Q_m + \rho_i SAR \qquad (3.2.1)$$

Where, ρ_i is the density of the tissue (kg/m^3), C is the heat capacity of the medium in $(kJ/(kgK))$, k is the thermal conductivity ($W/(mK)$), ω_b is the blood perfusion rate in volume ($kg/m^3/s$), T_t is the temperature elevation in °C, Q_m is the metabolic heat generation in the tissue and T_a is the constant body temperature 37 °C. ρ(SAR) is the absorbed power density caused by the exposure of the microwave radiation. In the model the blood perfusion is assumed to be uniform across the entire tissue.

The transient thermal simulation is based on Equation 3.2.1 requires the thermal properties of the biological tissue. The parameters are listed in Table 3.2 which are collected from multiple literatures, including the built-in library of the simulation package [35, 64]. Simulation also requires tissue response and thermal properties, which are obtained from literature [35, 65] as shown in Table 3.2. It can be seen clearly the metabolic rate and blood flow coefficient of skin is significantly higher than muscle and fat.

The microwave thermal therapy is categorised into three levels based on the elevated temperature as shown in Table 3.3. The table lists physiological effects, and the clinical applications based on the elevated temperature [56]. Low temperatures of up to 41.5 °C is a generally unharmed region with use microwave diathermy, intending to increase the metabolic rate for physiotherapy treatment. This temperature range is sufficient for vasodilation and therefore, can be the operating region of the hybrid system. While temperatures of up to 45 °C, this is the upper limit without causing immediate cell death, this region generally applied to non-invasive cancer hyperthermia in conjunction with chemotherapy. Temperatures between 45-50 °C are not commonly

Table 3.2: Thermal properties of biological tissue [35, 65].

Tissue	Thermal Conductivity $W/(mK)$	Specific heat $kJ/(kgK)$	Bloodflow coefficient $(W(m^3K))$	Metabolic rate W/m^3
Skin	0.293	3.50	9100	1620
Fat	0.201	2.50	1700	300
Muscle	0.530	3.55	2700	480
Bone	0.410	1.3	3400	610

Table 3.3: Applications of thermal therapy at different temperatures

	Low temperature 40-41.5$^{\circ}C$	**Moderate temperature 42-45**$^{\circ}C$	**High temperature** $>$**50**$^{\circ}C$
Application	Diathermy for physiotherapy	General non-invasive hyperthermia	Invasive thermal ablation
Effects	Increase blood flow and Metabolism in tissue	Improve sensitivity to all radiation therapy, by increasing tumour blood flow and cell oxygenation level	Cell damage, coagulation and vaporization
overall	Aid in accelerating tissue repair	Cell death overtime duration	Rapid cell death

considered for non-invasive devices, due to the increase in microwave exposure to the surroundings. High temperature with range of 50-100°C uses an invasive method with microwave or RF probe (also known as catheter) inserted inside the body. This has become an important therapy for Cardiac Arrhythmias, in which the heart beats irregularly [66]. This technique is known as RF ablation.

3.3 Chapter Summary

This chapter has covered the principles of EM propagation in a lossy media such as the biological tissue. The permittivity of the medium is a complex function, which was derived. The complex permittivity consisted of dielectric constant of the medium and the loss factor. This was extended to understand the dielectric properties as a function of properties, few models were derived for biological tissue estimation such as the Cole-Cole model. The wave impedance of an EM field interfacing between two dielectric medium has been characterised. Moreover, the transmitted wave was evaluated in terms of the amount of energy was absorbed by the tissue. The absorption mechanism is combined with a thermal model to characterise the elevated heat from the absorbed EM energy as a function of the cooling mechanism of biological tissue. This chapter will contribute to the understanding of the simulation models.

Chapter 4

Tissue Mimicked Phantom

4.1 Background

Biological tissue compromises of complex structure from anatomical composition to frequency-dependent electrical properties. Radiating devices are often approved through numerous validation methods before applied for human trials (*in-vivo*). Simulation's studies cannot be entirely relied on prior to clinical trials. Researchers require early stage *ex-vivo* testing of various medical modalities. This had been achieved with use of tissue mimicked phantom (TMP). Phantoms have already been used for development and testing of many medical diagnosis and treatment's applications, such as in PET/CT scans, ultrasound, RF heating and MRI thermal monitoring [67–69]. In EM field, TMP is designed specifically to mimic the dielectric properties of biological organs at predefine frequency range; operating at ultra-wide band (UWB) and some at a precise desired band[70].In field of microwave; phantoms are typically used to evaluate SAR, thermal distribution and breast cancer detection of microwave antennas [71, 69, 72]. For RF applications TMP can be fabricated indifferent states such as liquid [73], semi-solid [74, 70] and solid [75, 76].

Liquid phantom's are often used to mimic the average dielectric properties of tissue. This is achieved by controlling the concentration of water, sugar and salt. Water and salt increase the permittivity and conductivity respectively, while sugar reduces the relative permittivity. Liquid phantoms are low-cost, simple to make and easily produced in large volumes. They are typically used for antenna SAR measurements; however, it is not ideal for multi-layered thermal distribution measurements. In contrast semi-solid phantoms are commonly used for thermal distribution mapping, and heterogeneous structure can also be produced for realistic validation. The common materials of semi-solid phantom are either a polyacrylamide or gelatin based. Literature study reveals polyacrylamide based phantom are frequently used for hyperthermia studies as it can mimic electrical properties and also thermal properties of biological tissue [74, 77]. The down side of polyacrylamide is the limited shelf life of just few hours (can last longer when stored in an air-tight container) and restricted availability of chemical ingredients. Alternatively, oil-in-gelatin based phantoms are much more attractive due to longer shelf time (over nine weeks) ,wideband characteristics (500 MHz to 20 GHz), and construction of heterogeneous phantom [70]. Tissue mimicked phantoms with little oil are appropriate for high-water content tissues, while phantom

samples with a high percentage of oil are suitable for low water content tissue. Consequently, the dielectric constant of the phantom sample decrease with increasing oil percentages relative to other ingredients. The permittivity of the oil is 2.5 at 6 GHz while the electric conductivity is approximately 0.05 S/m. Preservatives are typically added to prevent the spread of bacteria and extend shelf life. il

4.2 Phantom Preparation

The fabrication of TMP requires the appropriate ingredient percentage for optimum tissue electrical properties at desired frequency, which was obtained from the literature [70]. The amount of ingredients required is calculated based on volume of the final molding for three-layered phantom and additional samples of each layer for dielectric measurements. The volume calculated based on the 12 cm diameter of air tight cylindrical container. The ingredients were not precisely of similar products to the literature, such as the use of higher strength 225 bovine bloom gelatin rather than 200 calfskin based bloom gelatin. The purpose of gelatin is to solidify the sample, however, derived from different animal will have some effect to the electrical properties. The oil concentration is based on 50% safflower oil that is commercially available and another 50% based on paraffin (Kerosene). Table 4.1 contains the phantom ingredient and concentrations mimicking tissue properties at 2.45 GHz adopted in this thesis. The construction procedure requires uniform temperature, which was achieved by immersing the solution beaker into a heated water bath. The detailed step of fabrication is based on the literature with some necessary modification as shown in Appendix A. The procedure, used in this thesis, for each layer is produced in the following order as described below.

Muscle layer:

The preparation of a muscle phantom is straight forward as it only requires approximately 8% oil concentration, which can be easily mixed with the water. Table 4.1 gives the corresponding weighting in percentage of the required materials to mimic the muscle phantom. The actual weight values are based on the calculated desired phantom volume.

Fat layer:

Fat has the lowest water content of the other tissues. To mimic the fat, concentration of oil increased to approximately 80% of the entire ingredient, hence making fabrication

process challenging as it becomes difficult mix water and oil togther. Slight modification is necessary to the method by gradually pouring the oil solution to the gelatin solution at 50%, important to maintain a uniform emulsion at all time. This procedure requires more time and better temperature control to maintain the solution at 50 °C. The volume of the solution is calculated based on the diameter of 12 cm and thickness of 10mm. The fat layer is molded on top of the muscle layer, separated by a cling film. This detachable approach between the two layers allows for future measurement of thermal distribution using IR camera on the muscle surface, by immediately removing the superficial skin and fat layer. The molded fat layer was not flat surface, resulted by the quick solidified solution

Skin layer:

The fabrication of skin phantom is equivalent to the muscle, although the skin has marginally lower water content, hence higher oil concentration of up to 30%. The volume measurement of mimicked skin is based on the same standard 12 cm diameter but with 2 mm thickness, achieving such thickness can be challenging. This is due to the molding of the fat was not uniform surface; therefore, the corresponding skin thickness can vary. To achieve 2mm thickness at the central location, a marked needle was inserted in the center as a guide when the solution of the skin layer is molded on top of the fat layer.

Table 4.1: Phantom Ingredients for all layers

Tissue type	n-propanol %	p-tolic acid %	De-ionized water %	Gelatin %	Formaldehyde %	Paraffin %	Safflower oil %	Detergent %	Total weight (grams)
Skin	2.48	0.06	59.03	10.56	0.25	13.08	13.08	1.46	22.62
Fat	0.76	0.02	18.08	3.24	0.08	37.40	37.40	3.00	113.10
Muscle	3.12	0.08	74.15	13.27	0.31	4.25	4.25	0.45	565.5

4.2.1 Dielectric Measurement Principle

All materials exhibit electrical characteristics that rely on its dielectric properties, which can be measured in numerous methods. Moreover, it is possible to measure the dielectric properties of the phantom over the desired frequency range for validation with actual tissue measurement. There are at least five common methods of measuring dielectric properties, including Parallel plate, coaxial probe, transmission line (free space and waveguide) and resonant cavity. Many factors must be considered for the appropriate method such as operating frequency, sample dimension, sample state (liquid, powder, solid), material contact, material loss, temperature and measurement conditions. Table 4.2 shows the basic characteristics of dielectric measuring techniques [78, 79]. The parallel plate approach is not considered due to operation on significantly low frequency range. The operating frequency is one of the fundamental factors; it can be seen from the table only open ended coaxial probe and transmission line methods covers the frequency of interest at 2.45 GHz. The accuracies of the instruments are also dependent on the electrical losses of the material. The open-ended coaxial probe offers good accuracy for a lossy dielectric medium; however, the accuracy decreases with the lower dielectric medium. Transmission line (waveguide) is an alternative low cost solution, as long as the specimen is inserted along the transmission line between two waveguide or probes. Resonant Cavity and Free space approach both provide the best possible accuracy but with a downside of frequency, sample size and possible destructive approach.

The open-ended coaxial probe was used in this research. It is a common dielectric measurement technique, used in many applications with high-water content samples,

Table 4.2: Dielectric measurement techniques [78, 79].

	Frequency	Material loss	Sample size	Accuracy
Coaxial probe	0.02-50 GHz	High	Small	1-10%
Resonant cavity	5-80 GHz	low	Small	0.1-2%
Free space	5-500 GHz	Moderate	Large	1-2%
Transmission line	0.05-70 GHz	Moderate	Moderate	1-5%

including biological tissue and phantom characterisation. The measurement technique is achieved by immersing the probe in the liquid or firm contact on a flat surface of the solid, which is a non destructive. Typically, The probe is connected to a calibrated Vector Network Analyser (VNA) and emits EM fringing field into the sample; The field is associated into complex permittivity. This measurement technique is known as the input reflection coefficient, or the scattering parameter $|S_{11}|$, the VNA needs to be calibrated to ensure the reflection coefficient is from the instrument end. The dielectric measurement setup of phantom is presented in Figure 4.1a, using a N5244A PNA-X microwave network analyser operating between 10 MHz to 67 GHz. In conjunction with PNA, a high temperature open ended coaxial probe by Agilent 85070E is used. Before measurement, the tip of the probe was calibrated for free space, short and in De-ionized water. For improved accuracy, the measurement acquired numerous times on different locations until a consistent measurement is obtained. Errors can occur if the air gap is presented between the sample and probe, hence the repetition of measurement is required. Figure 4.1b shows the setup of subject biceps measurement for comparison with three layered phantom. All measurements were obtained in room temperature of approximately 22°C.

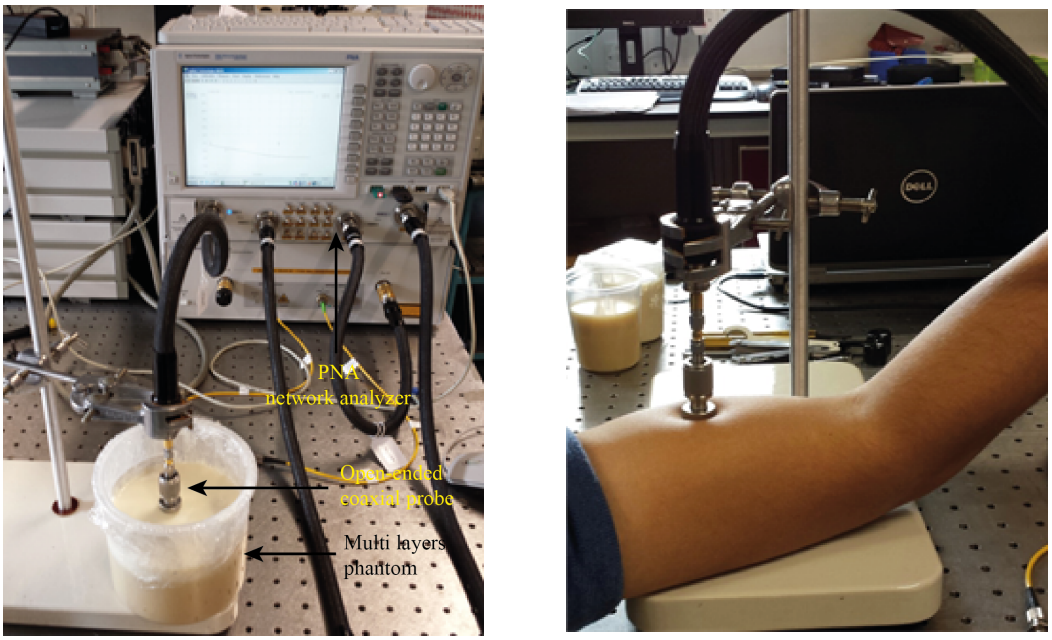

(a) (b)

Figure 4.1: Measured dielectric properties. (a) three layered phantom, (b) biceps

4.2.2 Skin Phantom

The dielectric properties of homogeneous skin mimicked sample was measured with open-ended coaxial probe at frequency range of 0.8 to 5 GHz. Figure 4.2a shows the relative permittivity of skin phantom. The marked dashed line indicates the frequency of interest covering the ISM band. The phantom, measurement is compared with the an actual tissue dielectric properties provided by literature[52–54]. The mimicked phantom closely matched with the biological tissue in the frequency band under the ISM region. The permittivity of phantom significantly deviates from the biologic tissue measurement at the upper frequency spectrum. This is to be expected as the mimicking ingredient was estimated for centre frequency, and is rather challenging to achieve very high bandwidth. Table 4.3 compares the relative permittivity of phantom and tissue at centre frequency (2.45 GHz), and the deviation between the two data set is 0.68%. Figure 4.2b shows the measured conductivity of the phantom, were the mimicked skin increase at a faster rate in the upper frequency range beyond 3 GHz. The skin phantom is approximately 8% higher than actual tissue measurement as shown in Table 4.3 In reality, biological tissue may vary from one human subject to another based on location and age, thus these changes are not significant to the measurement.

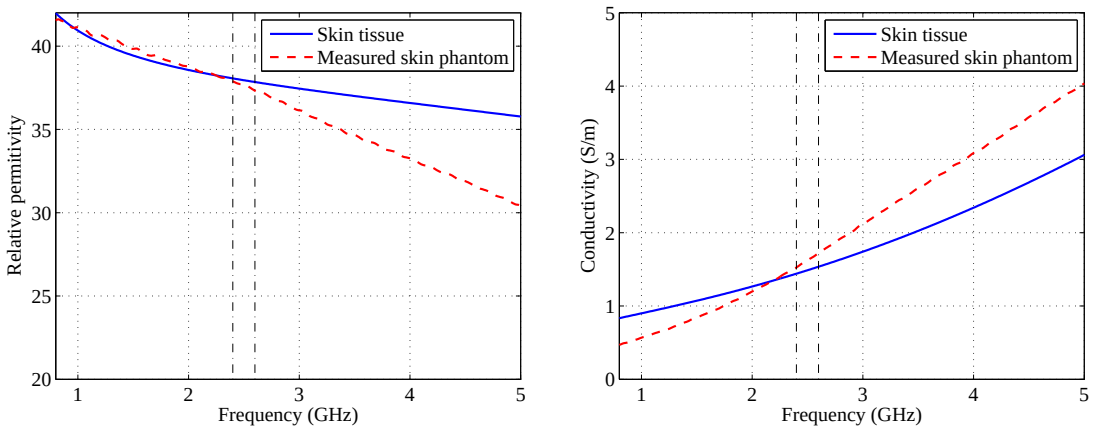

(a) (b)

Figure 4.2: Measured dielectric properties of skin mimicked phantom. (a) relative permittivity, (b) conductivity

Table 4.3: Compared dielectric properties of homogeneous skin with fabricated phantom at 2.45 GHz.

Tissue	Relative permittivity	Conductivity (S/m)
Skin tissue	38	1.46
Skin phantom	37.74	1.585
% Change	0.68%	8.56%

4.2.3 Fat Phantom

The electrical properties of homogeneous the mimicked fat sample was measured and shown in Figure 4.3. The Relative permittivity of fat is approximately 10 times smaller than of muscle phantom, caused by the increase in oil concentration. The permittivity of fat sample is higher at the lower frequency band and gradually decreases with the increasing frequency. The recorded permittivity intersects the biological tissue plot at approximately 3.5 GHz, away from the frequency of interest as shown in Figure 4.3a. The compared asset value of relative permittivity at 2.45 GHz is demonstrated in Table 4.4, the phantom deviate by about 4.69%, which is not significant. It is worth to mentioning the accuracy of the open-ended coaxial probe is reduced in a low loss dielectric medium as stated in Section 4.2.1. Figure 4.3b is the measured conductivity

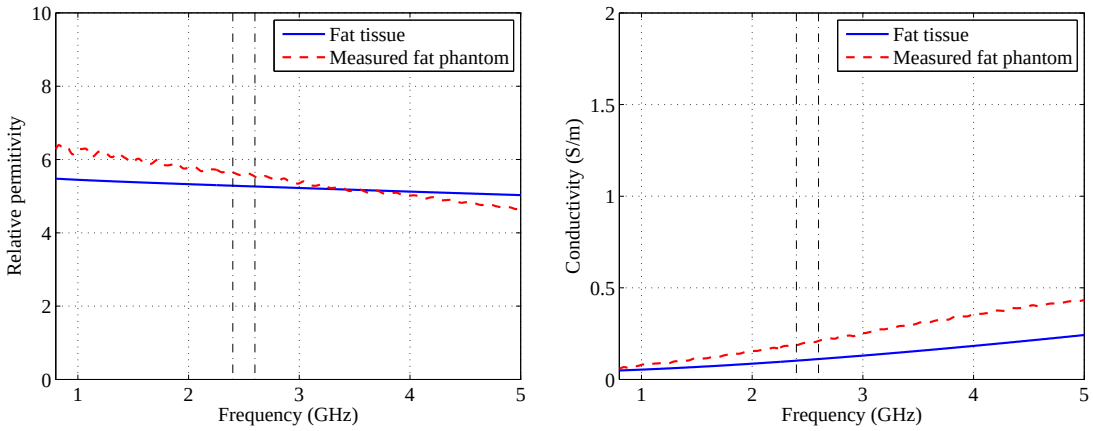

(a) (b)

Figure 4.3: Measured dielectric properties of homogeneous fat mimicked phantom. (a) relative permitivity, (b) conductivity

Table 4.4: Compared dielectric properties of fat tissue with fabricated phantom at 2.45 GHz.

Tissue	Relative permittivity	Conductivity(S/m)
Fat tissue	5.33	0.1
Fat phantom	5.58	0.19
% Change	4.69%	90%

of fat phantom. The conductivity of the phantom deviates with the increasing frequency, which is caused by a high-water concentration used during the fabrication. The comparison is made at 2.45 GHz in Table 4.4, the estimated difference between the tissue and phantom is about 90%. For such low electric conductivity, the mimicked layer becomes sensitive to the oil and water concentrations. This will have some impact to the measured thermal distribution. However, it will not be significant as the value remains low in contrast to skin and muscle layers.

4.2.4 Muscle Phantom

The measured relative permittivity of homogeneous muscle phantom is contrasted with the permittivity of biological tissue in Figure 4.4a. The dielectric constant of mimicked tissue decreases rapidly, matching the data of the actual muscle tissue at the frequency range of 3.0 to 3.4 GHz, where the two plots intersect. Figure 4.4b shows the con-

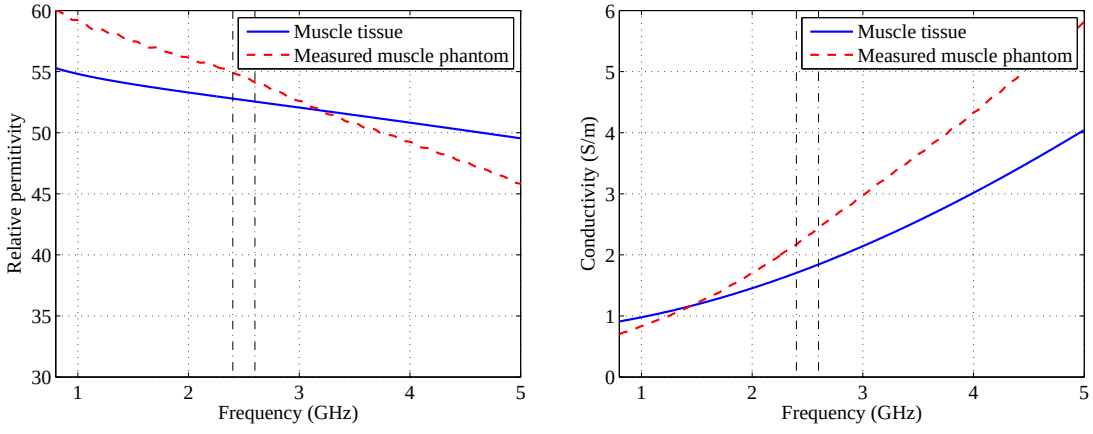

(a) (b)

Figure 4.4: Measured dielectric properties of homogeneous muscle mimicked phantom. (a) relative permittivity, (b) conductivity

Table 4.5: Compared dielectric properties of muscle with fabricated phantom at 2.45 GHz

Tissue	Relative permittivity	Conductivity (S/m)
Muscle tissue	52.73	1.71
Muscle phantom	54.72	2.2
% Change	3.5%	28%

ductivity of the muscle phantom increases at a higher rate in comparison to biological tissue, which can be explained the overdose of water in contrast to oil concentration. A comparison was made for dielectric properties at 2.45 GHz shown in Table 4.5, the difference of relative permittivity was only 3.5% where as the conductivity is 28%, which is caused by the increase in water concentration.

4.2.5 Multilayer Phantom

The electrical property of the assembled three-layered phantom was also measured with open-ended coaxial probe from the surface of the skin. For a valid comparison, other measurements were conducted on a subject calf and biceps. The recorded dielectric constant of three-layered phantom is comparatively identical to the human calf as shown in Figure 4.5a. The relative permittivity of mimicked tissue are greater by one unit to the biceps and two units to the calf, this was also noted by the homogeneous measurements of each layer. The calf has a higher permittivity than biceps, which is imposed by the anatomical variation of biological tissue. Figure 4.5b shows the measured conductivity of the tissue, and can be seen the phantom conductivity increases with frequency. Despite the characteristics at the operating frequency are closely matched, the variation can be mitigated in the future by reducing the water content accordingly. The increase in water content will have an extra impact to the microwave absorption, and hence the thermal distribution pattern. Further study was made to present the change in electric property's measurement with muscle contraction of the human biceps. This mechanism causes the muscle to push outward into a denser tissue, hence increasing the dielectric properties. The measured data presented in Figure 4.6, the relative permittivity of contracted muscle increases by approximately four units and the conductivity by 0.1-0.3 (S/m). This demonstrates one sort of variation that can occur

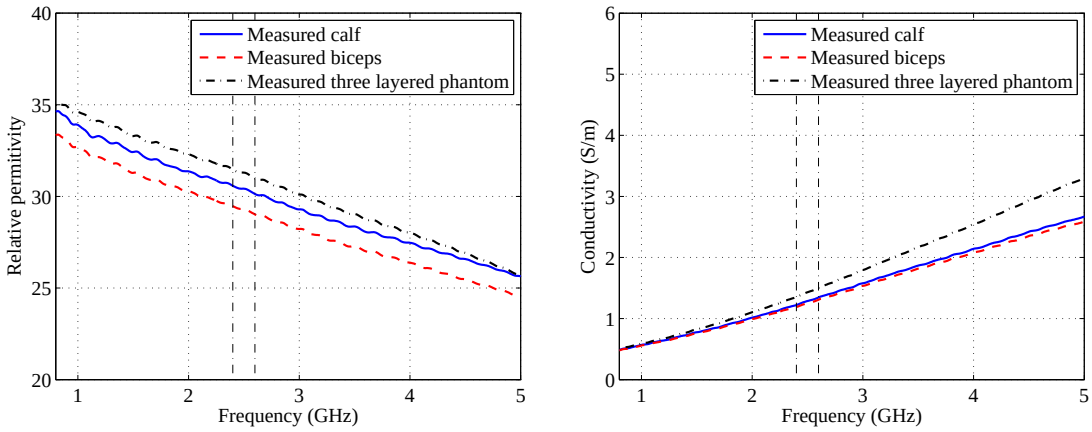

(a) (b)

Figure 4.5: Measured dielectric properties of three layered phantom in contrast to calf and biceps. (a) relative permittivity, (b) conductivity

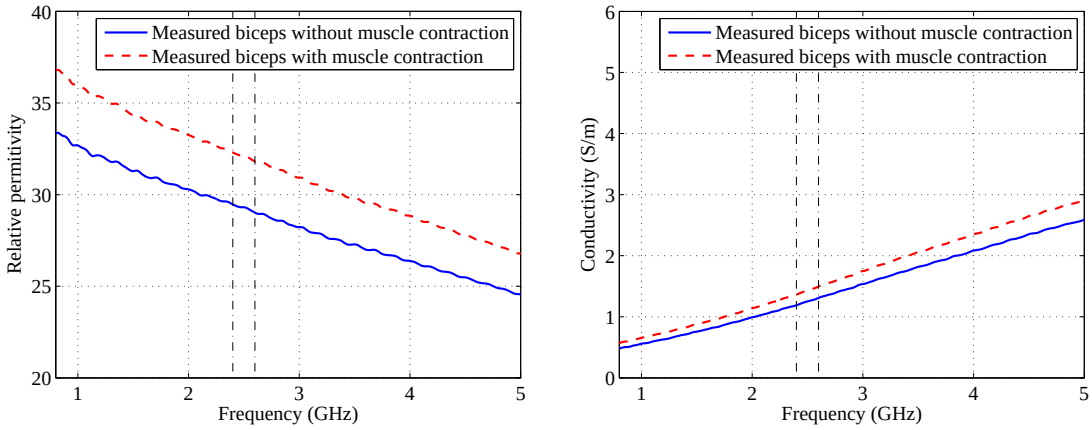

(a) (b)

Figure 4.6: Measured dielectric properties of human biceps with respect to muscle contraction. (a) relative permitivity, (b) conductivity

between different subjects, and the applicator design must be able to accommodate for the anatomical changes.

4.3 Chapter Summary

This chapter provides a brief introduction to a tissue mimicked phantoms, which they are essential for early stage trials and verifications of EM simulation. In this study, the primary focus was on the semi-solid gelatin based phantoms, which are optimal for thermal distribution evaluation at different layers. It was shown the tissue properties of each layer (Skin, Fat and muscle) are mimicked by adjusting the ratio of oil to water.

Mimicked skin and muscle are made up of high-water content with reduced oil concentration, where as the fat phantom contains larger oil concentration. The fabricated multi-layered phantom consists of skin, fat and muscle with thickness of 1 mm, 10 mm and 40 mm respectively. Simultaneously, a homogeneous phantom was produced of each layer for dielectric measurement to compare with modelled biological tissue. A high temperature opened ended coaxial probe was used to measure the electrical properties of three constituent layers and the multi-layered phantom. The dielectric properties of fabricated phantom shows a close match to the actual biological tissue, however, the fat later shows the largest deviation. The accuracy of the open-ended coaxial probe deteriorates with lower loss dielectric medium. Moreover, the non-homogeneous phantom shows a relative matching characteristic to the measured calf dielectric properties.

Chapter 5

Development of Hybrid System

5.1 System Overview

Over the last decade, the emergence of new medical technologies has vastly increased, to maintain and improve health care. Development of medicinal devices and systems undergoes many procedures, including prototyping and *ex-vivo* trails for appropriate functionality and maintained safety. This chapter presents the development process of the microwave-optical hybrid system, undergoes early stage development from off-the-shelf devices to a standalone prototype system. Figure 5.1 presents the complete system block diagram which consists of microwave/RF, cooling, NIRS and LDF system. The system drives all the elements in the applicator, including antenna, temperature sensors, optical emitter and detector. The developed hybrid system prototype is presented in Figure 5.2. The operation of microwave and cooling system is dependent on LDF probe for temperature feedback. This chapter discusses each subsystem in further detail.

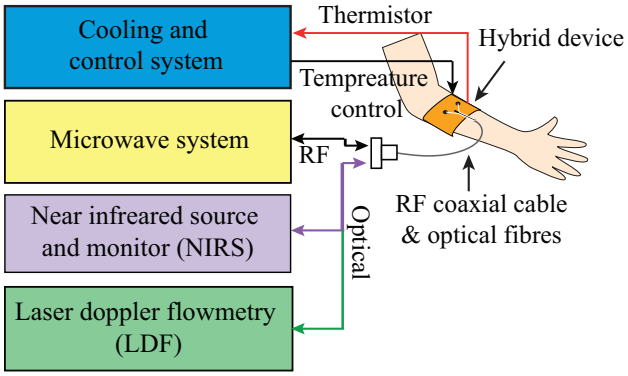

Figure 5.1: Block diagram of hybrid system.

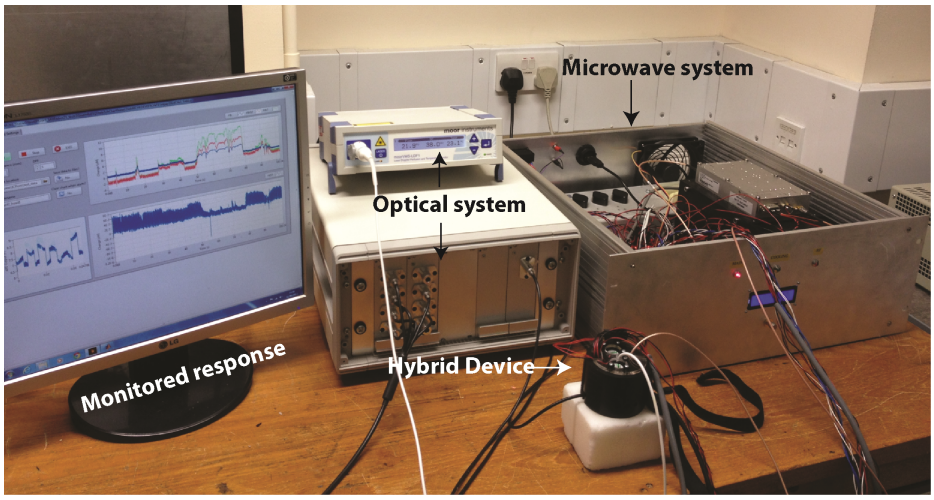

Figure 5.2: The developed hybrid system prototype.

5.2 Microwave System

While technology continues to advance, microwave system had been employed in the medical field for over the last three decades, and until this date more applications have emerged particularly for hyperthermia, diathermy and radiometry [80–82]. Microwave systems are often overlooked in contrast to applicator designs, which could further enhance safety concerns of the delivered dosage. For the appropriate and safe clinical operation of microwave applicators, the system must consider numerous safety protocol to ensure reliable operation. The basic system operation remains the same to this date, with additional sophisticated and miniaturized components. For therapeutic applications, systems often compromises of microwave source (CW or and pulsed), power meters and power limiter for safety mechanism. In 1938, a magnetic based vacuum tube known as magnetron was invented for generating microwave energy, but not until 1945 it was utilized as a microwave source, and was used in numerous medical applications, including microwave diathermy system [1]. The magnetron is capable of producing a mean power of 3.7 kW [83], and for clinical therapeutic purposes, the reported power was up to 250 watts [1][84]. The actual power used is dependent on operating frequency and duration of exposure. The radiation exposure can be either pulsed or continuous wave (CW), both methods have the same net average power deposition; however, these techniques have been reported to have a different impact on biological system [85, 86]. In the current wake of technological advancement, a sold-state based oscillators known as the frequency synthesizers are commonly used in the modern microwave and RF devices. The key advantage is the miniaturization that allows for complete system to be constructed on a single PCB. The minor disadvantage is the limited output power of approximate 1-5 mW, which can be resolved by linear RF power amplifier to attain the desired output power. Literature shows current microwave systems are capable of controlling and monitoring power levels for interstitial hyperthermia for cancer treatment at 2.45 GHz [87].

Clinical microwave diathermy system such as RADARMED 2500CP is commercially available with maximum power of 250 watts in continuous mode and 1600 watts in pulsed mode. The device is microprocessor based with a custom protocol and added safety mechanism [84]. In contrast to the BSD-500 microwave hyperthermia system, which consists of 8-output channels, were 60 watts is the maximum delivered power

per channel[88]. This system is typically used for interstitial hyperthermia in array configuration, in addition to the non-invasive applicator approach. This system radiates at 915 MHz using a solid-state microwave generator. Unlike the previous sophisticated systems, a low-cost and compact alternative offered by Emblation Microwave such as the ISYS245 is commercially available for scientific research purposes [89]. This system operates at 2.45 GHz with a frequency synthesizer and high-power microwave amplifier to achieve an adjustable output of up to 100 Watts. This system is attractive for the purposes of the hybrid device. Consequently, the delivered power is significantly higher than required and additional control is desired for embedding the cooling system. Developing application-specific system have many more benefits, including significant cost reduction, embedded system and software customization.

Based on published literature the essential requirement of a clinical microwave system is the monitoring, controlling and safety mechanism. During the early studies of the hybrid system, off-the-shelf devices were used such as Rohode&Schwarz signal generator operating between 0-20GHz in conjunction the 45 dB gain microwave amplifier (ZHL-16W-43, Mini Circuit). Moreover, R&S NRT Power Reflection Meter was used to monitor transmitted power, reflected power and VSWR during *ex-vivo* and *in-vivo* trial of Applicator I. The system was manually monitored and controlled. This set up lacks micro-controller and computer interface for automated operation and safety feedback loop, which is inherited in the developed prototype.

Microwave system in the medical field, rely on real time measurements of forward and reflected power, which act as fundamental safety features. This mechanism often detects changes in deposited power caused by impedance miss-match that arises during improper contact between the applicator and tissue. Changes in impedance produce a standing wave, where the energy at the load is reflected back to the source and reduce the overall radiated power. Anatomical composition of the tissue could also alter the impedance, leading to unpredictable deposited power. Consequently, it is essential to monitor the reflected power and often is evaluated as the Voltage Standing Wave Ratio (VSWR) given by Equation 5.2.1. Where $V_{\max}$ is the sum of amplitudes in constructive interference, and $V_{\min}$ is the difference between amplitudes during destructive interference. It can also be described in terms of the magnitude reflection coefficients $|\Gamma|$, where $1 \geq \Gamma \geq -1$. Reflection coefficient at 0 indicating a perfectly matched load,

while the maximum positive value (1) is an open circuit and minimum negative value (-1) is a short circuit. In a perfectly matched transmission line the VSWR is 1, indicating no reflection. However, if the transmission line is open or short circuited, the VSWR will be infinity and therefore the energy is all reflected back to the source.

$$VSWR = \frac{V_{\max}}{V_{\min}} = \frac{1 + |\Gamma|}{1 - |\Gamma|} \tag{5.2.1}$$

For system measurement, the loss in transmission line resulting from the impedance mismatch is estimated by return loss (RL) given by Equation 5.2.2. Where the measured input power is P_i, and the corresponding reflected power is P_r. The return loss is an essential parameter that links the relationship of VSWR and reflection coefficient as shown in Equation 5.2.3.

$$RL(dB) = 10\log_{10}\frac{P_i}{P_r} \tag{5.2.2}$$

$$\Gamma = 10^{\frac{-RL}{20}} \tag{5.2.3}$$

Despite the capability of estimating the VSWR of the applicator during diagnosis or treatment, the accuracy of the measurement is influenced by any small impedance and phase changes. The changes are often caused by the physical properties of tissue and components with respect to temperature. In the meantime, the standing wave is shifted with respect to phase, resulting in changes of maximum and minimum VSWR measurement. These inaccuracies can be addressed with the frequency sweep function, where the peak to peak ripple is apparent and can be mitigated to improve VSWR measurement accuracy. This feature is essentially used as a self-calibration method to eliminate the phase uncertainty before and during the diagnosis.

5.2.1 Developed System

The developed microwave system is built upon the essential features gained from literature with an additional specific functionality for hybrid device purposes. The complete RF system schematic is shown in Figure 5.3. Signal generator is the start of the chain, that was achieved with a frequency synthesizer chip (DSN-2700A-1119, Mini Circuit). The optimal operating frequency is between 2.3 GHz to 2.7 GHz, driven by external 25 MHz crystal local oscillator (LO). Majority of frequency synthesizers are based on

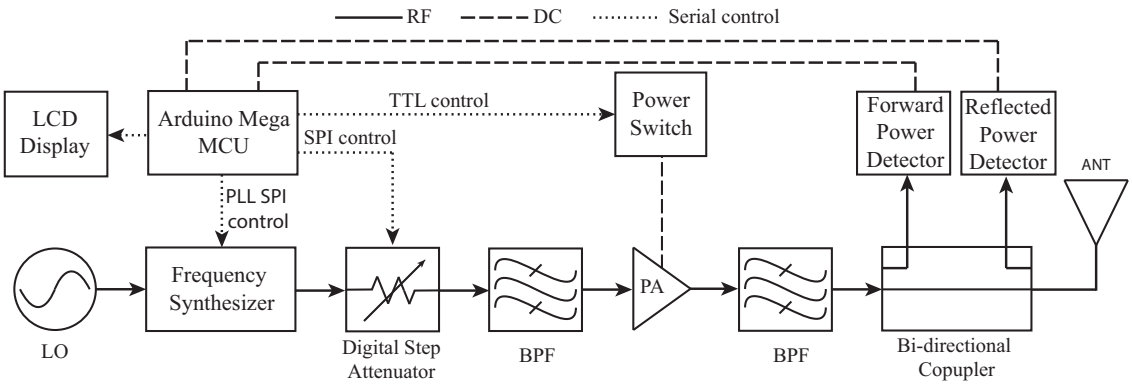

Figure 5.3: Schematic of microwave system.

phase locked loop (PLL), that produces high level of stability and accuracy, which operates by comparing the phase of the reference signal, and voltage controlled oscillator (VCO). A digital synthesizer requires a programmable divider ($N_{counter}$ block to the loop for the desired output frequency. The synthesizer chip was soldered on a fabricated PCB with a 50 Ω transmission line for RF output. The fabricated PCB design with the synthesizer chip is demonstrated in Figure 5.4. The synthesizer was controlled through a 24-bit serial peripheral interface (SPI) to the micro controller for VCO frequency tuning (f_{VCO}), achieved by adjusting programmable N divider as demonstrated in Equation 5.2.4. The counter binary relies on the desired f_{VCO}, the fixed R counter and the reference frequency (REF_{in}). The controller program was further expanded to accommodate for frequency sweeping of 2.3 to 2.7 GHz. This was achieved with appropriate logic transformation based on Equation 5.2.4 and with a for loop function for frequency incrementation by a desired factor. The synthesizer allow minimum frequency step size of 250 KHz during the sweep.

$$N_{counter} = (f_{VCO} \times R)/REF_{in} \tag{5.2.4}$$

The generated signal passes through an RF digital step attenuator (DSA) ZX76-15R5-SP, Mini Circuit, with maximum attenuation of 15.5 dB in 0.5 dB steps. The attenuation level is controlled by the Arduino micro-controller using a 5-bit serial interface. The DSA is essential in controlling the level of output power delivered to the applicator and used as part of cooling protocol to lower RF power, further discussed in Section 5.3.3. Generally the generated RF signal has high-frequency harmonics, which are undesirable and can be rejected with use of band pass filter. The in-line coaxial band

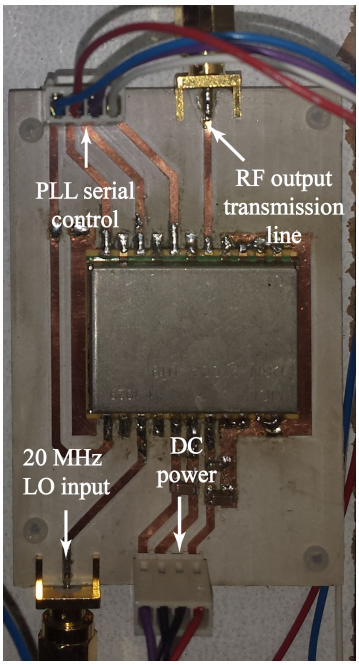

Figure 5.4: Frequency synthesiser PCB

pass filter (VBFZ-2340+.p, Mini Circuit), has a 3 dB cut-off frequency between 2.0 to 2.7 GHz with 30 dB harmonic rejection. The filtered signal is fed to a 45 dB gain high power amplifier (HPA), that was used in the early experimental trials. The operating range of the amplifier is between 1.8 - 4.0 GHz, and maximum saturated output power of 44 dBm ($\sim$16 watts). A second band pass filter is used after the HPA, to maintain harmonic rejection and other products may arise from the amplifier. The amplifier DC power is controlled via a logic relay connected to the Arduino, which serves as a safety feature during impedance missmatch of applicator to the tisue (high VSWR). The amplified signal passes through a high-power Bi-directional coupler (ZABDC20-322H, Mini Circuit), that is capable of coupling 20.5 dB of input and reflected power between the frequency range of 1.7 to 3.2 GHz. It is a four port transmission line based with input, output, forward coupled and reversed coupled. The output port is connected to the applicator via coaxial cable, while any mismatch in the applicator will cause a signal to reflect back and coupled at the reverse port. The coupled signals at each port are connected to 10 dB fixed attenuator to protect the input of the power detectors. The power detectors (ZX47-40+, Mini Circuit) converts RF input power to DC output voltage in a linear relationship. The operating frequency is up to 8 GHz and power level between -40 to 20 dBm. The output voltage is digitised in the micro-controller with built in 10-bit

analogue digital conversion (ADC). Then appropriate calculations are done to convert the voltage level into forward and reflected power, which are essential in estimating the return loss, reflection coefficient and VSWR. Real time VSWR measurement of the applicator combined with frequency sweep function, allow for optimal operating frequency detection without the use of external devices such a VNA. The microwave and cooling system are powered by 28 V, 10 A linear power supply (Calex 32024E/10R); the voltage is regulated down specifically for all other circuit requirements.

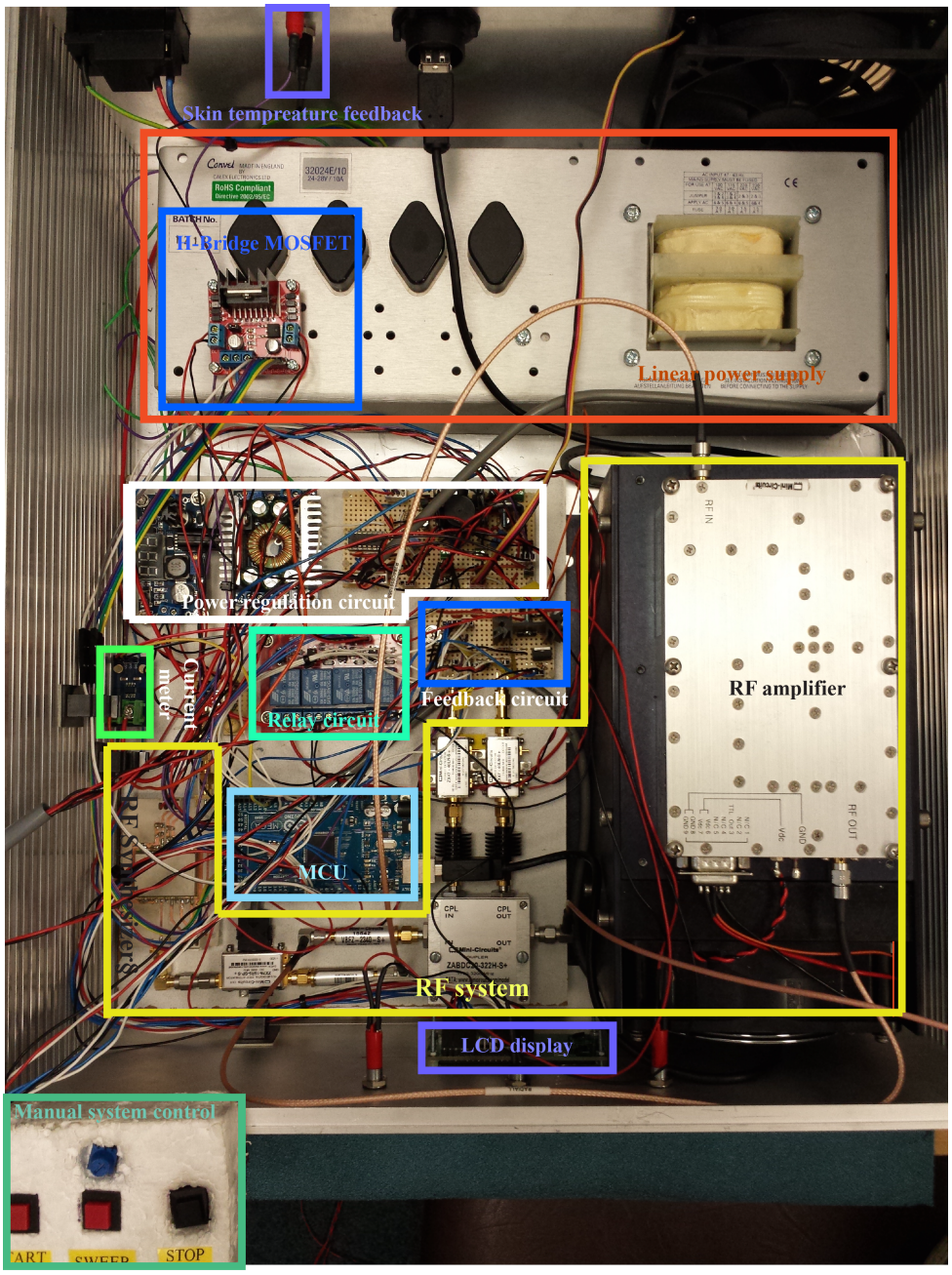

Figure 5.5: Developed microwave, cooling and control system.

The developed microwave system is embedded in a shielded metallic box to isolate any interference or leakage to the surrounding. The system compromises of other essential hardware including power regulators, switching devices and feedback circuits. This is demonstrated in Figure 5.5. The power regulation circuit consisted of multi-stage regulation to step down the 28 V source to 12.5,12, 5 and 3.3 V using Low-dropout regulators (LDO) to power RF circuits and less demanding circuits. A high-power regulator (step down DC-DC convertor) was designated for the active cooling modules (Peltier coolers), at maximum power of 40 W. The input voltage is fed directly from the main power source of 28 V, while the output voltage of the regulator was manually adjusted to the desired range between 3-5 volt for the suitable cooling power. However, this process has changed recently by introducing H-bridge MOSFET replacing the relay switching mechanism, which is capable of automatic power level adjustment controlled by the Arduino using Pulse Width Modulation (PWM) signals. The logic controlled relay circuit served as an emergency power off to the RF system. Additionally for the work conducted in this thesis, it was used as a thermostatic cooling switch. A Current sensor was recent addition to the system, which is used as a feedback circuit to indicate the operation and current level supplied to the active coolers. The SPI voltage level of frequency synthesizer is 3.3 Volt, whereas the micro-controller is 5 V. Therefore, a logic level shift was used to shift down the voltage according to the requirement. LCD display is included to interact with the micro-controller, displaying essential information to the user, including temperature, RF power and VSWR. A manual input control over the system was added as a secondary emergency function.

5.2.2 System Operation

The operation of the microwave system, has been characterized individually using spectrum analyser and a VNA. The initial step is studying the RF source, measuring the operating frequency and the output power. Figure 5.6a is the spectrum output from the RF synthesizer, while the frequency was set at 2.45 GHz. The frequency was with an error of about $\pm$2-3 MHz, which can be neglected, and the output power was approximately 3.5dB at 2.45 GHz. The measured spectrum over the frequency sweep is shown in Figure 5.6b, the operating range with in specification between 2.3-2.7 GHz. The output power of the source was not completely stable, there are peak to peak ripples of about

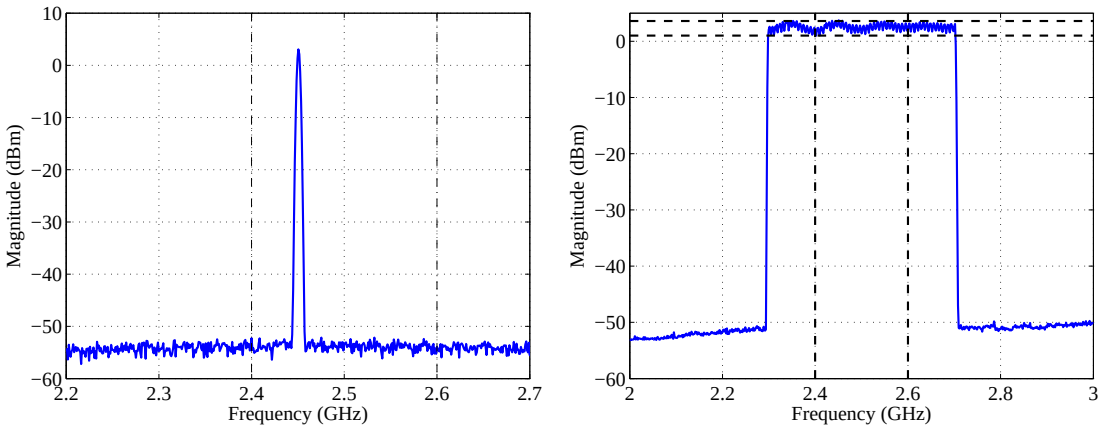

(a) (b)

Figure 5.6: Measured spectrum at the output of frequency synthesizer at. a) operating frequency, b) frequency sweep

1.5dB at the lower frequency band below 2.5 GHz. The changes in output power can be mitigated by the adjustment of in line digital step attenuator to provide a consistent output power. The characteristic of the remaining elements is analysed and discussed in Appendix B.

The uniqueness of this system is the ability to measure the VSWR of the applicator over the generated frequency sweep. It's beneficial to monitor the characteristics of the applicator when placed on the subject directly, without the use of external spectrum analyser or power meter. This is essential part of monitoring, which promptly allow for dosage control and safety protocol implementation. The measured data can be obtained real time in any external serial program that has the capability to record and plot the data in real time. Figure 5.7 presents the measured VSWR of Applicator II placed on calf and phantom through the microwave system and network analyser. The system based measurement is limited to the source operating range while VNA often significantly larger. The VNA based measurement is calibrated to the applicator. Consequently, the baseline VSWR is lower than system measurement; however, the trends between the two measurement are identical. The optimum operating frequency on calf is approximately 2.51 GHz measured by the VNA and also calculated by the hybrid system. Likewise, with phantom measurement, the pattern of VNA and system measurements are consistent at about 2.53 GHz. The system measurement sustains from large ripples across the frequency sweep, results in a phase shift of the standing wave.

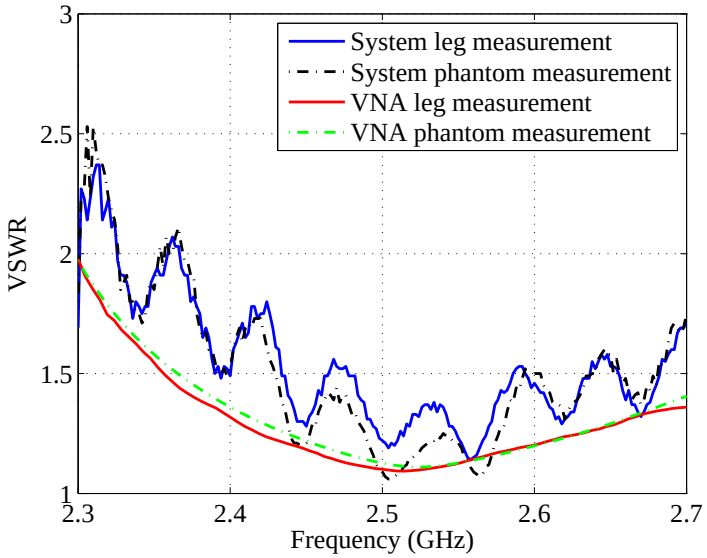

Figure 5.7: Measured VSWR of Applicator II using microwave system and VNA.

Elimination of system ripples can be achieved by estimating the peak to peak value of the ripple over the frequency range, were the largest peak-peak ripple was about 0.5 dB. Furthermore, the system linearity over the operating frequency range must also be considered as a function of the standing wave, which limits the accuracy of the estimation.

The system was also used to measure the VSWR of CP applicator placed on a calf, the results presented in Figure 5.8. The CP operating frequency is at the point where the two degenerate modes are orthogonal, therefore, it is the intersected region between the two excite modes. The general VSWR trends between the two measurements are identical. The VNA measurement shows the operating frequency is about 2.53 GHz, in contrast, the hybrid system VSWR reading cannot determine the CP operating frequency of the applicator. The system can only determine the best matching frequency in the linear operating region. The bandwidth of CP applicator is narrow, which increases the challenge.

Figure 5.9 presents the system measurement with 50Ω termination directly at the output of Bi-directional coupler in comparison to match loading at the end of the two-meter coaxial cable. The system VSWR measurement clearly shows the diminished ripples, when the system, is match terminated at the output of the coupler (before the coaxial cable). In contrast to the shifting of standing wave as a function of frequency

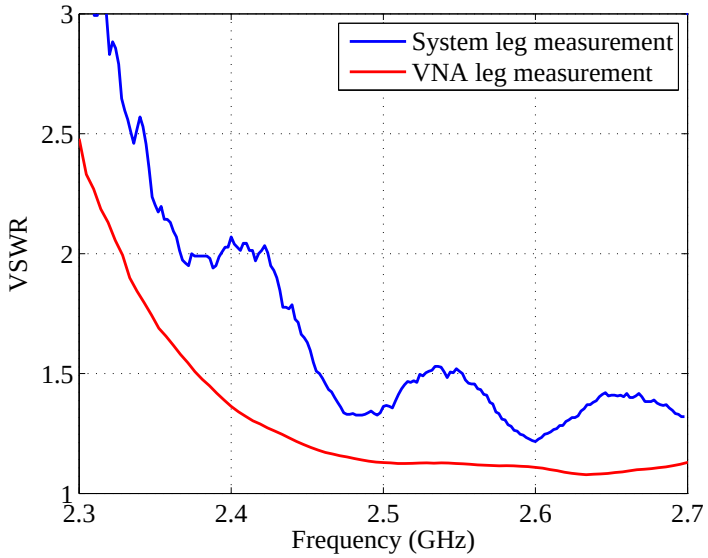

Figure 5.8: Measured VSWR of CP applicator using microwave system and VNA.

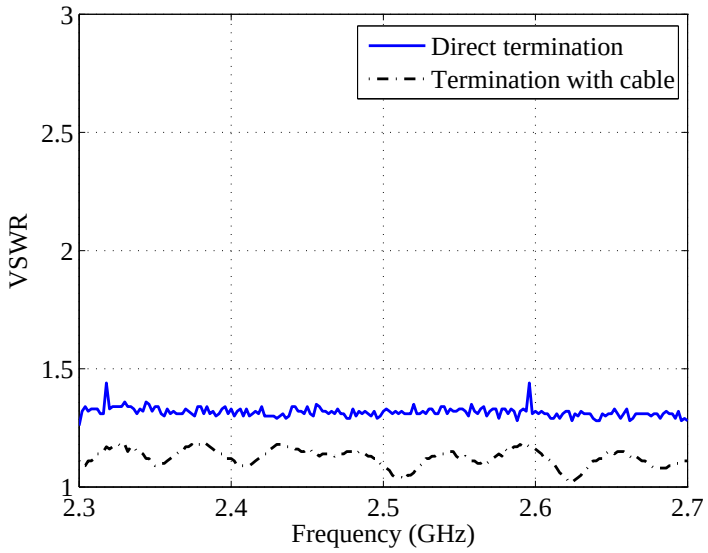

Figure 5.9: Match terminated system VSWR.

along the cable length, and cable attenuation contribute to the decreased VSWR. The mean VSWR value across the frequency sweep for direct termination is approximately 1.3 and 1.15 for cable termination.

The embedded power meter measures the corresponding input and reflected power of the system; the characteristic with added system attenuation is presented in Figure 5.10. The power coupled at the input of the Bi-directional coupler is approximately 27 dBm when the applicator is placed on the phantom and a leg (impedance matched).

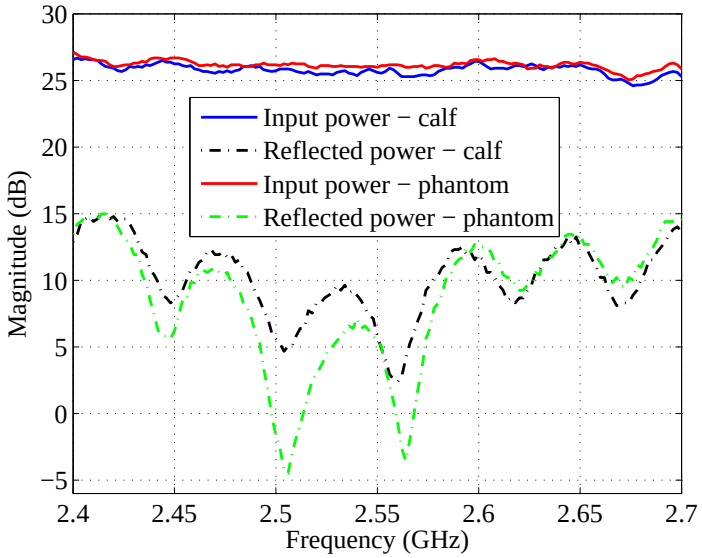

Figure 5.10: Delivered and reflected power of applicator applied on human calf and phantom.

This indicates the delivered power to the applicator is consistent and regardless of the test subject. In contrast, the reflected power fluctuates depending on impedance matching of the applicator to the tissue/phantom. At operating frequency approximately of 2.50 GHz, the returned power was 10 dBm lower with a phantom. This signifies the possible power changes when placed on different anatomical location of tissue, between subjects and the corresponding age.

5.3 Cooling System

Superficial heating in microwave warming is a typical challenge when deep tissue heating is desired. Therapeutic devices, including microwave and ultrasound modalities, often requires surface cooling when the radiation is applied externally in a non-invasive manner. Consequently, single element applicators may lead to the possibility of skin burns during hyperthermia treatment [90]. Cooling mechanism have been applied in the form of water or forced convection (Air cooling). Literature study shows water bolus cooling are used to mitigate the skin heating throughout EM hyperthermia, which dates back to 1980's [16, 31]. The bolus contains deionized water to prevent EM losses and was proved to reduce radiation leakage to surrounding as a result of the high dielectric properties [16]. Deionized water have a dielectric constant of $\varepsilon_r \approx 80$, and acts as a transmission medium to couple the EM energy into the tissue. It was also used to

provide the necessary spacing between applicator and tissue, ensuring uniform heating is applied [14]. The limitation of water cooling is the trapped air bubbles presents between the bolus and tissue, which shown in a study to have larger SAR in the vicinity [91]. The bubbles are introduced by the pumping mechanism for the water circulation. Air cooling have been previously used to lower the risk of skin burn and discomfort in microwave thermotherapy. This was achieved with use of a waveguide applicator, with required spacing and perturbation for increase air flow on skin surface [22, 90]. A microstrip patch antenna based applicators also been reported for the capability to be used in conjunction with air cooling, assuming a certain spatial arrangement between applicator and skin [92].

The applicator spacing is a limitation of the current used skin cooling modality, which is not adequate for this project. The hybrid applicator integrates optical probes that require direct skin contact for the diagnosis. Consequently, an indirect active cooling approach is an attractive solution; this was implemented with use of Thermoelectric cooling (TEC). Cooling the skin was achieved by indirectly cooling the applicator from its ground plane (Copper conductor side) to lower the temperature of the applicator, hence cooling the skin. The benefits of TEC are small dimensions, no moving parts, reliability and accurate temperature control. In contrast, air cooling is an alternative technique. Thermoelectric (TE) modules are found in many industrial applications, including laser diode cooling [93], infrared detectors and as a heat exchangers. The literatures of TE modules are limited in the medical sector, particularly as a skin cooling for applicators was not investigated previously. Some literatures were found using TEC for medical purposes such as liquid heat exchanger [94] and therapeutic used for reflexotherapy [95].

5.3.1 Thermoelectric Cooling

A thermoelectric module consists of two ceramic plates acting as a junction and semiconductor material of p- and n-type in between the plates as shown in Figure 5.11. The process involved in TEC is commonly known as the Peltier effect. This effect occurs when electric current passes through two distinct conductors, creating a temperature difference between the two junctions. This essentially can act as a heat pump, absorbing heat from the cold side of the module and release it to the hot side where it will be

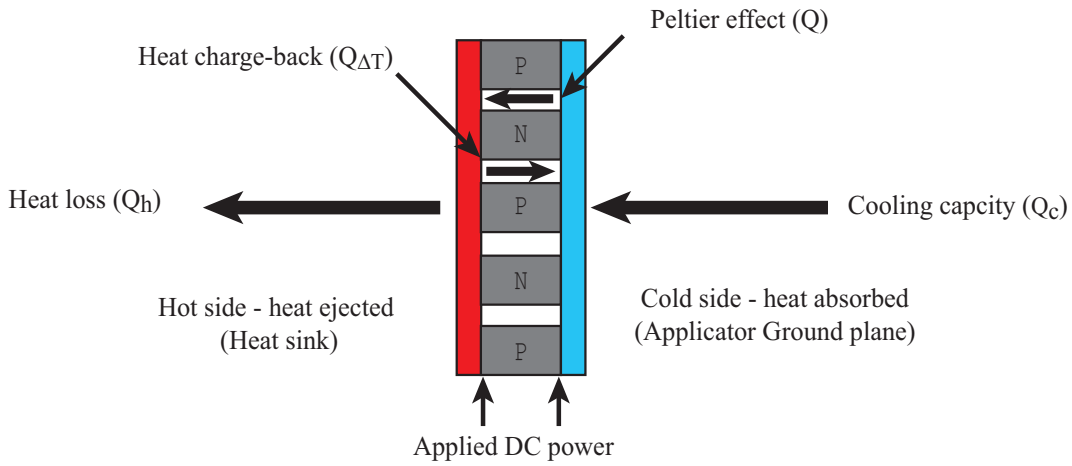

Figure 5.11: Thermoelectric cooling.

dissipated. The heat generated at the hot side (Q_h)can be mathematically estimated by combining the unit power P_{in}, and the cooling capacity(Q_c). A detailed theory can be found in the Appendix B Section B.2.

The configuration of the applicator consists of two Peltier coolers, where the cold side of TE module is attached on the back of the applicator (ground plane) with a double sided adhesive thermal pad for optimal heat conduction. The hot side of TE module is attached to a heat sink, which must be sufficient to dissipate the heat at the junction. For efficient heat dissipation across the heat sink, a dual axial fan was used to reduce thermal resistance of the heat sink by dissipating the heat at a faster rate to maintain a large temperature difference across the module. The cooling mechanism and configuration were performed in transient heat transfer simulation in conjunction with the microwave applicator to examine the effectiveness of skin cooling. The cooling problem was simplified by considering an equivalent thermal circuit is demonstrated in Figure 5.12. The thermal problem is considered to be in series, beginning with the heat source Q_{mw} which is induced by the microwave warming as a function of power and time. The junction temperature (T_j) is the skin temperature and is elevated during microwave warming from initial temperature of approximately 30 °C. The temperature at the skin surface is always lower than core temperature, which is caused by the high blood regulation at the skin in conjunction with the air convection. The excess of T_j is dissipated through the antenna, including superstrate and substrate that have a thermal resistance (R_{Ant}). This emphasizes the role of substrate thermal properties for effective heat transfer between

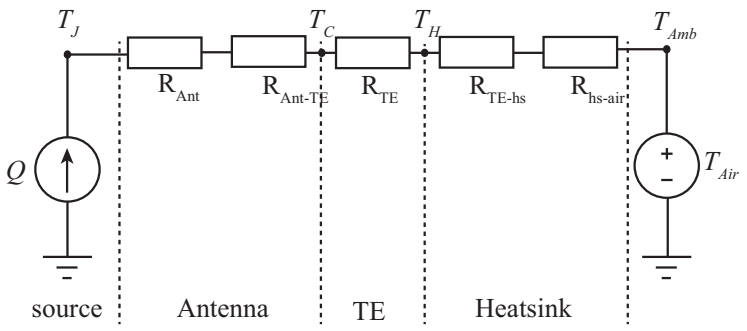

Figure 5.12: Equivalent thermal circuit.

the skin surface and the Peltier cooler. The R_{Ant-TE} of the interface between the cold side of TE module (T_c) and the antenna ground plane is the thermal adhesive, which is not considered in the simulation model. The TE module has a large thermal resistance to maintain high-temperature difference across the Peltier cooler, in a condition where the heat at the hot side (T_H) is effectively dissipated. The circuit is completed with the added thermal resistance of the heat sink combined with the adhesive (R_{TE-hs}) and with forced cooling (R_{hs-air}) The ambient temperature (T_{amb}) is typically set to 20 °C during the simulation model.

The operation and control of TEC are demonstrated in Figure 5.13. The skin cooling consist of two TE module and axial fans to lower thermal resistance of the heat sink. The cooling system operates using the skin temperature; thermistor which is located at the centre of the applicator. Additional thermistor for monitoring purpose is placed at the ground plane of the applicator in location of the radiating edge of antenna, where the maximum temperature is expected. The skin thermistor is integrated with the LDF optical probe, were the DC output of temperature reading is feed back to the microwave system Arduino micro-controller. The skin temperature reading is used to control the cooling system in a thermostatic manner. The Peltier cooler is activated through a relay switch when the skin temperature exceeds the set point value. The Forced convection fan is a PWM based switching using a logic MOSFET circuit, where the speed automatically adjusted by the micro-controller. The axial fan operates at 17000 RPM, which induces vibration into the applicator, causing an increase in the baseline of flux measurement and occasional large spikes, which was diminished by anti-vibration washers along with data post processing.

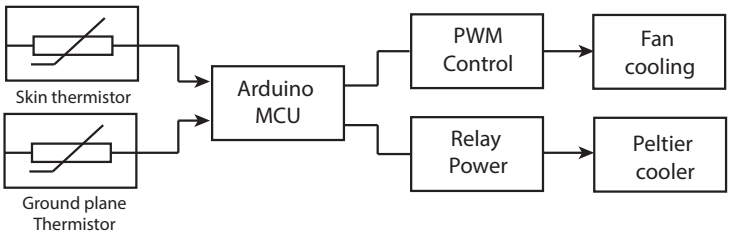

Figure 5.13: Basic schematic of the cooling system.

5.3.2 Thermometric Techniques

In the 16th and 17th centenary temperature estimation of the body was relied on the use of hands as a reference point [56]. A thermometer is considered as a device that measured the output changes with respect to temperature in a repeatable manner. In clinical thermal therapies, temperature monitoring participates a significant role in various treatments, and hence feedbacks are necessary to ensure safe delivery of therapy and minimize any potential risks from high dosage. In microwave warming the heating response may be likely to vary from one subject to another depending on the anatomical compost ion of tissue. In hyperthermia, the temperature is controlled at about 42 - 43 °C [7]. Temperature measurements can also be classified into invasive and non-invasive techniques. In clinical thermal therapies, an invasive thermometry is required due to the lack of technological means of non-invasive modalities. Monitoring temperature invasively require insertion of catheters into the tissue, this approach is used for precise accurate measurement in the critical location [56]. The three common invasive thermometers are thermistor, thermocouple and fibre optics [7]. These thermometers are necessarily to be used invasively, they can be used to measure superficial temperature integrated with other sensors. The benefit of each technique is compared in Table 5.1.

The first section of Table 5.1 presents the common invasive thermometry. Thermistor are thermal sensitive resistors, where the electrical resistance changes with the changing temperature. There are two types of resistors, first is metal based resistor known as the positive temperature coefficient (PTC) and second is semiconductor based, which is a negative temperature coefficient (NTC). Typically, thermistor operates in a smaller temperature range in comparison to other sensors, that allows for an increase in measurement accuracy (0.1 °C) [96]. The limitations of thermistors are the non-linearity effects with temperature [97], and possible interaction with EM field

Table 5.1: Thermometric techniques compared.

Modalities	Advantages	Disadvantages
Thermistor	Accurate	Non-linearity
Thermocouple	Easily integrated with sensors	Interaction with EM
Optical	No EM interaction	Calibration required
IR Thermography	Surface imaging	Low accuracy
Radiometry	Under surface monitoring	Limited lateral resolution
Ultrasound	Good spatial distribution	Interaction with bone and air

with the metallic PTC resistor based. Temperature monitoring in the hybrid system, achieved non-invasively with three NTC based thermistor measuring temperature of skin and antenna ground plane. Thermocouples are based on a junction that is created between two different metals. When applying heat or cold at the junction, a voltage is generated, which relates to a temperature value. Thermocouples are capable of measuring wide range of temperatures; however, more susceptible to EM field and limits the accuracy of the measurements (require shielding) [98]. The susceptibility of the EM energy can be avoided with use of non-inductive optical fibre thermometry. The probe has a phosphor thermosensor at the tip, which is excited by light-emitting diode (LED). Recent literature shows optical fibre thermometry also used in non-invasive skin temperature mapping [99]. The downside of the optical probe is the time consumed on calibrations [7].

The second half of Table 5.1 summarises some of the non-invasive approach of thermometry. Non-invasive modalities are attractive because it is capable of mapping thermal distribution of the tissue externally. IR thermography is a commercially available thermometry, utilises IR photo-detector to measure the emitted IR energy of object surfaces. The emission of IR is produced by the molecular vibration. For hybrid applicator, thermal distribution verification in this thesis was achieved using Flir i7 IR imaging, capturing immediately after 5 minutes of microwave exposure of phantom or human calf. The used IR imaging have an accuracy of ± 2 °C, sensitivity of 0.15 °C and a resolution of 60x60 pixels. The modality is simple to use and portable, however, is limited by surface measurement.

Unlike IR thermography, microwave radiometry is a non-invasive technique that is capable of mapping temperature distribution at depth (up to 30 mm). This technique can detect the elevation of temperature inside the tissue. This modality uses a specially designed antenna to measure microwave thermal noise emitted by the tissue with temperature above absolute zero [100]. Radiometry was used in clinical evaluation as a thermometric tool [101], breast cancer screening and blood flow measurement [102, 103]. Typical microwave radiometry operating frequency is around 1.0 - 3.0 GHz. Literature shows radiometry was used in conjunction with microwave hyperthermia for simultaneous heating and temperature monitoring [104, 105]. The Reported resolution of radiometry is approximately 0.1 °C [101] and signal sensitivity between 0.3 - 0.8 °C [105]. The trade-offs of microwave radiometry is between depth and lateral resolution which corresponding to operating frequency. For optimum depth, the lateral resolution is limited and reported at about 5.0 mm [101]. In contrast to ultrasound imaging, better lateral resolution can be achieved with the shorter sound wavelength in the tissue. However, the limitation is the rapid attenuation when bones or gasses is at the site [56]. Despite the limitation of radiometry, it remains an attractive future add-on to the hybrid system, which can provide an insight temperature change with respect to measure thermal responses using the optical system.

5.3.3 Control System

The coordination of microwave and cooling system relies on the micro-controller to execute the defined program. A brief control system flow chart is shown in Figure 5.14. The program was designed to operate at different conditions (Mode). The program consists of three essential modes starting with Mode-1 for VSWR sweep, Mode-2 for microwave heating with cooling (primary function), and Mode-3 is identical to Mode-2 excluding cooling system. In Mode-1, the output of the microwave system is reduced by controlling the DSA to increase the RF attenuation, and activates the HPA through the relay trigger to enable the microwave exposure. Meanwhile, a frequency sweep is triggered to loop the output frequency of synthesizer, and frequency sample is recorded with the corresponding transmitted power (TP) and reflected power (RP) measurement from the inbuilt power meter. The VSWR is then calculated for each frequency, which

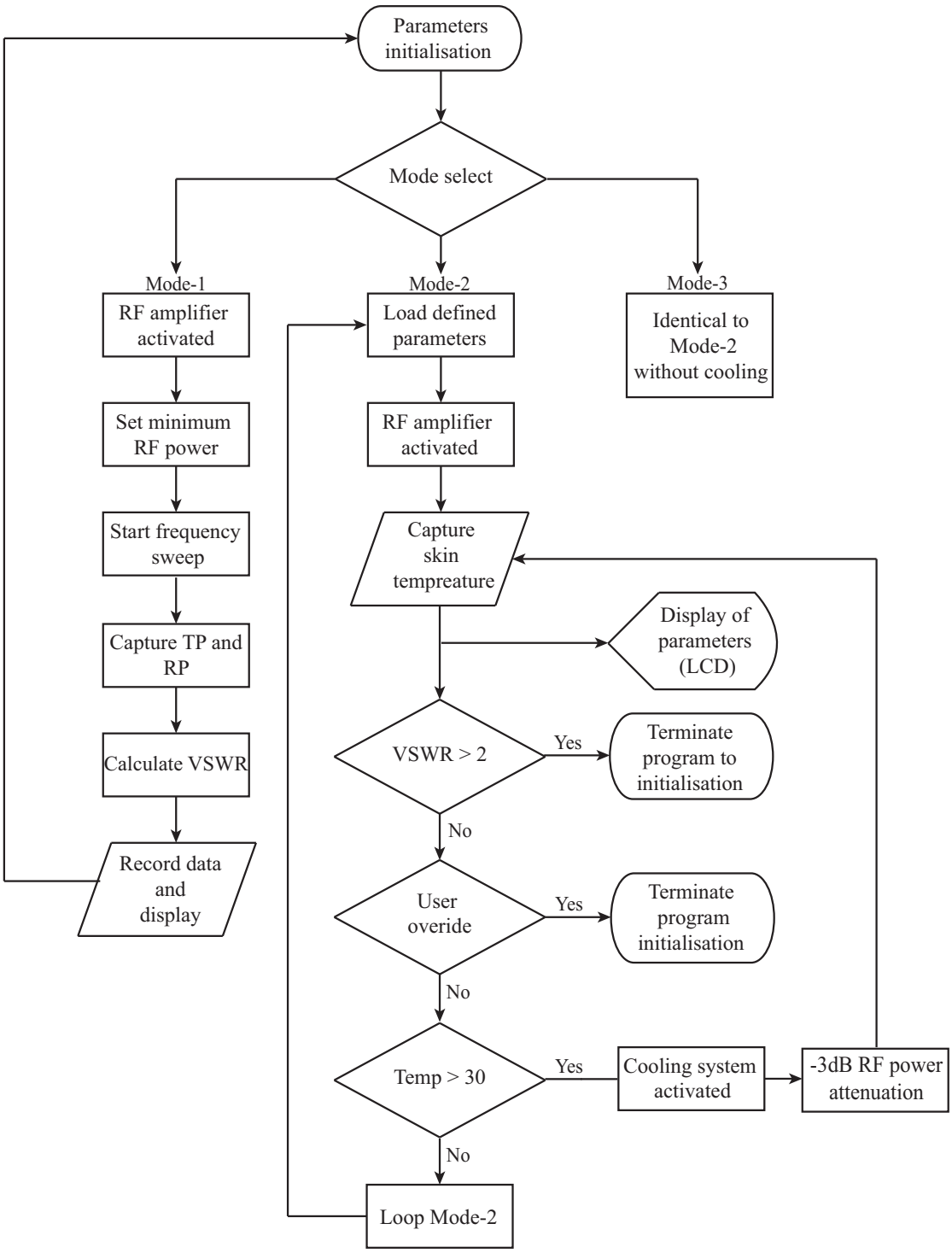

Figure 5.14: Control system flow chart for microwave and skin cooling.

is displayed and recorded through a serial interface. Optimum operating frequency can be selected manually based on minimum VSWR value; this could be achieved automatically in the future work. Mode-2, uses predefined parameters such as the frequency, output power, temperature set-point and VSWR limit. The applicator is radiating as

the microwave HPA is turned on and the system begins monitoring skin temperature, VSWR and the net delivered power. The cooling system is only activated when the temperature of skin exceeds the set point value, e.g. 30 °C, and at the same time the RF power is reduced by 3dB until the temperature is below or at the set point value. Furthermore, set points was added for VSWR and temperature limits as part of safety mechanism, when exceeded the system will shut off without microwave exposure.

5.4 Optical System

5.4.1 NIRS Monitor

Measuring the changes in blood volume using NIRS can be achieved in numerous methods depending on the application, these instruments require a minimum of three wavelengths to distinguish the absorption spectra of the local tissue. The simplest forms of spectrophotometry instruments are the commercially available continuous-wave NIRS. These devices are based on modified Beer-Lamber that capable of continuously measuring the changes in concentration level ($\Delta HbO_2/\Delta HHb/\Delta HbT$) [106]. However those devices are limited to only measuring changes from a baseline level without an actual quantitative value[107]. This factor can be resolved if the optical path-length and the light dispersion for each wavelength is known. Currently, complex devices with appropriate algorithms are able to measure the absolute concentration by utilising reflectance measurements of multiple detectors distributed at different distances; this is known as the spatially resolved spectroscopy (SRS) [108]. Despite the benefit of acquiring quantitative value, the continuous-wave NIRS remains to be advantageous in clinical use for its cost and practicality [109].

During the initial stage of the study, a commercially available Hamamtsu NIRO 100 was used to measure the changes in oxy and deoxy haemoglobin. The NIRO 100 was used in conjunction with the first proposed applicator to measure the changes in thermal response. The NIRO 100 equipped with a single source and dual detectors at different spacing, hence operating in SRS principle. Applicator I was designed specially to integrate the Hamamtsu Optical source and detectors (Optodes). The SRS system can measure the light intensity difference between each detector, that provides additional parameters such as tissue oxidation index (TOI) and the normalized tissue haemoglobin index (nTHI). The TOI is the ratio of the oxygenated haemoglobin to the

total tissue haemoglobin and given in Equation 5.4.1.

$$TOI = \frac{HbO_2}{HbO_2 + HHb}\% \tag{5.4.1}$$

During the development of the hybrid system, in-house built NIRS system was developed by the UCL BioMedical Physics and Bioengineering department to be used for hyrbid system. The instrument is based on CW-NIRS with modified beers-lambert for measuring changes in concentration, and uses single optical emitter and detector. The new probes are integrated with the more recent antenna designs beginning with Applicator II. The emitter consists of six laser diodes operating at six different wavelengths (670, 760, 780, 860, 904, and 980 nm). The light from the six laser diodes is coupled into one flexible optical emitter probe. The avalanche photo diode is used to detect the spectral response which is connected to a single-channel optical fibre. The separation between the emitter-detector is set to be 40 mm to ensure desirable light penetration to the muscle. The system acquires and control data through a DAQ with LabVIEW interface. The captured data requires some necessary conversion to account for the optodes separation and the Differential path factor (DPF). The DPF value of 4.94 is typically used for human calf. This value was obtained from the literature [110].

5.4.2 LDF Skin Monitor

The primary objective is to measure thermal responses in deep tissue induced by the microwave warming. However, skin temperature is also increased in the process, resulted by the high-water content in the superficial layer. A secondary optical monitoring system based on LDF was introduced for applicator II and onward. This instrument is the moorVMS-LDF1 commercially available by Moors instruments. The device uses a single 6 mm diameter optical probe with an integrated emitter and detector spaced at 0.5 mm. The reduced separation limits the measuring depth of up to 1 mm, that is essentially used to measure the micro-circulation, particularly the capillaries, arterioles and venules. The skin measurement will be used to evaluate the efficacy of the skin cooling and to verify if the NIRS measurement from the deeper tissue. Equally, to the NIRS, the laser Doppler measurement is not an absolute perfusion value. It's rather expressed in arbitrary units of perfusion in flux. The LDF monitor also integrates a thermistor which is used to measure the skin temperature, with accuracy of 0.3 °C. The laser doppler operates at a single wavelength of 785nm that is in the NIRS operating

band and causes interference to the NIRS measurement when both systems operated simultaneously. The current method used to mitigate this problem is by repeating the experiment with each instrument independently. This is further discussed in the protocol in Chapter 8.

5.5 Chapter Summary

The full operation of the hybrid system was reviewed in this chapter. The microwave system was designed and built to adapt any changes in operating frequency caused by the anatomical aspect of tissue or applicator designs accuracy. The system was built around the synthesizer as a signal source which undergoes to amplification process for the required output dosage. The transmitted and reflected power is monitored as part of a safety mechanism during improper placement of the applicator, where the impedance miss-match will be detected. Moreover, thermistor was used to monitor skin temperatures and used as part of cooling feedback, to minimize skin heating. Several cooling methods were investigated including water bolus. However, the limitation was the applicator to tissue spacing is not appropriate for integrated optical probes. Peltier cooling was implemented as a skin cooling mechanism, which is a new application domain that has not been investigated previously. The combination of microwave and cooling systems function accordingly by using a micro-controller for the necessary cooling or heating protocol and other implemented features to ensure patient safety. The induced physiological changes are monitored by the two independent optical systems. NIRS was the primary instrument to measure blood volume in greater depth where as the LDF to measure the micro circulation in the superficial layers. Both devices use near-infrared light, which causes cross interference when operated simultaneously, thus the experiments were done independently for each monitoring instrument.

Chapter 6

Linearly Polarised Microwave Applicator

6.1 Introduction

This section introduces the development and design stages of the hybrid microwave applicators. The development procedures involved various design investigations, including operating frequency, coupling layer and applicator proximity to the skin surface. Moreover, the study goes over the details of anatomical contribution of tissue to the deposited EM energy by the aid of EM and thermal simulation. There are three developed applicators based on linear polarisation, which have been modelled, fabricated and validated. Each stage of the applicator, evolved upon previous design, primarily to reduce skin heating and promote deep tissue warming. Applicator I design concentrated on EM and thermal study of the applicator at different anatomical conditions, while Applicator II in-cooperated skin cooling and additional optical probe (LDF). Furthermore, Applicator III was introduced to enhance the cooling efficiency of the predecessor.

6.2 Design Requirements

The operation of antenna in therapeutic or diagnostic application is different to the standard free space environment. In therapy, applicators typically operate in the near-field region by interacting with lossy dielectric medium. This arises numerous antenna design challenges with consideration of penetration depth and uniformity of deposited EM field. The field distribution, penetration depth and applicator dimension are largely dependent upon the operation frequency, the proximity of the applicator and the coupling medium. These parameters have been investigated in depth as they form the essential concept of optimum applicator design. The operating frequency choice was 2.45 GHz for compact applicator size, localised heating, reduce power requirement and aviliable ISM band.

6.2.1 Applicator proximity

Applicators can be either as non-contact (in free space), or in direct contact to patient skin. The induced EM energy is assessed with accordance to the distance of the antenna source to the biological tissue, as shown in Figure 6.1. In the far field-region, the radiating source is approximately $2D^2/\lambda$ away from the biological tissue in free space. The incident field is characterised as a plane wave in a cosine distribution, where the electric and magnetic field are in phase with each other radiated. Moreover, the radi-

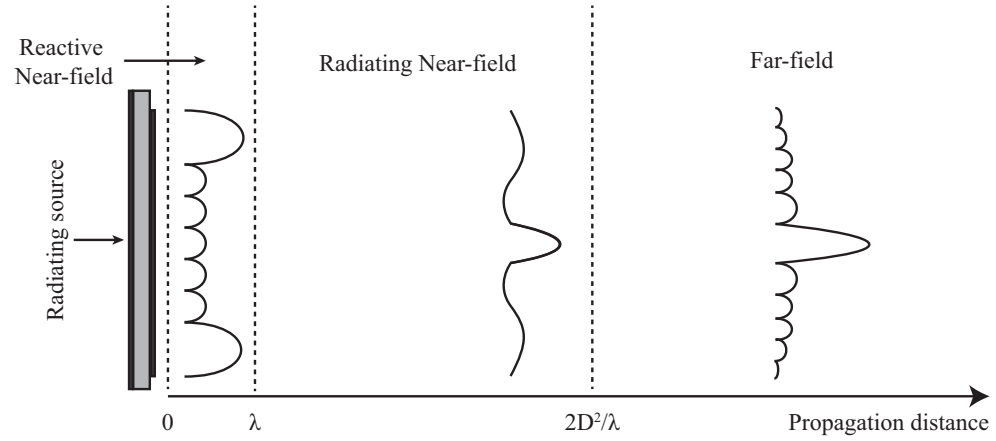

Figure 6.1: Antenna field distribution at different transition zones.

ated energy decreases with the square of the propagating distance. When operating in free space, the applicator physical dimension becomes larger as it is matched to the intrinsic impedance (η) of the medium at 120π. This is derived from the permittivity and permeability of free space. In therapeutic applications, far-field approach is limited because of the radiation leakage to the surrounding.

In the reactive near-field the electric and magnetic field are quadrature out of phase and thee corresponding maximum amplitude varies with respect to the distance in the medium. Therefore the wave impedance is no longer the same as intrinsic impedance, and hence also changes from point to point in the tissue. In this configuration it is expected to observe a standing wave between the applicator and the tissue, due to operation at high frequency spectrum in a multi-layered dielectric tissue [111]. The interaction of incident EM energy to the high permittivity of skin surface at the near-field region is expected to be weaker. Consequently, the deposited EM energy into biological tissue is a function of antenna current distribution, composition of tissue and the spacing of source to the skin surface. Applicators in close proximity (near-field / Fresnel zone) are commonly used in hyperthermia [25, 26, 60, 14] Direct contact applicators are separated from the tissue by a coupling medium layer such as water bolus. A close proximity applicator with appropriate design can easily couple the EM energy into organic medium with uniform field pattern and reduced stray radiation in comparison to non-direct contact applicators [112, 1] Additionally, with high permittivity tissue loading, the induced warming is localised as applicator size is miniaturised.

In this thesis, the radiated field is mostly considered as in near field region and for

finite size applicator, the field is in the form of spherical waves. For hybrid system, the optical probes can only operate in contact to the skin along with the active cooling. Consequently, A direct contact applicator design was adopted with the use of superstrate layer to introduce some spacing between the radiator and the tissue. In the close proximity, the antenna operates in near-field and/or Fresnel regions depending on the chosen superstrate thickness. This layer is of importance in the EM absorption, heating and cooling mechanism.

The reactive region is an ideal case for the direct contact applicator, defined as the region directly surrounding the applicator, where the reactive power density is significant in this region making the EM field sensitive to absorption. As for the radiating near field also known as Fresnel, is the case considered for the non-direct contact applicators, it can be seen at this region the field is semi radiative with peak power density at centre which can cause surface heating when interacted with skin [1].

6.2.2 Coupling layer

The impedance of the applicator can be matched to the biological tissue when it is in direct contact (with appropriate loading) for enhanced EM coupling [113]. In previous therapeutic studies, direct contact microwave applicators are often spaced by water bolus for skin cooling [114, 31, 91, 115]. Literature also shows wave-guide based applicator have a bolus bag filled within the aperture to effectively improve impedance match and reduce stray radiation[31, 115]. A skin dielectric equivalent gel was previously investigated to improve impedance matching to the human skin and heating uniformity [113]. However, this was achieved at operating frequency under 400 MHz. An alternative approach was the use of a substrate material suspended over the radiating element, this is known as a superstrate layer. The first analysis of microstrip antenna covered with a dielectric medium was investigated back in the 1980, where numerical solution for effective dielectric constant of two medium was investigated[116]. The primary use was as a protecting layer of the radiating element. The superstrate material was then further investigated in term of the operating frequency as a function of thickness and input impedance [117]. The superstrate layer was also known as the " low loss dielectric cover layer", was initially investigated on a rectangular microstrip radiator in a local hyperthermia [118]. The dielectric medium was used to improve impedance matching

and the radiated E-field pattern. In wireless medical telemetry, superstrate layer was used to optimise the antenna surface area [119]. Superstrate was also discovered to increase the directivity/Gain and bandwidth of the antenna [120, 121]. In our study, we focused on a superstrate layer to isolate the antenna element from the tissue. The superstrate layer used was equivalent to substrate, a low loss dielectric medium. The study focus on applicator matching with appropriate superstrate thickness, for optimal heating and cooling pattern.

6.3 Microstrip Antenna Theory

The interests in microstrip antennas are continuously increasing in every day applications, the attractiveness is led by its low profile, easy to fabricate and low cost. Printed antennas can be in the form basic shapes to more complex shapes, rectangular patch are most frequently used in variety of application, due to its simplicity in design and impedance matching. Microstrip radiators in medical application were reported in 1979 and 1980 [122, 123]. Antenna comes in many different shapes and applications, such as a spiral [124],an annular ring for hyperthermia [123], slotted patch antenna for microwave breast imaging [125] and dual concentric conductor in an array approach[126, 14]. The field distribution impact of contact flexible microstrip applicators on curved biological tissue have been recently investigated for superficial hyperthermia [127].

A microstrip antenna consists of a conducting radiating element on a substrate material with an optimal dielectric constant ϵ_r, thickness H, and a ground plane at the bottom side. Figure6.2 shows the schematic of a standard rectangular patch antenna. Generally, in order for the antenna operates in the fundamental TM_{01}(Transverse Magnetic) mode, the patch length L must be at approximately $\lambda_g/2$. Where λ_g is the guided wavelength, and can be calculated from $\lambda_g = \lambda_0/\sqrt{\epsilon_{eff}}$. This estimation is required

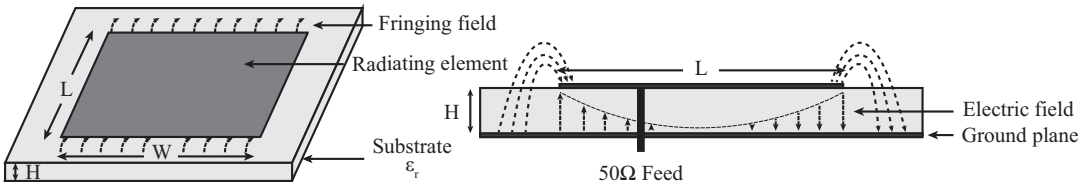

Figure 6.2: Microstrip patch antenna theory.

when the phase velocity in air and dielectric medium are different. The effective dielectric constant ϵ_{eff} is a parameter which considers the propagation of fringing field between dielectric substrate and air as given in the equation. Typically this value is lower than ϵ_r of substrate, due to the spread of wave in air ($\epsilon_r = 1$). The effective dielectric constant estimation is a function of ϵ_r , substrate height H and patch width W as shown in Equation 6.3.1[128].

$$\varepsilon_{reff} = \frac{\varepsilon_r + 1}{2} + \frac{\varepsilon_r - 1}{2}[1 + 12\frac{H}{W}]^{-\frac{1}{2}} \tag{6.3.1}$$

The electric field along the width of the patch is maximum, where the current is minimum due to the high impedance at the ends. Figure 6.2 shows the normal components of the fringing field are out of phase at the two edges. This caused by the $\lambda_g/2$ patch length L which causes the field to cancel out at the centre. In contrast, the excited tangential field between patch edge and ground plane are in phase and therefore field is radiated normal to the surface of the patch. It can be observed, the fringing field extends further than the physical patch length L. For improved estimation the effective length can be estimated from the given Equation 6.3.2.

$$L_{eff} = L + 2\Delta L \tag{6.3.2}$$

Where L is the physical patch length calculated from Equation 6.3.3 and ΔL is the extended fringing field length which is a function of ϵ_{eff}, W and H as shown in Equation 6.3.4[129, 130].

$$L = \frac{c}{2f_o\sqrt{\varepsilon_{reff}}} \tag{6.3.3}$$

$$\Delta L = 0.412h\frac{(\varepsilon_{reff} + 0.3)(\frac{W}{H} + 0.264)}{(\varepsilon_{reff} - 0.258)(\frac{W}{H} + 0.8)} \tag{6.3.4}$$

The width of the patch W can be estimated with the following expression

$$W = \frac{c}{2f_o\sqrt{\frac{(\varepsilon_r+1)}{2}}} \tag{6.3.5}$$

Microstrip patch antennas may have various feeding techniques to couple the EM energy in or out, such as Inset feed, pin fed and aperture coupled [14, 125, 131]. The inset feed a transmission line is required at the radiating surface which is not suitable for this particular application due the near field operation region where the transmission

line will disturb the field propagation from the radiating element. A common feeding technique is probe feed shown in Figure 6.2, where a coaxial SMA connector is connected from the ground with isolated 50Ω pin through the substrate and soldered to the patch element surface. Consequently, mitigating the fringing transmission line to the superficial tissue [114]. This approach was adopted for the Hybrid probe. The feed position location can be calculated from radiation conductance, further detail found in literature [132]. The aperture feeding method compromises of stacked approach where the transmission line is shielded by conducting plane with gap to transmit energy to the patch, This method could prove to be more useful than probe fed microstrip, due to the coaxial soldering at the surface of patch which may cause air gap between antenna and phantom. The design of applicator operating in close proximity to the tissue relies heavily on numerical calculations, by studying the E-field and SAR distribution. With microstrip antenna theory it is possible to estimate the optimal geometry for the desired frequency in free space. Therefore the applicators were designed without tissue loading (in free space). The is because it is impossible to estimate the ϵ_{eff} of heterogeneous biological tissue with a dielectric substrate. The applicator is then optimised appropriately with EM simulation when placed on layered tissue model.

6.4 Modelling and Simulation

6.4.1 Numerical Study

Measuring the EM energy inside a living biological tissue is a major challenge for RF engineer working in the medical sector. The operation of newly developed RF devices ranging from daily uses such as mobile phones to therapeutic applicators, they all must comply with the regulated dosage. Consequently, RF engineers are forced to rely on computer simulation for design and development of new devices before commencing to the *ex-vivo* and eventual *in-vivo* trials for validations. The method of acquiring the deposited EM energy can be achieved analytically or numerically. Analytical techniques are achieved by solving Maxwell's equation for simplified geometry such as the homogeneous canonical models. The rapid development of computing capability, meant the numerical dosimetry is the dominant method in calculating RF dosimetry in either simple geometry to vast complex inhomogeneous structures. The numerical methods allow for near-field studies of an external non-plane wave source [133]. There are few

numerical techniques have been employed over the last several years in order to solve bio-electromagnetic problems. Presently, the finite difference time domain (FDTD) is the most common computer simulation technique, which is based on partial differential form of time dependent Maxwell's equations [134–136]. The implementation began by dividing the simulation problem into cubes. This is known as the Yee space cell or the grid mesh as we know it today [137]. The field components are approximated at the centre of each cell at a given time. Alternative technique that been used is based on finite-element method (FEM), which analyses the field components at the nodes of the cell [138]. the final technique which was considered during the development of the hybrid applicator, based on finite integral technique (FIT) used with Computer Simulation Technology (CST) microwave studio package[139].

FIT was initially proposed by Wieland in 1977 as frequency-domain solver, by solving Maxwell's equations in the integral form [140] However, it has expanded and now is capable of solving in time and frequency domains among with other techniques. FIT provides a spatial discretisation scheme, where the domain (3D model) is divided up into grid (Hexahedral mesh), and field components are solved within each cell. FIT strength lies with in meshing of three-dimensional models and staircase approximation for curved structures [140]. Literature study shows both FDTD, and FIT have been employed in numerous studies of microwave dosimetry on biological tissue [141–144]. The availability of CST studio in the Electronic Engineering department, meant it was unnecessary to investigate into FDTD method unless additional verification is needed in the future development. Consequently, CST was used to develop the hybrid applicator from dosimetry calculations to transient thermal solution of the combination of induced microwave and skin cooling mechanism.

6.4.2 Simulation Model

In the simulation study, the characteristics of EM deposition in biological tissue have been previously investigated with a simple homogeneous and heterogeneous models [145, 146]. Canonical models (multi-layered) are customary approach when time and computational resources are restricted. It can be modelled in a different form of geometry, such as the basic superimposed model [147], sphere for simulating the human head[148, 149] and cylindrical for curved anatomical locations[150]. Planar three lay-

ered model was proposed with the use of essential tissue composition of skin, fat and muscle [147, 151]. This approach was taken into account in the design and simulation study of the hybrid applicator. This was justified by the computational efficiency, and to be compatible for comparison with the experimental three layered phantom. Recent studies show greater interest in anatomical models for realistic analysis on deposited EM energy [142]. Current anatomical models of the individual body, are based on a voxel (cubic staircase) with a predefined resolution and dielectric properties [65]. The models were originally obtained from either CT or MRI scans, which both are complicated problems to solve. In this study, simulation with anatomical model was used for verification of the final design before fabrication. The used voxel model was provided by CST Microwave Studio with a resolution of $2.08 \times 2.08 \times 2.00$ mm^3. To reduce computational time, only the human calf was extracted, neglecting the remaining of the biological model.

The developed applicator is designed using the combination of microwave and thermal co-simulation. The applicator was first adapted from the basic antenna theory, then transformed into a parametric digital model for optimisation and further study. The applicator model is combined with a three-layered tissue model consisting of skin, fat and muscle with the following thickness of 1.0, 7.0 and 50 mm respectively. The thickness of muscle is limited to 50 mm which has sufficient losses and depth to absorb all the energy, therefore there is no reflection from the simulation boundary. The combined model undergoes a series of configurations, simulation and analysis as shown in Figure 6.3. The early stage configuration involves mesh optimisation and boundary conditions. In the CST microwave studio, a Hexahedrial mesh is deployed and refined based on the upper operating frequency which was 5.0 GHz. The frequency limit is twice larger than the desired centre frequency, this to ensure adequate meshing employed. Furthermore, a predefined local mesh size was set manually to ensure sufficient mesh lines inside the thin layers of skin. The boundary condition is essential in obtaining the desired reading for the proposed application. In microwave simulation, the boundary condition is set to open boundary in all directions except for at the negative z-axis, where the applicator is interfaced to the skin surface. During microwave simulation the scattering parameter and SAR is evaluated at first, and enhanced accordingly before proceeding to thermal simulation.

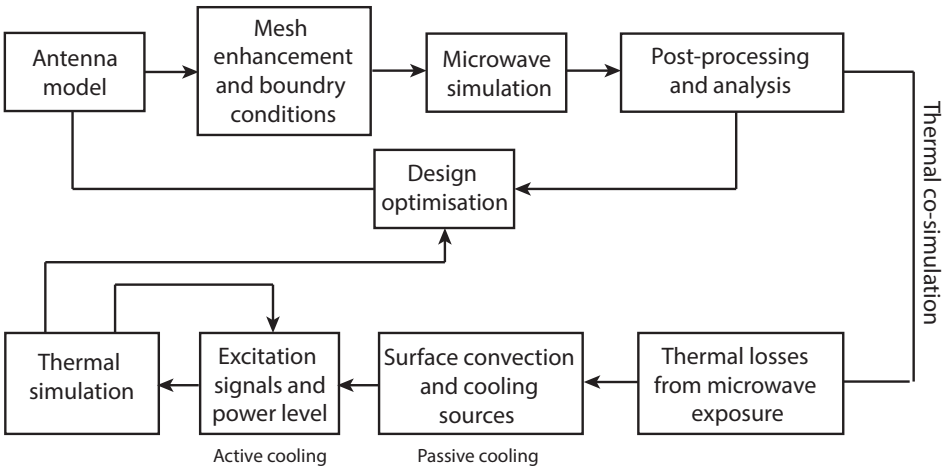

Figure 6.3: EM and thermal simulation procedure for applicator designs.

Thermal boundary condition is also considered and applied to the model appropriately. Adibatic condition is applied along the x-axis, y-axis and z-max as shown in Figure 6.4a. This condition ensures no heat flows past the boundary, hence the temperature distribution is not constant. This is typically used for multi-layered tissue models with biological heat. Open condition is applied to z-min, to emulate free space where surface convection can be used. For experimental phantom validation, the thermal boundary is changed to open space for all directions to match the phantom condition exposed air. Surface convection is applied, where the convection rate is the standard passive convection of 7 W/m^2. Figure 6.4b shows the temperature of the three-layered tissue phantom with and without applied surface convection. Thermal boundary condition cannot resolve skin convection. Consequently, the skin and deep tissue temperature are identical to approximate 37 °C. The model with skin convection, has a skin temperature of about 34 °C. In contrast, when the applicator is placed on the tissue with passive cooling, the skin temperature drops to 32 °C and 29.5 °C with added heat-sink on applicator. The final adjustment would be the excitation signal and microwave power scaling. Continuous and pulsed excitation signals have been investigated to emulate thermostatic cooling and heating. The power levels are also adjusted accordingly along with the active cooling, further discussed in Section 6.6.3.

6.4.3 EM Simulation Procedure

The simulation package was used to establish general understanding of a standard microstrip patch antenna on the modelled three-layered phantom. The basic simulation

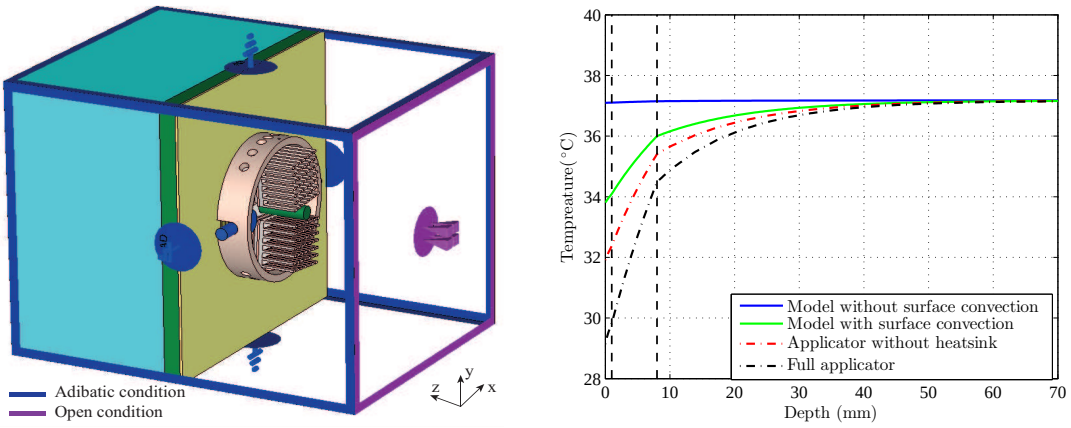

(a) (b)

Figure 6.4: Tissue model with appropriate boundary conditions. (a) three-dimensional model of applicator and phantom, (b) the simulated tissue temperature as a function of surface convection

model is shown in Figure 6.5. The simple antenna geometry is presented in Figure 6.5a, and it is suspended at a proximity of S_a above the three layered phantom as shown in Figure 6.5b The biological model uses the corresponding electric and thermal properties for each layer. This study investigates the antenna performance with respect to S_a. This is an essential parameter for early stage design of the hybrid applicator. The modelled tissue thickness is currently based on 1.0 mm skin, 7.0 mm fat layer and 40.0 mm muscle. However, the original model thickness of 2.0 mm skin and 10.0 mm fat layer was used previously during the development of majority of applicators. It was later discovered the values were over estimated for a calf/arm tissue. The modelled rectangular microstrip antenna was calculated by the given theory to estimate the length (l_p) and the width of the patch (w_p). The design is then optimised accordingly to operate with the phantom and the proximity parametric study. The substrate was based on Rogers 5880, ($\epsilon_r = 2.2$) and operating frequency was maintained at 2.45 GHz. The simulated result is evaluated in term SAR at different antenna spacing as demonstrated in Figure 6.6. The results is evaluated horizontally, where the first column corresponds to the yz-plane cut (a,b,c,d), and the second column is the xz-plane cut (e,f,g,h). Results evaluated vertically from the top to bottom. Each row corresponds to the antenna spacing (S_a) in the following order, 5.0 mm and 2.0 mm in free space, direct contact and 1.58 mm of superstate.

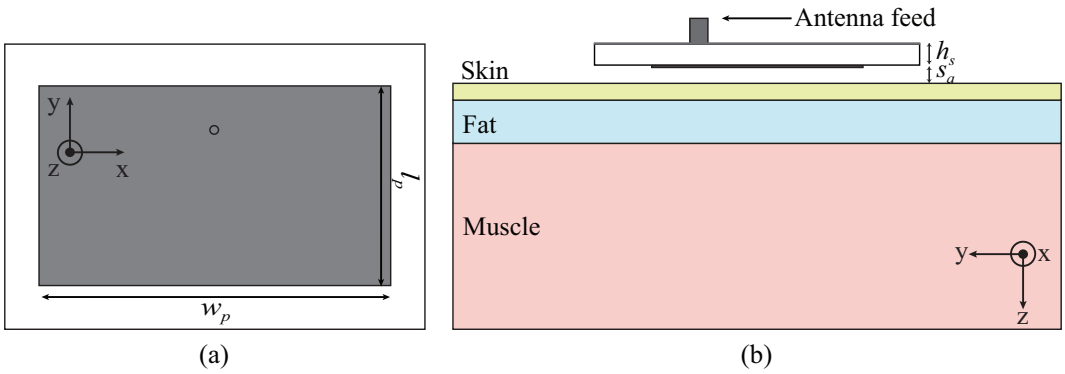

Figure 6.5: General rectangular microstrip patch antenna model. (a) simple antenna geometry,(b) antenna placement on a modelled phantom

From the simulated SAR plots, it can be observed the absorbed field in the tissue changes its performance as a function of spacing. In the scenario of $S_a = 3.0$ mm Figure 6.6(a and e) the antenna is spaced further away. Therefore, the electrical length of the antenna becomes longer to maintain the same operating frequency. Consequently, larger area is radiated at the surface of the skin. This is undesirable effect and will not be considered. Moreover, the field pattern in the yz-plane is not identical to xz-plane, caused by the radiating electric field at the antenna edges which can be only seen across the yz-plane in this current geometry. This can be described with respect to antenna orientation as the E-plane for yz, while xz is the H-plane. The radiating edges become more apparent when the antenna proximity is closer to the phantom, hence the reacting near-field region. Figure 6.6(b and f) have a reduced area absorption when the separation is 2.0 mm, where as in the direct contact, the SAR is significantly larger at excited edges as illustrated in Figure 6.6(c and g). The final approach was to load the antenna by adding a superstrate later, which is an equivalent dielectric material as the substrate, at thickness of 1.58 mm. The SAR achieved was localised in comparison to the other studies as presented in Figure 6.6(d and h).

Alternative evaluation of the SAR data by recording the maximum peak values across tissue depth for each corresponding plane. The optimal measurement is considered by the muscle to skin ratio, were the skin is at depth of 1.0 mm, and muscle is anywhere between 8.0 - 50 mm. Figure 6.7a is the peak SAR comparison across the yz-plane The result clearly shows the direct contact approach has a peak SAR at the skin surface is more than twice larger to other spatial arrangements. The effect is

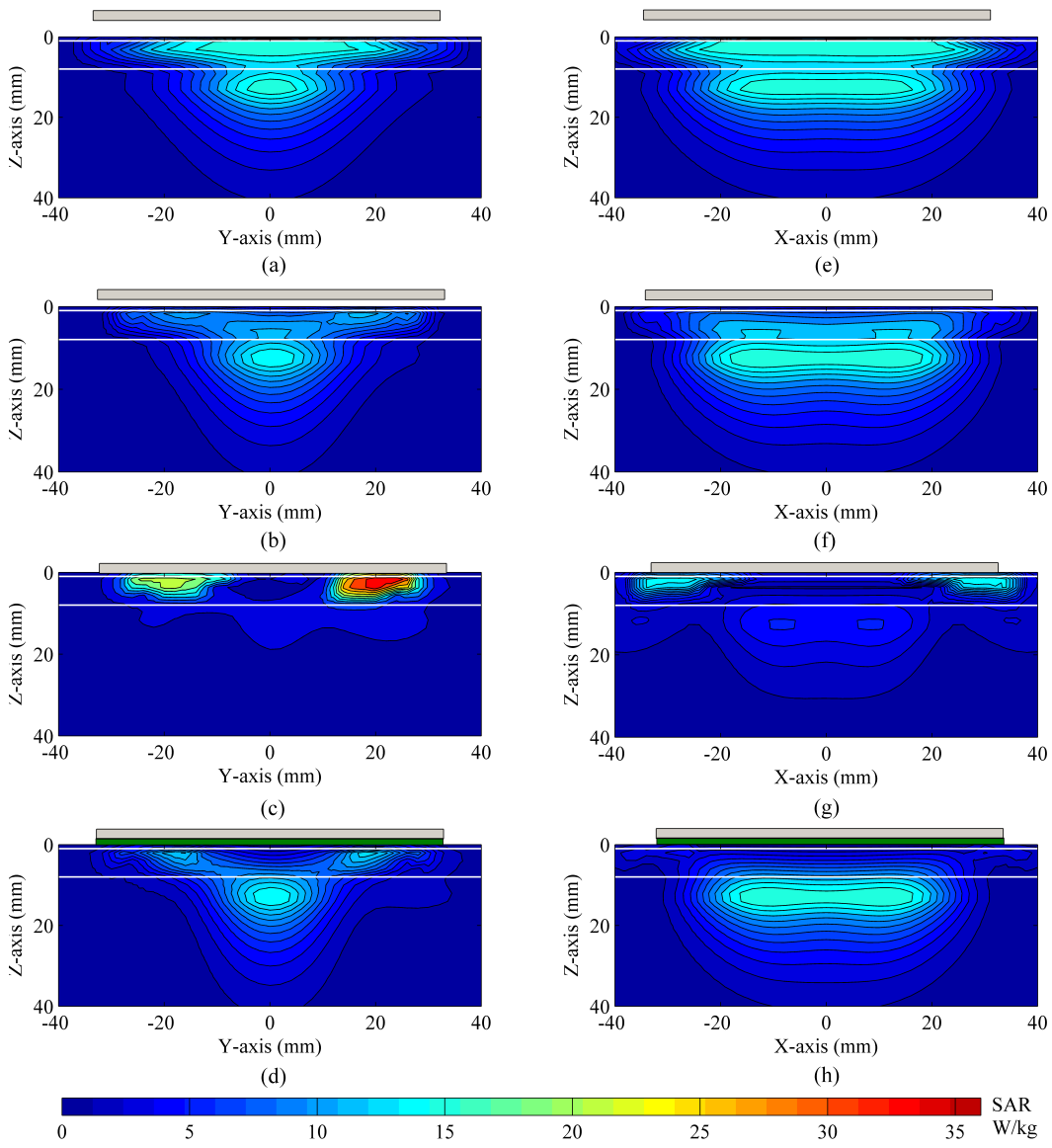

Figure 6.6: SAR distribution of simulated patch antenna at different separations between the applicator and skin. (a, e) 5.0 mm, (b, f) 2.0 mm, (c, g) direct contact, (d, h) 1.58 mm thickness superstrate ($\epsilon_r = 2.2$)

undesirable, particularly where only 13.7% of the EM energy is absorbed in the muscle. Antenna spaced by superstrate is the most efficient, when considering the peak across both planes. In contrast to the antenna suspended in free space, the fat absorption is greater, and it further increases as the proximity to tissue gets larger. The result observed are from the EM field absorption perspective, thermal study will also be beneficial in providing different insight from heat transfer point of view.

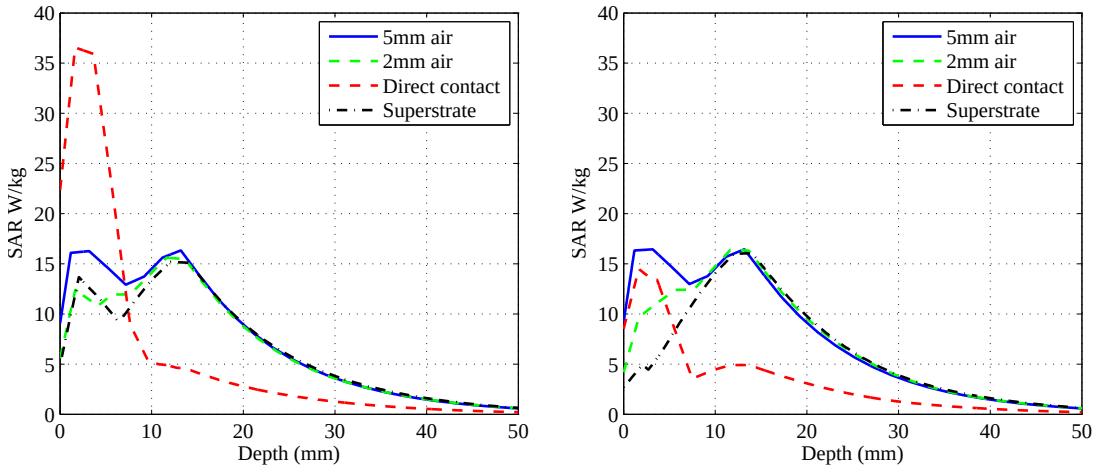

Figure 6.7: Peak SAR at different proximity across (a) *yz*-plane, (b) *xz*-plane

6.4.4 Thermal Simulation Procedure

The corresponding thermal simulation of antenna proximity is demonstrated in Figure 6.8. The result was based on transient thermal simulation at 5-minutes of microwave exposure, using biological heat parameters and a 5 watts of microwave power. The thermal pattern are equivalent to the observed SAR distribution. It can be seen in Figure 6.8(a,e,b,f)the elevated temperature covers larger area under the antenna with muscle warming at about 42 °C. The direct contact approach shows large peak temperature at skin and almost minimal muscle temperature change in the muscle. Figure 6.8 is the simulation result using superstrate, were temperatures at the skin surface is lower in contrast to other studies. The heating pattern is localised due to the increase in permittivity of the superstrate, producing a shorter electrical length. The peak temperatures are recorded and shown in Figure 6.9. The overall peak temperature is 50 °C at the skin surface in direct contact approach, which is completely unsafe design. The other parametric study shows as the proximity in free space increases, the temperature rises in the exposed area, particularly the skin surface at 43 °C. In contrast, the applicator with superstrate decrease in temperature peaking at 40.5 °C at the skin-fat interface and in the muscle. The advantage of the superstrate appears clearly in the xz-plane shown in Figure 6.9b, where the surface temperature is just about 37.5 °C in contrast to 2.0 mm free space of 40 °C. That is 2.5 °C lower, while the muscle temperatures are nearly identical to 40.5-41 °C.

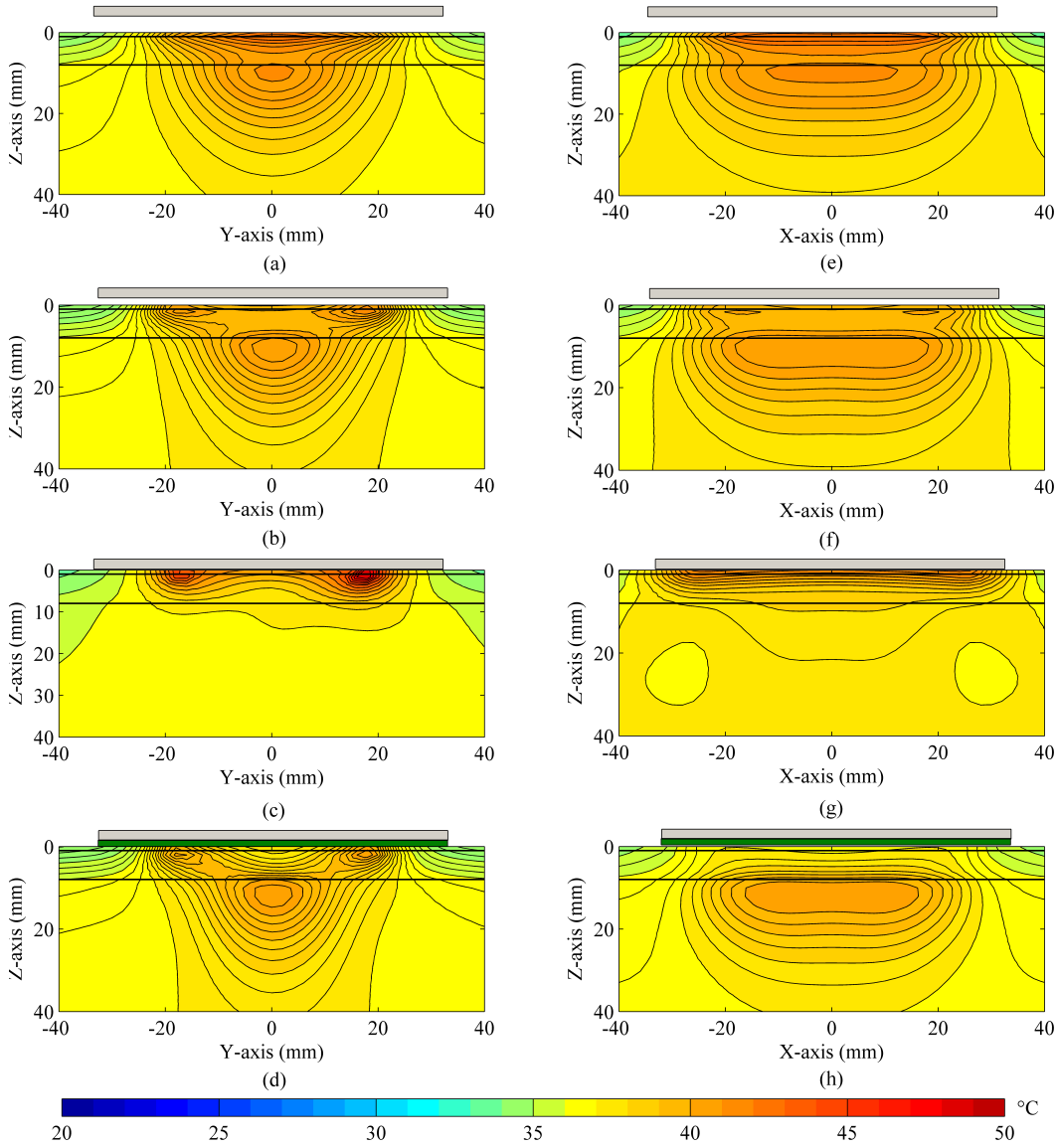

Figure 6.8: Thermal distribution of simulated patch antenna after 5 minute of microwave exposure at different separations between the applicator and skin. (a, e) 5.0 mm, (b, f) 2.0 mm, (c, g) direct contact, (d, h) 1.58 mm thickness superstrate ($\epsilon_r = 2.2$)

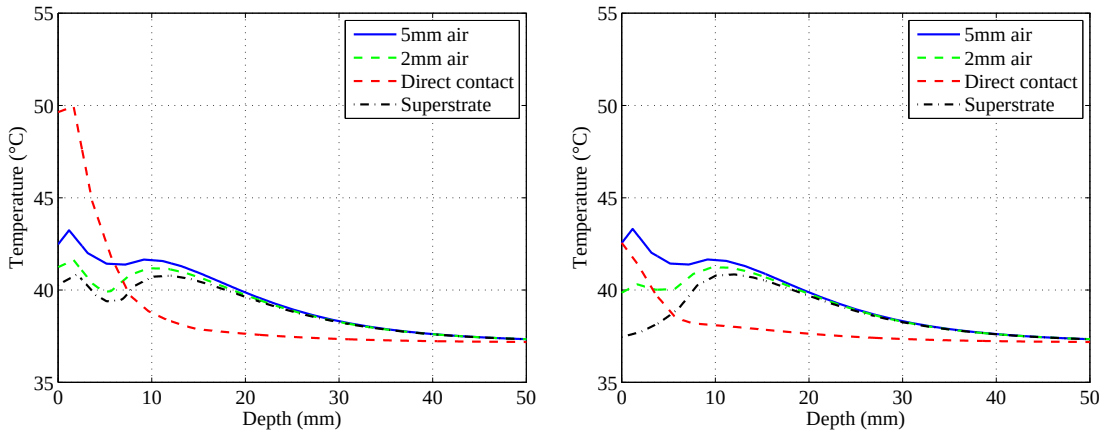

(a) (b)

Figure 6.9: Peak temperature at different proximity across. (a) *yz*-plane, (b) *xz*-plane

6.5 Applicator I

The previous sections introduced the foundation of applicator design from simulation conditions to antenna configurations. The study clearly indicates that a superstrate layer enables localised warming and reduced superficial heat on the skin layer in the mean of passive heat transfer. The other added benefit of the superstrate is the size reduction and provides electrical isolation between the radiating element and tissue. Based on those early studies, Applicator I was proposed with integration of optical sensors that provided by the Hamamtsu NIRO-103 oxygenation monitor. Figure 6.10 is the modeled and developed applicator, the design is based on the previous microstrip antenna study with use of Rogere 5880 for substrate and superstrate ($\epsilon_r = 2.2$).The substrate and superstrate thickness are both 1.58 mm ($\lambda_o/100$), where λ_0 is the wavelength in free space at 2.45 GHz. Figure 6.10a shows the radiating element geometry from an inherited rectangular patch antenna with patch length is l_p and width is w_p. The optical emitter and detector spacing is l_s and diameter is d_s, and the probes are inserted through the applicator to make contact to the tissue as presented in Figure 6.10a,b). The full antenna dimensions and parameters are given in Table C.1.

The applicator was modelled with the same configuration previously mentioned using a planar three layered phantom, with aim to operate at 2.45 GHz. The performance of the applicator is studied by its current distribution, particularly contribution of the integrated probes. The probes are modelled as common plastic with $\epsilon_r = 3.0$.

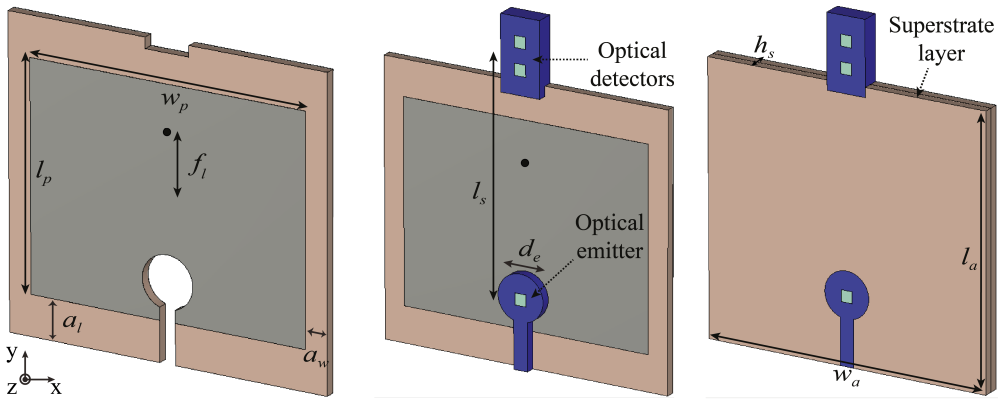

(a) (b) (c)

Figure 6.10: Modelled applicator I. (a) patch antenna parameters, (b) optical probes geometry, (c) applicator surface

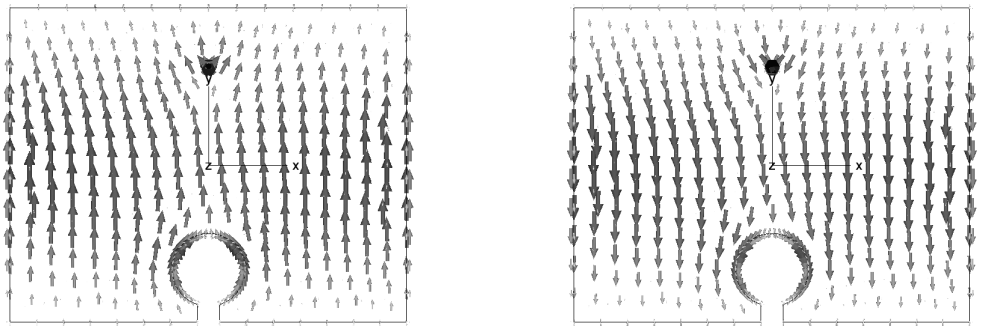

(a) (b)

Figure 6.11: Applicator I surface current distribution. (a) phase=0, (b) phase=180

The current distribution in Figure 6.11a shows the vectors flow towards the positive y-axis at phase 0 and negative y-axis during phase of 180. This clearly indicates the linear operation of antenna along the length l_p. The current distributes along a longer path at the lower centre of the patch, caused by the circular emitter cut-out. This essentially increases the electrical length of the patch, which leads to lowering the operating frequency and consequently, simple applicator minimisation was achieved. The applicator has been parametrised for further study in the following sections.

6.5.1 Integrated Optical Sensors Study

The optodes spacing (l_s) and the emitter diameter (d_s) have been further investigated with a parametric study. The desired optodes separation is 40 mm. However different lengths were studied to assess the applicator response. Figure 6.12a shows the s-parameter study of the (l_s), the results indicate the frequency shifts as the separation

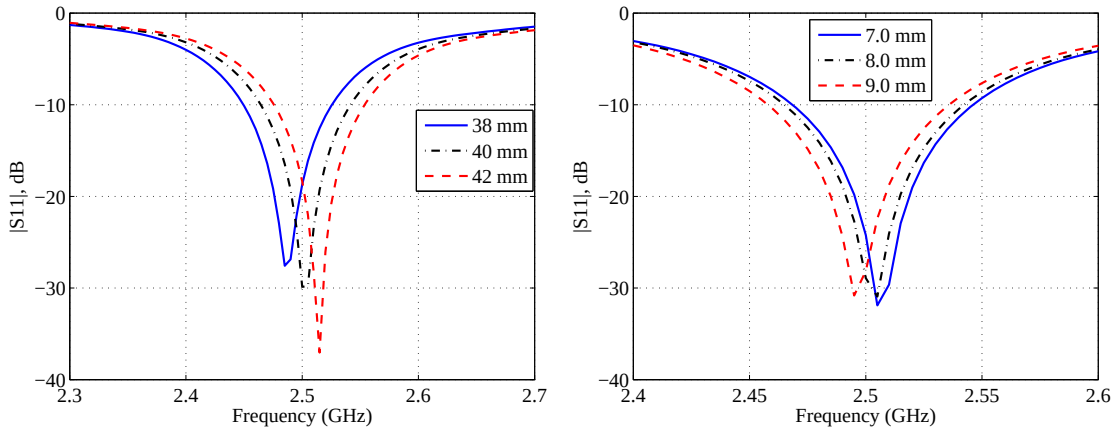

(a) (b)

Figure 6.12: Simulated $|S_{11}|$ for parametric study on. (a) optodes separation, (b) optical emitter diameter

increase which is explained by the decrease in electrical length as the emitter perturbation is moving away from the radiating element. The optical emitter diameter had a similar effect during the study shown in Figure 6.12b. The increase in emitter diameter meant, there is a decrease in frequency, caused by the circulating current around the emitter perturbation.

6.5.2 Superstrate Analysis

Previously, applicator proximity was studied with free space and compared with superstrate performance. In this study, the superstrate was investigated at thicknesses that are approximately equal to that of commercial substrate. The implication of the superstrate to the applicator design is investigated by analysing the scattering parameter, SAR and thermal distribution. The simulated $|S_{11}|$ is presented in Figure 6.13, the result clearly shows an increase shift of in resonance frequency with the thicker superstrate. The increase in superstrate thickness, produces a larger spacing between the antenna element and the high dielectric tissue properties (lower ϵ_r). Consequently the radiating fringing field is engaged in the lower dielectric medium of the superstrate; which leads to shift in operating frequency. Superstrate has a relatively low dielectric constant $\epsilon_r = 2.2$ in comparison to a skin layer which is $\epsilon_r = 37$. For a greater spacing, larger physical antenna length is required to maintain same operating frequency of the original 1.6 mm. Thinner superstrate thickness was also investigated. However, the performances are

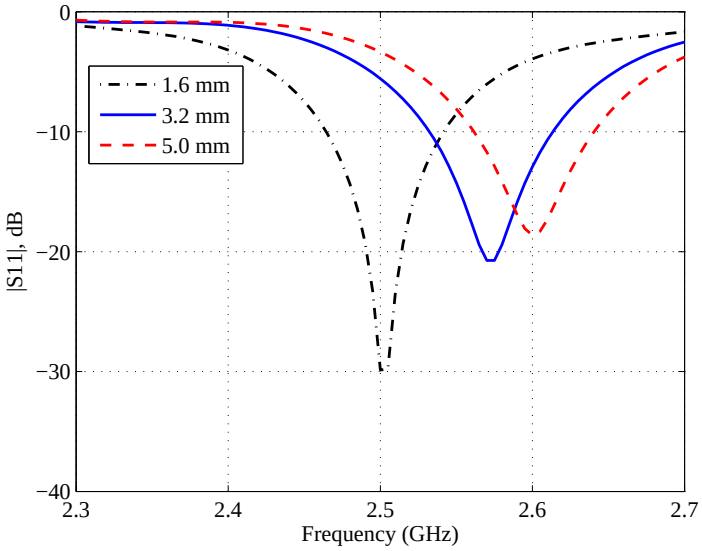

Figure 6.13: Simulated $|S_{11}|$ for superstrate parametric study.

undesirable, as it works much like the direct contact study discussed in sections 6.4.3 and 6.4.4.

The study of superstrate thickness, is observed in the form of SAR shown in Figure 6.14. The vertical orientation from top to bottom corresponds to the increase in superstrate thickness, while horizontally from left to right corresponds to *yz*-plane and *xz*-plane. The result leads to a similar conclusion as to the previous study interfacing free space. The increased thickness of the superstrate leads to higher deposition of energy in the centre of the skin and muscle tissue, while the peak absorption is in the muscle. Decrease in thickness causes the deposited energy at the centre of the superficial layer to spread apart, resulted by the confined fringing field directly under the radiating edges of the applicator (reactive near-field). The results are further evaluated with the peak SAR plots along the tissue, shown in Figure 6.15. The 1.6 mm loaded superstrate has a maximum SAR peak in the superficial layer at about 23 W/kg, and 21 W/kg in muscle. In contrast to 5.0 mm thickness, the maximum superficial SAR peak is about 16 W/kg and 25 W/kg in the muscle. Based on this study, the ideal superstrate thickness is above 3.2 mm, were the applicator is operating in radiative near-field region. Consequently, surface peak absorption is minimised, and a uniform EM distribution is attained.

The study of the superstrate is expended to transient thermal distribution of 5-minute microwave exposure at 5 watts RMS power. The simulation result is presented

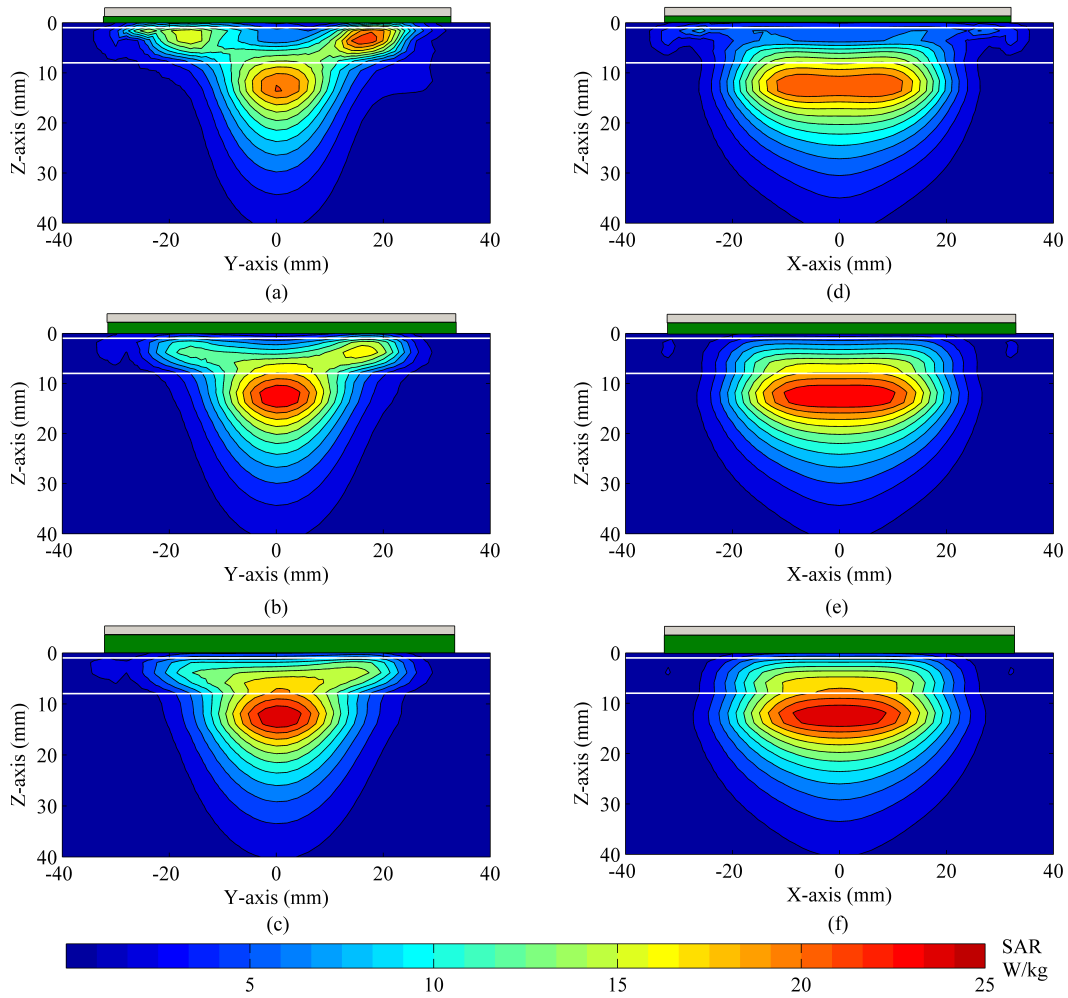

Figure 6.14: SAR distribution at of simulated patch antenna at different superstrate thickness. (a,b,c) *yz*-plane at 1.6, 3.2, 5.0 mm, (d,e,f) *xz*-plane at 1.6, 3.2, 5.0 mm

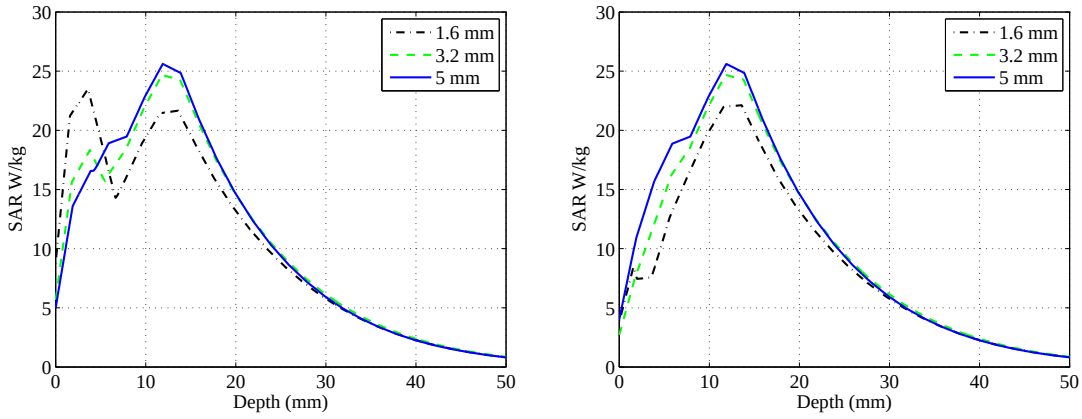

Figure 6.15: Peak SAR at different superstrate thickness. (a) across *yz*-plane, (b) across *xz*-plane

in Figure 6.16. Similar characteristics can be observed with SAR distribution, at 1.6 mm thickness the peak temperature is at the skin-fat interface. The increase in spacing, causes a uniform superficial heating distribution at the centre of the phantomn in a spherical form, which can be observed in the *yz* and *xz* planes. Thin superstrate have lower superficial heating in the non-radiating edges *xz*-plane, as the maximum temperature is observed in the *yz*-plane. The peak temperatures of this study presented in Figure 6.17b. The maximum temperature at the skin is 42.6 °C with 1.6 mm superstrate, other recorded temperatures are 40, 39 °C for thickness of 3.2 mm and 5.0 mm respectively. In contrast, the temperature in the muscle at depth of 12 mm is approximately 41.5 °C, 42.4 °C and 42.6 °C in the ascending manor of superstrate thickness. This clearly shows the 1.6 mm thick superstrate have muscle temperature of approximately 1 °C lower than skin temperature. The peak temperature profile at the non-radiating edges *x*-plane in Figure 6.17b, shows the 5.0 mm superstrate have an identical temperature profile in both planes. Transient thermal graph of 1.6 mm superstrate is shown in Figure

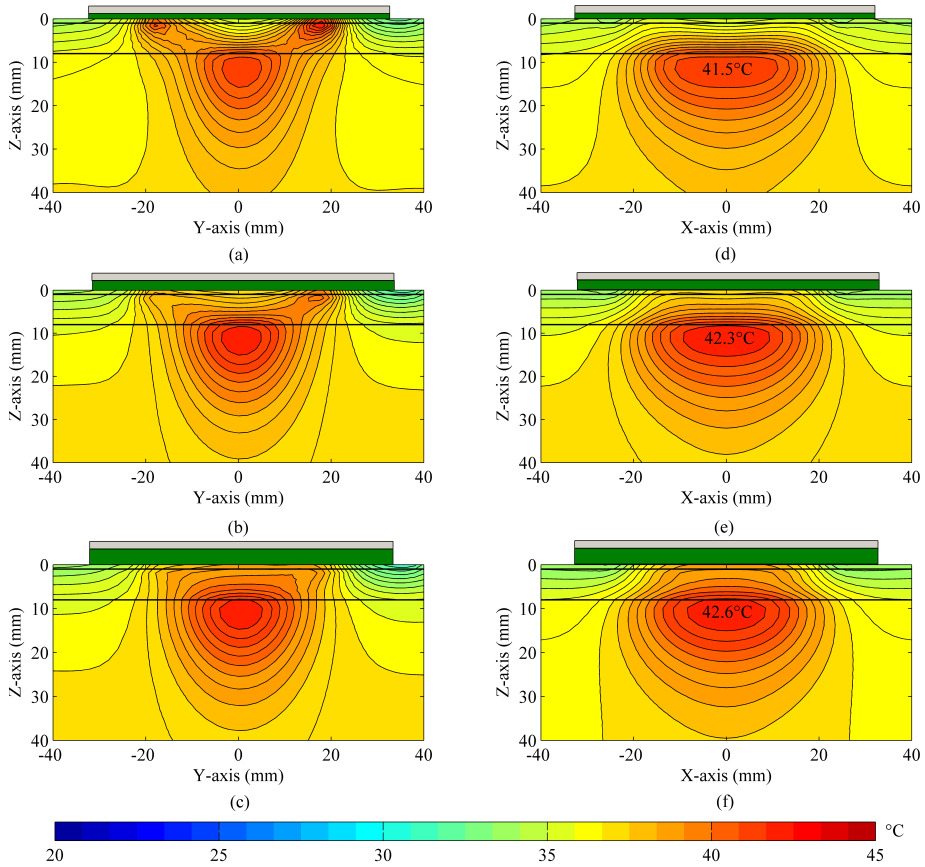

Figure 6.16: Thermal distribution at of simulated patch antenna at different superstrate thickness. (a,b,c) *yz*-plane at 1.6, 3.2, 5.0 mm, (d,e,f) *xz*-plane at 1.6, 3.2, 5.0 mm

6.18. It can be observed in Figure 6.18a the elevation of temperature at the skin-fat (1.0 mm in z-direction) interface over exposure duration. The point 0.0 mm corresponds to the centre, 17.5 and 17.5 mm are the points away from the centre in the y-direction under the excited edges, where the peak temperatures are expected. It can be observed the temperature of two radiating edges are 5-7 °C higher than at the centre. Figure 6.18b are the transient thermal analysis in the centre of tissue along the depth of (z-axis) at 0.0, 1.0, 8.0, and 10.0 mm. The depth of 8.0 mm and over corresponds to elevation in muscle temperature, where it is approximately 5 °C higher than skin at the centre. However, it is 2 °C lower when compared to the superficial hot spots. The transient pattern over 5-minutes have not reached a steady state. Thus further continuation may lead to high-temperature increase approaching to hyperthermia. Consequently, the duration is restricted to 5-minutes only.

The study shows 5.0 mm superstrate is the most optimum in terms of distribution uniformity, and reduced superficial heating. The downside is 5.0 mm is not an available thickness and stacking multiple of 1.575 may lead to undesirable air pockets in between each layer. The objective of task 1 was to design an applicator with integrated optical probes to warm and measure tissue response as a preliminary study of the combined devices. For that purpose, the 1.575 mm substrate was readily available and inevitably applicator was developed based on that substrate/superstrate thickness.

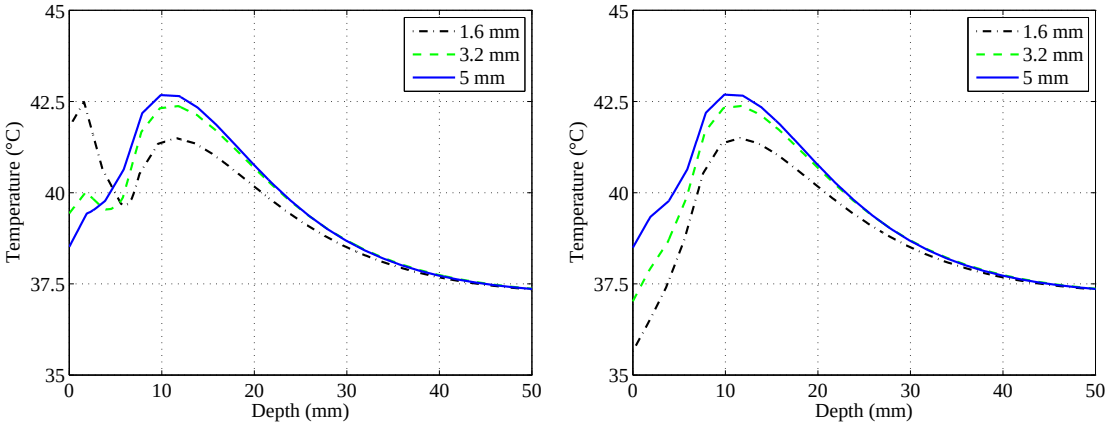

Figure 6.17: Peak temperature at different superstrate thickness after 5-minutes of exposure. (a) across *yz*-plane, (b) across *xz*-plane

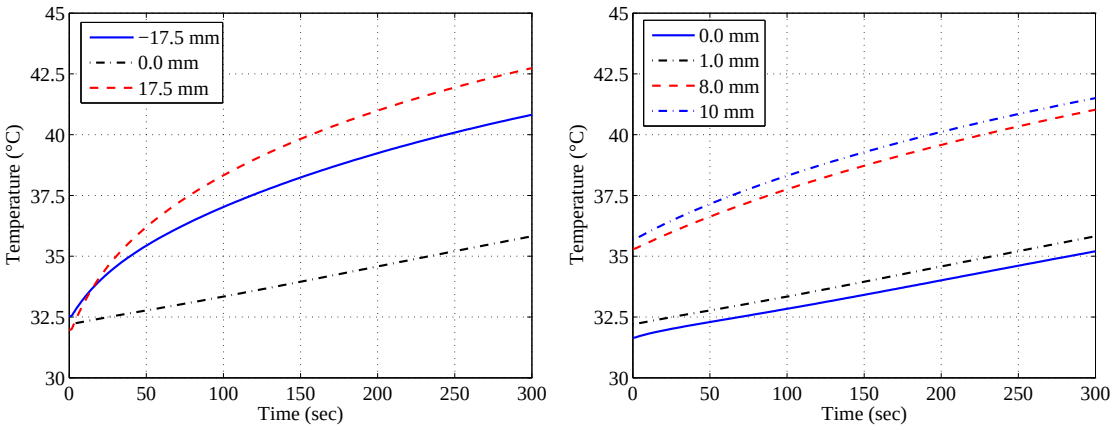

(a) (b)

Figure 6.18: Transient thermal simulation at fixed points,(a) along y-axis, with z=1mm, x=0mm,(b) along z-axis, with y=0 and x=0

6.5.3 Fat Thickness

The anatomical composition of biological tissue can vary from position to another and from one subject to another. This is a common problem RF engineer face during design of applicators or implanted communication devices, as the change of tissue thickness had an impact to the impedance and radiation pattern of the device. This study looked at the effect of changing fat thickness at 4.0, 7.0, and 10 mm, these are the common thickness in human body. The change in resonant frequency corresponding to the changes in fat thickness can be observed in the simulated $|S_{11}|$. It can be observed from Figure 6.19, the increase in fat thickness leads to a fractional frequency shift to lower frequency. The dielectric constant (ϵ_r) of fat at 2.45 GHz was taken as 4.5. When thickness is increased the radiating fringing field extends longer before being reflected by the high dielectric of muscle. This further extension lowers the resonance frequency. The operating bandwidth of the applicator at -10 dB is 85 MHz, which is sufficient to cover the frequency shift of approximately 20 MHz.

The impact of fat thickness was studied and represented in SAR distribution across both antenna planes as shown in Figure 6.20. The thickness increases vertically from each sub-plot. The results clearly show the fat thickness has an impact on the deposited EM energy. The maximum SAR observed is deposited in the muscle, while the absorbed power in the skin-fat interface is minimum. The result illustrates the SAR distribution between the muscle, and skin is a function of fat thickness for an incident EM

energy. Larger intermediate layer introduces a standing wave in the layer as the thick-

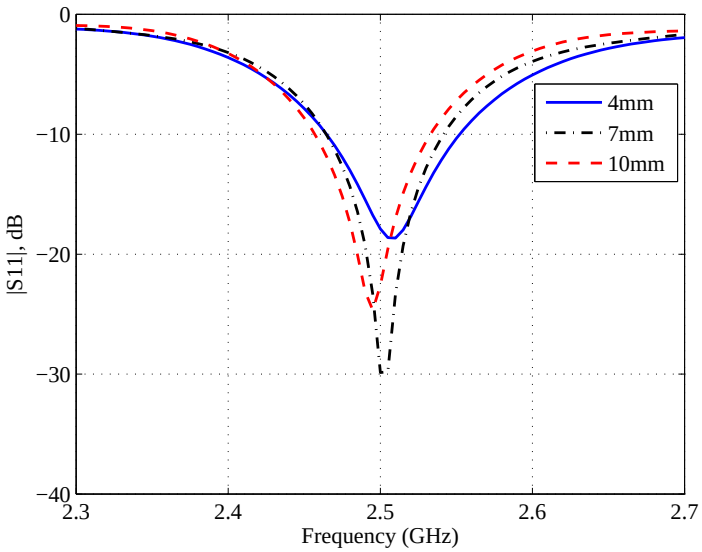

Figure 6.19: Simulated $|S_{11}|$ of applicator at different fat thickness.

ness approaches $\lambda_o/4$, consequently introducing a superficial hot spot. This common limitation of microwave applicators operating at 2.45 GHz, which have been previously investigated with a plane-wave [152]. Furthermore, SAR in the muscle varies substantially with the fat thickness, which becomes a challenge to estimate the appropriate level of exposure with patients at different fat thickness. This effect can only be mitigated by operating at lower frequency such as 900 MHz or 430 MHz. The first is not licensed in the UK, while the latter is undesirable due to larger applicator and heating pattern. Consequently, the most convenient solution is by suppressing the skin heating with cooling.

The peak absorption rate of tissue in the *yz*-plane and the *xz*-plane is illustrated in Figure 6.21. It can be seen the increase in fat thickness at the *yz*-plane promotes to an increase of skin absorption and reduction in muscle absorption. This effectively can be translated it into heat pattern, where a superficial hotspot is dominant in a subject with thicker fat. At 10 mm, the peak SAR at fat layer is 25 W/kg, where as in the muscle at 16 mm depth, it is 15.1 W/kg. In contrast, thinner fat thickness have higher peak SAR at the same depth of 16 mm. This clearly indicates, the fat thickness have a large factor on the superficial heating pattern and the penetration depth. Figure 6.21b shows the superficial layer have lower SAR in the *xz*-plane when the fat thickness is higher.

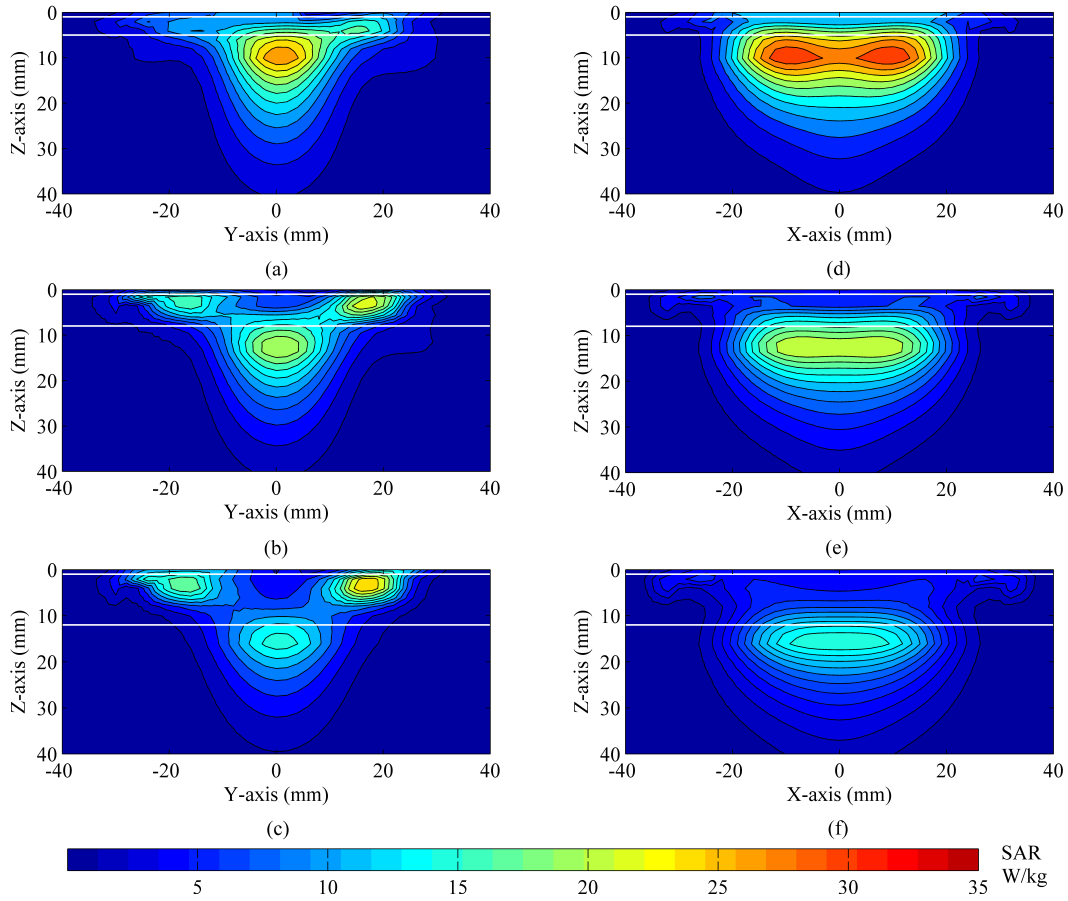

Figure 6.20: SAR distribution at of simulated patch antenna at different fat thickness. (a,b,c) *yz*-plane at 4.0, 7.0, 10 mm, (d,e,f) *xz*-plane at 4.0, 7.0, 10 mm

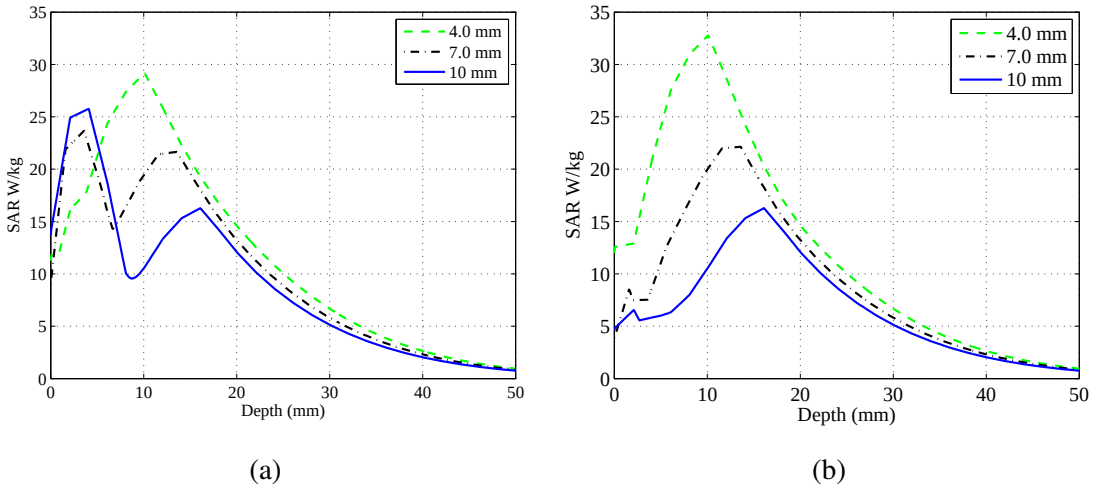

Figure 6.21: Peak SAR at different fat thickness. (a) across *yz*-plane, (b) across *xz*-plane

This is caused by the spread of the fringing field at the other plane cut (radiating edge) as seen in the *yz*-plane.

6.5.4 Skin Thickness

Having established the contribution of fat thickness in the previous study, the following investigation is based on skin thickness. This was implemented by varying the thickness from 0.5 mm to 2.0 mm in four equal steps. The current default study is based on 1.0 mm skin thickness. However, the actual design study was based on 2.0 mm skin thickness. The $|S_{11}|$ simulation in Figure 6.22 shows a frequency shift with respect to the skin thickness. As the thickness increases the resonant frequency detune down from 2.53 GHz at 0.5 mm thickness to 2.46 GHz with 2.0 mm skin. The reduction in frequency as a function of thickness is explained by the proximity of antenna to the skin, and the extension of fringing field in a high loaded dielectric of skin layer. The centre frequency shift is about 2.8%, where as the bandwidth of the applicator is about 3.6% at -10 dB. This is just about sufficient bandwidth to adapt for the frequency shift arises from skin or fat thickness.

The SAR study illustrated in Figure 6.23 shows the contribution of skin thickness to the SAR distribution. The *yz*-plane in figures 6.24(a,b,c,d), it can be observed a marginal increase in superficial absorption with the extended skin thickness, where as the muscle absorption has decreased. The *xz*-plane presented in Figure 6.23(e,f,g,h) shows the effective absorption area has decreased with the increasing skin thickness. The logical answer is the contribution of higher permitivity of skin ($\epsilon_r = 38$) which

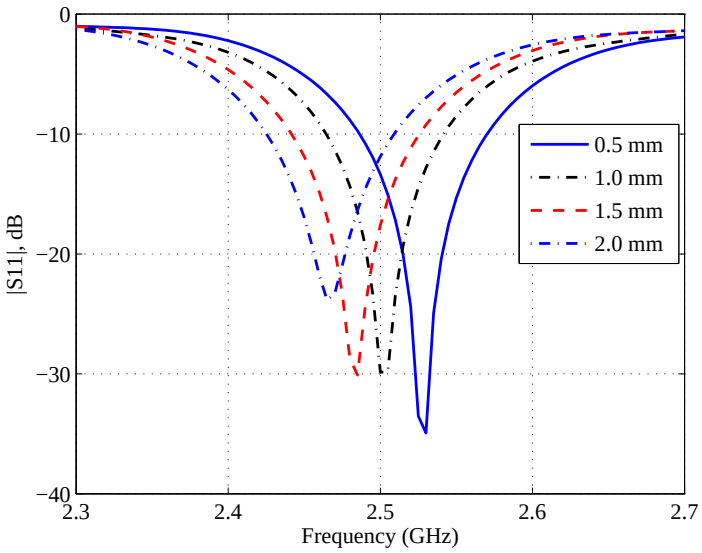

Figure 6.22: Simulated $|S_{11}|$ for applicator at various skin thickness.

confines the field in a localised area. Further details are presented in Figure 6.24b, demonstrating the peak SAR value in the vertical and horizontal plane. At 0.5 mm skin thickness, the peak SAR in the muscle is about 5 W/kg greater than the skin absorption. Meanwhile increasing thickness to 1.0 mm or higher have almost no further impact on the peak skin absorption. However, notable decrease in muscle can be observed. The peak SAR in the horizontal plane in Figure 6.24b clearly shows the absorption dimension for 0.5 mm skin thickness is larger in the fat-muscle area.

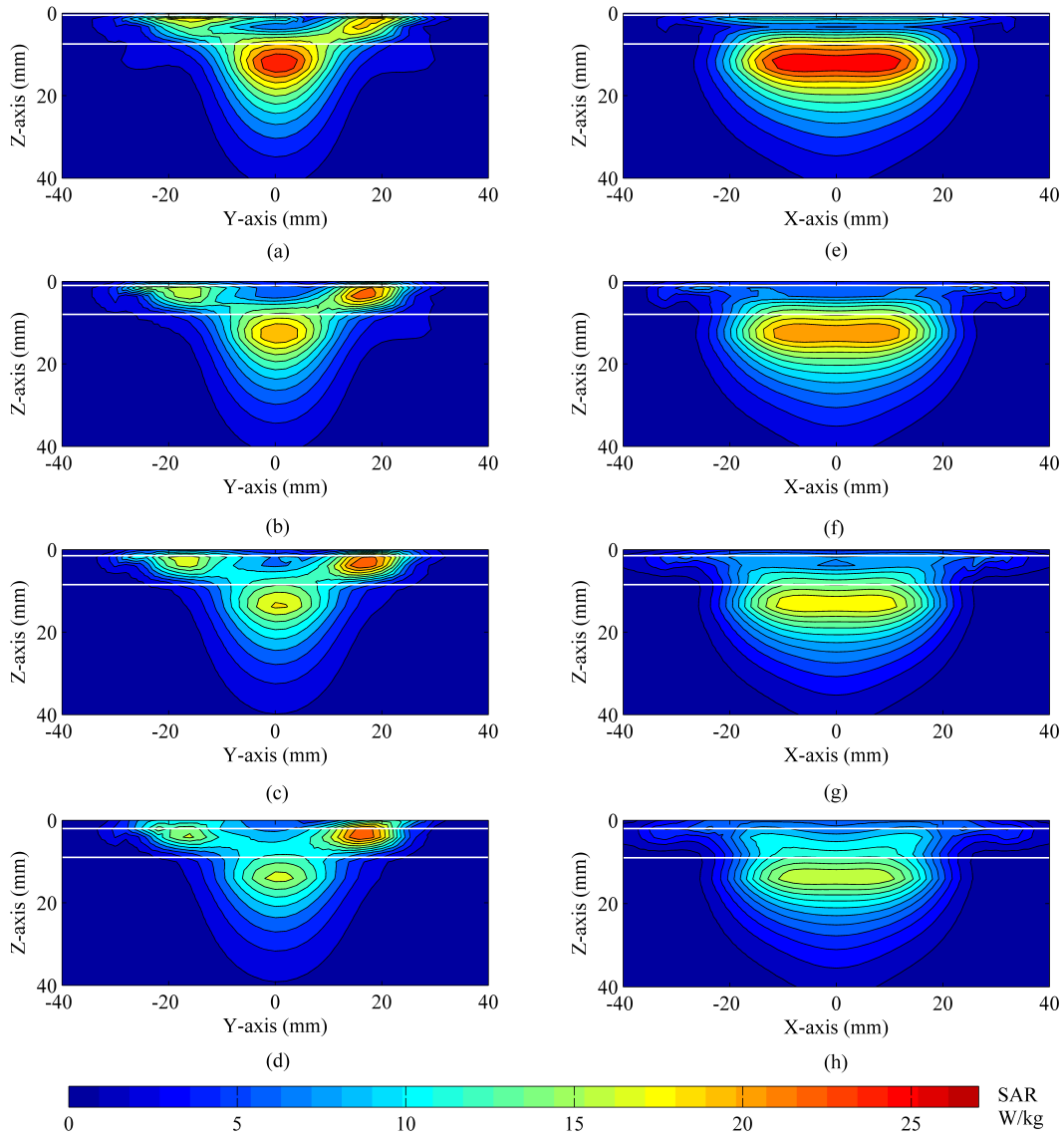

Figure 6.23: SAR distribution at of simulated patch antenna at different skin thickness. (a,b,c,d) across *yz*-plane at 0.5, 1.0, 1.5 and 2.0 mm respectively, (e,f,g,h) across *xz*-plane at 0.5, 1.0, 1.5 and 2.0 mm respectively

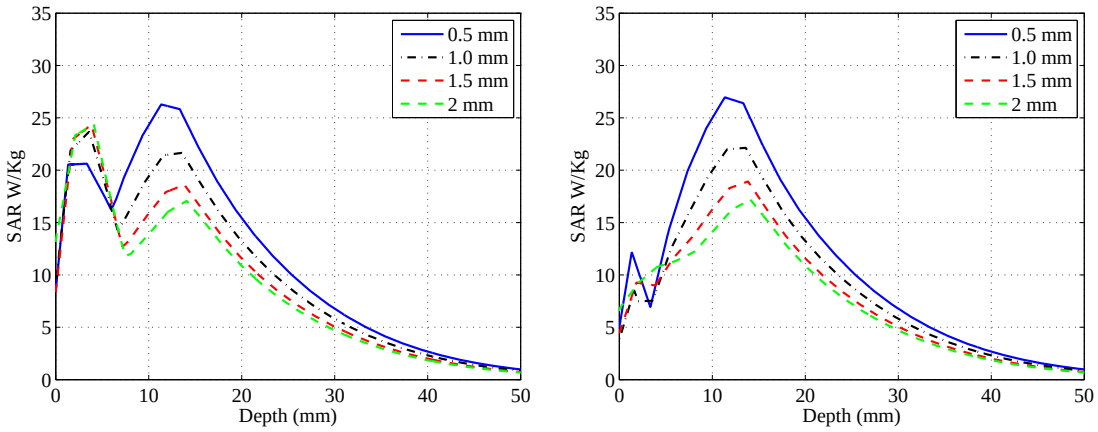

Figure 6.24: Peak SAR at different skin thickness. (a) across *yz*-plane, (b) across *xz*-plane

6.5.5 Anatomical Model

Study with a male anatomical model (Voxel) have been conducted for verification and applicator optimisation. The model was localised to only single calf with the placed applicator, which essentially reduce computational time. The numerical configuration shown in Figure 6.25. In contrast to the three layered model, it can be seen the added complexity of model curvature, inconsistency of tissue thickness and also the addition of bone. The tissue uses the appropriate electrical and thermal properties. The microwave simulation was carried out, and the SAR distribution is shown in Figure 6.26. The results illustrate identical features to the planar model in 6.16. The peak SAR in the anatomical model is 5 W/kg higher than the layered model. This is caused by the increase of skin and fat thickness, which varies along the model. The average thickness of the anatomical calf was 1.5 and 10.0 mm for skin and fat thickness respectively. Figure 6.26 shows the *xz*-plane of the SAR distribution. It can be seen the non symmetrical EM absorption in tissue, caused by the lack of consistency in the tissue thickness and possible reflection from the bone.

The 5-minute thermal distribution was simulated and shown in Figure 6.27. The peak temperature is in the skin-fat interface approximately 44 °C, which is 2.0 °C higher than the layered model. The muscle temperature was elevated from 3.0 °C to 40.0 °C. Despite the crucial difference between the two models; the layered model is more optimal as the corresponding tissue thickness was measured with ultrasound imaging, discussed further in Chapter 8.

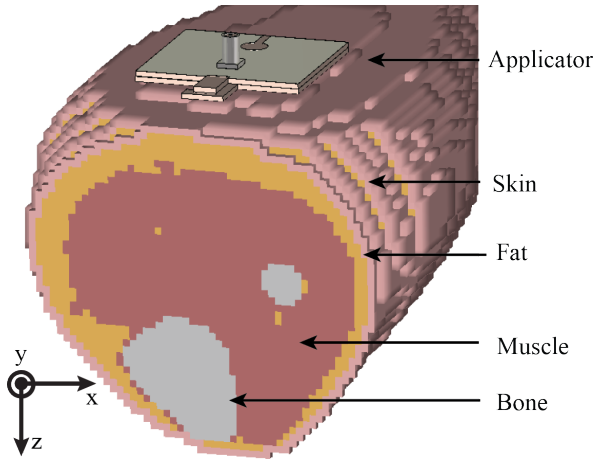

Figure 6.25: Anatomical leg model used for evaluations study.

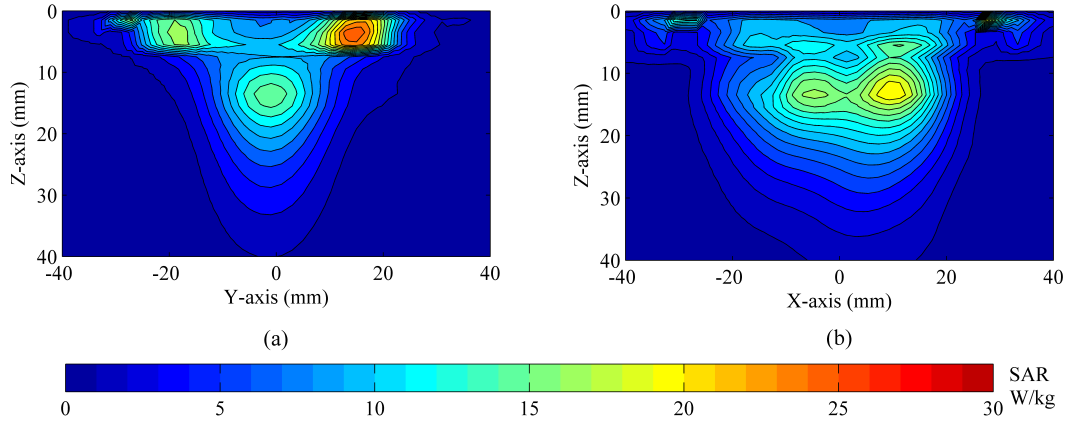

Figure 6.26: Simulated SAR distribution with anatomical model. (a)*yz*-plane cut, (b) *xz*-plane cut

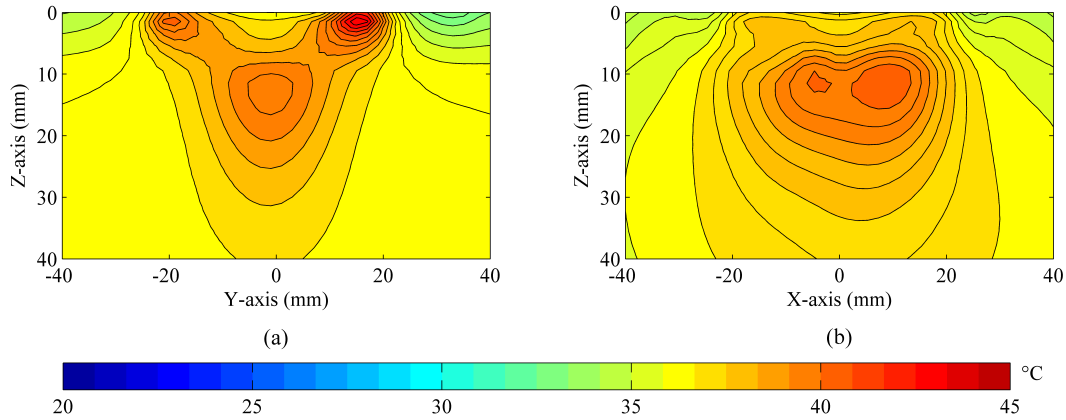

Figure 6.27: Simulated thermal distribution with anatomical model. (a) across *yz*-plane cut, (b) across *xz*-plane cut

6.5.6 Fabrication and Validation

The developed applicator and the ex-vivo setup is illustrated in Figure 6.28. This was before the implementation of the microwave system. Applicator I experiments was achieved with external off-the-shelf microwave generator and power meter. The setup in Figure 6.28b was for chicken breast temperature monitoring with the inserted thermocouple. The initial study was the antenna design, by evaluating performance in clear air and on biological tissue. The measurement is illustrated in Figure 6.29, where the return loss ($|S_{11}|$) in free space shows higher operating frequency at about 2.74 GHz, as the intended working frequency was 2.45 GHz. This was expected when the antenna operates in air, as it was optimised when loaded by the high dielectric properties of biological tissue. The purpose of in air measurement was to examine the performance of the applicator to the simulation without the liability of tissue composition. Consequently, the antenna impedance is matched to the tissue, operating in free space result in high return loss at about -7.9 dB. The measured data also indicates a 50 MHz increase in operating frequency from the numerical study.

The measured $|S_{11}|$ of the applicator placed on human calf is illustrated in Figure 6.30. The measurement was obtained from two human subjects prior to in-vivo study. It can be seen the resonance frequency is -24.0 dB at 2.55 GHz, that is discrepancy of 3.9% (100 MHz) from the intended operating frequency at 2.45 GHz. The measured -10.0 dB bandwidth was about 100 MHz, which is also 3.9%. Therefore, the bandwidth

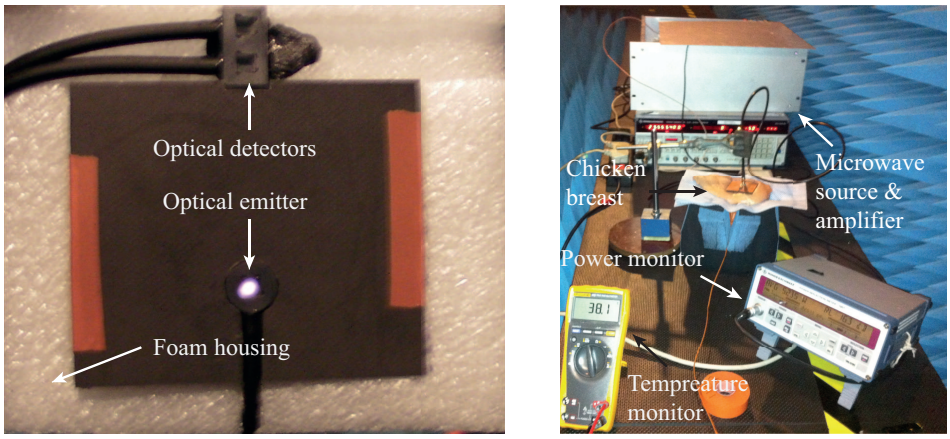

(a) (b)

Figure 6.28: Applicator development. (a) fabricated applicator with integrated optical probes, (b) deployed system for *ex-vivo* trial

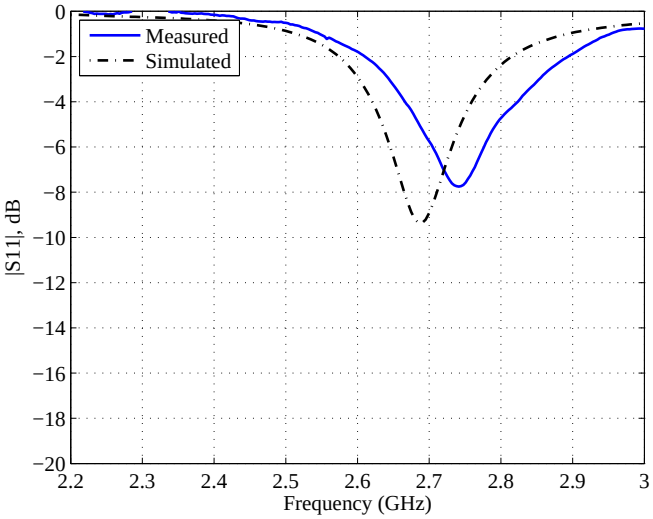

Figure 6.29: Applicator I measured $|S_{11}|$ on human subjects.

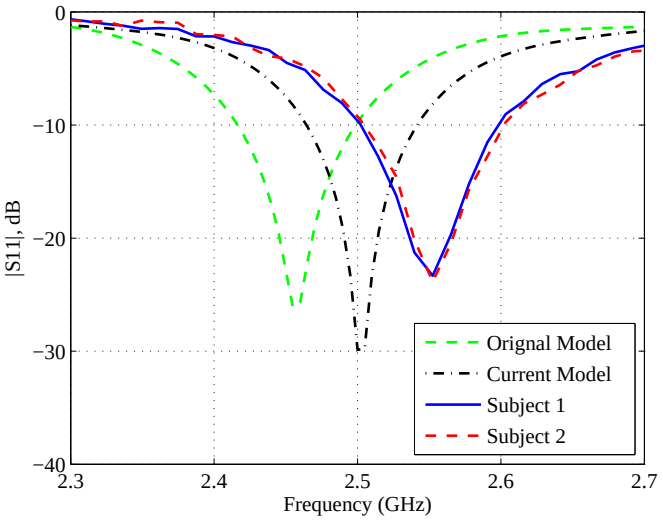

Figure 6.30: Applicator I measured $|S_{11}|$ on human subjects.

is not sufficient to cover the ISM operating range. The large deviation was caused by the numerous factors, including the modelled tissue thickness, electrical properties, fabrication errors, including introduced gaps with the stacked superstrate/substrate. Applicator I, II & CP applicators where developed based on the assumption of 2.0 mm skin and 10.0 mm fat thickness (original model). This was later discovered not accurate representation of a calf tissue, hence the change in the numerical model to 1.0 mm skin and 7.0 mm fat thickness (current model). The current model is 40 MHz lower than measurement, which coincide with the shift in free space result.

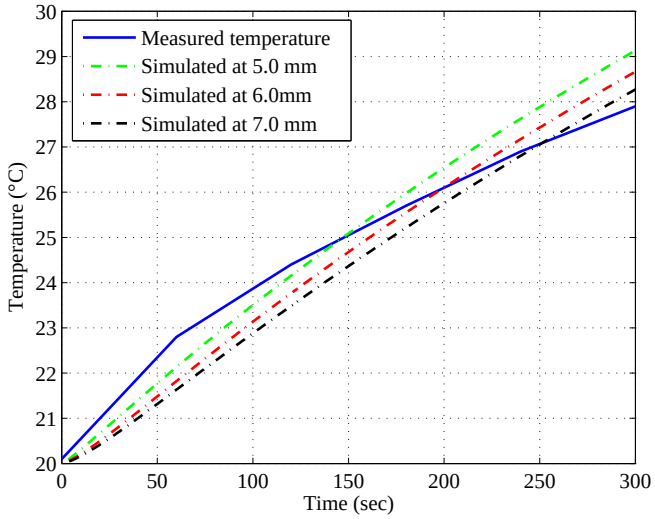

Figure 6.31: Measured transient temperature inside breast phantom.

The ex-vivo trial was implemented on a chicken breast, which is a single layer equivalent to a muscle. During the trial the applicator was placed on the surface of the chicken breast . A thermocouple temperature probe was inserted from the bottom to a fixed position at approximately 5.0 mm under the surface, where the temperature was recorded over the 5-minute of microwave exposure. The measure data was compared with the simulation result at equivalent configuration using appropriate dielectric and thermal properties of chicken breast, which was acquired from literature[153, 154]. The dielectric constant of chicken breast was 55, that is a 4.3% increase over the properties of human muscle. The electrical conductivity used was 2.5, which sees an increase of 43%. The thermal conductivity and heat capacity was 0.53 W/(m*K) and 3.546 kJ/(Kg*K) respectively. The result of a single measurement is presented in Figure 6.31, which shows the measured temperature against the simulation study at different depths to accommodate the possible region of probe placement. During the 5-minute of exposure, the recorded temperature was 27.9 °C, in contrast to the simulation at 7.0 mm depth was 28.2 °C. The general tendency shows a rapid increase in the first 60 seconds, after which the gradient was reduced to of the numerical study. The deviation in the measurement was limited by the number of samples taken at about every 60 seconds. Regardless early stage study indicated some consistence between the two data set. The variation was expected and was only marginal difference because of probe accuracy (1 °C) and positioning. Further evaluation and analysis were obtained with the use of

three layered phantom and IR thermal camera.

The fabricated tissue mimicked phantom was used to evaluate the deposited EM energy by measuring the thermal distribution for each applicator. The applicator was placed on the phantom, and kept at room temperature until thermal equilibrium on the skin surface is met. Figure 6.32 demonstrates the *ex-vivo* trial setup for Applicator I, where the tomographic camera clamped above the phantom to capture skin and muscle distribution after 5-minutes of exposure. The two layers are separated by a cling film, therefore muscle measurement was captured by removing the superficial layers. The initial temperature (microwave off) of skin layer varies between 21.5-22.5 °C, and the muscle was typically lower at 19.5-20.0 °C. The surface convection on the exposed surfaces causes the temperature to be equivalent to the surrounding. However, the muscle phantom is not exposed to air, and hence the temperature inside is preserved unless exposed for very long duration. This is illustrated in the Appendix C in Figure C.3. The captured thermographic image on the skin phantom is shown in Figure 6.33a. It can be seen a typical characteristics of applicator with superficial hot spots at the radiating edges when the microwave warming was on. The peak temperature at the skin was 33.0 °C, and 24.8 °C in the muscle (Figure 6.33b). The measured distribution was validated with simulation based on equivalent phantom configuration. The simulated skin temperature was just 1.0 °C inferior than measurement, and 0.2 °C in the muscle as shown in Figure 6.34. The variation in the skin layer was caused by the thicker skin

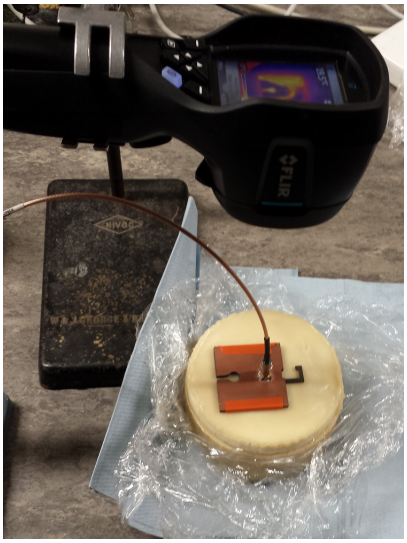

Figure 6.32: Ex-vivo experiment setup with multi-layered tissue mimicked phantom.

layer at the edge of the phantom, that lead to microwave absorption increase in the superficial layer. The measured skin thermal distribution shows identical features to the numerical study. The results in both scenarios conclude that is possible to warm up the muscle. However, larger increase was observed in the skin layer. This early stage validation assists in optimising the simulation model for enhanced accuracy of future applicator development and understanding.

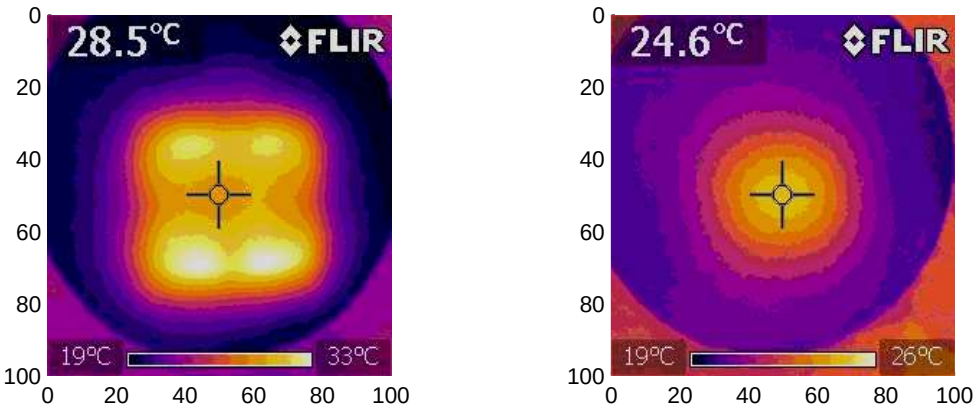

Figure 6.33: Measured thermal distribution after 5-minutes of microwave exposure. (a) Phantom Skin surface, (b) Phantom muscle surface

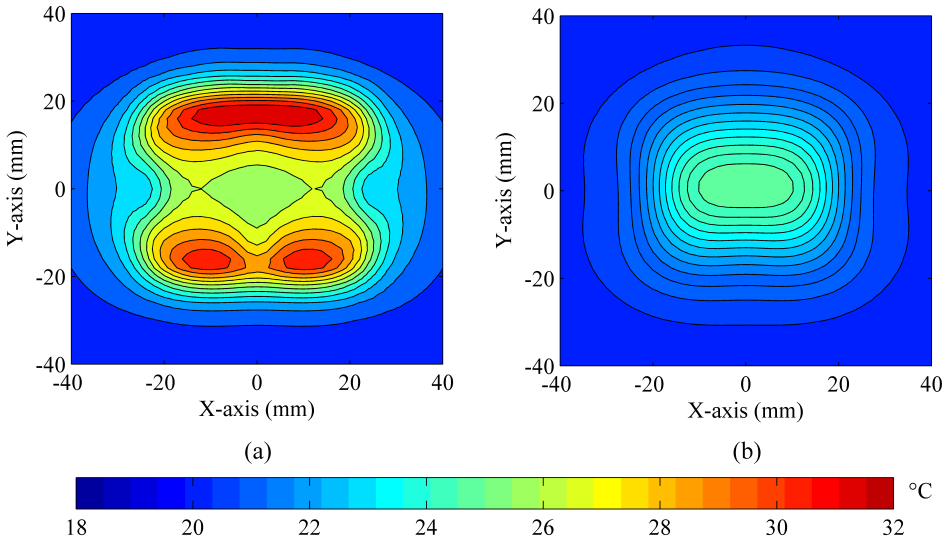

Figure 6.34: Simulated Thermal distribution after 5-minutes of microwave exposure. (a) phantom skin surface, (b) phantom muscle surface

6.6 Applicator II

The initial goal of Applicator II, was to reduce skin heating while mantling deeper tissue warming. This was achieved with use of TEC, and a high thermal conductive (HTC) substrate and superstrate. The modelled applicator deign is illustrated in Figure 6.35. It can be seen, a new circular geometry was introduced to accommodate the changes of the NIRS optodes and the addition of the LDF probe at the centre of the antenna. The diameter of the applicator, including the external casing is 67.5 mm, while the actual radiating element is only 29.6 mm ($\lambda_o/4$). The substrate and superstrate material is based on Rogers 6035 HTC, with higher dielectric constant $\epsilon_r = 3.5$ than previous applicator design. This was essential in reducing the radiating element dimension. The substrate and superstrate thickness (h_1, h_2) are 1.52 mm and about 2.0 mm. It was previously discovered thicker superstrate was beneficial for uniform heating and eliminating the warm spots caused by radiating edge. However, increasing thickness further will raise the thermal resistance and hence reduce cooling efficiency. The superstrate thickness was chosen based on combination study of EM SAR absorption and thermal analysis with applied active cooling. This section goes through Applicator II development, fabrication and validation by comparing its warming performance with and without the use of the cooling system.

The microstrip antenna element was based on annular ring geometry with a non-conducting concentric centre. This is an attractive solution to embed LDF probe at the centre of the patch without causing significant EM interaction to the opti-

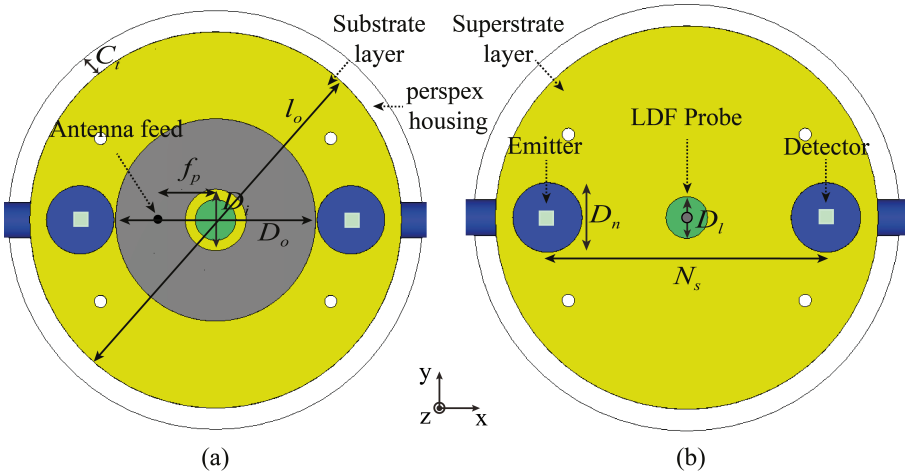

Figure 6.35: Modeled Applicator II. (a) antenna parameters, (b) optical probes geometry

cal/temperature sensor. The ring approach had been previously studied in medical and non-medical applications [144, 123]. The geometry allows the current to flow around the concentric centre, hence increasing the electrical length and allows for additional antenna minimisation. Essentially to meet the requirements of NIRS optodes spacing at 40 mm from the centre of each probe, without causing any perturbation the element. The modeled geometry based on theoretical estimation of the wanted operating frequency, which is adjusted by the inner diameter and outer diameter D_i and D_o respectively. The calculations were based on numerous studies from the available literature [123, 155]. The diameters of the antenna are calculated from the derived equations 6.6.1 and 6.6.2. Where f_r is the desired operating frequency and k_n is the wave number. It can be seen ϵ_e are typically used based for microstrip antenna designs, however, estimating effective permittivity with loaded biological tissue cannot be achieved. Therefore, EM simulations are used to optimise the antenna from initial free space approximation. The wave number is obtained from choosing the antenna operating mode integer (n), where the fundamental mode is TM_{11}, hence $n_m = 1$. The annular ring radius's are a ($D_i/2$) and b ($D_o/2$), which was obtained by selecting the desired value of one radius in order to solve for the other. However, a condition must be followed during the calculation, where $(b-a)/(b+a) \leqslant 0.35$ and $n_m \leqslant 5$. The complete design parameter is given in the Appendix C Table C.2.

$$f_r = \frac{ck_n}{2\pi\sqrt{\varepsilon_e}} \tag{6.6.1}$$

$$k_n \approx \frac{2n_m}{a+b} \tag{6.6.2}$$

The three-dimensional model of the applicator is presented in Figure 6.36. This illustrates all the essential components that compromise the hybrid applicator. It can be seen the model include all the optical probes, cooling elements and the microwave antenna. The model was also planned to accommodate magnetically loaded silicone microwave absorbers to reduce microwave leakage outside the diagnosed site. However, this was not included in the developed design, but to be incorporated in the future development.

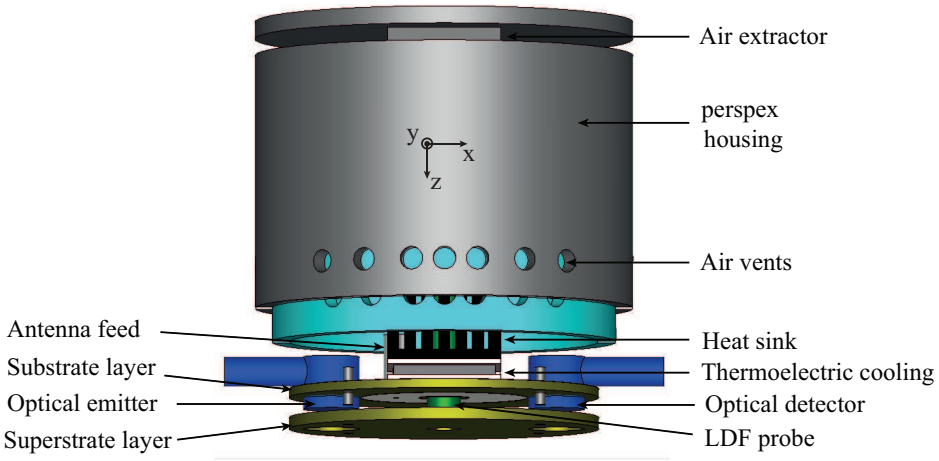

Figure 6.36: Three-dimensional model of the complete Applicator II.

6.6.1 Substrate Material

The influence of the substrate/superstrate material to the passive skin cooling was studied. Applicator II uses HTC substrate material with thermal conductivity of 1.44 W/(m*k), in contrast to 0.2 W/(m*k) of Applicator I. Numerical study comparisons were made for Applicator II at different superstrate materials. Thermal distribution of biological tissue with microwave warming using low thermal conductive material is shown in Figure 6.37(a and c). The result clearly shows a hot spot at the skin surface

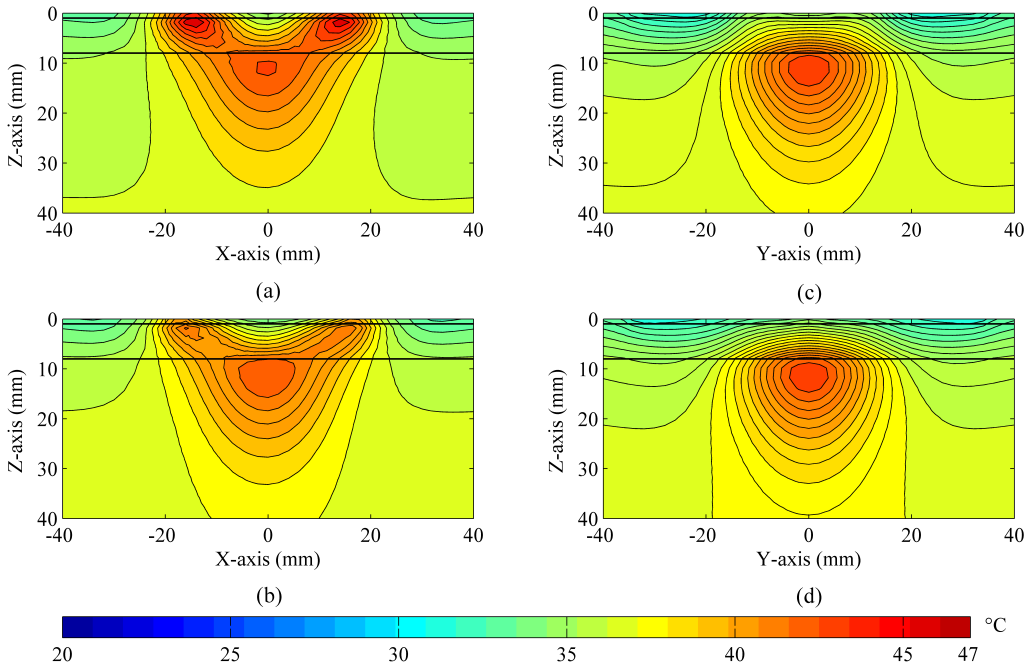

Figure 6.37: Simulated thermal distribution as a function of substrate thermal properties. (a)*xz*-plane cut, (b) *yz*-plane cut

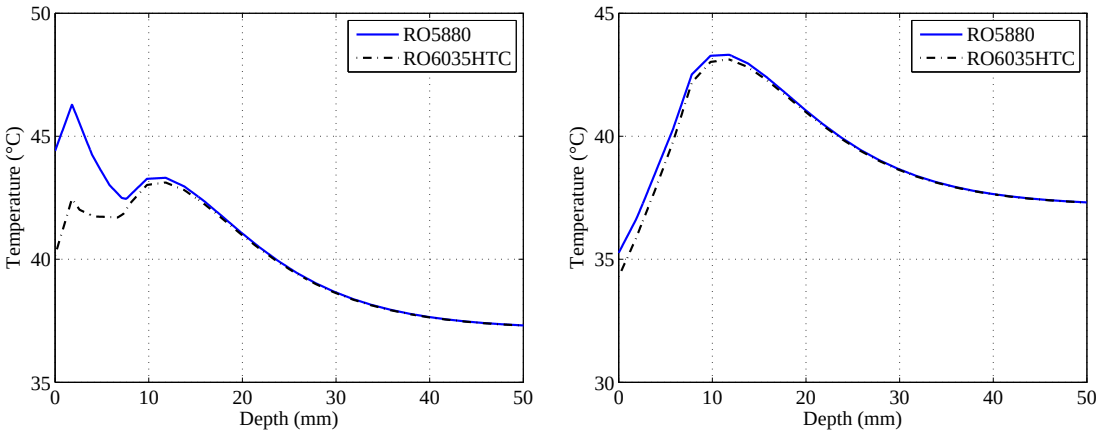

Figure 6.38: Simulated peak SAR as a function of D_i. (a) across *xz*-plane, (b) across *yz*-plane

at approximately 46.3 °C in the *xz*-plane In contrast to the distribution of the new HTC material displayed in Figure 6.37(b and d), where peak skin temperature was 42 °C. A difference of 4 °C by just passive cooling with the HTC substrate used. Regardless the muscle temperatures are identical in both scenarios and also in the *yz*-plane This was further evaluated with direct peak temperature comparison in Figure 6.38.

6.6.2 Annular Ring Analysis

The design parameter of Applicator II lies within the inner diameter of the concentric centre (D_i). The initial diameter choice was realised from theory before an optimisation process was applied in the EM simulation. As diameter D_i increases so does the electrical path length. Therefore, the resonant frequency shift down as demonstrated by the $|S_{11}|$ simulation in Figure 6.39. A D_i of 7.0 mm has an external patch diameter (D_o) of 31.0 mm, which is over the 30.0 mm limit set by the NIRS probe spacing. Consequently, a $D_i = 9$mm can achieve D_o under 30.0 mm, a reduction of about 2.5 mm. Further study was conducted, to demonstrate the peak SAR in the tissue as a function of D_i. The results are presented in Figure 6.40a for the *xz*-plane, and Figure 6.40b is the *yz*-plane It can be observed the SAR in the superficial layer is lower for $D_i = 7.0$ mm than the larger concentric diameters. When $D_i = 9.0$ mm the SAR in the muscle is maximum, in comparison to other diameters. Despite high superficial SAR by 3 W/kg, these study leads to the selection of 9.0 mm concentric diameter based on the dimension limitation and improve SAR in the muscle.

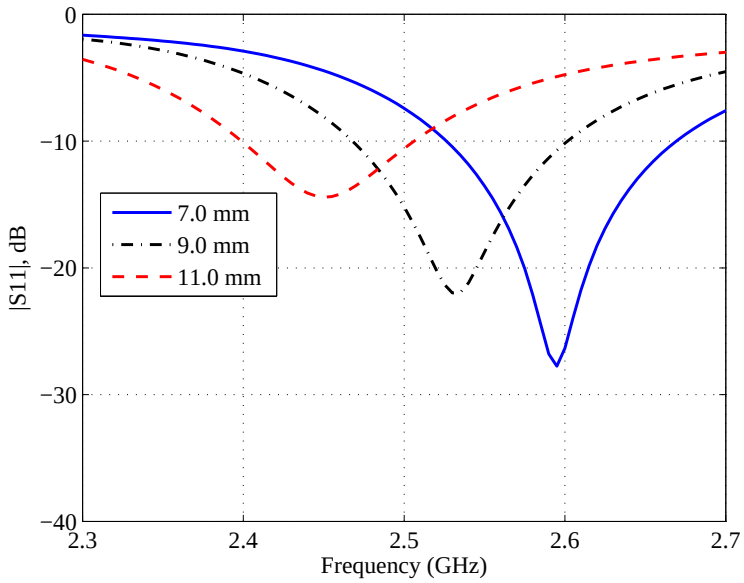

Figure 6.39: Simulated $|S_{11}|$ for parametric study of D_i.

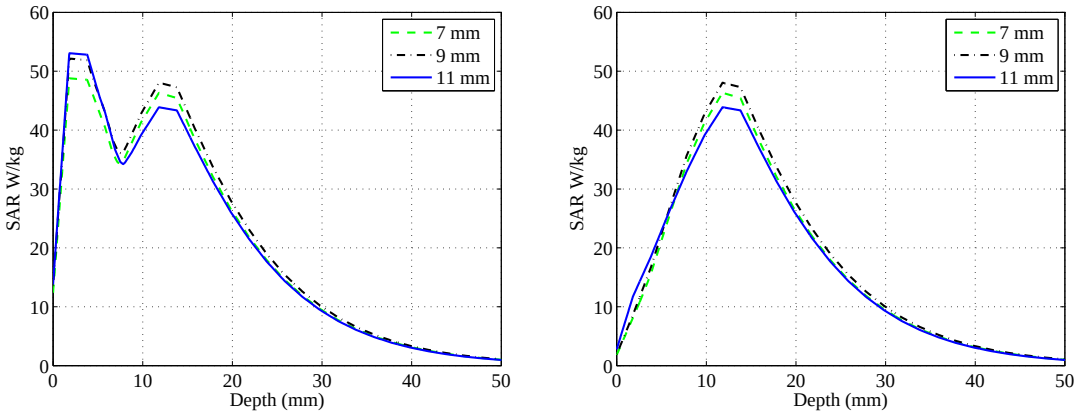

Figure 6.40: Simulated SAR peak of Applicator II with different substrate thermal material. (a,c) RO5880, (b) RO6035HTC

6.6.3 Skin Cooling

The skin cooling using TE module, was introduced for Applicator II. The cooling technique was based on thermostatic cooling. Increase temperature beyond the set point, triggers the TEC unit and simultaneously lower RF power by 3.0 dB (half power). This is the typical cooling experimental protocol used, which was difficult to implement to the simulation model. However, the periodicity of thermostatic triggering was estimated and modelled as an excitation signal, as shown in Figure 6.41. The magnitude is

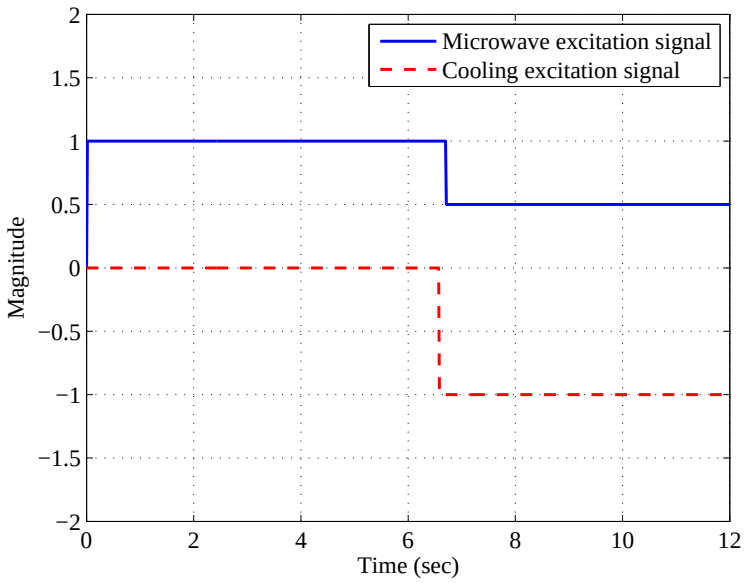

Figure 6.41: Applicator microwave excitation signal for the thermal simulation.

a scaling factor for actual RF and cooling power. The first 6.5 seconds, the RF power is maximum and active cooling is turned off. The following 5.5 seconds (thermostatic trigger), the RF power is cut to half while the cooling is activated (negative magnitude to represent cooling power). The mimicked excitation signal was periodic, and hence repeated for the 5-minute of microwave exposure.

The simulated thermal distribution of Applicator II with and without the active cooling was studied in further details with the use of the thermostatic excitation signal. Figure 6.42(a and c) show the cross-section cut of thermal distribution with microwave warming only. By inspection, the figure clearly shows greater heating in the superficial and muscle area across the *xz*-plane. The *yz*-plane is typically dominated by the muscle heating. In contrast, Figure 6.42(b and d), the skin cooling was applied and promptly reduces skin heating in both planes. The thermal distribution data presents the clear advantage of active cooling, by suppressing the undesired hot spots caused but the close proximity near-field operation of the applicator. However, warming the fat layer was not mitigated completely.

The peak temperature of the thermal distribution across the horizontal and vertical plane is presented in Figure 6.43. The result in the *xz*-plane clearly shows the skin temperature is reduced by approximately 3.5 °C and 2.0 °C in the deeper tissue. Despite the reduction, superficial heating was still present by about 4.0-5.0 °C from the starting

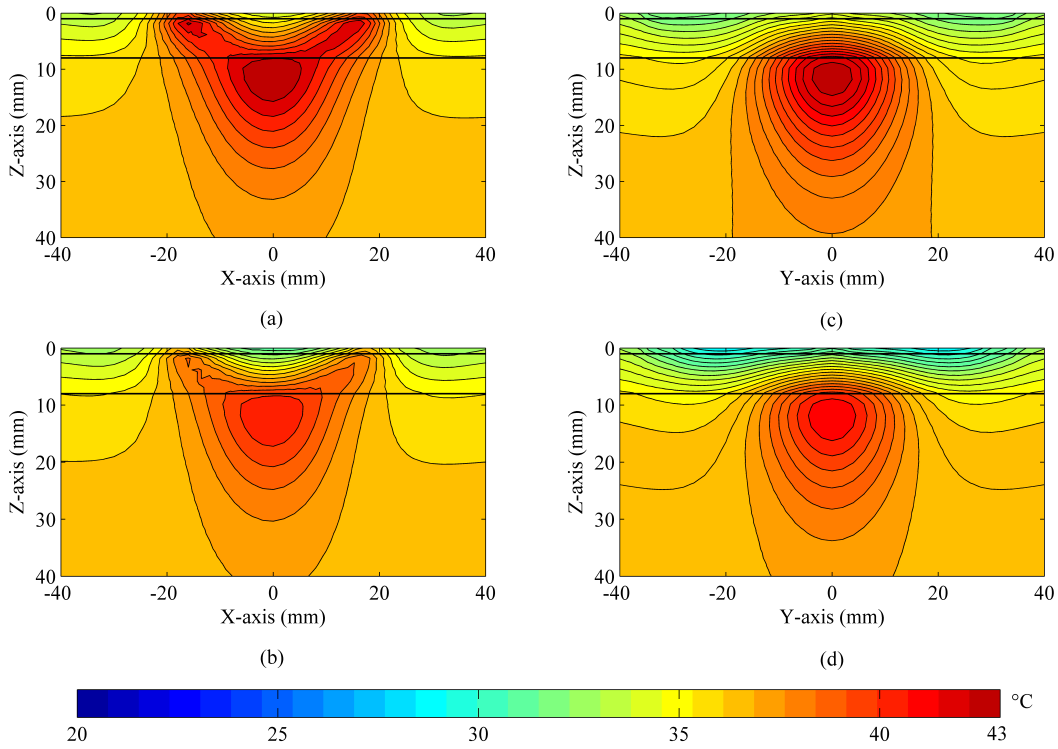

Figure 6.42: Thermal distribution of simulated Applicator II with different substrate material. (a,b) across *xz*-plane using RO5880 and RO6035HTC respectively, 5.0 mm, (c,d) across *yz*-plane using RO5880 and RO6035HTC respectively.

skin temperature. Figure 6.43b shows the peak temperature in the *yz*-plane, where superficial heating is minimal. The muscle warming reduction can be seen clearly in both planes. This is caused by the combination of pulsed RF power (when skin cooling is used) and the applied active cooling through thermal diffusion.

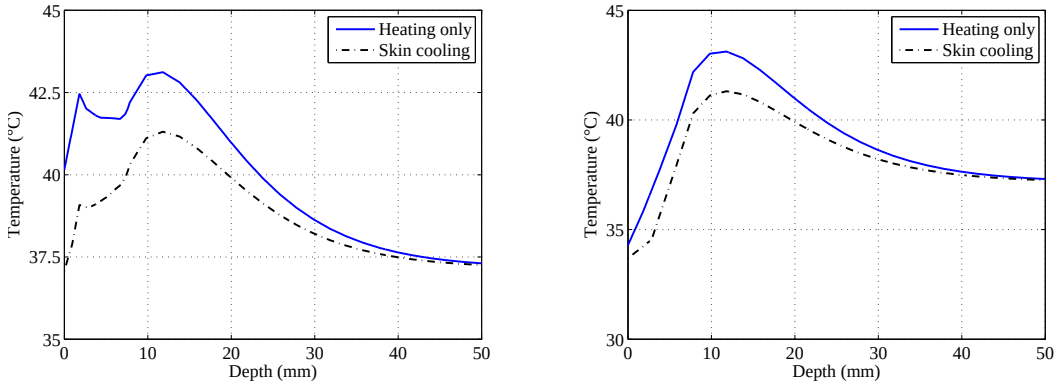

Figure 6.43: Peak simulated temperature with and without cooling. (a) across *xz*-plane, (b) across *yz*-plane

The thermal study, was extended to show the transient plot at a predefined points in the centre of the tissue at different depths, as illustrated in Figure 6.44. The solid lines correspond to the simulation with no skin cooling (NC), and dashed lines are with skin cooling (SC). The defined depths are; at the skin surface 0.0 mm, skin-fat interface 1.0 mm, fat-muscle interface is 8.0 mm and 12.0 mm for deep tissue. The results in the figure clearly show skin heating reduction of 2.5 °C over a 5-minute of exposure. The muscle temperature was also reduced by about 1.75 °C, primarily caused by the pulsing RF power when cooling is active. The actual hot spots are located under the radiating edges at about ± 17.5 mm on the x-axis. Figure 6.45 shows the transient thermal profile around the hot spot region (at depth of 1.0 mm) and compared to the centre of modelled tissue. The rate of temperature elevation is decreased with applied cooling by about 2 °C..However, the peak temperature remains over the actual starting value by approximately 5 °C.

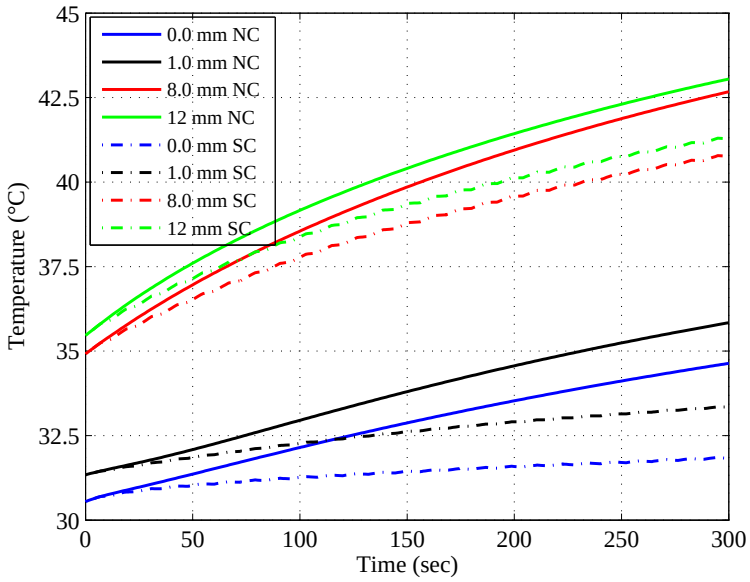

Figure 6.44: Transient thermal simulation at fixed points along z-axis (depth) for with and without cooling, where y=0 mm and x=0 mm.

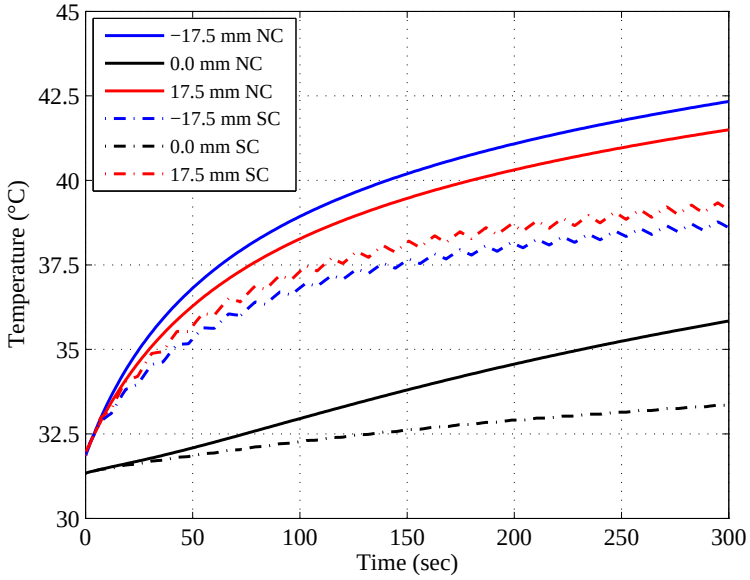

Figure 6.45: Transient thermal simulation at fixed points along x-axis for with and without cooling, where y=0 mm and z=1 mm

6.6.4 Fabrication and Validation

The simulation study was sufficient for initial optimisation of applicator; therefore, anatomical model simulation was also used prior to antenna development. However, measurement and validation are a necessary step to ensure the reliability of the simulation model. The fabricated applicator is demonstrated in Figure 6.46, where (a) is the microstrip antenna ground plane with placement of Peltier cooler with heat sink, microwave coaxial input, a ground plane thermistor and the optical probe. Figure 6.46b shows the front end of the applicator excluding the superstrate. The annular ring patch antenna is clearly shown with the soldered feed point. As with the model, the optical probe placements are demonstrated, LDF in centre and NIRS across the horizontal plane. The applicator is housed inside a Perspex casing with added straps for secure placement on human calf/arm. Figure 6.46c shows the back-end of the hybrid probe, where the axial fans are attached to extract away the excess of heat generated by the TE modules.

The applicator performance was assessed by the free space $|S_{11}|$ as illustrated in Figure 6.47. The measured data was compared with the simulation model, to study the shift in operating frequency and the return loss of the antenna. The measured $|S_{11}|$ was -3.8 dB at 2.75 GHz. In contrast, the simulated $|S_{11}|$ was -3.6 dB at 2.73 GHz. That

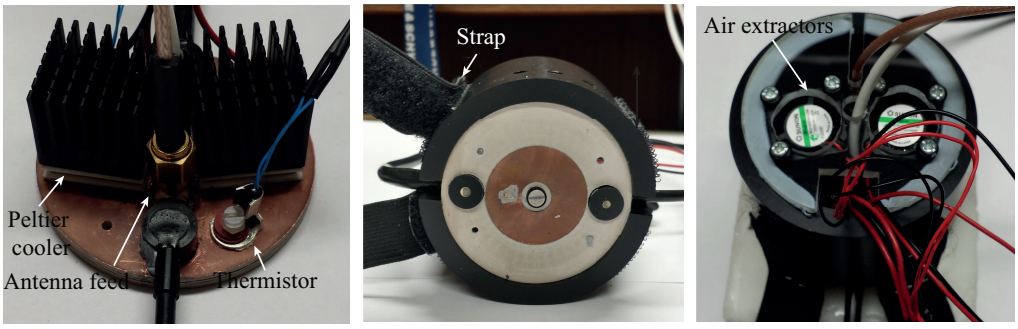

(a) (b) (c)

Figure 6.46: Fabricated applicator II. (a) Back view of ground plane and the included cooling, (b) Front view of patch antenna, (c) Overall applicator

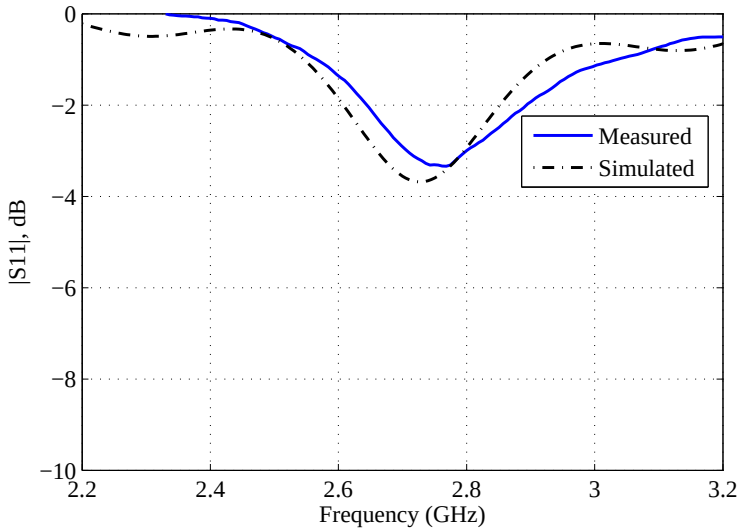

Figure 6.47: Measured s-parameter of Applicator II in free space.

is about 20 MHz (0.73%) difference between the numerical study and measurement. The results clearly state the antenna is not operable in free space, with high VSWR is expected when connected to the microwave system. This is the mechanism that was used to ensure microwave only operates at lower VSWR, were a maximum of 1.5 is set when applied to human calf.

The hybrid probe was placed on the calf for input reflection measurement. The data is plotted against the simulation and presented in Figure 6.48. The measured $|S_{11}|$ agrees with the current updated simulation model (1.0 m skin and 7.0 mm muscle) with only difference of about 5.0 MHz. The optimum operating frequency was at 2.53 GHz with low input reflection of -19.0 dB. A discrepancy of 3.3% was observed, which is outside the ISM band range. The -10.0 dB bandwidth is 160 MHz ranging from 2.45

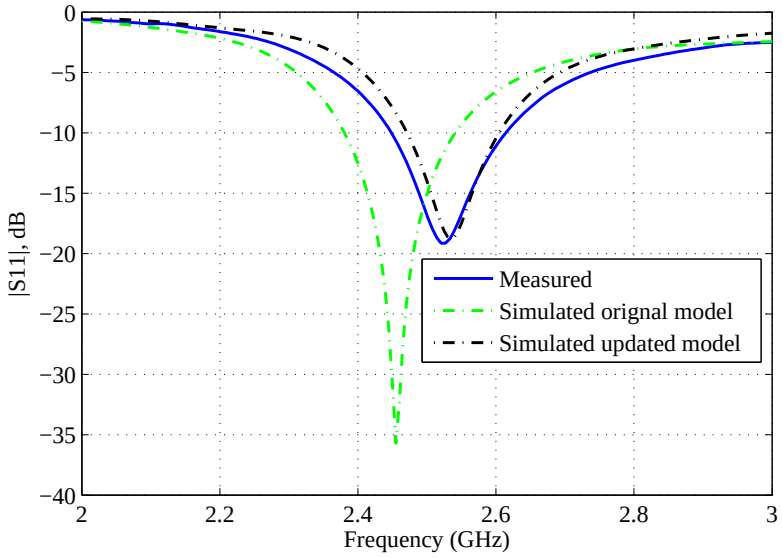

Figure 6.48: Measured s-parameter of Applicator II on human calf.

to 2.6 GHz. This is a 6.3% achieved bandwidth, which is 1.0% higher than the numerical study. The improved bandwidth of applicator II was influenced by the antenna geometry with the use of larger relative permittivity of substrate/superstrate laminate. Consequently, this allows the antenna to operate at ISM band.

The basic assessment of antenna performance was completed before proceeding to thermal validation on tissue mimicked phantom. The applicator was placed on the phantom for duration about 10.0 minutes to ensure skin temperature was stabilised before applying microwave warming. The duration of warming was the standard 5-minutes of exposure at 3W RMS power. Figure 6.49 shows the captured heat distribution of skin and muscle phantom surfaces during microwave warming without skin cooling. The obtained image was compared with an equivalent setup in EM/Thermal simulation, where the results are presented in Figure 6.50. It can be seen the skin surface temperature was raised from 22 °C to 31.0 °C in a dual hot spot produced by applicator operating in the near-field. This was comparable to the simulated peak temperature of 31.0 °C. The notable difference is the temperature at the centre of the distribution, where the measurement was about 2.0 °C. This was possibly caused by the inaccurate modelling of the LDF probe (located at the centre of the applicator), and the limited resolution of the IR camera (140x140 pixels). The muscle surface temperature was about 27 °C after the exposure, that is an elevation 19.5-20.0 °C. The muscle

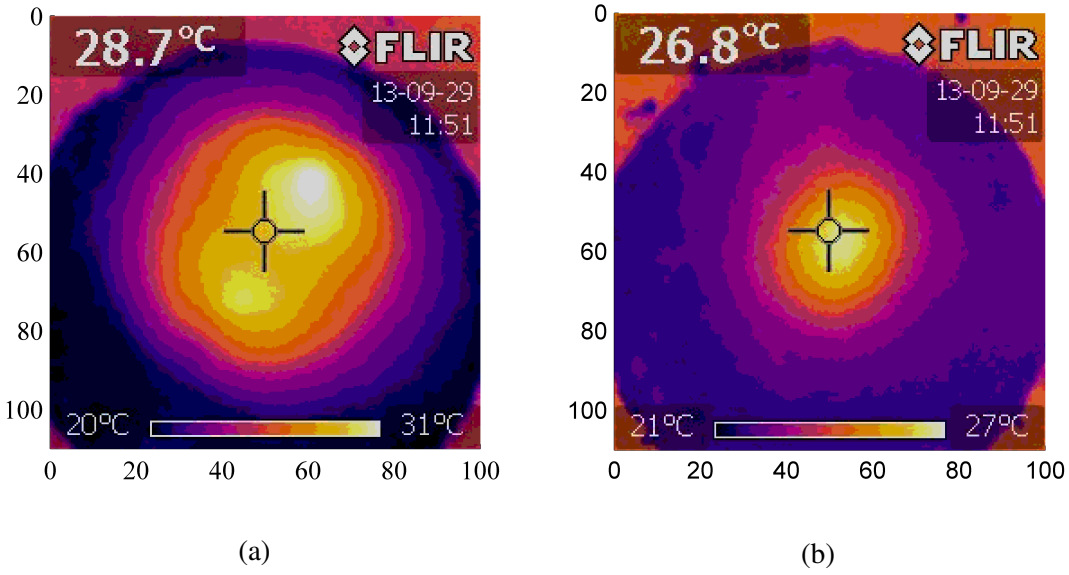

(a) (b)

Figure 6.49: Measured Thermal distribution after 5-minutes of microwave exposure. (a) phantom Skin surface, (b) phantom muscle surface

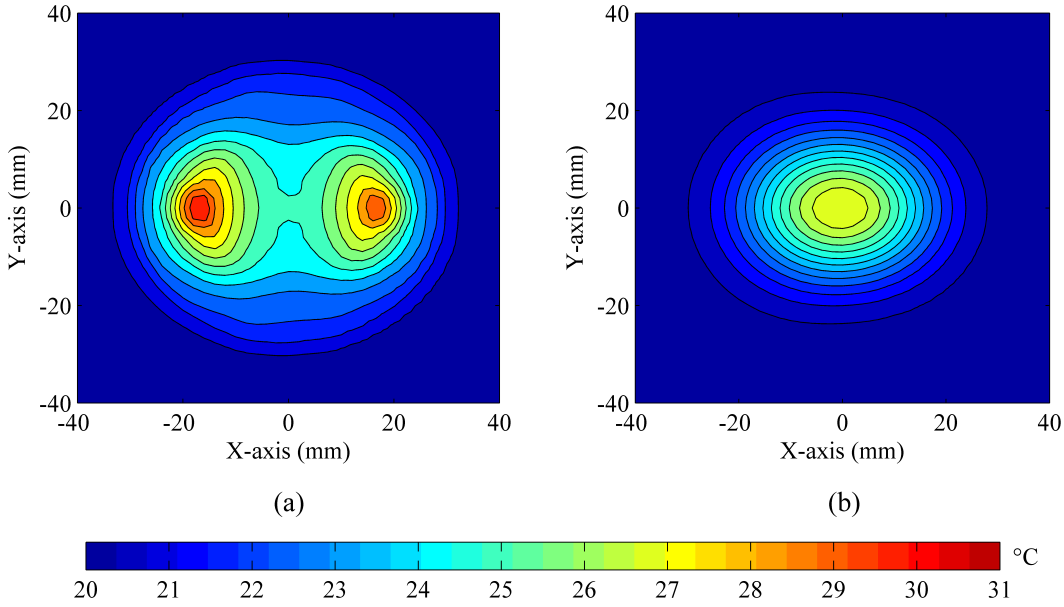

(a) (b)

Figure 6.50: Simulated Thermal distribution after 5-minutes of microwave exposure. (a) phantom skin surface, (b) phantom muscle surface

starting temperature was at least 2.0 degrees lower than skin. Figure 6.51b shows the simulated muscle phantom with peak temperature of 27.3 °C, which is a 0.3 °C increase over the measurement. Overall, skin elevation was only 2 °C higher than muscle, which was also validated by the numerical study.

The tissue mimicked phantom experiment was repeated with the addition of active

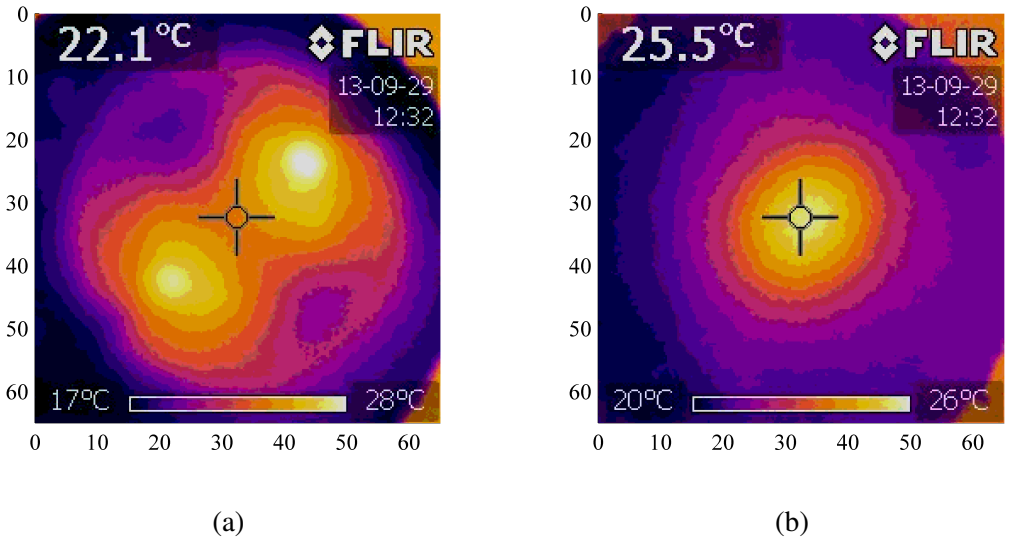

Figure 6.51: Measured Thermal distribution after 5-minutes of microwave exposure with active cooling on. (a) phantom Skin surface, (b) phantom muscle surface

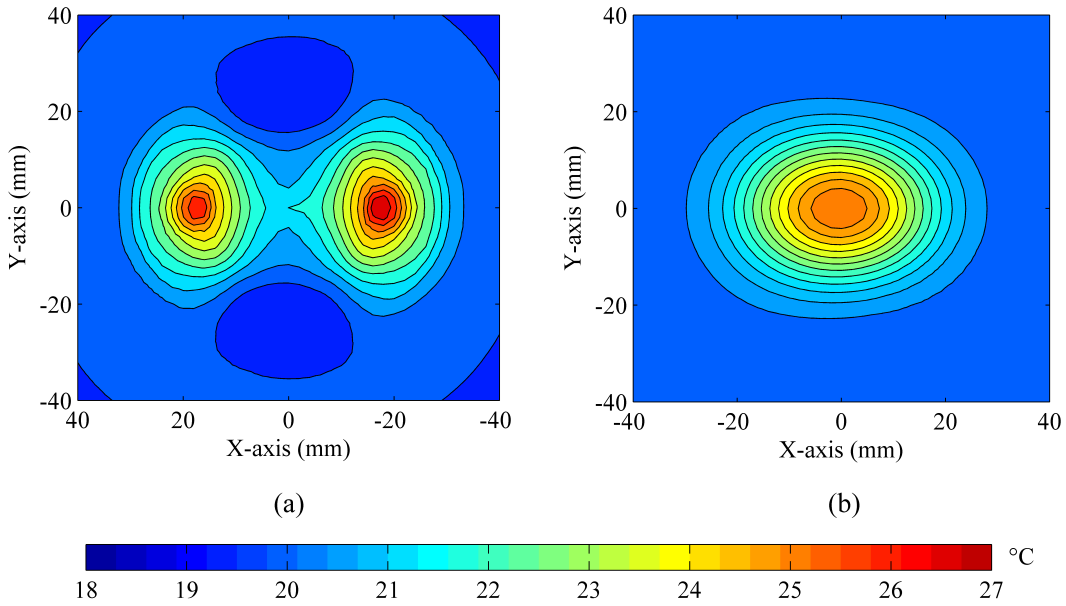

Figure 6.52: Simulated Thermal distribution after 5-minutes of microwave exposure with active cooling on. (a) phantom skin surface, (b) phantom muscle surface

skin cooling. Figure 6.51 and 6.52 are the measured and the simulated thermal surface profile of skin and muscle respectively. The plots show the peak measured skin temperature was 28.0 °C and 26.0 °C for the muscle. In contrast to warming only, the skin temperature was reduced by 3.0 °C and 1.0 °C in muscle.

Figure 6.51a, clearly illustrates the two warm spots and adjacent cold spots (19.0

°C) on the skin surface. These findings were validated with the numerical investigation, which showed marginal difference of up to 0.6 °C on the skin surface. The variation between the measurement and simulation, could be affected by the variation in room temperature, the non-planar phantom thickness and the dielectric properties of the phantom. The simulated muscle temperature was 0.4 °C lower than the measured value. This study highlighted the importance of TE module placement on the applicator. In Applicator II, the Peltier coolers are placed on the non-radiating edges (across the Y-axis). The cooling elements are not capable of uniform distribution. Therefore, maximum cooling efficiency is directly under TE element as it is demonstrated in the Appendix C in Section C.2.2. Cooling system relies on the temperature set-point and the thermistor which is located at the centre of the applicator and hence the thermal distribution. It can be observed from Figure 6.51a, the temperature at the centre was 22.1 °C after 5-minutes of microwave warming and cooling. This temperature was the actual starting value, and it was maintained by the active cooling because it was the location of the thermistor reading. Consequently, it is possible to mitigate the hot spots if the set-point value was lower than starting temperature by over 2 °C. The limitation of this approach is skin over-cooling becomes significant, which will also affect the physiological measurements.

The transient skin temperature was measured, and compared with the thermistor

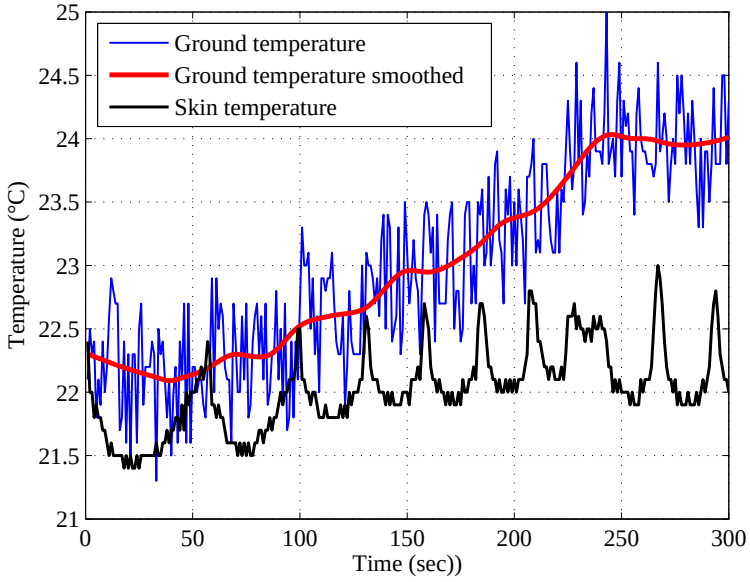

Figure 6.53: Measured skin temperature and ground plane temperature with active cooling.

reading at the ground plane as it was shown in Figure 6.53. The starting temperature of both thermistors begins at approximately 22.3 °C, which is the typical of the skin phantom. The result shows the skin measurement fluctuates between 21.5 °C to about 22.8 °C, which is a standard operation of a thermostatic controller. In contrast, the ground plane measurement, have large self-fluctuation caused by the cable extension length which was filtered and smoothed, represented in the red line fit. The temperature of the ground plane was decreasing in the initial 50 seconds, which follow the similar pattern to the skin. However, the remnant duration of exposure shows the ground plane temperature was gradually increasing until after 240 seconds, were it stabilises at 24.0 °C. This is approximately 1.5 °C higher than the skin temperature probe. The results clearly indicate the set point temperature was not sufficient to cool the area where the radiating edges, and the ground plane thermistor was located.

In vivo validation of microwave warming on calf skin was measured and presented in figure 6.54. By inspection Figure 6.54a shows the skin hot spots elevated to 41.0 °C during microwave exposure without cooling. This was validated with the simulation model using the biological heat equation (unlike phantom validation) as shown in Figure 6.55a. As previously discovered in the simulation results, the skin warming at the centre of the distribution is typically lower than measurements by around 2.0-4.0 °C

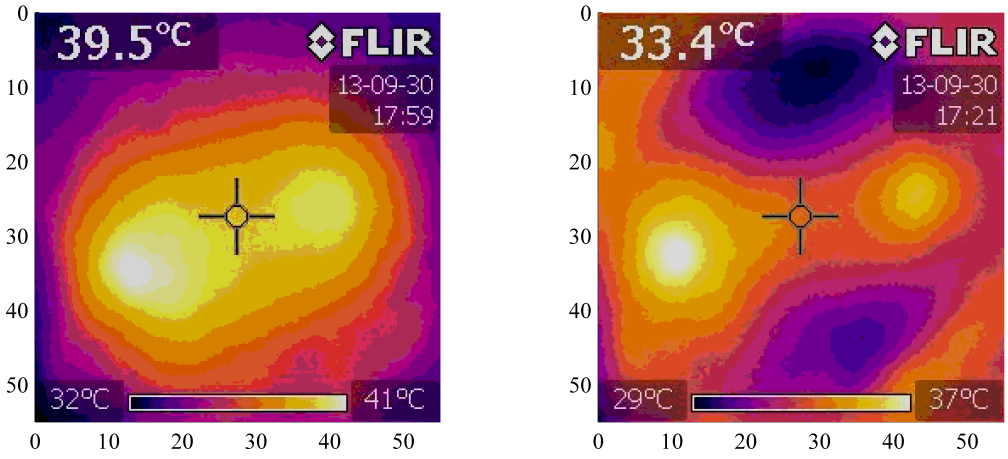

(a) (b)

Figure 6.54: Measured skin thermal distribution after 5-minutes of microwave exposure on human calf surface. (a) without skin cooling, (b) with skin cooling

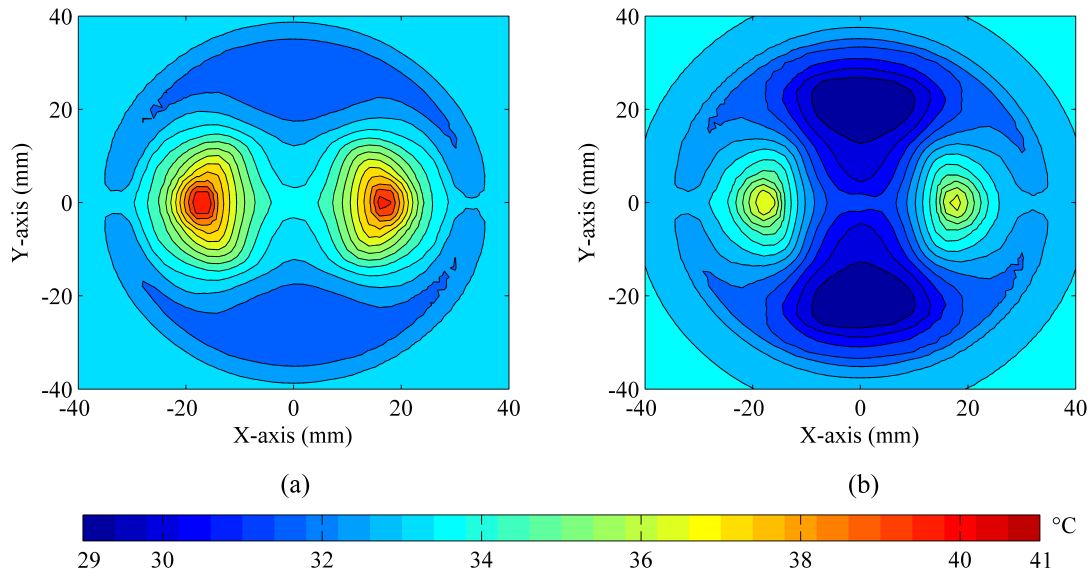

Figure 6.55: Simulated skin Thermal distribution after 5-minutes of microwave exposure with bio-heat. (a) without skin cooling, (b) with skin cooling

depending on the protocol. The experiment was repeated with inclusion of skin cooling. The measured result is illustrated in Figure 6.54b and compare with the numerical study in 6.55b. By inspecting the results, it can be observed the active cooling reduced the peak hot spot temperature by approximately 4.0 °C. However, adjacent cold spot was observed, located under each of TE modules. The minimum temperature was of the diagnosis site was 29 °C. The captured distribution and temperature values were a match to the equivalent set-up of the simulation presented in Figure 6.55. The same simulation study also showed the muscle temperature was elevated to 41.25 °C.

6.7 Applicator III

The limitation of applicator II was clearly in the geometrical placement of the cooling modules. The coaxial pin feed design approach meant that, the Peltier cooler can only be placed on the non-radiating edges of the applicator. Therefore, it was difficult to sufficiently cool the adjacent hot spots produced by the radiating edges. Moreover, Applicator II was over-cooling the adjacent regions to the hot spot, therefore the thermal distribution showed hot and cold spots. This limiting factor was improved by the developed applicator III geometry as shown in Figure 6.56. The microstrip antenna design adopts identical configuration of the previous applicator, using HTC substrate/superstrate material, thickness and optical probe's allocation. The primary

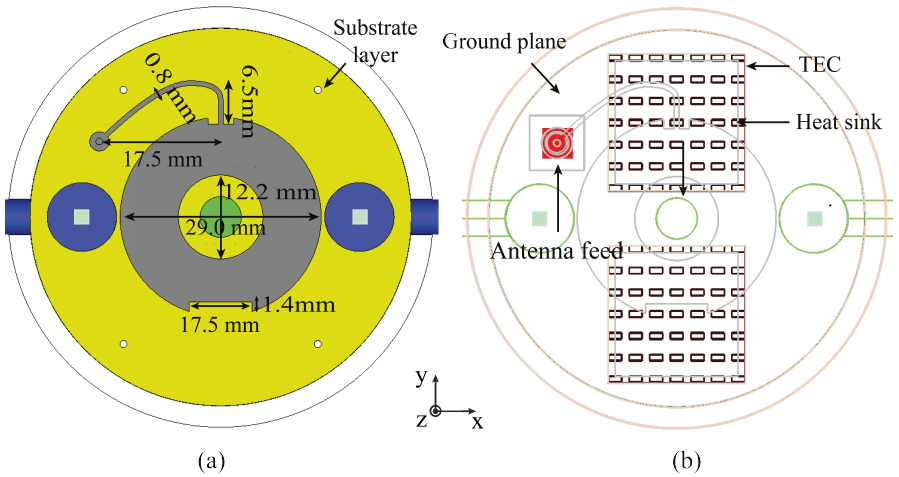

Figure 6.56: Modelled Applicator III. (a) radiating element geometry, (b) wide frame view

change is the antenna feeding approach, using an arced transmission line feed network with inset feeding to the patch, as illustrated in Figure 6.56a. The transmission line was feed by the same coaxial pin feed approach. The purpose of this was to shift the back pin feed away from the radiating element and to allow the placement of Peltier cooler right above the E-field plane (y-plane). The TE module placement can be seen clearly in the wide frame view of the modelled Applicator III in Figure 6.56b

6.7.1 Numerical Study

The performance of the applicator was assessed, by studying the current distribution around radiating patch and the transmission line. An arced transmission line was inherited to minimize back reflection from the intersection of feed line and the inset feed. Applicator III includes a notch at the opposite side of the feed point, which was introduced after SAR study. The purpose of the notch was to balance antenna impedance, for identical radiated E-field from both edges across the y-plane. The width of arc are usually calculated from the standard transmission line equation for optimal impedance at 50Ω. However, in this application theoretical transmission line equation cannot be relied on, thus EM simulation was used for general impedance optimisation.

The primary focus of this section is about the improvement of skin cooling, and this was analysed with the transient thermal simulation equivalent protocol to Applicator II. The SAR distribution did not improve upon the previous applicator. In fact, the numerical investigation shows the SAR of Applicator III was outperformed by the previous design. This is caused by the introduction of the transmission line, which also

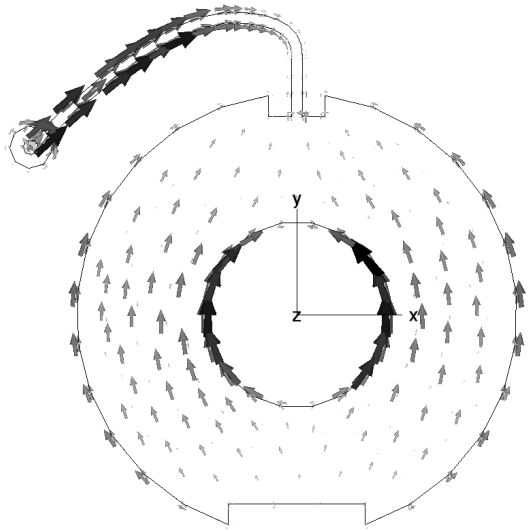

Figure 6.57: Simulated current distribution of Applicator III.

radiates at the near-field proximity, hence increasing SAR absorption in the skin. For conciseness, the simulated SAR is summarised in the Chapter 9 Table 9.1. The thermal simulation study for Applicator III with skin cooling is illustrated in Figure 6.58. The figure shows *xy*-plane cuts of the modelled tissue, (a) skin, (b) skin-fat interface and (c) muscle. The result clearly shows the skin surface is cooled and minimised superficial hot spots. The peak temperature at the skin was 33.30 °C, that is about 1.0 degree elevation from the starting temperature. This increase was produced by the coaxial feed-point to the transmission line. In fact, the results also indicate skin over-cooling at approximately -25 mm of the Y-axis, where the temperature was 31.0 °C. In contrast to Applicator II, the peak simulated skin temperate with cooling was 37.0 °C, that is a 3.7 °C increase over Applicator III. The temperature was elevated in the skin-fat interface peaking at 35.7 °C, that is 1.9 °C higher than the surrounding tissue. Figure 6.58c illustrates the muscle warming at about 40.4 °C, an increase of 3.4 °C. The peak temperature induced in the tissue of the two applicators are compared in Figure 6.59. Figure 6.59a is the radiating plane, where Applicator III has reduced the superficial hot spots but also 1.0 °lower in the muscle. In contrast, Figure6.59b shows the non-radiating plane, where Applicator II has overcooled the superficial layers caused by the geometrical placement of Peltier cooler.

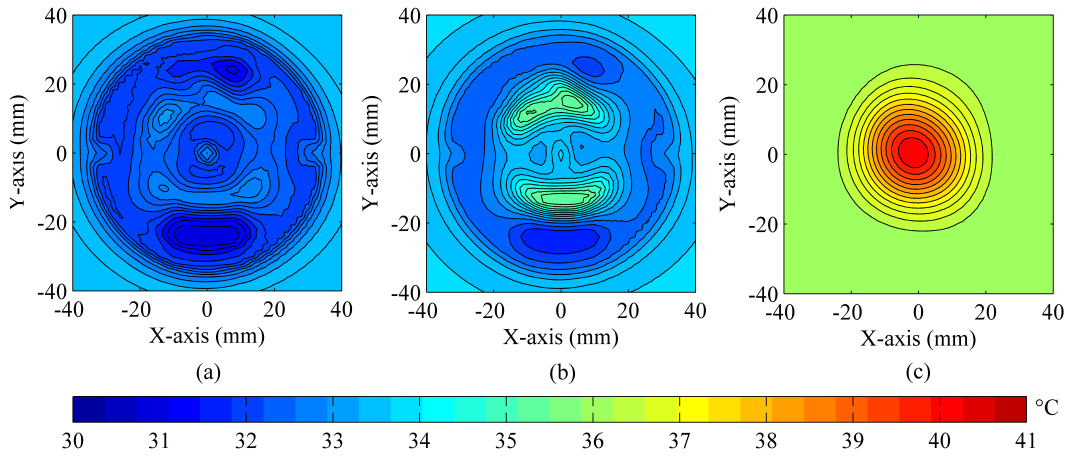

Figure 6.58: Simulated thermal distribution of Applicator III with skin cooling. (a) skin (b) fat (c) muscle

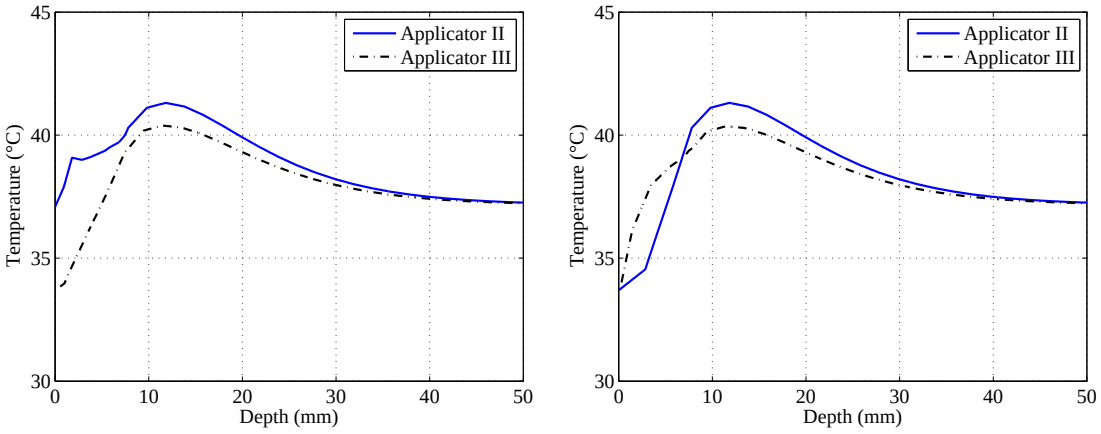

Figure 6.59: Peak thermal distribution of Applicator II & III. (a) across the radiating plane, (b) across non-radiating plane

6.7.2 In-vivo Thermal Validation

Applicator III was established on the current updated simulation model using skin thickness of 1.0 mm and fat layer for 7.0 mm. The fabricated antenna performance was assessed by a series of $|S_{11}|$ measurement in free space and on biological tissue. Figure 6.60 shows the measured $|S_{11}|$ plotted against the simulation. It can be seen the measured return loss is lower over wider frequency range. However, they overlap at the same frequency of 2.55 GHz at about -7.0 dB. Overall, the impedance of antenna is mismatched in air, therefore, not operable in this condition. The measurement was repeated with applicator placed on human arm and calf. The measured data is contrasted

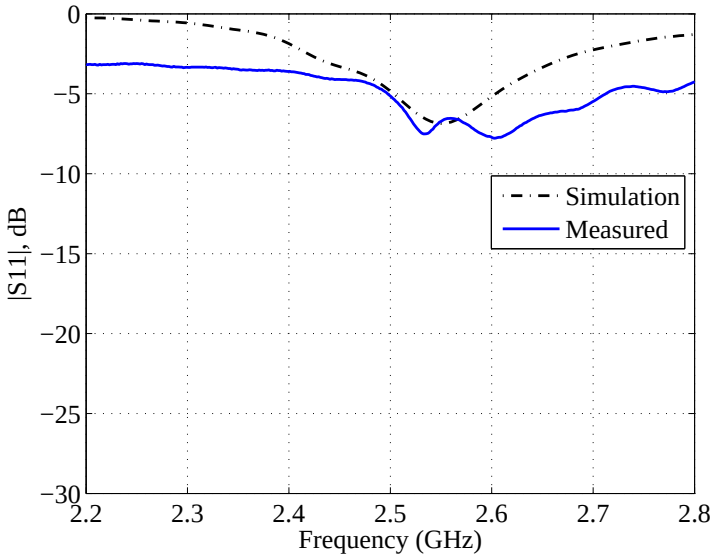

Figure 6.60: Measured s-parameter of Applicator III in free space.

with numerical study as shown in Figure 6.61. The simulation data was similar with the arm and calf measurement. The arm return loss was -39.0 dB at 2.453 GHz, an 3.0 MHz increase from the simulation and 17 MHz higher than calf measurement. The difference between the measurement was based on tissue thickness. Healthy human arms have typically thinner fat layers, which explains the increase in resonant frequency. The calf measurement had a return loss of -19.0 dB at 2.36 GHz, only drifting by 9.0 MHz from the simulation. The antenna bandwidth on human calf is 7.1% (168 MHz), which is 3.1% wider than the numerical study. This is sufficient to cover the ISM band to cover any circumstances of subjects with dissimilar tissue thickness.

The applicator was placed on human calf for *in-vivo* thermal measurements. The operation of the applicator follows the previous protocol of 5-minute microwave exposure with and without skin cooling. Figure 6.62 is the captured IR images of human calf (under the applicator) directly after the microwave exposure. The skin thermal distribution of tissue warming without skin cooling is shown in Figure 6.62a. The peak measured temperature was 37.1 °C, just about 0.5 °C lower than the simulated applicator shown in Figure 6.63a. The heat distribution shows the warming achieved covers large area under the applicator with peak temperature located at the feed point. In contrast, the simulation study shows two distinct hot spots from each radiating edge, a particularly under the feed location at the positive Y-axis. Regardless of closely matched peak

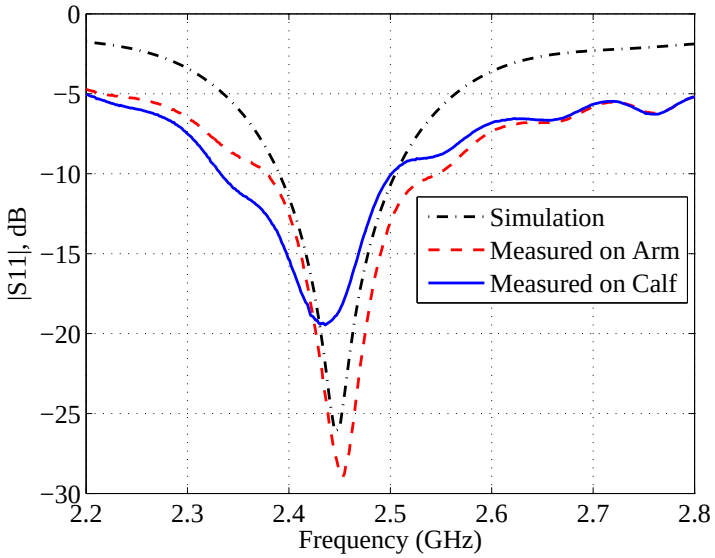

Figure 6.61: Measured s-parameter of Applicator III on human calf and arm.

temperatures, the distributions at the centre of the applicator are not identical to the measurement. This was believed to be the modelling approach of the LDF probe at the centre which was adopted as a single dielectric medium, where in reality it also contains a metal conductor for temperature measurement. Another possibility is the resolution and dynamic range of the IR camera, when the temperature values are within a 1.0 °C. The experiment was repeated with active skin cooling, the measured and simulated data are compared in Figure 6.62b and Figure 6.63b. The measured profile clearly indicates a cooling pattern at the sides of the thermal distribution. Peak measured skin temperature was 33.20 °C, which is elevated by 1.2 °C to the actual skin temperature (32.0 °C) and just 0.1 °C lower than the numerical study. Captured thermal distribution illustrates some identical features to the simulation study. This includes the two cold spots at the edges, and the feed-point hot spot located in the positive Y-axis. The minimum skin temperature was 30 °C and also equivalent to the simulated distribution. At the centre of the thermal profiles, the features diverge between the two studies as it was illustrated in the warming only pattern.

The geometrical changes of active cooling, has proven to be effective in partially mitigating skin heating. It was possible to eliminate skin heating all together, which was achieved by lowering the set point temperature by 2.0 °C than the initial temperature. This is essentially over-cool the entire region under the applicator uniformly.

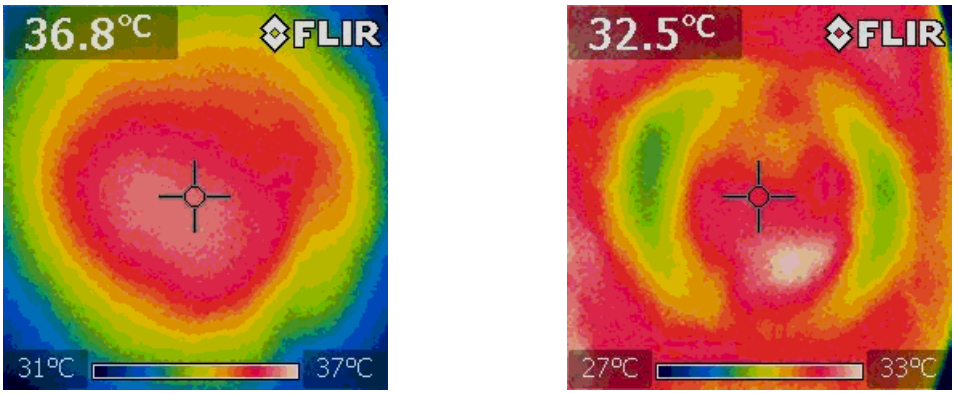

(a) (b)

Figure 6.62: Captured thermal images of human calf after exposure. (a) tissue warming only, (b) tissue warming with skin cooling

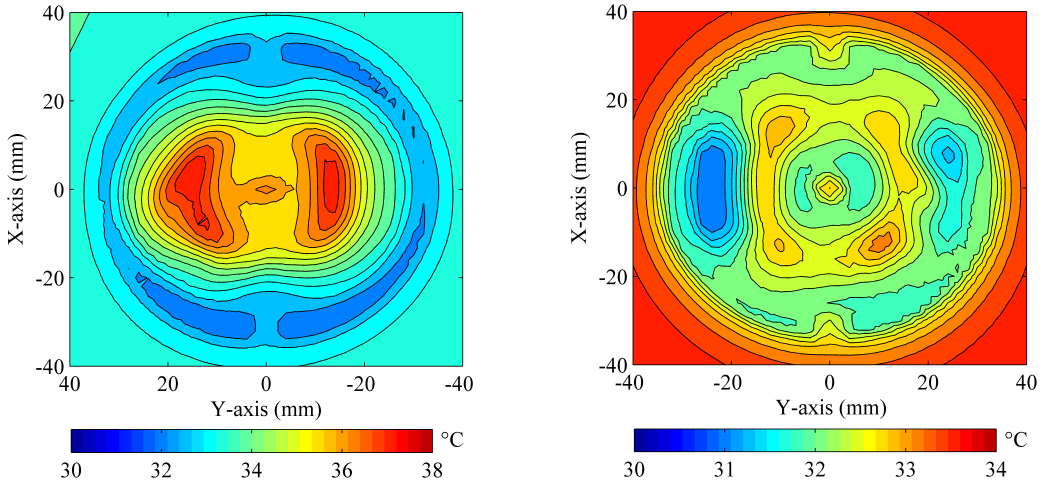

(a) (b)

Figure 6.63: Simulated thermal distribution of human calf after 5-minutes microwave exposure. (a) tissue warming only, (b) tissue warming with skin cooling

The limitation of this approach was the exterior axial fan was not able to compensate the heat generated from the TEC when over-cooling and operating at 3 watts RMS. However, this was achieved by lowering the microwave power to 1.0 watts RMS over 60-minute of exposure. This investigation was carried on to demonstrate the capability of the skin cooling system, regardless of the physiological data. The *in-vivo* trial was conducted after protocol verification with numerical study, ensuring the safety of the procedure. The thermographic images were captured and presented in Figure 6.64.

Figure 6.64a is the 60-minutes of microwave warming excluding active cooling.

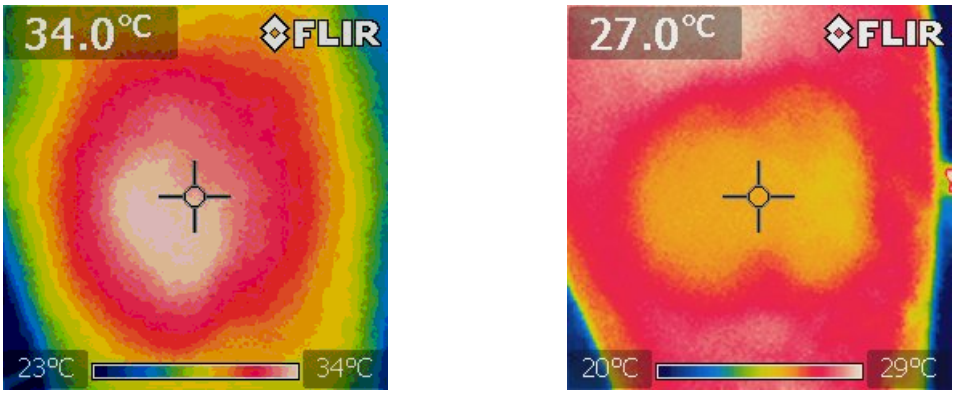

(a) (b)

Figure 6.64: Captured thermal images of human calf after 60-minutes of microwave exposure (1W RMS). (a) tissue warming only, (b) tissue warming with skin over-cooling

It can be seen the skin temperature was elevated by just 3.0 °C, from initial temperature of 31.0 °C. Based on simulation. The Muscle temperature can reach the thermal steady state at 39.5 °C. In contrast, Figure 6.64b shows the measured heat distribution of human calf with skin over-cooling. The starting temperature was 29.0 °C, and set point temperature were set to about 27.0 °C. The resultant distribution after 60-minute, clearly indicates the effectiveness of the cooling system, skin temperature was maintained to the desire value. According to the simulation, the muscle temperature is elevated to 39 °C, which is sufficient for muscle dilation. However, detection of muscle dilation will be challenging when the skin capillaries are restricted by the over-cooling.

6.8 Chapter Summary

In this chapter, the development of the linear applicators was presented. This was initiated from simple requirements that include operating frequency, proximity and the impedance matching layer. Consequently, it was possible to develop applicators with aid of theoretical and numerical studies. The basic of microstrip antenna was introduced and applied for early stage estimation of antenna dimension. Moreover, EM simulation was the core aspect of the development and understanding of deposited energy. Computational technique, including; simulation methods, tissue modelling and boundary conditions were introduced. Majority of simulation presented were based on a planar three layered tissue model consisted of skin, fat and muscle layers. Microstrip antenna was evaluated with the numerical model, to investigate applicator proximity.

It was found that the superstrate layer was the superior option for optimal in SAR and thermal pattern. Consequently, Applicator I inherited the design with appropriate modification to accommodate the NIRS optical probes. The development and performance of the applicator were extensively evaluated. The study showed the contribution of different skin or fat thickness to the SAR and thermal distribution. Generally, it was found the skin was most sensitive to the applicator impedance as it is directly loaded to the applicator. Therefore, variation in thickness of tissue, particularly of skin leads to detune of resonance frequency, hence the need for sufficient operating bandwidth. Anatomical study was also implemented for final evaluation of the applicator prior to fabrication. The thermal performance of Applicator I was validated with the fabricated tissue mimicked phantom. The study showed a close match between measurement and simulation. The limitation of the first design, was the lack of active cooling, real time skin temperature and an effective way to place on the calf.

Applicator II was introduced to resolve the limitation of the predecessor design. This was achieved by introducing new geometry, which accommodate NIRS probes, LDF probe, A thermistor and TEC. Moreover, the applicator uses HTC dielectric mediums for substrate and superstrate layers, which was able to reduce the superficial warming. The skin temperature was reduced by about 3.5 °C with Peltier cooling. However, despite the cooling the superficial temperature was elevated by about 3-4 °C of the actual skin temperature. The Applicator was then fabricated and validated on tissue mimicked phantom. The contrast between the numerical study and measured heat distribution were closely matched. The result showed cold spots were produced, directly under the TE module. Final evaluation was on human calf, again some agreement with the numerical and the phantom investigations. The limitation of this applicator lies within the geometrical placement of Pletier cooler, which was situated on the non radiating edges. This problem was resolved by the design of Applicator III, which effectively places the active cooling directly above the hot spot region. The investigations were repeated accordantly, and the results were conclusive by further mitigating the skin heating. All the measured and simulated parameters of the Applicators are placed in tables for quick comparison. This can be found in Chapter 9 Table 9.1 and 9.2. Applicator III was efficient in cooling. However, the SAR in the skin-fat interface was higher compared to the predecessor. In the next section, we investigate SAR

reduction in the superficial layers, using CP Applicator design.

Chapter 7

Circularly Polarised Microwave Applicator

7.1 Overview

The vast majority of applicators in the medical domain are based on linear polarisation, where the electric and magnetic fields are orthogonal to each other and travelling in a single direction in the far field region. Therefore, the field vector is always at a fixed point, and the radiated EM energy occurs in one particular plane producing large peak absorption. Circular polarisation radiates the electric field in all planes in a rotating manner with respect to time. In medical applications, CP applicators for therapy have not been investigated in great depth, particularity numerical study of SAR absorption comparison against linear applicators in the near-field region. Some literature study suggests CP applicator was a technique to reduce the stray radiation during clinical diathermy treatments operating at 2.45 GHz [156]. In another literature study, a direct contact circular waveguide applicator for microwave diathermy was developed to excite CP at far-field with uniform distribution, which reduces the steep temperature gradient [25]. Moreover, a single-fed microstrip CP antenna was investigated recently for wearable technology. The study focuses on antenna matching on rectangular and curved structures at close proximity to tissue [157]. The results from the study suggested, the CP antenna impedance match was best achieved at twice the spacing of a linear polarised antenna[157]. A dosimetry study on rats inside a CP waveguide was previously conducted. The investigation focuses on measuring of average SAR as a function specimen size and exposure orientation [158]. However, no real comparisons were made between CP and linear applicator. In this chapter, we introduce detailed EM study of CP applicator based on SAR and compared with the already developed linear applicator. The thermal profiles will then be validated on tissue mimicked phantom and on human calf.

7.2 Multi-Fed Circularly Polarised Microstrip Antenna

The initial investigation of CP applicators commenced by employing the multi-feed approach to demonstrate the effectiveness of circular polarisation concept in reducing peak SAR. This is a common direct method to excite circular polarisation. The study focuses on the peak SAR distribution ratio between the superficial layer skin/fat and deeper tissue in the muscle. The antenna design was based on the previous annular ring design of Applicator II, maintaining all the core features including substrate, superstrate

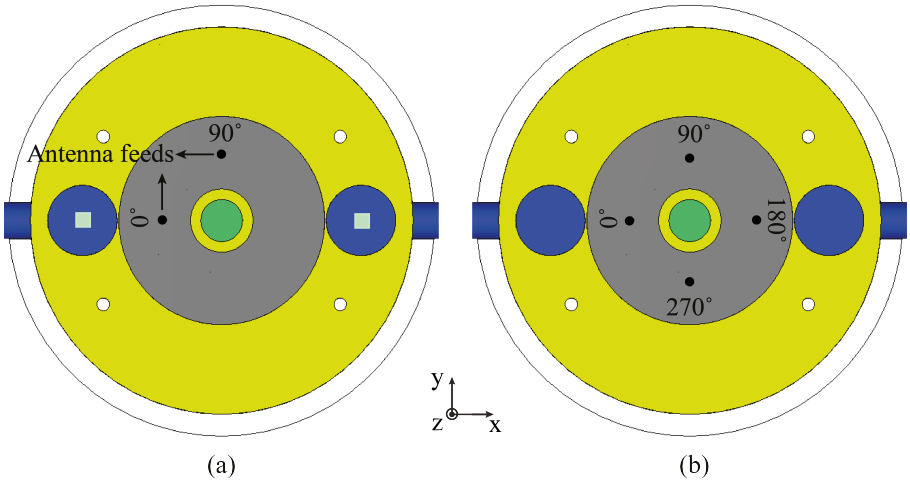

Figure 7.1: Modified Applicator II for CP operation in the following configuration. (a) dual input ports, (b) quad input ports

thickness and the dielectric properties. The change was implemented in the model, with the addition of feed ports. The placements of input ports are orthogonal to each other with a 90 °phase difference between each port, as demonstrated in Figure 7.1. The EM simulation solves each port independently before combining the data with appropriate amplitude weighting and phase shift. A dual feed geometry was initially adopted as demonstrated in Figure 7.1a. The addition of feed point, introduces a change in patch impedance (increase in inductance), thus the feed position is adjusted accordingly for 50Ω match. The study was compared with a four feed port scenario in Figure 7.1b. The assessment of CP antenna performance is achieved by evaluating the ratio of vertical to horizontal field components, which is known as the axial ratio. This is a common method used to predict the operation of circular polarisation in free space. However, the applicators are designed to operate in contact with biological tissue. Consequently, far-field axial ratio assessment cannot be considered for this study. Surface current, is an alternative method that was used to study the current distribution and the corresponding operating mode of the antenna.

7.2.1 Dual Feed CP

The simulated SAR distribution of dual feed CP applicator using the original three layered model is presented in Figure 7.2. It can be seen a circular SAR distribution in the skin layer with a minimum absorption of 28.0 W/kg and maximum of 40.0 W/kg. The non-uniform absorption level is caused by the asymmetrical composition of the

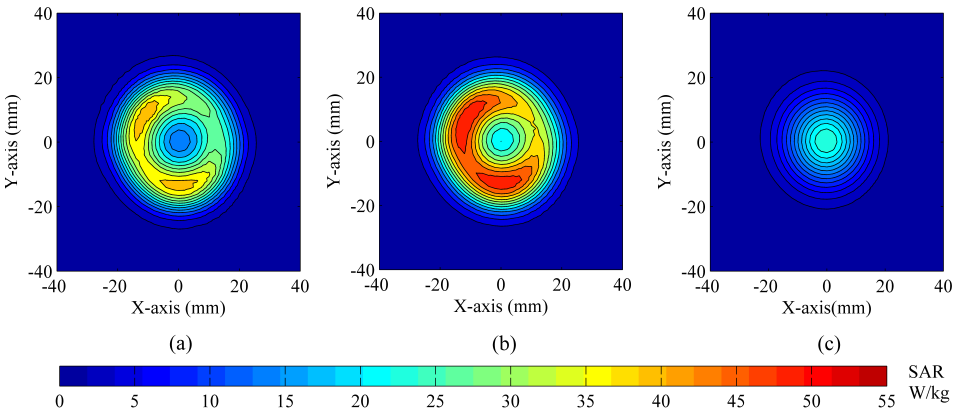

Figure 7.2: Simulated SAR distribution of dual-fed CP excitation on biological model. (a) skin surface , (b)fat surface, (c) muscle surface

applicator (Optical probes) and the operation in the reactive near-field. Figure 7.2b shows the highest SAR in the fat layer at 3.5 mm depth, where peak absorption is 55.0 W/kg. In contrast, the absorption in the muscle was 26 W/kg at a depth of 16.0 mm from the skin surface. The initial impact of this study, shows EM energy is distributed over the applicator area to reduce peak absorption spots produced by the linear applicators. The deposited energy in muscle remains the same as with linear polarisation. A full comparison of CP applicator is presented in the next section. The reflection coefficient of each port was simulated and demonstrated in Figure 7.3. By inspection, $|S_{11}|$ is the primary port at phase 0°set at operating frequency of 2.45 GHz. However, $|S_{22}|$ is the orthogonal port added for CP operation, where the resonance frequency shifted down by about 30.0 MHz it is also desirable, as the two orthogonal modes should not be as the same frequency for wideband CP operation . The change in frequency is caused by the asymmetry of the applicator. The low dielectric optical probes are not used in the *y*-plane, hence change in electrical length with respect of port position.

7.2.2 Quad Feed CP

The dual-port study, showed non-uniform circular distribution, which was expected to be caused by the reactive near-field operation. A more uniform distribution on the skin surface can be achieved with four orthogonal ports as it was illustrated in Figure 7.1b. Each port is incremented with 90 °phase difference in clockwise. The orientation of phase can define the direction of current circulation. In the given configuration, the applicator operates in right hand circular polarisation (RHCP). The numerical study in

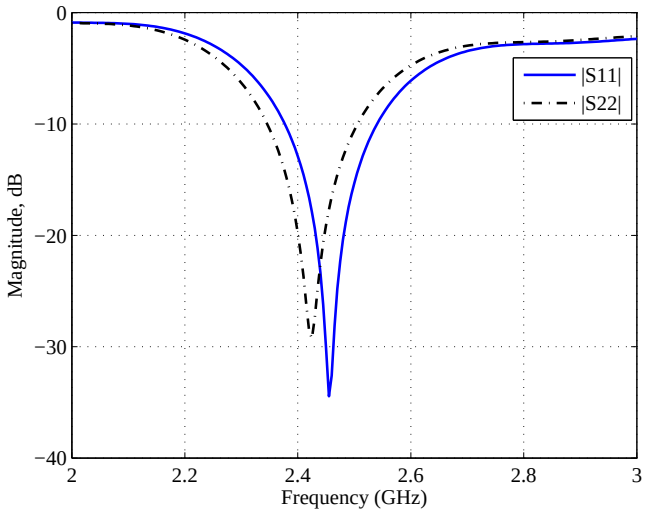

Figure 7.3: Simulated S-parameter of dual-fed circular polarised applicator.

Figure 7.4 shows uniform SAR distribution can be achieved with four ports. The peak SAR in fat layer is 40.0 W/kg, while 21.5 W/kg in the muscle. The overall SAR is generally lower than the dual-fed. This is caused by the unoptimised impedance of the design, it was only for distribution demonstration. The multi-feed study demonstrated the potential of CP applicators. However, it was not feasible with the current spatial limitation at the back of the antenna, where the feed ports occupy the majority of ground plane space. An external power divider and phase shifter will also be required for dual/quad feed operation. These limitations can be solved with the single feed CP radiator.

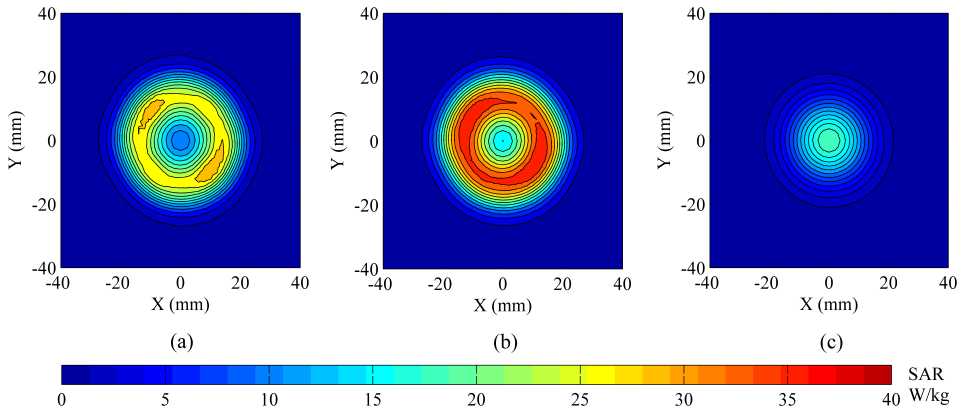

Figure 7.4: Simulated SAR distribution of quad-fed CP excitation on biological model. (a) Skin surface, (b) Fat surface, (c) Muscle surface

7.3 Single-fed Circularly Polarised Microstrip Antenna

Single fed CP radiators are commonly known for its simplicity, compactness and ease of fabrication[159]. It eliminates the requirement of additional feed point and network divider [160]. This approach maintains the same spacing arrangement of linear polarised applicators for effective placement of TEC. This can be accomplished by introducing a perturbation to the radiating element, which is a pair of symmetrical notches in the 45°diagonal plane of the vertical axis as shown in Figure 7.5a. This essentially splits the degenerate mode into two orthogonal modes (TM_{11}) at 90 °phase difference and equal magnitude. The introduced modes resonate at two frequencies, which is about 150-200 MHz apart for 2.45 GHz. Therefore, CP excitation and is the frequency between the two degenerate modes. There are other techniques for a single probe-fed CP found in literature, such as, crossed slot at the centre of the patch, truncated elliptical geometry and strip-line inside the inner ring [161–163]. The development of CP applicator, was based on the described perturbation method. The notch size was calculated using the following Equation 7.3.1 and 7.3.2 obtained from the literature [164].

$$\left|\frac{\Delta \mathrm{s}}{S_a} = \frac{1}{1.841 Q_o}\right| \tag{7.3.1}$$

$$\left|\Delta s = \frac{\pi a^2}{1.841 Q_o}\right| \tag{7.3.2}$$

Where Δs is the area of the total perturbation segments on the patch, S_a is the area of the original circular patch and Q_o is the quality factor of the unmodified antenna. These approximations are based on the assumption of antenna operating in free space and based on circular patch antenna. The developed applicator is an annular ring design, which was not investigated previously with perturbation. Therefore, the effective area was of the concentric centre subtracted from the area of the circular microstrip antenna. As the applicator placed on the biological tissue model, the impedance characteristic of the antenna is altered including the notch size. For optimal CP operation, EM simulations were required to tweak the perturbation size. The characteristic of antenna was evaluated by current and SAR distribution. The CP antenna design was further improved by the addition of a pair of symmetrical stubs on the mirrored diagonal axis, demonstrated in Figure 7.5b This modification allowed for improved impedance band-

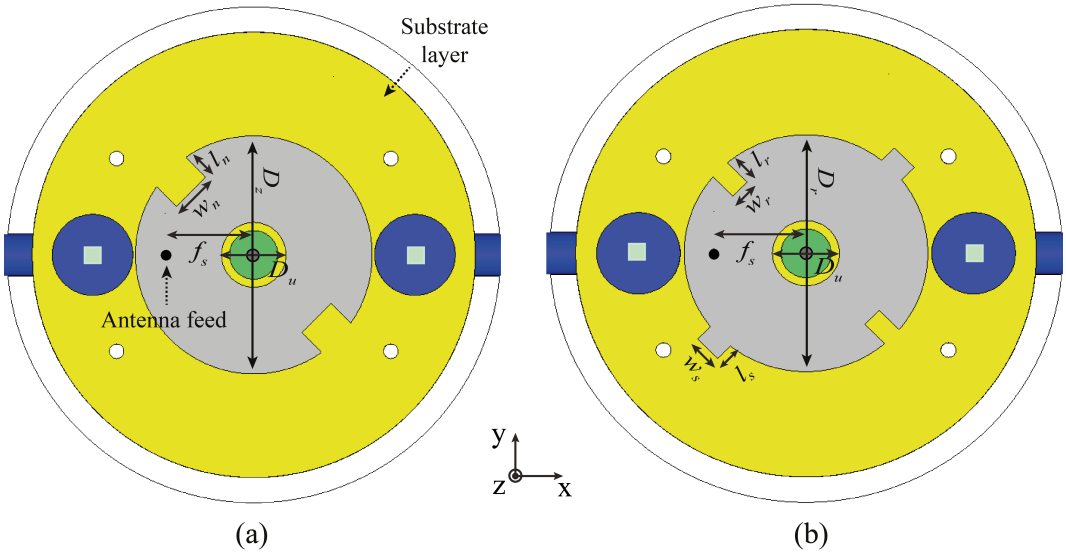

Figure 7.5: Single-fed CP applicator. (a) original basic model / Model I, (b) improved new model / Model II

width and optimised SAR distribution. The dimensions of both designs are presented in Appendix C Table C.3.

7.3.1 Perturbation Study

The optimisation process of the perturbation size was studied using EM simulation. The investigation established with a simple design using a pair of symmetrical notches to excite CP. Applicator parametric study was realised for the notch length (l_n) and width (w_n) . The performance of CP was evaluated with the simulated $|S_{11}|$, where the two orthogonal modes can be distinguished. The result of the study is presented in Figure 7.6. By inspecting Figure 7.6a, variation in l_n causes the two degenerate modes to shift, where the modes either combine into a fundamental mode or spread further apart at larger frequency difference. The optimal condition is when the two modes are orthogonal, where the centre frequency for CP is represented by the flat region in the $|S_{11}|$ This is the case when $l_n = 3.4$ mm, as the impedance bandwidth of CP is enhanced. Decreasing the length of perturbation further causes the two modes to spread apart, and the return loss at centre frequency is increased. Moreover, increasing l_n causes the two modes to combine into a single fundamental mode, therefore, operating as a linear polarisation applicator. Figure 7.6b illustrates changes in CP impedance bandwidth with the width of the perturbation. Consequently, both parameters are optimised accordingly

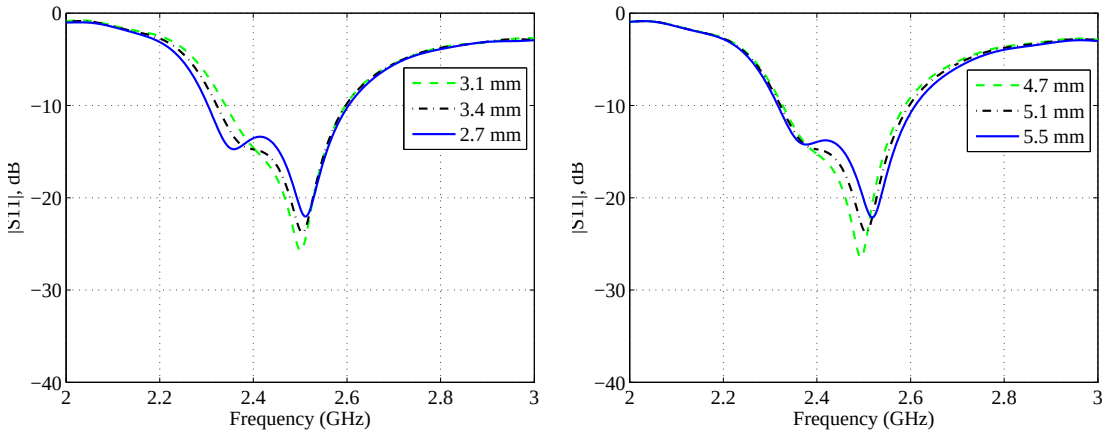

(a) (b)

Figure 7.6: CP Model I $|S_{11}|$ parametric study/ (a) perturbation length l_n (b) perturbation width w_n

to obtain optimal CP excitation with sufficient bandwidth. The final values were 3.4 and 5.1 for l_n and w_n respectively.

7.3.2 CP Applicator Performance

The CP Model II, consists of four parameters which all required to be optimised simultaneously. This added complexity was beneficial for lowering the return loss by about 3.2 dB. The simulated $|S_{11}|$ of the two models is illustrated in Figure 7.7. The operating bandwidth is only 20 MHz between 2.38 and 2.40 GHz. The performance of the excited CP was evaluated by the numerical current SAR distribution. The current distribution (in Amps/m) of the improved CP applicator design (Model II) is presented in Figure 7.8. It can be observed the surface current vector is a function of phase. By considering over the four shown phase steps, a circular rotation of the current vectors is generated in an RHCP manner. The CP bandwidth was evaluated by analysing the SAR on the superficial tissue at different operating frequency, typically this was found to be about 20 MHz. Exceeding operating frequency by over$\pm$10 MHz of the centre frequency, the SAR and current distribution will deteriorate.

The numerical study of CP applicator was extended to assess the SAR distribution in the skin, fat and muscle at a depth of 1.0, 4.0 and 16.0 mm respectively. The assumption made during the CP simulation (before fabrication), the biological medium was based on the original model of 2.0 mm skin and 10.0 mm fat layer. Using Model II

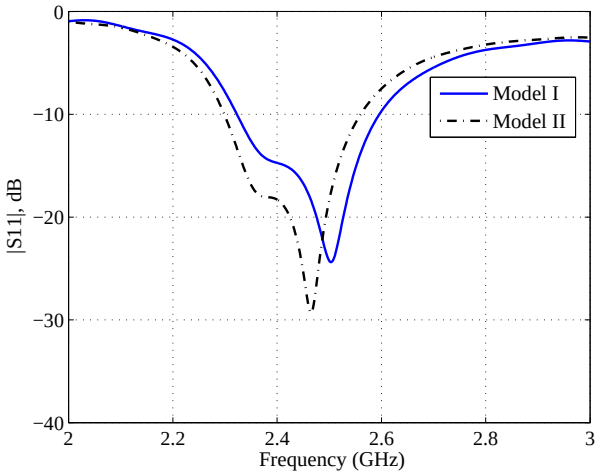

Figure 7.7: Simulated $|S_{11}|$ of circular polarised applicator with single-fed CP Model I&II.

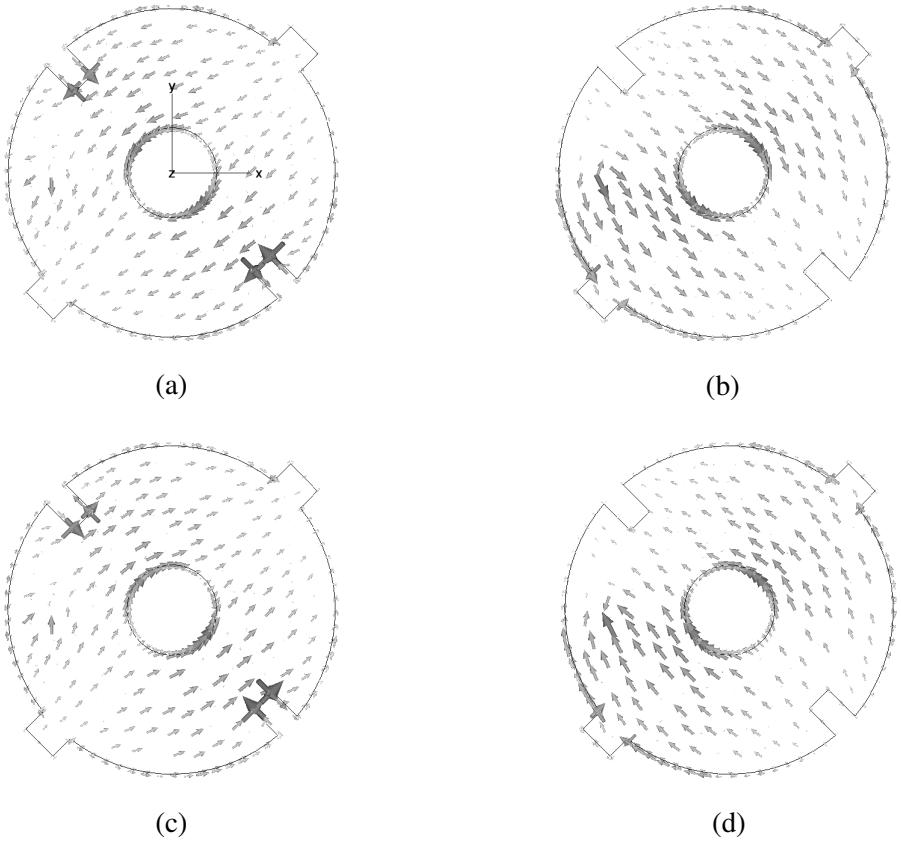

(a) (b)

(c) (d)

Figure 7.8: Single-fed CP Applicator current distribution at the following phases. (a) 0°, (b) 90°,(c) 180°, (d) 270°

may deteriorate the CP analysis, as it was very sensitive to tissue composition. Therefore, Applicator II was simulated on similar condition for comparison with CP designs. The SAR distribution induced by the linear and circular polarised applicators is illus-

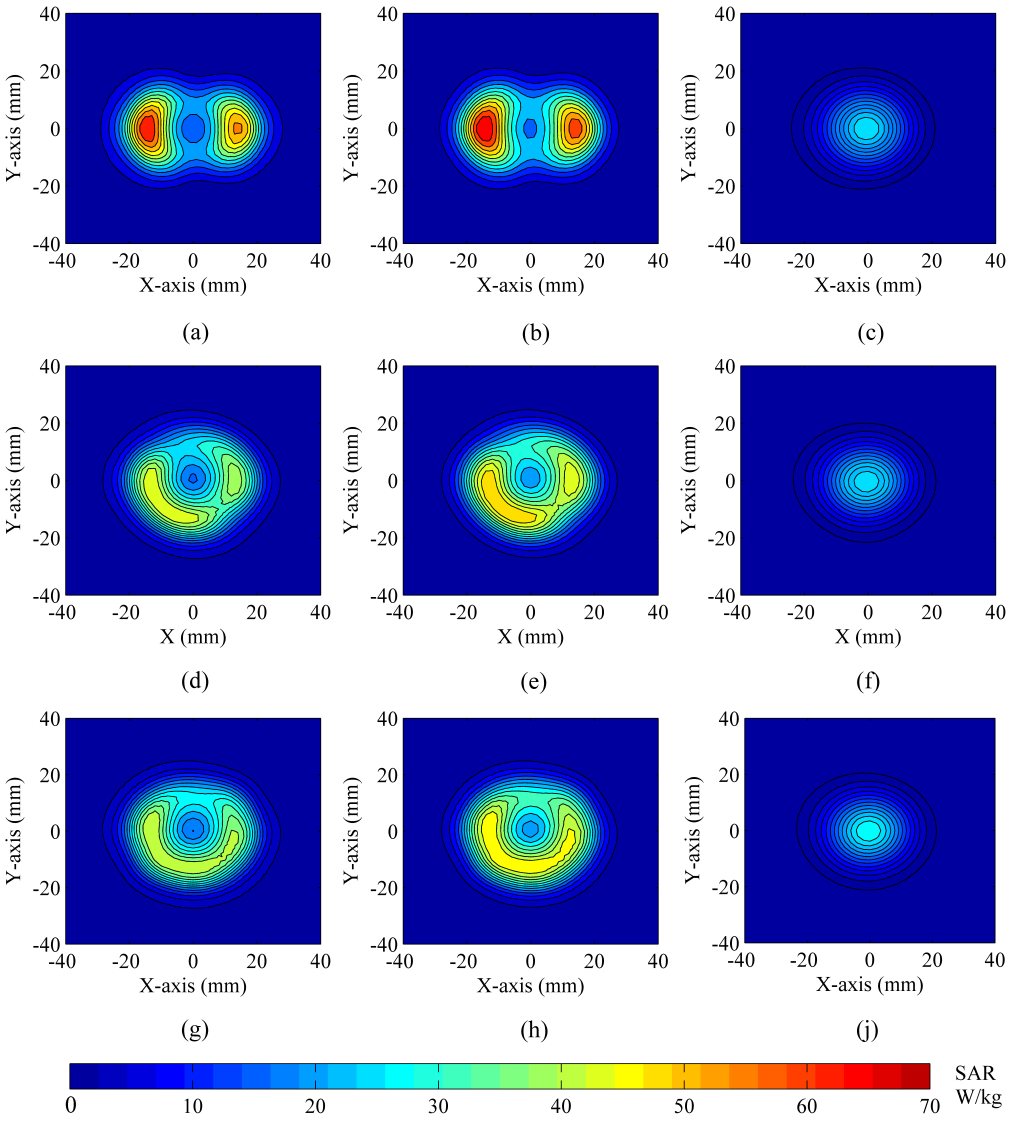

Figure 7.9: Simulated SAR distribution in biological medium on skin, fat and muscle. (a,b,c) Linear Applicator II, (b,e,h) CP Applicator I, (c,f,j) CP Applicator II

trated in Figure 7.9. The results demonstrate SAR distribution in each consecutive layer horizontally with respect to depth inside the tissue. The evaluated types of applicators are compared vertically from a linear applicator (a,b,c), CP Model I (d,e,f) and the updated CP Model II (g,h,j) of Figure 7.9. The absorption on the skin surface is 65 W/kg for linear applicator, which is about 20 W/kg higher than CP applicator (30.7% decrease). The Model II shows an improved circular deposition with skin SAR is 4.7% lower than the original designed CP applicator. Figure 7.9(b,e,h) shows the SAR distribution on the fat layer deposited by the various applicators. It can be seen the peak SAR is in the fat, which is produced by the standing wave between the skin and the muscle

when operating at 2.45 GHz. Applicator II has the greatest SAR at approximately 70 W/kg in the fat layer, this also about 28.8% higher than with CP applicators. The muscle absorption in Figure 7.9(c,f,j), indicates all three applicators have equal absorption magnitude at about 27 W/kg.

The finding was further evaluated with peak SAR plots across the depth (z-axis) inside the biological tissue at the horizontal and vertical plane cuts as shown in Figure 7.10. The study across the horizontal plane is shown in Figure 7.10a, were the linear polarised applicator has the maximum peak absorption in the fat layer. In contrast, the muscle absorption was the same for both applicators. In the vertical plane shown by Figure 7.10b, the linear applicator is at the non-radiating edge. The peak SAR in the fat layer was induced by CP applicator at about 50 W/kg equivalent to the horizontal plane. This clearly indicates the spread of the deposited energy over the two planes, minimizing the large peak absorption in one plane. The applicator performance was characterised by SAR ratio of peak muscle absorption to superficial peak absorption. The current study shows SAR ratio of 38.7%, 41.2% and 54.56% for Applicator II, CP model, I and CP model II respectively. Consequently, CP model II is the primary CP applicator which was later developed.

The bandwidth of single fed CP microstrip antennas is always a challenging problem in many applications. By studying the SAR distribution the optimal applicator bandwidth was 20 MHz. Moving operating frequency by $\pm$ 10 MHz of the given band-

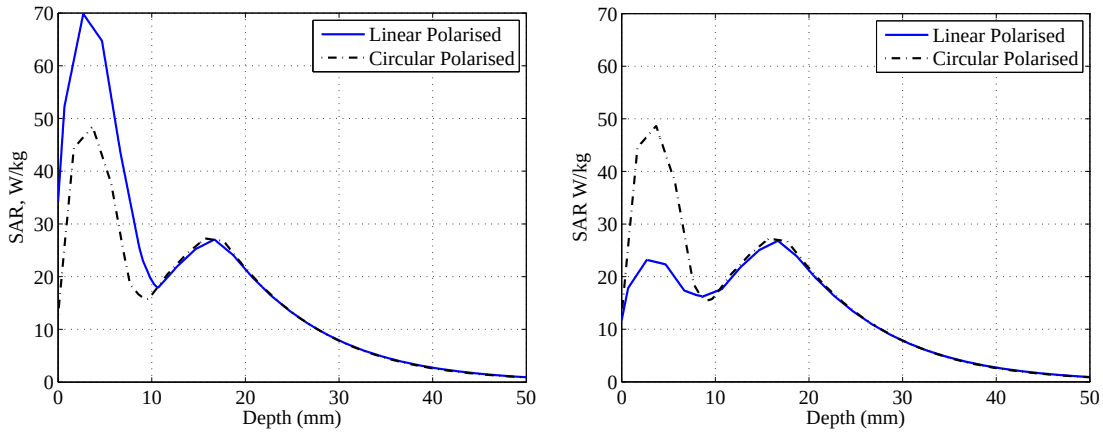

Figure 7.10: Simulated Peak SAR in phantom with linear and CP applicator. (a) xz-plane (b) yz-plane

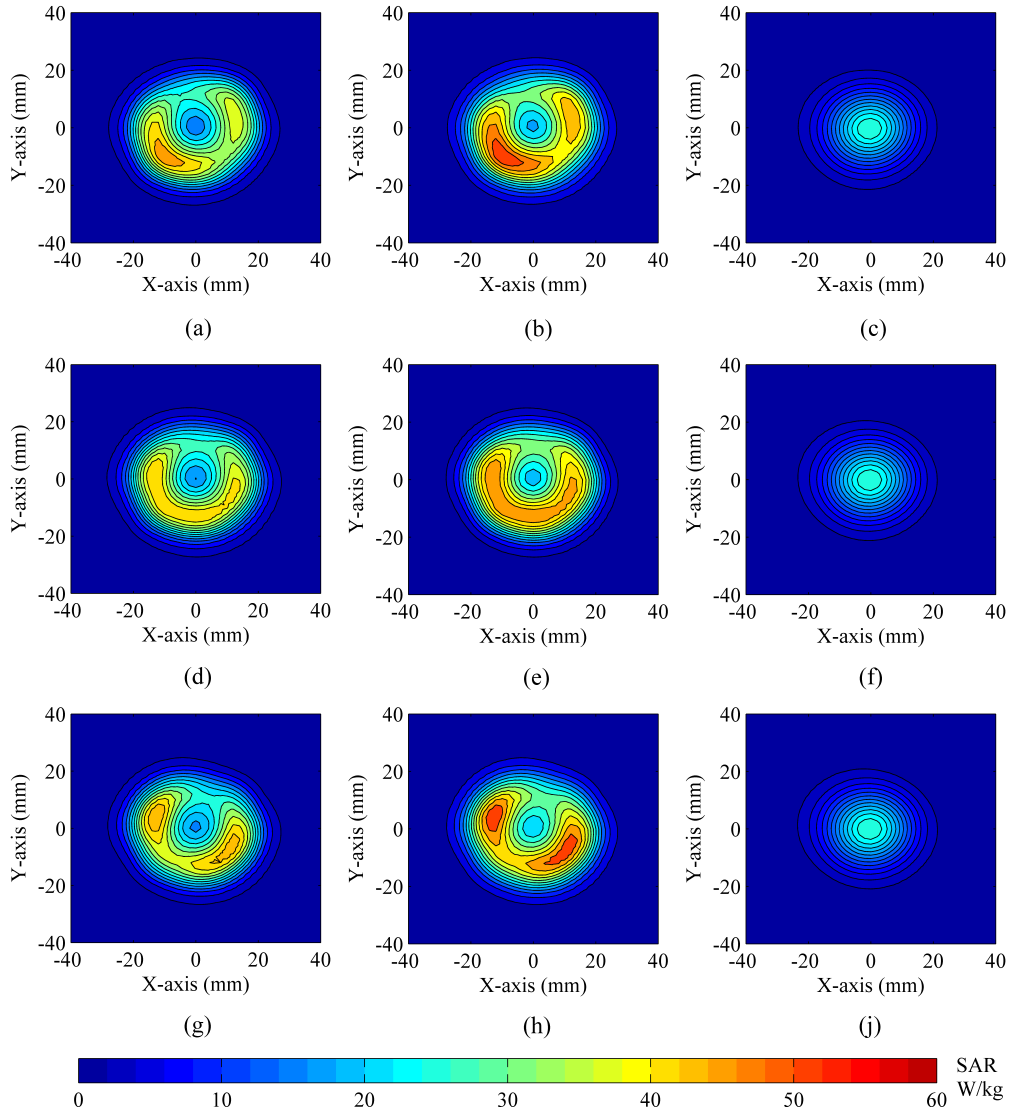

Figure 7.11: Simulated SAR distribution of CP applicator on skin,fat and muscle at the following operating frequencies. (a) 2.39 GHz, (b) 2.4 GHz, (c) 2.42 GHz

width will start to deteriorate current distribution and therefore, the emitted radiated electric field. Figure 7.11 illustrates the layered SAR distribution of optimised CP applicator at 2.38 GHz, 2.4 GHz and 4.2 GHz. The simulation study presented in Figure 7.11)a,b,c) is the SAR distribution on the surface of skin, fat and muscle respectively at 2.38 GHz. The absorbed EM energy is deviating to elliptical polarisation and approaching to linear operation when the frequency is lowered further. The two peaks are apparent in a positive gradient diagonal line, indicating the degenerate mode at the lower frequency. This is contrasted with the CP operating region at centre frequency of 2.4 GHz shown in Figure 7.11(d,e,f), where the peaks are distributed in a circular man-

ner. The peak SAR in the fat layer is 17 % increase at the lower and upper frequency bands, while the muscle remains the same. This is about 14.3% decrease than of the full linear applicator. Figure 7.11(g,h,j) is the absorption rate at the upper frequency of 2.42 GHz. It can be seen the distribution is mirrored of the lower frequency band (a,b,c) at the y-axis. The two radiating peaks are in the negative gradient line, which is the second degenerate mode. The combination of those two modes will produce the observed CP distribution of the centre frequency, which agrees with the theory.

The significance of wide operating bandwidth is emphasized in the tissue composition study. Figure 7.12a shows the simulated $|S_{11}|$ of CP applicator at different skin thickness of 1.5, 2.0 and 2.5 mm. It can be observed, as the thickness increases to 2.5 mm, the two degenerate modes add up into a single fundamental mode operating in linear polarisation. Lower skin thickness with also deteriorate CP operation, where the two modes are no longer orthogonal. The applicator is clearly very sensitive to skin thickness, and thus improving impedance bandwidth will not enhance this operation. However, this problem can be resolved by increasing the spacing of the applicator to tissue, from reactive near field to radiating near-field. Therefore, reduce the applicator sensitivity to the change in tissue composition. Figure 7.12b shows the simulated $|S_{11}|$ of the applicator at different fat thickness. By inspection, the performance deteriorates less by the fat thickness or deeper tissue composition. In this study, improving the impedance bandwidth is of benefit, as it can be seen the bandwidth deteriorates further

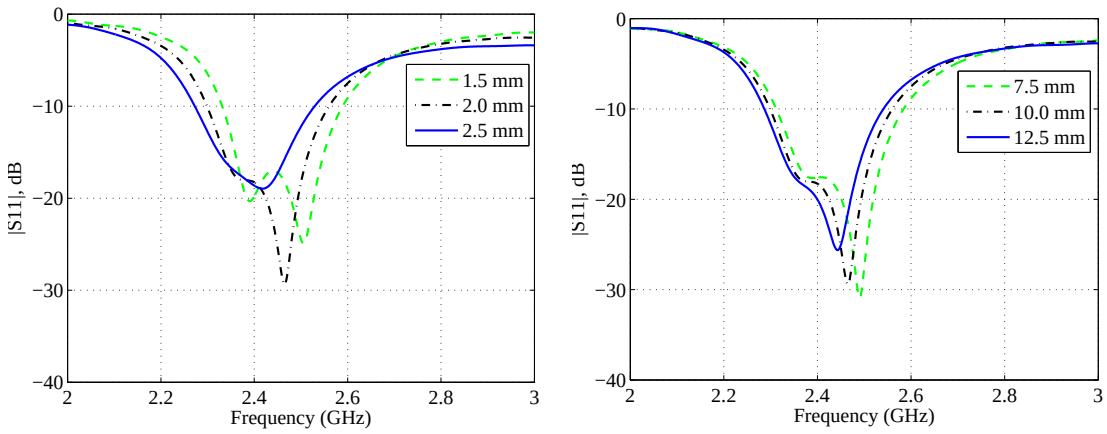

(a) (b)

Figure 7.12: Simulated $|S_{11}|$ of CP applicator for various tissue thickness. (a) skin thickness (b) fat thickness

as the thickness increases to 12.5 mm.

7.4 CP Applicator Development

The simulated and optimised CP model was fabricated on an identical substrate material of Applicator II&III, and same optical probe's geometry. The overall substrate dimension is fixed for quick integration to the exterior housing. This fabricated CP applicator is demonstrated in Figure 7.13. The critical feature in the fabrication process is the feed point soldering to the radiating element surface. The surface of the microstrip patch antenna with the soldered feed point must be flat surface to eliminate any air gap introduced when it is loaded by the superstrate. A lumped soldering at the feed point could introduce large surface current at the location, and therefore, imitation to the skin layer.

The return loss of the developed CP applicator was measured in free space and on human calf using VNA. The measurement in air was compared with the simulation study as shown in Figure 7.14a. The resonating frequency is 2.68 GHz, which agrees with the numerical results. However, the return loss of the measurement was about 5.0 dB higher, which it may have been caused by the approximated values of dielectric material of the optical probes and the exterior housing. The applicator was placed on a human calf, and the $|S_{11}|$ was measured accordingly. The measurement was compared with the current updated simulation model presented in Figure 7.19. The operating CP

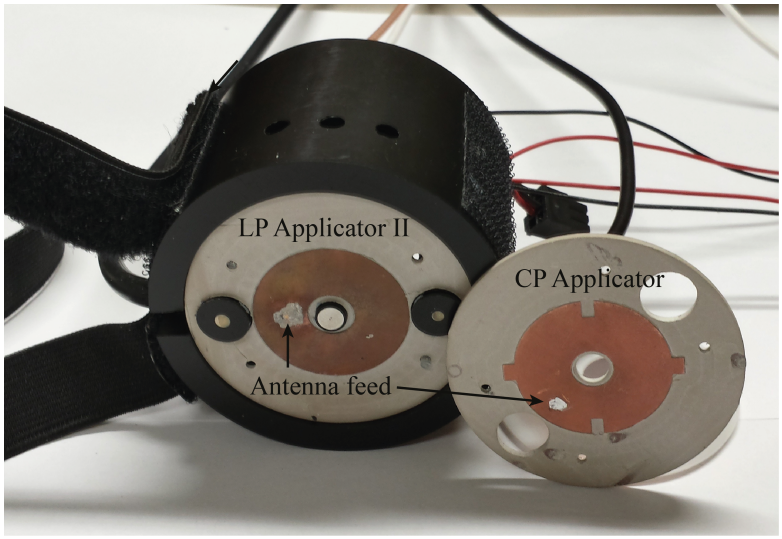

Figure 7.13: Fabricated CP applicator.

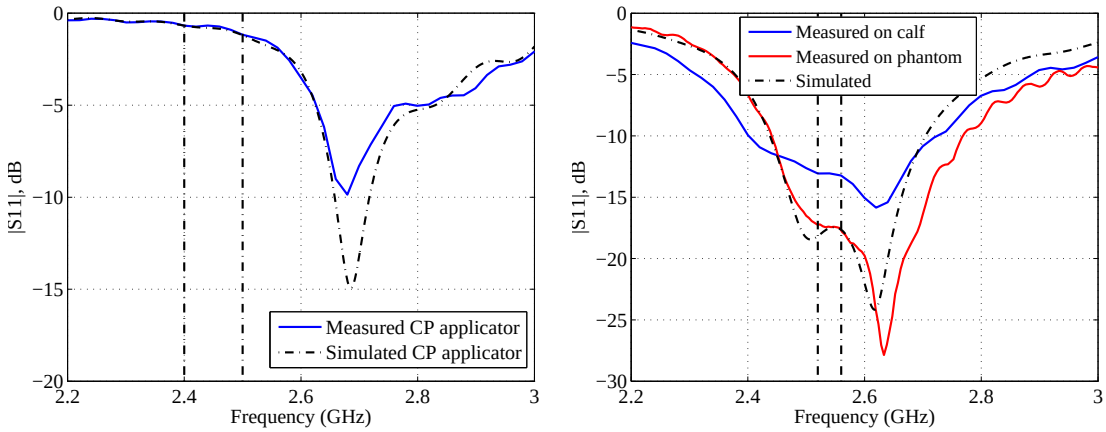

(a) (b)

Figure 7.14: Measured and simulated $|S_{11}|$ of CP applicator. (a) free space (b) on human calf and phantom

frequency in agreement with the simulation at 2.53 GHz. The measurement was repeated on the phantom with identical center frequency. The bandwidth was narrower because of thicker fat layer in the fabricated phantom. This analysis was based on previous observation of the simulated tissue composition, if skin thickness is varying, then the change in resonance frequency will be noticeable. Therefore, this change is mostly influenced by the fat thickness. The measurement on calf had the largest return loss at -13.0 dB, which is 4.0 dB higher than phantom measurement and simulation. The $|S_{11}|$ assessment authenticates CP operation frequency, by observing the two degenerate modes. This measurement was repeated each time the applicator position was changed, to ensure where about the operating frequency.

7.5 CP Applicator Validation

The performance of developed CP applicator was assessed on mimicked phantom and human calf. The result compromise of measured thermal distribution and corresponding simulation with equivalent tissue model thickness for each scenario.

7.5.1 Phantom Validation - Warming Only

The applicator was placed on the phantom, and $|S_{11}|$ was measured to attain the optimal operating frequency for CP. The experimental protocol is identical to the Applicator II with input microwave power of 3.0 watts RMS over 5-minutes of exposure. The obtained thermographic images of skin and muscle surfaces are presented in Figure

7.15. The measured skin profile agrees with the corresponding setup in the simulation as shown in Figure 7.16. The peak skin temperature was comparable to the Applicator II at about 31-31.5 °C. However, the CP applicator measurements were affected by the phantom starting temperature, which was about 1.5 °C higher than previous studies.

The captured muscle surface had a thermal distribution with peak temperature of 29.1 °C is shown in Figure 7.15b. The temperature is also greater at approximately 2.0

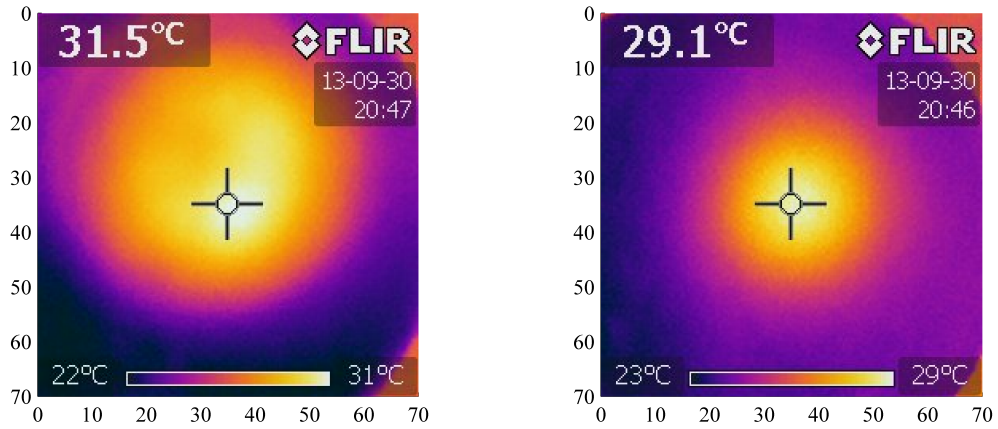

(a) (b)

Figure 7.15: Measured thermal distribution after 5-minutes of microwave exposure. (a) phantom skin surface, (b) phantom muscle surface

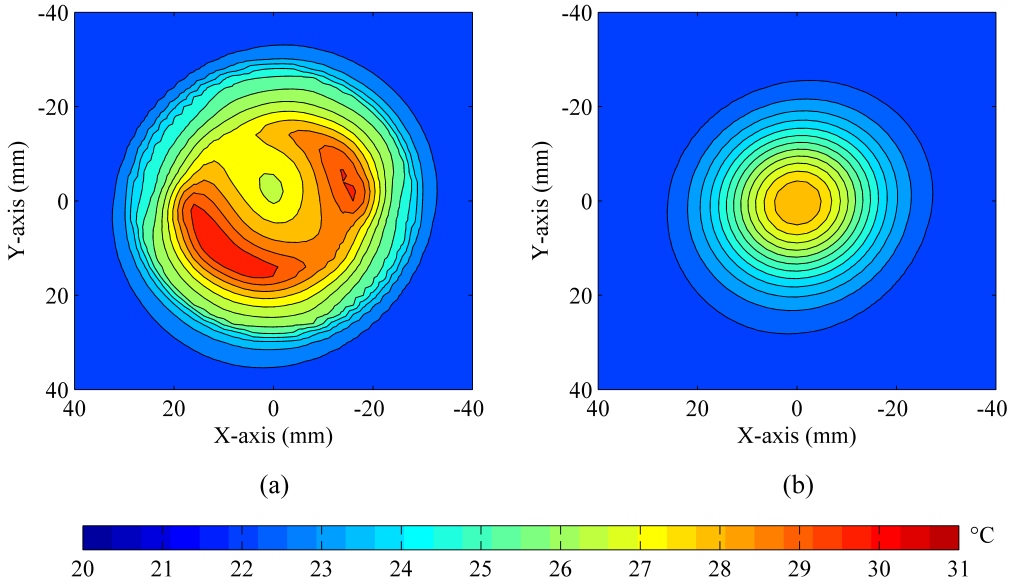

(a) (b)

Figure 7.16: Simulated thermal distribution after 5-minutes of microwave exposure. (a) phantom skin surface, (b) phantom muscle surface

°C than the measurement of linear applicator II. Therefore, these set of measurement were influenced by the background temperature. Taking this condition to account, the corresponding result actually indicated skin temperature is reduced with CP antenna, while muscle elevation is maintained the same for both polarisation. The simulated muscle distribution in Figure 7.15b, shows peak muscle temperature is 1.0 °C lower than the measurement. This clearly indicates the influence of room temperature to the measurement.

7.5.2 Phantom Validation - Skin Cooling

The experiment was repeated with applied skin cooling, the recorded IR images are presented in Figure 7.17. The skin thermal distribution shows an identical pattern to the SAR study. The peak skin temperature was 26 °C with skin cooling, which is about 4 °C lower. Moreover, Figure 7.17b is the measured muscle distribution with identical peak surface temperature of 26 °C. In contrast, the reciprocal simulation result is illustrated in Figure 7.18. The phantom simulation with skin cooling was 1.0 °C higher than the measurement of the skin and muscle surfaces. The peak temperature of both layers is consistent with the measurement. Therefore, the possible difference was the background temperature. The performance of CP applicator is compared against measurement of the linear Applicator II that was presented in Chapter 6 Section 6.6.4. The results demonstrate the CP applicator can reduce the skin temperature by 2 °C, while the muscle temperature was maintained the same for both polarisation technique. This measurement conforms with the SAR simulation, where peal skin absorption is reduced with CP applicator.

7.5.3 In-vivo Validation

The final study of CP applicator was based on thermal measurement on human calf. The return loss of the applicator on the calf was repeated for each measurement, to ensure appropriate operating frequency for exciting CP. The first acquired thermographic measurement in Figure 7.19a was without active cooling. The distribution on human calf is not as clear with phantom measurement, due to the inclusion of blood perfusion where the heat is regulated and diffused at a faster rate. Regardless, arc shaped warming profile is observed, which share equivalent features of the corresponding simulation in Figure 7.20a. The modelled thermal distribution is based on the current tissue con-

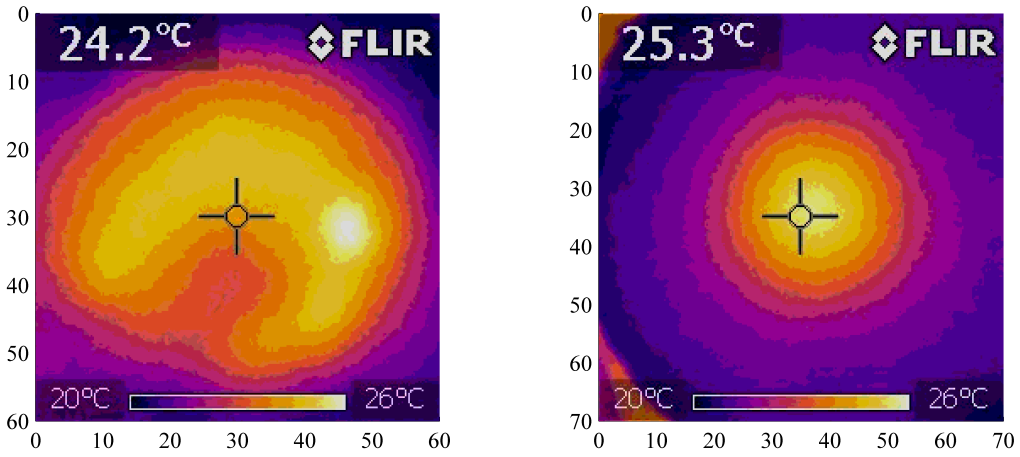

Figure 7.17: Measured thermal distribution of CP applicator after 5-minutes of microwave exposure. (a) phantom Skin surface, (b) phantom muscle surface

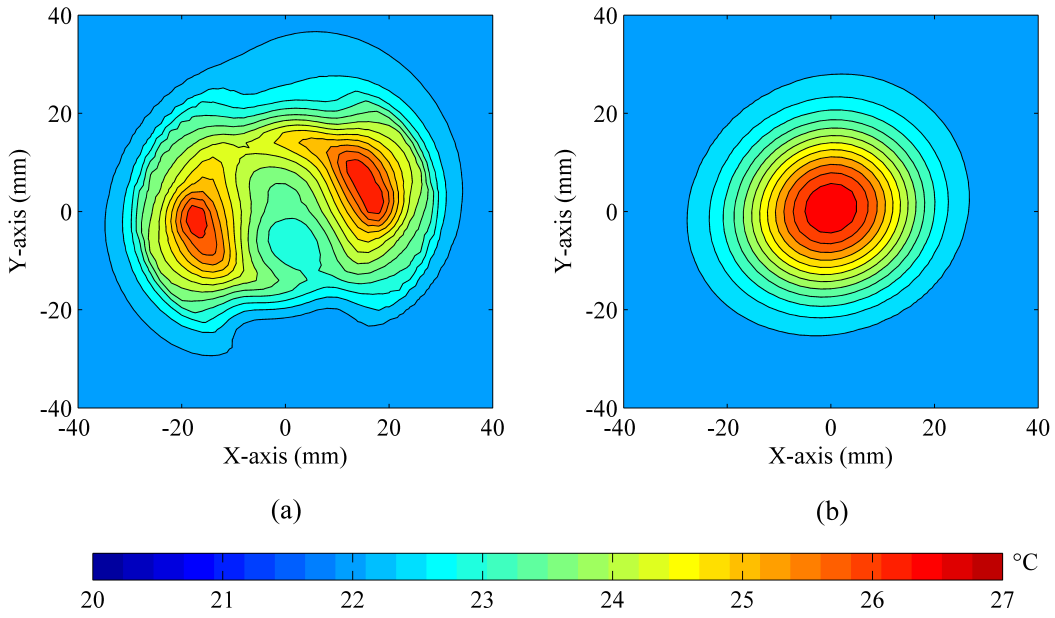

Figure 7.18: Simulated Thermal distribution of CP applicator after 5-minutes of microwave exposure. (a) phantom skin surface, (b) phantom muscle surface

figuration of 1.0 mm skin and 7.0 mm fat layer. The peak skin temperature is 37.2 °C, in contrast to 28 °C of the simulated skin model. According to the simulation model to estimate the muscle temperature, which was 43.4 °C. Therefore, the total elevation in the superficial layer is 6.9 °C assuming average skin temperature of calf is 30.3 °C (see Figure C.5 for details). In contrast, the absolute elevation in the muscle is 6.4 °C

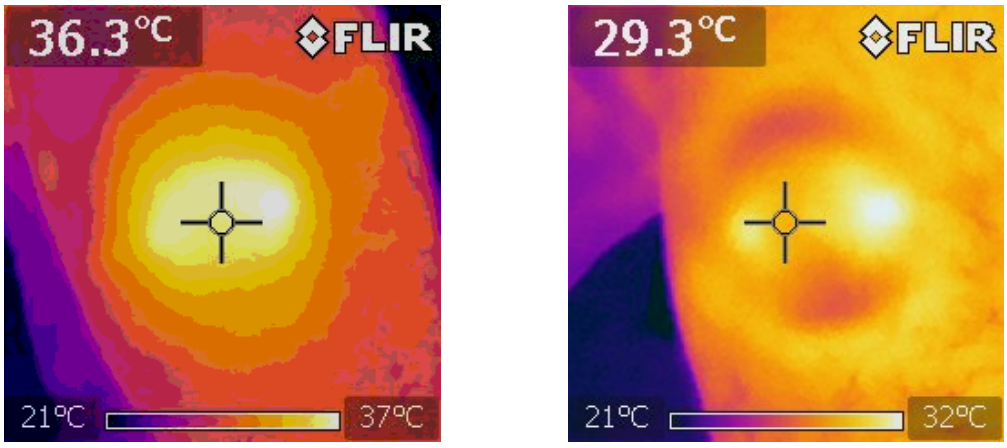

(a) (b)

Figure 7.19: Measured Thermal distribution of CP applicator after 5-minutes of microwave exposure on skin surface. (a) without active cooling, (b) with active cooling

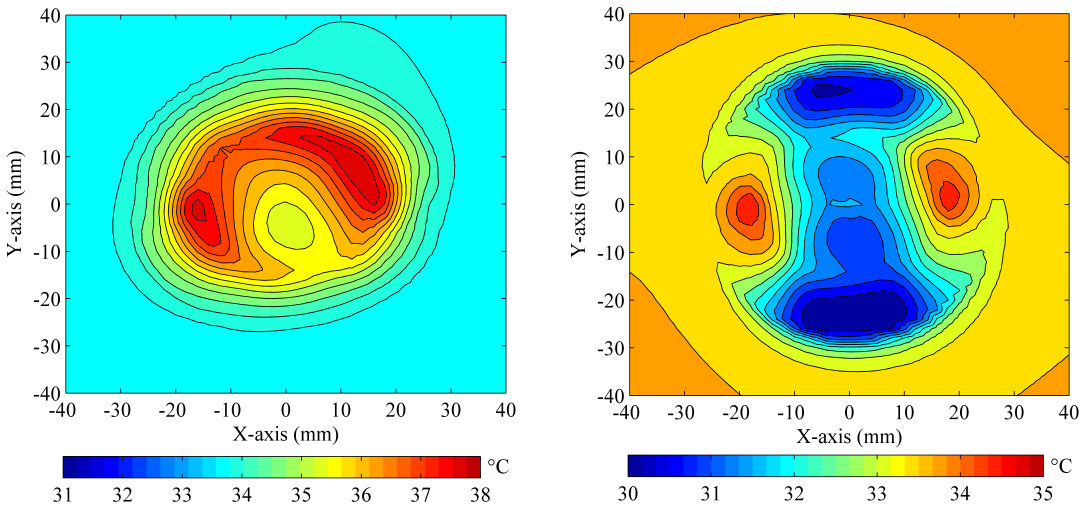

(a) (b)

Figure 7.20: Simulated thermal distribution of CP applicator after 5-minutes of microwave exposure on skin surface. (a) without active cooling, (b) with active cooling

assuming deep tissue temperature is 37.0 °C. This study is compared with the thermal measurement of linear Applicator II, were peak skin temperature was 41 °C. This is an increase of 3.8 °C over CP measurement and 0.4 °C lower in the muscle according to the simulation.

The *in-vivo* measurement was repeated to incorporate active cooling. The captured thermal distribution of human calf after 5-minutes of microwave exposure is presented in Figure 7.19b, and the corresponding simulation in Figure 7.20b. By inspection, the

measured thermal distribution shows an identical pattern of previous Applicator II with two horizontal hotspots and two vertical cold spots. The peak temperature was 32.3 °C that is only raised by approximately 2.0 °C of initial skin temperature. This is also a reduction of 4.5 °C from the previously assessed Applicator II with active cooling. The thermal distribution was validated with the numerical study, illustrating identical thermal patterns. However, the peak temperature value is about 2.7 °C higher than measurement. This was believed to be an anomaly in the measurement, which was repeated and equivalent results were achieved again. Therefore, this large indifference could be based on the optimal CP operation as a function of tissue composition. The simulation model is based on fixed thickness, where the measurement can vary from position to another, which may have enhanced the excited CP.

7.6 Chapter Summary

This chapter introduced alternative solution to reduce peak energy absorbed in the superficial using the circularly polarised applicator. This approach promotes the electric field vector to circulate at a given point in space as a function of time, which radiates the EM energy in the diagnosed area. We have studied the techniques of achieving CP by the use of either multi-fed or single-fed microstrip patch antenna. Specific absorption rate simulation of dual-fed and quad-fed applicators was investigated for early stage performance assessment of CP. The observed result shows clearly the energy can be distributed and effectively reducing peak SAR on the superficial layer. However, th multi-feed approach was not desired for it sheer space limitation and additional requirement of a network divider. Consequently, single-fed design was adopted by introducing perturbation and stubs to the original linear Applicator II model. The performance of CP microstrip antenna was analysed by observing the S-parameter and surface current distribution. The simulated SAR showed the CP applicator reduces the peak absorption in the fat layer by about 28.8%, while muscle absorption was kept the same. The narrow impedance bandwidth and near-field operation were one of the major limitations of CP applicator. Changes in tissue composition thickness, can result in deteriorating the performance of CP. The design was developed, improved and fabricated for thermal validation. The operating frequency of the applicator was in agreement with the current simulation model in free space, on human calf and on phantom. The *ex-vivo*

thermal distribution was in agreement with the EM model for with and without cooling. The general trend was the skin temperature was reduced by around 1-2 °C when using CP applicator. The experiment was repeated on human calf, and the results were conclusive showing a significant temperature decrease in either with or without cooling. The reduction was about 3-4 °C in the skin, while simulation shows equivalent muscle temperature. The overall trend the thermal distribution of simulation and measurement are comparable with a certain degree of accuracy. However, with circularly polarised applicator, the simulation was usually about 1 °C higher than measurement. This was believed to be by the unpredictable CP performance as a function of tissue thickness.

Chapter 8

Results and Discussion

8.1 *In-vivo* Measurement Preparation

This chapter integrates the microwave applicator with the hybrid system for *in-vivo* thermoregulation monitoring. The developed microwave applicators was proven to be capable of inducing localised heat in the muscle and superficial layers. The elevated heat causes the blood vessels to dilate and therefore, change in tissue oxygenation. These changes are measured with the integrated optical probes based on NIRS, which is used for all physiological assessments. The study with Applicator I was based on general tissue warming and was limited to only blood volume measurement with the NIRS. Applicator II was then introduced to included numerous sensors for skin temperature, blood flow and active cooling element. Therefore, comprehensive measurements were obtained. This includes tissue oxygenation and blood flow during microwave warming with and without active cooling. Each applicator has a distinguished protocol which is essential to the result analysis. This will provide information regarding the efficacy of the hybrid system in terms of superficial and deep tissue monitoring.

8.1.1 Safety and Ethics

The subject safety is always top priority during all *in-vivo* experiments. The main risk factor arises from tissue heating over long exposure duration. Human experiments were conducted only after simulation, and phantom validation was done. This ensures the level of induced heat is within the estimation and under the safety margins. Typically non-invasive microwave hyperthermia induces heat of about 42 to 45 °C over a duration of 30 minutes. This is when cell death occurs over constant high temperature and long period of time. The intention of the hybrid system, is to induce heat for sufficient vessel dilation. This can be achieved over lower induced temperature at about 40-41 °C in muscle and duration of just 5-minutes. The study acquired approval by the UCL Ethics Committee for up to 5 human subjects. During the experiments, three male subjects were recruited to participate in the study. The operator closely monitors the power levels, skin temperature and the change in oxygenation levels.

Microwave exposure to surrounding is another factor that was considered for the safety of operator and the subject. Measuring the leakage is a standard procedure for all therapeutic applicators. When operating at microwave region of 2.45 GHz; the maximum power density must be less than 10 mW/cm^2 at 5.0 cm away from applicator

[58]. The power density in space equates to $S = E^2/377$, where S is the power density in W/cm^2 and E corresponds to the electric field strength in (V/m). The 377Ω corresponds to the intrinsic impedance of free space. The measurement in most scenarios are achieved with use of external horn antenna operates at same frequency. This was achieved using a wide-band horn antenna with Gain of approximately 11.0 dBi at 2.45 GHz and placed 5.0 cm away from the applicator. The horn is connected to a spectrum analyser to measure the power leakage. The measured power for applicator II was -8.0 dBm (0.16 mW) when the horn antenna positioned along the radiating edge, which was the maximum leakage. The obtained parameters are used in Equation 8.1.1, where P_r is the received power and A_{eff} is the affective area of the receiver horn antenna.

$$P_r = A_{eff}S \tag{8.1.1}$$

The antenna effective area in Equation 8.1.2 describes the amount of EM power captured by the receiver antenna. Where G is the antenna power gain (unit less), hence the horn antenna gain is converted to the power gain for the necessary calculation to take place. The estimated leakage power density of applicator I was 4.0 μW/cm^2, when the applicator was operating at 5 watts. The calculated power density of applicator II operating at 3 W RMS was 1.06 μW/cm^2, and the operating power was 3 watts. In both cases, the exposed microwave is lower than the standard limit of 10 mW/cm^2.

$$A_{eff} = G\frac{\lambda_o^2}{4\pi} \tag{8.1.2}$$

8.1.2 Tissue Thickness

The fat thickness of two subjects was measured using an ultrasound scanner. From the real time images, the thickness was estimated to be 6.8 mm and 5.0 mm for subject one and two respectively. The measurement is combined with the physiological study listed in Table 8.1. The estimation of tissue thickness was based on the contraction of muscle calf. An example of subject one calf image is presented in Figure 8.1. Figure 8.1a is the captured image when the muscle calf was relaxed. During contraction, the muscle pushes outward with a dominant tissue movement apart from the superficial layers of fat and skin as observed in Figure 8.1b. Consequently, it was possible to predict the fat thickness of the tissue. The skin layer was not estimated, as it was difficult to measure in this approach. The measured thickness contributed to the evaluation of the modelled

fat thickness, which in turn the model was changed from 10.0 mm thickness to 7.0 mm thickness.

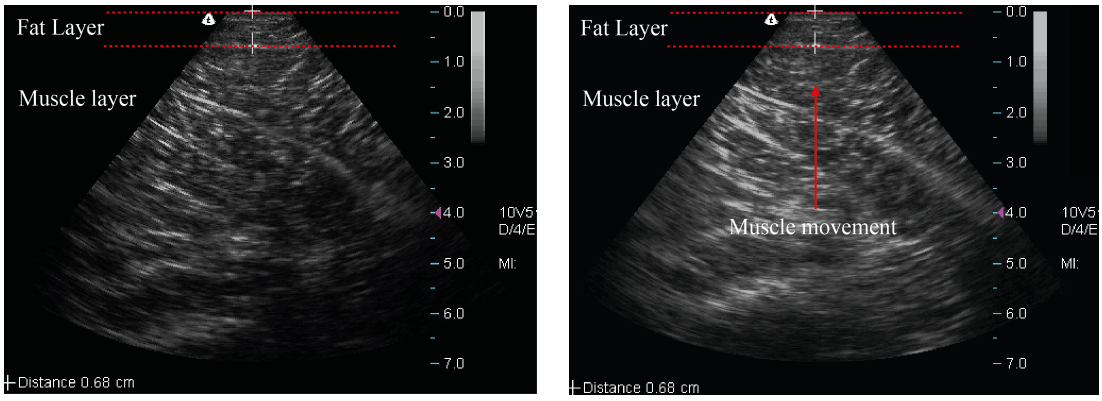

(a) (b)

Figure 8.1: Measured fat thickness on subject calf using ultrasound imaging at different states. (a) relaxed muscle, (b) contracted muscle

8.2 *in-vivo* Applicator I

Applicator I with the integrated optodes are housed in a rectangular foam as observed in Figure 8.2a. Figure 8.2b shows how the device was securely placed on a calf with elastic warping to ensure secure positioning and to eliminate external light to the optical detector. The foam has typically an ϵ_r approximately equivalent to free space, which has negligible influence upon the antenna performance. The scattering parameter of the applicator while placed on calf was initially measured for each subject to ensure appropriate operating frequency. Figure 8.3 demonstrates the in *in-vivo* protocol for Applicator I. The experiment procedure consists (i) Placement of applicator and initialisation of NIRS probes, (ii) begin NIRS measurement at rest for 180 seconds, (iii) followed by microwave warming for duration of 5-minutes and (iv) stop microwave warming and maintain rest duration for additional 5-minutes.

Figure 8.4 illustrates the time versus measured haemoglobin concentration of subject (a) one, (b) two. For both subjects, the concentration remained at a stable level during the initial 1-minute of rest, which is expected as no temperature difference introduced. During the 5-minute microwave exposure period, the ΔHbO_2 and ΔHbT increased, caused by the temperature elevated in the tissue. In contrast, no distinct changes in the measured deoxy-heamoglobin concentration (ΔHHb) during microwave

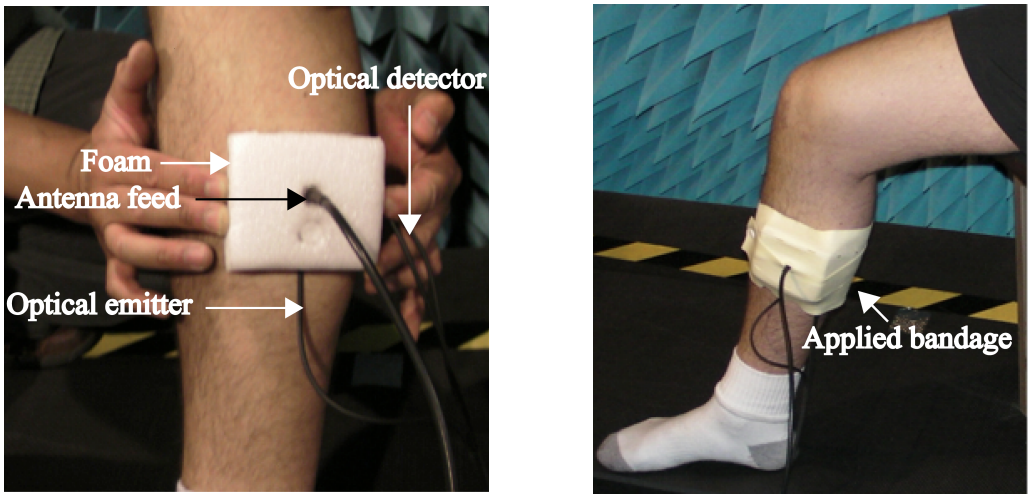

(a) (b)

Figure 8.2: Measured fat thickness on subject calf using ultrasound imaging. (a) relaxed muscle, (b) contracted muscle

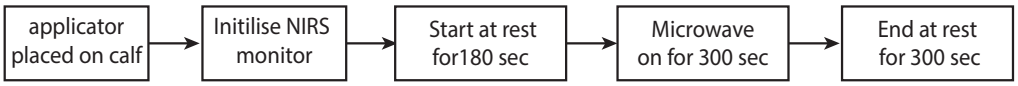

Figure 8.3: *in-vivo* Applicator I protocol

exposure, indicating, the vasodilation occurs in the arterial blood vessels. The thermal response of the subject was estimated from the ratio between concentration increase and the time duration of microwave exposure (5-minutes), hence the gradient of the best-fit line fit for ΔHbT The response value (7.7×10^{-3} μ M/s)can be used to compare the physiological changes between different subjects. After the microwave was turned off, the ΔHbO_2 concentration further increase for approximately 70 seconds, at which thermal equilibrium is reached. This observed delay is defined as "latency". The heat stored in the tissue from the exposure, takes longer time to dissipate before reaching the original state, therefore, the blood vessels remained dilated. The subject blood perfusion continues to take the local heat away until the temperature approaches to normal state. Consequently, ΔHbT began to drop as a result of the constricted blood vessel. The latency can be defined a function of perfusion and thermoregulation process. The estimated data for both subjects are listed in Table 8.1.

The measurement were repeated for subject two as depicted in Figure 8.4b. The measurement have identical general response to the first subject, wereΔHbO_2 and ΔHbT both increases during microwave exposure. Moreover, ΔHHb decreases dur-

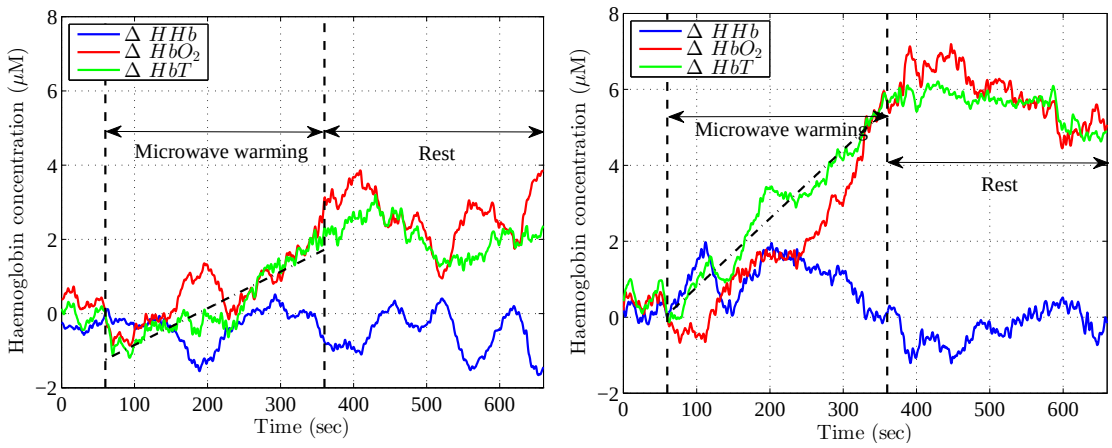

Figure 8.4: Measured haemoglobin concentration during 5-minutes of Applicator I microwave warming on human calf. (a) subject one (b) subject two

ing the exposure, which also indicate arterial dilation. The estimated thermal response of subject two is larger than that of subject one, by almost about twice the difference between the two measurements. This can be the explained by the different physiology between the subjects. The other factor is the fat thickness difference, subject two has fat thickness of 5.0 mm, in contrast to 6.8 mm to the subject one. This can be explained by the fat thickness study of microwave applicator in Chapter 6, were larger EM energy is deposited in the deep tissue as the thickness decreases. Therefore, this is a possible influence of deep tissue warming combined with the already measured microcirculation of the skin layer. The estimated latency of ΔHbT for subject two was about 69.5 seconds before the response has dropped, which was approximately equivalent to subject one.

The NIRS system used for Applicator I utilises SRS. Therefore, additional measurements were obtained, and they are TOI illustrated in Figure 8.5a and nTHI in Figure 8.5b of both subjects. Tissue Oxygenation index of both subjects shows, various oscillations which are random even during microwave warming. In contrast, the measured nTHI of both subjects decreases with the applied microwave warming. This suggests a reduction in blood volume, which contradicts the haemoglobin concentration measurement. The normalised haemoglobin index is calculated based on attenuation slope measured by the two spaced detectors. Therefore, decrease in nTHI means high optical attenuation in the first detector(shorter spacing to the emitter). This only occurs

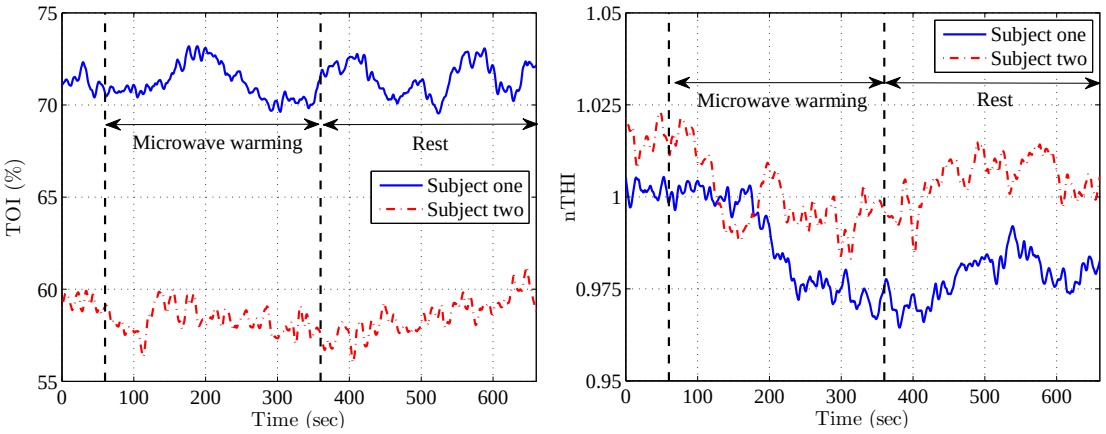

(a) (b)

Figure 8.5: Measured TOI and nTHI of two subjects during 5 minute of microwave warming on human calf. (a) TOI % (b) nTHI

Table 8.1: Measured results for subject one using Applicator I

Subject	Fat layer thickness (mm)	Thermal response ΔHbT (μM/s)	Latency (sec)
1	6.8	7.7×10^{-3}	70
2	5.0	18.0×10^{-3}	69.5

when the local blood volume dilation is closer to the detector,, which is dominated by the superficial heating. The nTHI calculation also indicates; subject one had the larger decrease. This can be explained by the increased fat thickness, which promotes superficial heating, this was previously evaluated in the EM simulation study of fat thickness in Chapter 5 Section 6.5.3.

8.3 *In-vivo* Applicator II

The protocol procedure for Applicator II was altered by introduction of LDF monitor, which was not used simultaneously with NIRS measurement. Figure 8.6 shows the protocol used for the study of Applicator II on three participated human subjects. Initially, the hybrid applicator was first placed on a subject's calf shown in Figure 8.7. The microwave applicator was switched off while the monitoring systems, including the NIRS/laser Doppler and skin temperature sensors, were on for just monitoring pur-

pose. The skin temperature decreased from approximately 32.5 °C to about 29.7 °C depending on room temperature. This was another evident demonstration of the applicator passive cooling, which was illustrated in Appendix C Figure C.5. There were also fluctuations of the tissue oxygenation signals ($\Delta HbO_2/\Delta HHb/\Delta HbT$) at the start of rest duration caused by the unsettled haemodynamics in the tissue. After both the skin temperature and the tissue oxygenation signals became stable, the experiment then began. The measurement for each subjects is classified into microwave warming with and without skin cooling. Therefore, for each set of result the experiment was repeated with different optical monitoring system. In the first experiment, LDF monitor was used to measured the skin blood flow as the NIRS system was turned off to avoid optical light interference between the two systems. The experiment is the repeated again with the NIRS system to measure tissue oxygenation signals. The result is bases on the following protocol: (i) 3 minutes of rest time is recorded and the skin temperature at this point was used as a reference for cooling experiment, followed by (ii) 5-minutes of microwave warming, and (iii) 4 minutes of rest duration with microwave warming off.

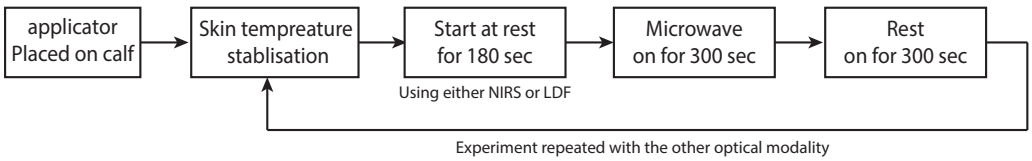

Figure 8.6: *in-vivo* Applicator II protocol.

Figure 8.7: Applicator II placement on human calf for *in-vivo* measurement.

8.3.1 Subject One

Figure 8.8 shows the results of two independent experiments for subject one in terms of flux, which is a relative measure of the skin blood flow in an arbitrary unit obtained by the laser Doppler flowmeter. Figure 8.8a shows LDF measurement without skin cooling, while Figure 8.8b is the result for the same experiment with active cooling. In both measurements, the baseline skin perfusion was stabilised during rest duration, with marginal decreases over time caused by the minor reduction in skin temperature. The starting skin temperatures of both experiments at around 30.0 °C. During the microwave exposure, the result without skin cooling shows rapid change flux caused by the dilation in capillaries, and hence skin microcirculation. After 5-minute of exposure, the peak temperature approached 34.2 °C. When the microwave was turned off, the perfusion and skin temperature began to drop rapidly as the heat being regulated until approaching to original state over 5-minutes of rest duration. This result indicates any measurement obtained by NIRS without cooling is expected to be influenced by skin perfusion. The experiment was repeated with same subject with use of active shown cooling in 8.8b. During the microwave exposure the skin temperature varied within 1.0 °C over time, showing the effectiveness of the skin cooling system when the skin temperature exceeded the preset threshold temperature. The flux signals during microwave warming were also stable. The stability of flux signals and skin temperature suggests that the active cooling system has partially mitigated the hot spots on the skin caused by the microwave applicator and subsequently prevented the skin blood flow from significant changes. The peak temperature was maintained at around 30.0 °C during warming, where the starting temperature was 29.8 °C. This was an increase of just 0.2 °C. In contrast, without cooling the skin temperature was raised by about 4.1 °C. The following step is to repeat the experiment with use of NIRS monitor.

Figure 8.9 shows tissue oxygenation changes in the tissue in terms of $\Delta HbO_2/\Delta HHb/\Delta HbT$, for two repeated experiment (a) without active cooling (b) with cooling. The measurement without cooling in Figure 8.9a shows ΔHbO_2 and ΔHbT gradually increases while ΔHHb decreases during microwave exposure, indicating arterial warming. After the 5-minute exposure, the haemoglobin concentration rapidly decreases as the temperature return to original state. The latency was just under 10 seconds, in contrast to 70 seconds of the previous applicator. This big difference

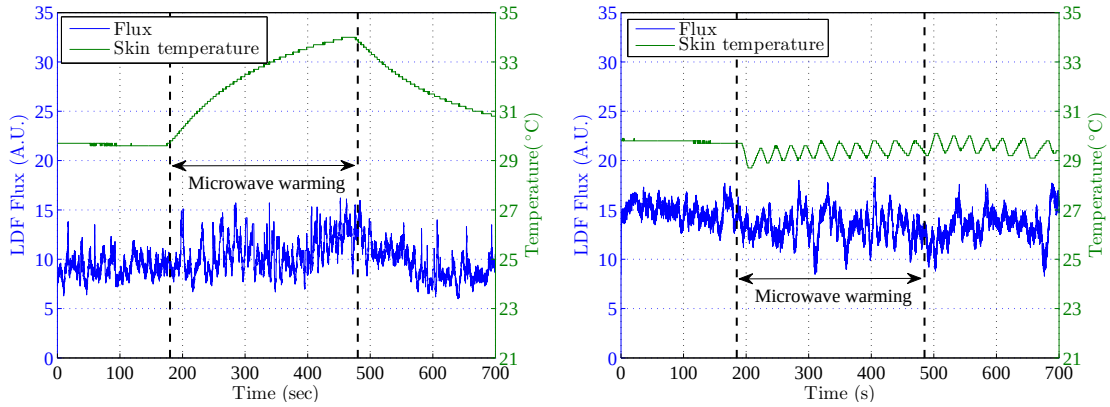

(a) (b)

Figure 8.8: Measured flux and skin temperature with 5-minutes of Applicator II microwave warming for subject one. (a) without active cooling (b) with active cooling

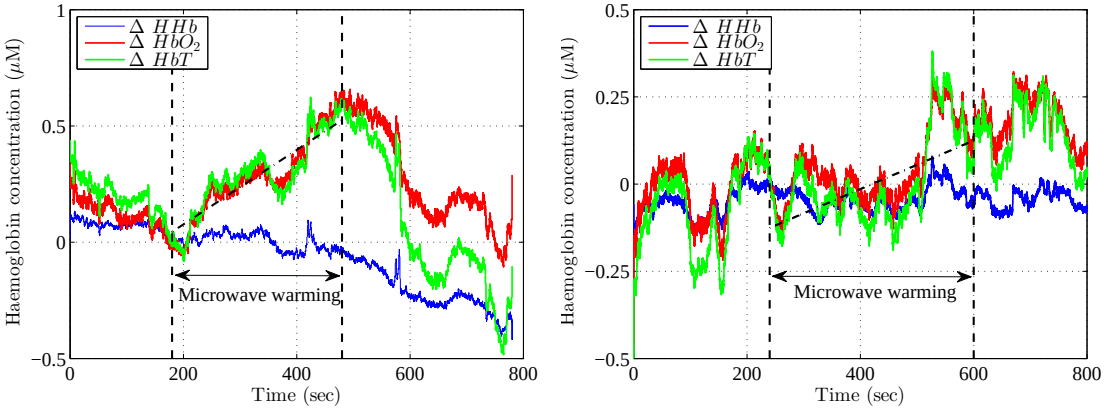

(a) (b)

Figure 8.9: Measured haemoglobin concentration during a 5-minutes of Applicator II microwave warming for subject one. (a) without active cooling (b) with Active cooling

was caused by the foam housing and warping of the Applicator I, which keeps tissue temperature warm for longer duration. Applicator II uses HTC superstrate, which increases heat dissipation. The experiment results with active cooling is depicted in Figure 8.9b, showing unchanged characteristics in haemoglobin concentration for about 4 minutes of microwave exposure. The microwave exposure was extended for an additional 1-minute to some physiological changes, which was just about 0.25 μM/s The thermal responses were obtained and listed in Table 8.2. This marginal increase is resulted by the skin cooling which constricts the blood vessels and muscle dilation in deep tissue. The physiology overcomplicates when the accumulation of cooling

Table 8.2: Measured results for subject one using Applicator II.

Condition	Initial temperature (°C)	Peak temperature (°C)	Thermal response ΔHbT (μM/s)	Latency (sec)
NC	30.1	34.2	1.67×10^{-3}	30.0
SC	29.8	30.0	0.78×10^{-3}	10.0

and heating introduces. It is difficult to predict if the marginal increase was caused by muscle dilation and therefore, further measurements are required.

8.3.2 Subject Two

The protocol was repeated for Subject two, and LDF results are shown in Figure 8.10. During the 5-minutes of microwave warming the skin temperature peaked at 34.0 °C, and the measured flux were fluctuating from baseline of 7.0 (A.U) to 22.0 (A.U). The fluctuation was caused by unknown physiological reasons, which require further study. After the microwave, warming was switched off, the temperature and flux gradually decreased to original state. The second experiment based on same subject, but with active cooling is demonstrated in Figure 8.10b. The protocol and applicator placement remained the same. The starting skin temperature was at the steady state of 29.8 °C, and during microwave, warming it was fluctuating ($\pm$0.4 °C) under the set point temperature. The temperature oscillation is a resultant of thermostatic temperature control. The flux result shows a small increase in skin perfusion after 3 minutes of warming. This could mean the skin cooling was not sufficient to mitigate skin heating. However, the flux seemed to decrease just before microwave was switched off.

Figure 8.11 shows the corresponding experiment with use of NIRS monitor presented for (a) without cooling and (b) with active cooling. The measured ΔHbO_2 and ΔHbT increases during tissue warming and approaching steady state at about 4 minutes of exposure. The changes in ΔHbb is of similar response but at minimal scale. This contribution of response is from venous dilation; however, the increase in oxyhameoglobin was greater which, indicates the largest portion is from arterial warming. The thermal response of subject two was higher than subject one as it did with Applicator I study, which was explained by the difference of fat thickness. Moreover,

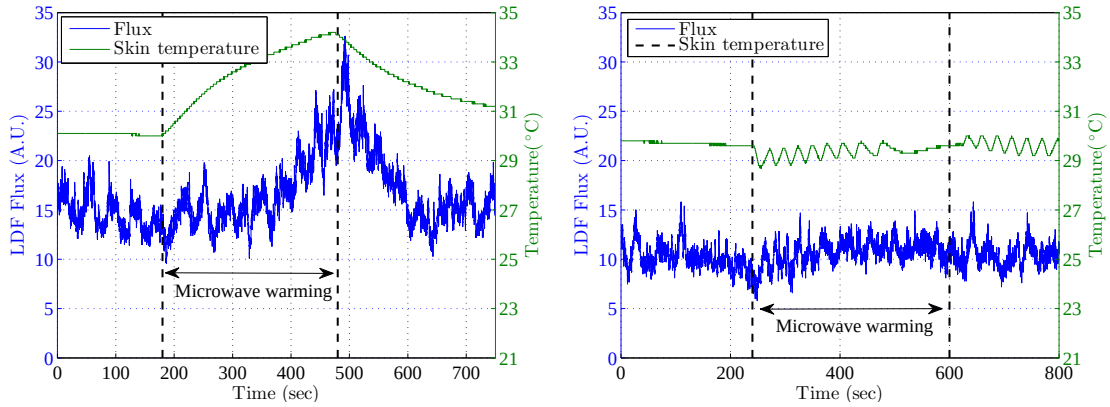

Figure 8.10: Measured flux and skin temperature with 5-minutes of Applicator II microwave warming for subject one. (a) without active cooling (b) with active cooling

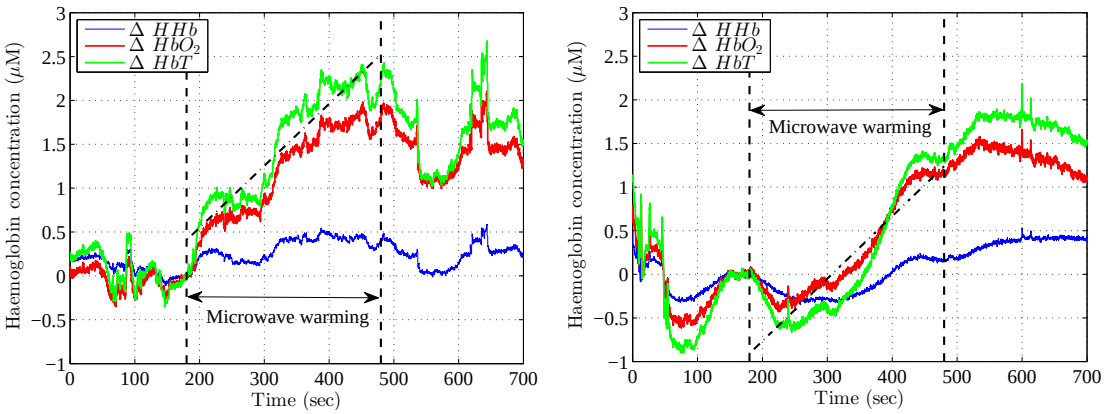

Figure 8.11: Measured Haemoglobin concentration during a 5-minutes of Applicator II microwave warming for subject two. (a) without active cooling (b) active cooling

when the microwave is off the temperature rapidly drops, with short latency, and again consistent with subject one measurement. The results are listed in Table 8.3. The second tissue oxygenation measurement with subject two using active cooling is shown in Figure 8.11b. In the first 3 minutes of baseline recording before the microwave was switched on, there were some natural, spontaneous variations in the tissue oxygenation signals which were typical of NIRS muscle measurement. When the microwave was switched on, both the ΔHbO_2 and ΔHbT signals, and to a lesser degree the ΔHbb signal, went up. This increment shows that the microwave applicator successfully induced warming in the muscle, initiating vasodilation in the arterial blood vessels which carry

Table 8.3: Measured results for subject two using Applicator II.

Condition	Initial temperature (°C)	Peak temperature (°C)	Thermal response ΔHbT (μM/s)	Latency (sec)
NC	29.7	34.0	6.67×10^{-3}	10
SC	29.5	29.7	6.8×10^{-3}	50

more oxygenated blood than de-oxygenated blood. After the microwave was switched off, the ΔHbO_2/ΔHHb/ΔHbT signals continued to increase for another 50 seconds before they began to decrease. It should be noted that even after the microwave was switched off, the skin temperature can increase above the preset threshold due to heat diffusion from the muscle to the skin surface. The skin cooling system was therefore operating during the rest duration for consistent measurement. The thermal responses of both experiments were identical, indicating the cooling was not effective in reducing skin perfusion. This was validated by the thermographic images in Chapter 6 Section 6.6, showing the introduced hot spots was under the NIRS optodes. Consequently, The results for both experiments correspond to complete tissue heating from skin to muscle.

8.3.3 Subject Three

The experiment was repeated with the third participated subject, to verify if the measurement were consistent. Figure 8.12 shows the LDF experiment for with and without cooling as implemented previously. The initial temperature was 29.7 °C and was elevated to 34.0 °C, a difference of 4.3 °C equivalent of other tested subjects. The changes in flux were small in contrast to previous subjects. However, it is observed just toward the end of 5-minutes of microwave exposure. The subject skin perfusion was less sensitive to skin temperature change. During the rest period, the flux and temperature reduced accordingly as expected. The study was repeated with active cooling, where the temperature was held at about 29.8 °C. The measured perfusion shows a general decline of baseline during the microwave warming, and larger flux attenuation was observed only during the warming. This is believed caused by the instantaneous cooling and the warming mechanism producing ripples in flux. When the microwave turned off, the flux increases slenderly to normal state. This result concludes the skin was

constricted, hence the reduction in blood perfusion.

Figure 8.13 shows the tissue oxygenation changes in the localised tissue in terms of $\Delta HbO_2/\Delta HHb/\Delta HbT$ signals. Without cooling, the blood volume increases rapidly with microwave warming, and peaking at the end of the 5-minute exposure identical to the LDF measurement. When RF is off, the decline in ΔHbO_2 and ΔHbT was also rapid, with latency of only 5.0 seconds. The result is identical to previous subject, where the haemoglobin signals are dominated by superficial dilation. The repeated experiment with active cooling in Figure 8.13b shows an increase in concentration signals after 40 seconds of tissue warming. After 18 seconds of switched off microwave, the blood volume immediately began to contract corresponding to the temperature drop in tissue, where the cooling was not influenced by. The thermal response with active cooling was surprisingly larger by 1.4 $\times 10^{-3}$ μM/s than the measurement with just tissue warming. It was expected with skin cooling the dilation in superficial layer is reduced and therefore, the measured signals are dominated by the muscle haemodynamics. However, as previously mentioned Applicator II thermographic results indicate hot spots are apparent directly under the NIRS optodes, which has influence to the deep tissue measurement. The thermal response and temperature measurement of subject three is listed in Table 8.4

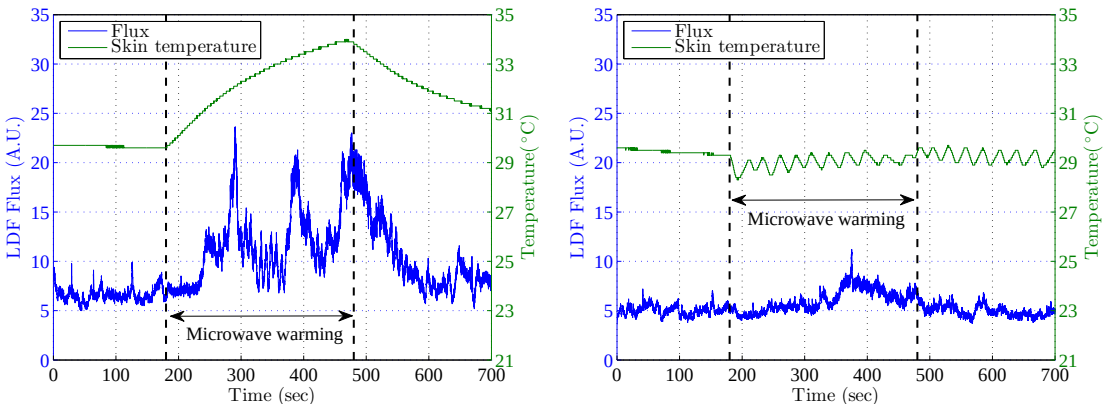

Figure 8.12: Measured flux and skin temperature with 5-minutes of Applicator II microwave warming for subject one. (a) without active cooling (b) with active cooling

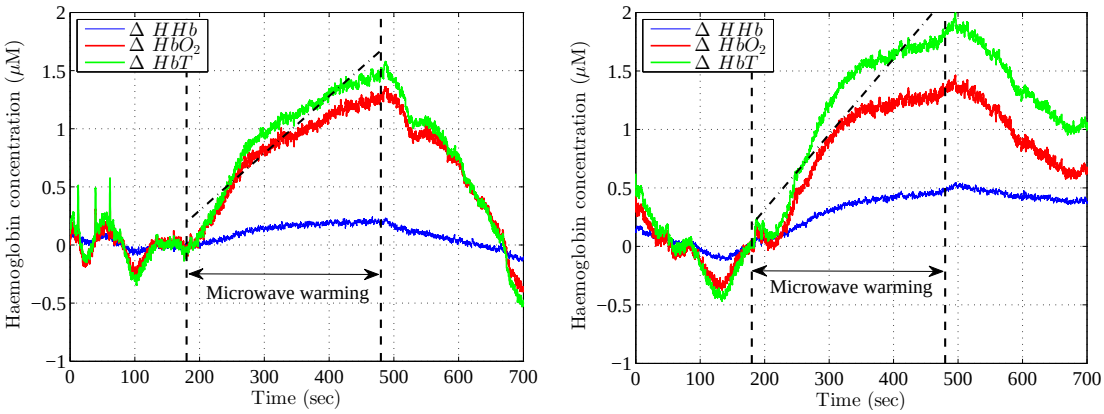

Figure 8.13: Measured haemoglobin concentration during a 5-minutes of Applicator II microwave warming for subject thre. (a) without active cooling (b) active cooling

Table 8.4: Measured results for subject three using Applicator II.

Condition	Initial temperature (°C)	Peak temperature (°C)	Thermal response ΔHbT (μM/s)	Latency (sec)
NC	29.7	34.0	4.6×10^{-3}	5
SC	29.8	30.1	6.0×10^{-3}	18.0

8.4 *in-vivo* Applicator III

Applicator III was developed to minimise the superficial heating caused by the misplacement of the active coolers. Consequently, the NIRS and LDF signal are expected to be reduced due to the deficiency of skin dilation. The measurement was limited to a single subject with interchanging protocol. The procedure begins with applicator placed on a human calf for about 10-minutes until the skin temperature is stabilised. Monitoring devices starts recording blood flow and skin temperature during the 5-minutes of rest duration. Then microwave is turned on for 60-minutes at 30 dBm (1 watt RMS) RF power for the first set of experiment without active cooling. In the second case the experiment is then repeated with skin over-cooling. The final scenario was based on 15-minutes of exposure at 34.8 dBm (3 watts RMS) with moderate skin cooling (maintaining temperature). After microwave warming is switched off, the monitoring system records the remaining rest duration.

Figure 8.14a, shows the LDF measurement of the subject without skin cooling. The graph shows some fluctuation in flux for the initial 5-minute of rest duration, which may have led by various physiological changes. The skin temperature was stabilised at 29.6 °C during the rest duration. When the microwave warming is activated, the skin perfusion immediately increased with the temperature simultaneously, which could be part of the natural variation. However, after 15-minutes of microwave exposure the flux continues to increase with the elevating temperature until approaching steady state after 55-minutes. The temperature peaked at 33.2 °C. This finding clearly indicates the skin is vasodilated. The microwave was switched off, and it can be seen the temperature and skin blood flow decreases over the time. The experiment was then repeated with skin over-cooling as demonstrated in Figure 8.14b. The set point temperature was 1.0 °C lower than initial temperature. During the rest duration, the flux was sustained and the average skin temperature was maintained during the microwave warming. This indicates the skin cooling mitigated the skin warming, and therefore, skin was not dilated. The temperature was decreased during the exposure as it was expected by 1.0 °C. The microwave and cooling system were then turned off, which caused the temperature to rapidly increases by 3 °C (at 4,000 seconds). This was caused by the Peltier cooler hot junction diffused to the cold junction when the cooling system are disabled after long operation. Incidentally during this external resistive heating in rest time, it can be seen the skin blood flow has increased with the respect to the change in temperature. This result is significant as it can verify during the 60-minute of microwave warming the skin was not dilated, and therefore, the muscle warming will be more effective.

The experiments were repeated on the same subject but with use of NIRS, the measured results are illustrated in Figure 8.15. In the first case illustrated in Figure 8.15a was without skin cooling. The temperature and the haemoglobin concentration signals were stabilised in the initial 5-minute (rest time) followed by microwave warming. The skin temperature noticeably increases from the initiation as it was demonstrated previously in Figure 8.14a. However, ΔHbO_2 and ΔHbT concentration increased only after the 12-minutes of microwave exposure at which the temperature was elevated by about 2.5 °C. In contrast, the previous LDF measurement had a large natural variation at the start, and only 12-minute of exposure, the increase was rapid and identical to the NIRS measurement. Both results are in agreement and clearly demonstrating

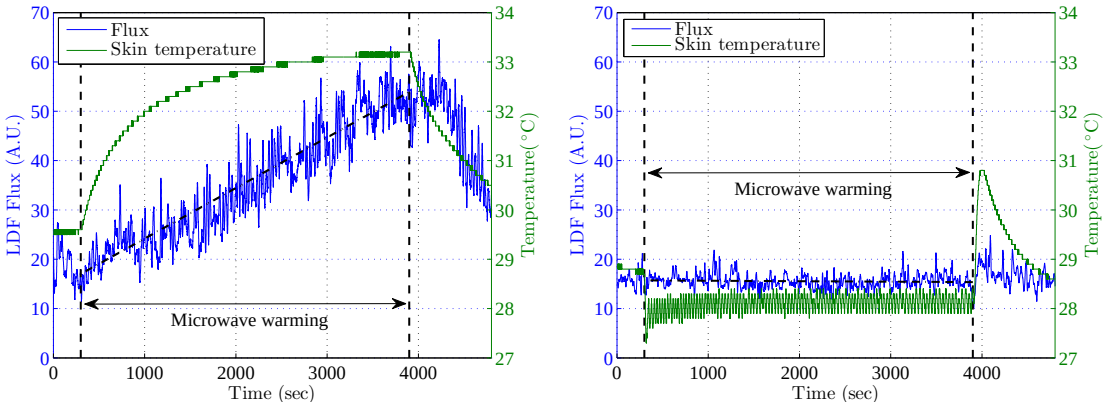

Figure 8.14: Measured flux and skin temperature with 60-minutes of microwave warming using Applicator III (1 watt). (a) without active cooling (b) with active cooling

the NIRS response was primarily from skin vasodilation. The ΔHHb concentration decreases during the microwave warming indicating an increased blood flow in the tissue. The blood volume gradually returned to initial state during the final rest duration when tissue warming was turned off. The measured thermal response in Table 8.5 is 0.83 $\times 10^{-3}$ μ M/s, which is lower than previous measurement by the factor of six to nine times due to the low RF power. The latency was not applicable for these experiments, because the temperature and the NIRS measurements have reached the steady state before turning microwave off. The procedure was repeated with active skin cooling. Figure 8.15b illustrates the NIRS signals for microwave exposure on the subject calf with skin over-cooling by approximately 1°C below the initial temperature. The corresponding ΔHbO_2 and ΔHbT concentration has decreased with respect to the microwave warming while deoxy-haemoglobin was relatively stable. The estimated thermal response as shown in Table 8.5 was -0.08 $\times 10^{-3}$ μ M/s, which is unlike the previous NIRS responses, were the blood volume generally increase even with skin cooling. This behaviour is known when the arterial vessels are vasoconstricted, which can be expected when tissue is cooled. This physiological effect is masking the haemodynamics changes from deeper tissue, and therefore, it is unknown if the muscle was dilated. In Chapter 6 Section 6.7, it was illustrated in the simulation studies, the muscle temperature was increased despite skin over-cooling, and it was verified with thermal images of the skin. After microwave warming is turned off, ΔHbO_2 and ΔHbT stopped

decreasing but rather began to fluctuate. In contrast, ΔHHb remained fairly stable.

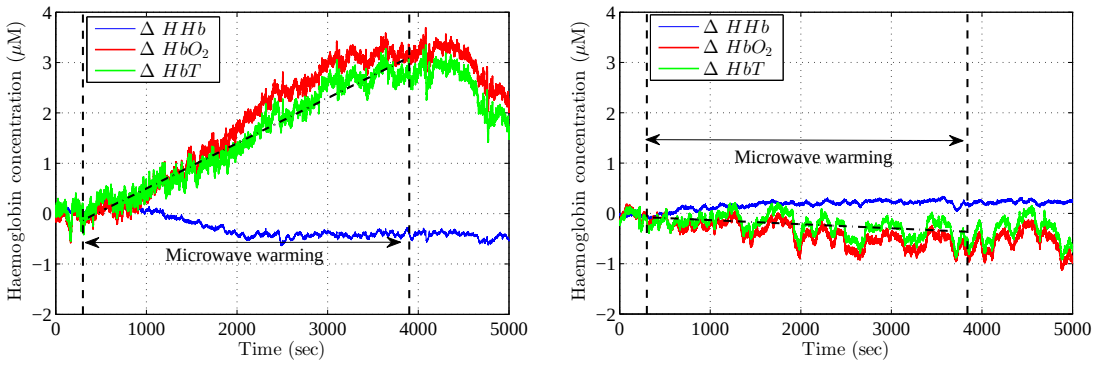

Figure 8.15: Measured haemoglobin concentration during a 60-minutes of Applicator III microwave warming (1 watt). (a) without active cooling (b) active cooling

Table 8.5: Measured results for subject one using Applicator III.

Condition	Initial temperature (°C)	Peak temperature (°C)	Thermal response ΔHbT (μM/s)	Latency (sec)
NC	29.6	33.2	0.83×10^{-3}	NA
SC	28.8	30.8*	-0.08×10^{-3}	NA

* Peak temperature after microwave was switched off.

Figure 8.16 shows the NIRS measurement with moderate skin cooling set at 0.2 °C below starting temperature. The output microwave power was increased to 3 watts for shorter exposure duration to minimise excessive muscle heating. The initial 3-minutes of microwave warming shows a decrease in haemoglobin concentration, which was caused by the initial triggering of the skin cooling. For the remaining 12-minutes of microwave warming, ΔHbO_2 and ΔHbT concentrations have increased steadily above the baseline opposing to decreasing ΔHHb The change in blood volume was about 0.5 $\times10^{-3}$ μ M/s, which is about three to four times smaller than the previous measurement (Applicator II) with skin-cooling. Subsequently, The new cooling geometry in Applicator III is effectively minimising skin dilation. This also implies, that the blood volume changes in deeper tissue was possibly the dominant factor in this measurement, where the skin was not over-cooler or warmed up as previously. After microwave is

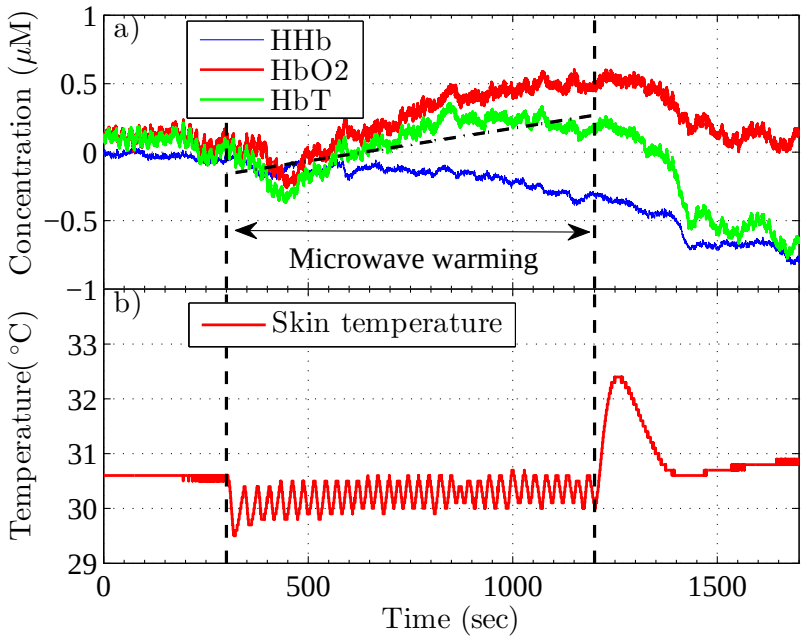

Figure 8.16: Measured haemoglobin concentration during a 15-minutes of Applicator III microwave warming (3 watt) with moderate skin cooling

switched off, ΔHbO_2 concentration decreases and returns to original state, where as ΔHbT ΔHHb continues to decrease. This effect might be the response to the resistive heating produced when the cooling system is switched off, by which the skin is warmed. The duration is about 5-minute at which temperature rise and return to original state.

8.5 Chapter Summary

This chapter introduced the procedure and the results of the *in-vivo* study. The results were presented and discussed accordingly for the first two introduced applicators. As part of aim of this project, detecting thermal response induced by microwave warming was achieved in Applicator I measurement The result clearly shows a rapid increase in the local blood volume when microwave warming was on, and hence dilating the blood vessel. The study on two human subjects was analysed based on identical protocol, at different fat thickness. The result illustrated an increase oxy/total-hameoglobin concentration for the subject with thinner fat thickness. This study coincides with the preliminary EM simulation result, indicating larger muscle warming is achieved with thinner superficial tissue layers. This was an early indication of deep tissue warming, and thermal responses were measured and presented for each subject.

Applicator II was introduced for additional *in-vivo* investigation on three human subjects. The thermal responses of the first two subjects were conclusive with the results of Applicator I. The measurement showed subject two with thinner fat thickness had a larger thermal response in both scenarios with and without cooling. Subject three NIRS signals also responded to the microwave warming, particularly when cooling was used. The addition of LDF monitor indicates the cooling system was sufficient in reducing local superficial dilation. However, the thermal measurement from previous chapters shows that the NIRS signals are still likely to be dominated by skin heating introduced under the optodes of NIRS.

Applicator III was introduced for brief study using alternative protocol, to investigate the hybrid system operation over longer duration and with efficient skin cooling. The results indicates, the tissue can still dilate under lower microwave power. Microwave exposure over longer duration allowed the temperature and the haemoglobin concentration to reach the steady state before turning it off. The measurement with skin over-cooling causes the blood flow in the superficial layer to constrict and therefore ΔHbT concentration was decreasing during microwave warming. The muscle response was masked by this effect. The final experiment with standard cooling protocol, proved to be an essential result. This measurement indicates the skin dilation was reduced by four times of the previous applicator design, and demonstrating the muscle response is considerably smaller than the superficial layers. These results demonstrate different approaches and methods to minimise skin perfusion. Consequently, this also agrees with the theory, were the skin perfusion is significantly larger than deeper tissue and possibly faster response to environmental changes.

Chapter 9

Conclusion and Future Work

9.1 Summary of Findings

The work presented in this thesis involves multi-disciplinary prospective of RF engineering in the medical field. The aim during the PhD, was to develop a novel non-invasive probe to investigate the human thermoregulation, with particular interest in the muscle responses. An effective heater is one crucial component of a thermoregulation monitor. The current commercial solution is a simple resistive skin heater which has limited penetration. In this work, a tissue warming has been proposed by exploiting microwaves to induce heat in the tissue, including superficial and deep tissue. An optical NIRS probe has also been integrated with the microwave applicator to monitor tissue oxygenation changes in the tissue in response to local warming. All developed applicators were based on microstrip antenna design, for ease of fabrication and compactness. Various microstrip applicator designs were developed in this thesis, primarily aimed at improved coupling and skin heating reduction by specific applicator design and the use of active cooling. Each applicator was modelled and fabricated for thermal validation and *in-vivo* study. The probe was controlled by the developed hybrid system, which included microwave, cooling and NIRS system. The microwave system was fully functional, delivering the desired power to the applicator, while monitoring the operation for predefined safety mechanism. In later stages, LDF probe was introduced for additional monitoring of skin perfusion alone. This served as a validation tool to confirm the blood volume increase in NIRS signals were dominated by superficial or deeper tissue.

In the development stage, the interaction of EM fields in the biological tissue has been modelled to optimize the applicator coupling to the skin, which directly affects the penetration depth of EM energy and reduction of superficial heating introduced by the standing waves. The simulation study showed that the superstrate thickness can significantly alter the SAR pattern and particularly coupling the energy into the tissue. For a deep and uniform SAR deposition, the simulations suggested a superstrate thickness of 5.0 mm, the absorption spreads across the tissue, rather than localized spots at the fat / skin interface. Thicker superstrate, meant the applicator operating at the radiative near-field region, where the E-field components are tangential to the tissue, and hence enhancing penetration depth. In contrast, thinner superstrate causes the interaction with the tissue at the reactive region, where the fringing fields at the radiating

edges are perpendicular components to the tissue, and therefore, producing hot spots in the superficial layer. Regardless, Applicator I was used for preliminary study of general tissue heating. Therefore, a superstrate of 1.58 mm was opted for the developed applicator with appropriate output power to ensure the warm spots are controlled. The thermal simulation result shows that the temperature in the muscle can be elevated by about 4 °C, also the skin and fat layers were warmed up as well, causing blood volume to increase in all layers. The applicator was fabricated, and the measured S-parameter indicates that a 100 MHz shift in resonance frequency, the discrepancy was due to the composition of patient tissue thickness with respect to the simulation modelled. With applicator was developed, a validation medium was required. This was achieved with the fabricated tissue phantom, which mimics the electric properties of biological tissue at 2.45 GHz. The developed phantom consisted of multi layers, including, skin, fat and muscle. The dielectric properties of each layer were verified against the parametric model developed in the literature. The phantom electrical properties were nearly identical to the biological tissue. However, the thermal characteristics remained undiscovered. The mimicked tissue was then used to validate and calibrate the thermal simulation model for the developed applicators. The *ex-vivo* thermographic images showed identical thermal distribution to the numerical study. Moreover, muscle warming was demonstrated as well as to skin hot spots.

The developed Applicator II, was based on annular ring microstrip antenna with increased bandwidth and reduced radiating element size. The new design uses HTC substrate material, active cooling elements and LDF monitor. The thermal simulation and measurement on human phantom both indicate reduction of superficial warming by about 4.0 °C of the Applicator I. The thermographic measurement showed the cooling was not efficiently reducing skin hot spots due to the geometrical placement of Peltier cooler. The superficial hot spots are located under the optodes. Consequently, Applicator III was introduced to enhance cooling efficiency by placing TE cooler on the same axis as the radiating edges. The thermal measurement showed skin temperature with active cooling was reduced from 36.8 °C of Applicator II to 33.2 °C with the updated design. While the cooling effectively reduced skin heating, the muscle temperature was sufficiently higher for deep tissue dilation. All linear polarised applicators showed a consistent validation with the numerical study, often there are fluctuation at about

1.0 °C caused by the room-temperature change during each experiment. Applicator III operation was also verified with the *in-vivo* study. The measured results showed the skin dilation was eliminated with the use of skin over-cooling. In contrast, it the temperature was only minimised when using standard cooling protocol. The analysis have showed the skin dilation dominates all other responses particularly from deeper tissue due to the increased blood perfusion in the superficial layer. Therefore, the changes in haemoglobin concentration in the final measurement was marginal, indicating the response could have been dominated by the arterial vessels within the muscle. Despite the effective cooling, we still believe superficial warming was not completely eliminated (in a cooling standard protocol), thus a large-scale investigation is required to verify these studies.

While the focus was on active cooling to reduce skin hot spots, an alternative approach was introduced using circular polarisation. CP Applicator was developed for distributing the EM field in all directions, therefore, reducing peak absorption in a particular region. The developed applicator was based on single-fed CP microstrip design. The early numerical analysis indicated the superficial peak SAR was reduced by approximate 28.8 % when using CP applicator. As with previous design the antenna was validated on phantom, and human subjects. The measured skin temperature was 32.30 with active cooling, which was an indication of superficial heat reduction. On the contrary, the major restriction of single fed-CP was the limited impedance bandwidth. For optimal operation, the input reflection coefficient was measured before each experiment, to spot the intersection between the two modes (CP excitation). The performances of all developed applicators are listed in Table 9.1 for *in-vivo* experiment and Table 9.2 for the phantom measurement. This result clearly shows the development process, where superficial heat is being reduced from one applicator to another. However, the bandwidth and operating frequency was enhanced between each model converging to the required operating frequency of the 2.45 GHz ISM band. SAR ratio of muscle to skin is also listed in table for contrasting current and original numerical models.

The purpose of applicators was to introduce dilation to local tissue, for optical monitors to measure the changes. The oxygenation result has validated the operation of the applicator. The thermal response indicated that an increase in blood flow due

to the microwave heating. However, the skin hot spots in applicator I contribute to the obtained oxygenation measurements. Since NIRS measurement is more sensitive to changes in the superficial layer, therefore, the measured thermal response was predominantly due to the change in skin blood flow. The two investigated subjects had distinctive physiological responses, which partially caused by the difference in fat thickness. This was an early indication of muscle response, as lower fat thickness will increase thermal response due to larger EM penetration in deep tissue. Experiment trial was repeated for Applicator II with the incorporated skin cooling system which can reduce superficial hotspots caused by the microwave warming. In addition, a temperature sensor and a laser Doppler probe were also incorporated with the applicator. The hybrid monitor was used for *in-vivo* human experiment on calf. The LDF result showed a decrease in microcirculation during microwave warming with active cooling. However, the LDF and temperature measurement is located at the centre of the applicator. Therefore, the measurement is only valid for localised region. Based on those reasons, the measured NIRS signals (ΔHbO_2/ΔHHb/ΔHbT) with and without skin, cooling had large thermal responses, subsequently the vasodilation was also in all tissue layers. All the obtained measurement indicated the hybrid system can successfully induce heat into the muscle and simultaneously can be detected along with the superficial blood volume. The new developed applicators will be used to reduce the skin dilation, with its effective cooling technique.

Table 9.1: Overall measured and simulated applicator results

Applicators	**f_o (GHz)**	**BW (MHz)**	**Power (W)**	**Duration (Sec)**	**Peak SAR Simulation (W/kg)**			**Peak tempreature of simulation with biological heatagainst measurement on human calf (in-vivo) (°C)**					
								Without skin Cooling (NC)			**With Skin Cooling (SC)**		
					Superficial	Muscle	Ratio of peak superficial SAR to muscle %	Simulated Skin	**Measured Skin**	Simulated Muscle	Simulated Skin	**Measured Skin**	Simulated Muscle
Applicator I	2.55	100.00	5.00	300.00	24.10	22.00	91.29	42.50	**NA**	41.30	NA	**NA**	NA
Applicator II	2.53	160.00	3.00	300.00	57.00	49.20	86.32	41.00	**41.00**	43.00	37.00	**36.80**	41.25
Applicator III	2.44	168.00	3.00	300.00	54.40	38.50	70.77	37.60	**37.00**	41.80	33.30	**33.20**	40.40
CP Applicator[1]	2.51	20.00	3.00	300.00	52.50	50.35	95.90	38.00	**37.20**	43.40	35.00	**32.30**	41.70
Applicator I[2]	2.44	NA	3.00	300.00	29.66	12.80	43.15						
Applicator II[2]	2.45	NA	3.00	300.00	70.00	27.10	38.71						
Cp Applicator[2]	2.40	NA	3.00	300.00	49.80	27.17	54.56						

[1] Un-optimised CP operation with current model of 1.0 mm skin and 10.0 mm fat thickness

[2] Simulation model optimised for orignal model of 2.0 mm skin and 10.0 mm fat thickness

Table 9.2: Measured and simulated thermal results of all developed applicators on phantom.

Applicators	**Peak tempreature of simulation against measurement on phantom (ex-vivo) (ºC)**							
	Without skin Cooling (NC)				**With Skin Cooling (SC)**			
	Simulated Skin	Measured Skin	Simulated Muscle	Measured Muscle	Simulated Skin	Measured Skin	Simulated Muscle	Measured Muscle
Applicator I	32.00	**33.00**	25.00	**24.80**	NA	**NA**	NA	**NA**
Applicator II	31.00	**31.00**	27.30	**27.00**	27.00	**27.60**	25.10	**25.60**
Applicator III*	30.60	**31.00**	27.50	**27.00**	27.00	**26.00**	27.00	**26.00**
CP Applicator	31.00	**31.50**	28.20	**29.10**	27.00	**26.00**	27.00	**26.00**

* Measurement were recorded 7 months after the fabrication of phantom

9.2 Future Work

The experience gained from the carried out work in this thesis is invaluable, and consequently, can be used to highlight the prospective development of the hybrid system. This section discusses some of the upcoming and future development of the system which is sub divided accordingly.

Applicator

- Further investigate the use of thicker superstrate layer at 3.5 to 5.0 mm. This essentially allows for uniform deposition of EM energy since it will be operating in the radiating near field. In this configuration, a TEC module can be placed right at the centre of the applicator for equally even cooling distribution. The obvious limitation of this configuration is the increase of thermal resistance, hence the requirement of in-depth study on the efficiency of the cooling in this method with higher HTC material.

- Applicator III showed a potential of mitigating skin temperature. However, the feed point and transmission line had an influence to the elevating skin temperature. This problem can be resolved by either increasing superstrate thickens or by increasing substrate dielectric properties to confine the fringing field within the medium. The SAR deposition will also be enhanced by this approach, as the transmission line is not radiating to the tissue.

- CP Applicator has a potential if multi-feed approach is adopted. This can be implemented with exploitation of transmission approach used in Applicator III. Dual-fed transmission line can be implemented to provide consistent CP excitation regardless of tissue thickness. This is achieved with two orthogonal inset transmission line with the coaxial feed point can be implemented from the side of the applicator to provide larger surface area for the TEC placement.

- The leakage power was relatively low and under the standard. However, microwave absorbing material will be added inside the applicator to reduce leakage to the patient and interference to other devices.

- Developed applicators may require SAR validation in the future, for deeper understanding and validation to the simulation model. This step is essential in ver-

ifying the absorption caused by the feed point, where it is expected to be significantly higher than simulation.

- The applicator placement on human calf, provided some discomfort to the subjects from the straps. Additionally, on some occasion the applicator placement was not even on the surface, where one strap is tighter than other. This could introduce air gaps between applicator and tissue, where the undesired effect may occur. This was just recently resolved with the use special calf wrap that covers the applicator for even placement to human subject as shown in Figure 9.1.

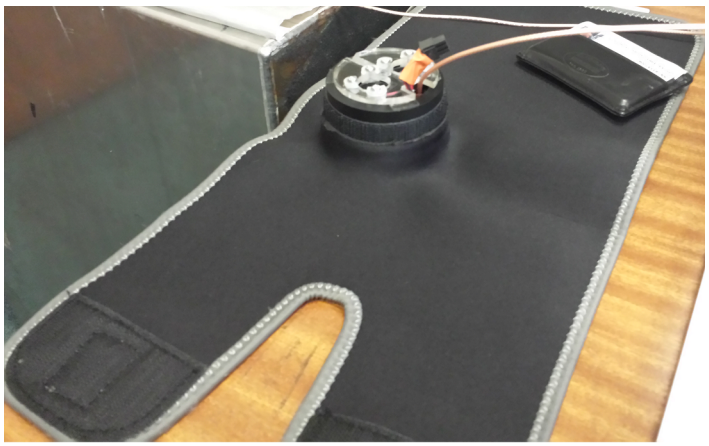

Figure 9.1: Applicator embedded into a calf wrap.

Cooling system

- The current system is based on thermostatic approach, which has its limitation with the continues temperature variation (hysteresis) of 1 about 1 °C. This can be mitigated with use of PID controlled for gradual applied cooling. This is already in working progress, where H-bridge MOSFET configuration is currently added to control the TEC. Therefore, only PID program will be implemented on the microcontroller.

- One of the limiting factors of the cooling system, is the feed back temperature which is allocated at the centre of the applicator. The cooling system aims to maintain the skin temperature at that specified local region. Consequently, For sufficient monitoring and cooling the temperature probe needs reallocation in a more effective region. Furthermore, investigate other techniques with an embedded SMD thermistors to the superstrate or by optical thermometry.

- Dividing the peltier coolers into smaller multi elements array configuration will provide a configurable cooling. This is useful to cover the entire region of the applicator, and each element can be configured to specific cooling power with respect to geometry and the microwave heating pattern.

RF system

- The system requires RF isolator for protection from high-power reflection when the applicator is not matched to tissue. This can be easily integrated between the bi-directional coupler and applicator.

- Calibrated VSWR measurement, which can be achieved by collecting all series of measurements of terminated cable, just terminated system to eliminate the standing wave produced by the cable. In addition, real time system response is measured and can be a self-correction by data processing.

- From our studies, we have never surpassed output power of 5 watts RMS. Therefore, RF system could be miniaturized with selection of low gain power amplifier and system integration onto single PCB.

- Embedding the user interface to LabView is an essential step to combining simultaneous operation of microwave and optical systems.

Optical system

- The operation of NIRS and LDF monitors cannot be used simultaneously at the same time, which is caused by the light interference. This can be mitigated by sampling the lasers of each system accordingly to prevent such interference.

- The current NIRS system is based on a simple CW with the single detector at predetermined separation. Deploying NIRS system based on SRS would be an interesting for enhancing validation and understanding of the hybrid system concept. This allows to include several detectors spaced accordingly for blood volume measurement at different depths. This technique can be used for.

- The LDF monitor provides an indication of skin perfusion by a measure of blood velocity. The data cannot be fused with the NIRS measurement as it is completely

irrelevant. However, an added expansion to the used LDF system (moorVMD-OXY) will allow the same probe configuration to monitor the skin oxygenation as well as the perfusion. This could be useful for directly comparison of skin oxygenation with the deeper measurements obtained by the NIRS. This will provide further insight of blood volume contribution from the muscle.

Protocol

- The majority of studies have been focused on short duration of 5-minutes of microwave exposure. It is important to understand human physiological respect to the induced warming and duration. We are currently exploring other protocols such as operating at approximately one hour of exposure and with just 1 Watt of RF power. Change in protocol requires adaptation of RF and cooling power levels until optimum solution is met.

- Larger clinical trial with at least 20 subjects is required for statistical analysis and allows for further evaluation of different parameters, including age, gender and placement of the applicator.

- Distinguishing core applicator, as have been discussed previously this technology can be used already used for diagnostic of superficial layers in many clinical areas. However, we are aiming at deeper tissue studies such as with free flap reconstruction and perhaps other domains might be promoted after larger-scale trials.

Appendix A

Phantom Preparation

The general phantom preparation procedure based on literature is shown below.

- Mix p-toluic acid powder with propanol, place in a beaker which is placed in a hot water bath, let the acid dissolve.
- With stirring insert bloom gelatin with de-ionized water.
- Mix both solutions in a beaker and cover with cling film to avoid evaporation, place inside the hot water bath for uniform heating.
- Use kitchen thermistor to monitor the solution temperature.
- When the mixture reaches approximate 85 °C it should be clear and no air bubbles on the surface of the solution.
- Remove the beaker and stir the mixture to remove any air bubble from the surface.
- Immerse the beaker in a cool bath of water and Stir the mixture until it cools to 50 °C and add liquid detergent (fairy liquid).
- In parallel heat up the oil solution to approximately 50 °C, then pour the gelatin solution to the oil solution at 50 °C with continuous stirring until the solution. becomes uniform of single color.
- Cool the emulsion to 40 °C by immersing the beaker to the water bath, at this point no longer need to stir.
- Cool the solution to approximately 35 °C, and pour into the container for molding.

Appendix B

System Design

B.1 Microwave System Characteristics

This section presents the measured characteristics of the microwave system. The measurement's compromise of scattering parameters of individual components, by analysing through measurements ($|S_{21}|$). The measurement was possible with full two ports calibration Rohd&Shwarz ZVH8 network analyser (VNA). Figure B.1 shows the measured $|S_{21}|$ of the digital step attenuator at user defined attenuation of 0 dB, 7 dB and 15.5 dB. The insertion loss of the attenuator at the reference point (no attenuation) between the frequency of interest 2.4-2.6 GHz was approximately 2.5 dB, which matches the manufacturer specification. However, at 7 dB attenuation the in line lose is almost negligible; this is occurring due to the change in impedance with respect to attenuation step. The in-line loss was approximately 2 dB, during the maximum applied attenuation of 15.5 dB. The fluctuation of insertion loss has an impact to the actual delivered power during the diagnosis when variable power might be of interest. This factor is mitigated with the use of power meter and adjusting the attenuation accordingly.

The characteristics of band pass filter using through measurement is shown in Figure B.2. The 3 dB cut of is between 1.7 to 3.2 GHz, the maximum insertion loss in the pass band at the desired frequency is about 2 dB. About 35 dB rejection at about 4 GHz, which is essential for minimizing harmonics.

Figure B.3 shows the measured $|S_{21}|$ characteristics of the RF power amplifier. To measure the high-power amplifier, was achieved with 10 dB and 40 dB input output attenuation to prevent damage to the VNA. The characteristic of each attenuator was

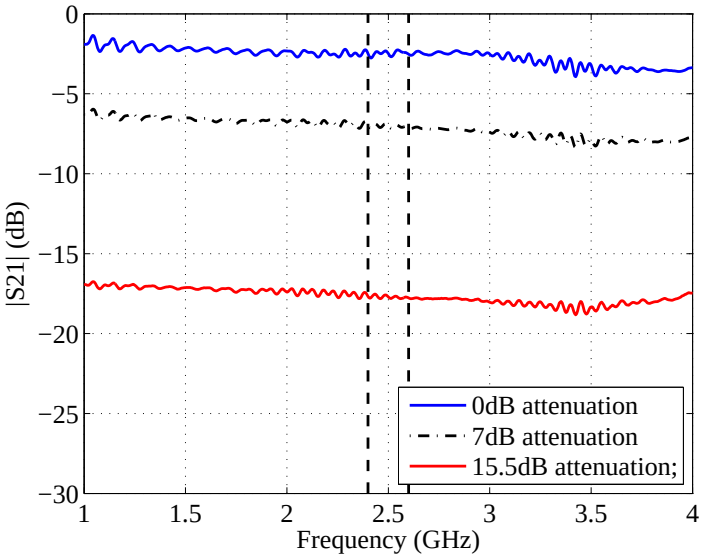

Figure B.1: Characteristics of digital step attenuator.

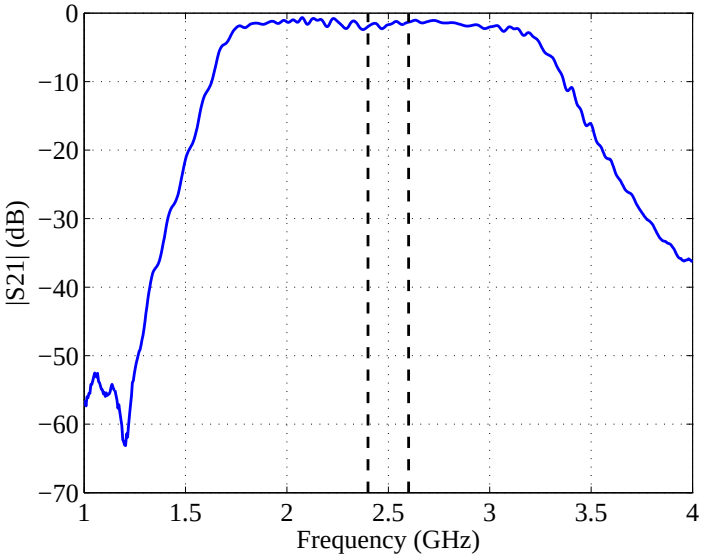

Figure B.2: Characteristics of band-pass filter.

obtained and subtracted from the full measurement. The amplifier stand-alone reading is presented in Figure B.3, using a reference input power of 0 dBm. At frequency range of 2.4-2.6 GHz, the gain of the amplifier was estimated at 44 dB with fluctuation of about 0.5dB , in contrast to 45 dB gain in the data sheet. The maximum saturated output power is 42dBm (approximately 16 watts) given by the data sheet.

The Bi-directional coupler has four ports, through measurements were completed with two ports at a time, while other ports are terminated with 50Ω match load. Port

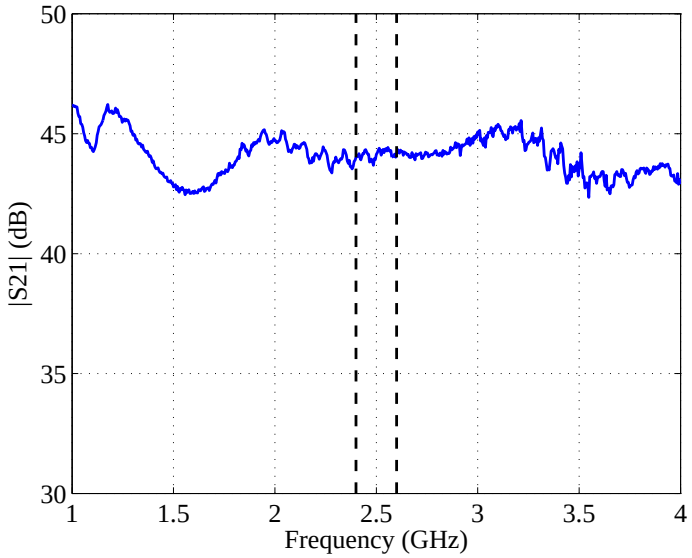

Figure B.3: Characteristics of RF power amplifier.

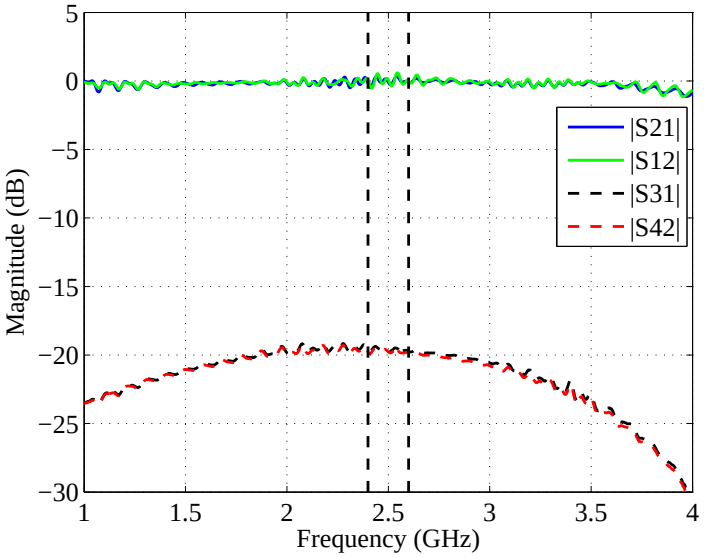

Figure B.4: Measurement of bi-directional coupler.

1 and port 2 and the input and output respectively. Port 3 and ports 4 are the coupled input and reflected power correspondingly. The measured $|S_{21}|$, $|S_{12}|$ shown in Figure B.4, where the insertion loss is just a fraction at about 0.25 dB and have linear characteristics between 1-3.5 GHz. This clearly indicates there is no isolation between the input and output port. This indicates the system is vulnerable without any reverse high-power protection. The through measurement of coupled ports $|S_{31}|$, $|S_{42}|$ show an approximately 20 dB coupling between input and the forward coupled port and similar

characteristics for output to reverse coupled port. The power received at the coupled ports are always 20 dB lower of original signal, which is necessary to estimate the actual delivered and reflected powers. The coupled port has non linear characteristics with the operating frequency; however, it can be neglected at the operating frequency range.

B.2 Thermoelectric Theory

Cooling or maintaining a temperature of an object can be achieved by defining the cooling requirements. This includes the amount of heat to be dissipated (pumped away by the TE), the heat sink efficiency along with forced-air cooling. Low heat loads require reduced TE power unless further cooling is desired. The heat load can be either active, passive or both simultaneously. Active head loads are generally related to the power of device being cooled, and this is expressed by the standard power equation shown in equationB.2.1. In hybrid applicator scenario, this active cooling is directly related to the absorbed RF power in the tissue.

$$Q_{active} = V^2/R = VI = I^2R \tag{B.2.1}$$

the parasitic or passive heat load's compromise of conduction, convection and radiation. In most applications, including hybrid applicator, the conduction heat load is the most superior and considered in the effectiveness of TEC devices. The general expression for passive heat load (Q, watts) is described in equation B.2.2.

$$Q_{passive} = Q_{cond} + Q_{conv} + Q_{rad} \tag{B.2.2}$$

Heat is transferred by internal collision means of an object resulted by changes from high to a low-temperature region. Heat conduction occurs in the entire thermal model, from heat transferred from the skin surface to the applicator to TE module and finally to the heat sink for dissipation. The basic equation of heat transfer by conduction (Watts) in the steady state is given by equation B.2.3. Where k, A and L are thermal conductivity (W/m°C), cross sectional area (m^2) and length of the heat path (m). Temperature difference (°C) between hot and cold objects is represented by T_h and T_c

$$Q_{cond} = \frac{kA}{L}(T_h - T_c) \tag{B.2.3}$$

The remaining passive heat loading is from convection, give by equation B.2.4. Where h is convective heat transferee coefficient (W/m^2°C). Convection is considered for heat transferred from the surface of heat sink and applicator.

$$Q_{conv} = hA(T_h - T_c) \tag{B.2.4}$$

In the case of hybrid system operating in short duration time, when the thermal equilibrium of the system is not met, it is essential to model as a transient temperature change as shown in equation B.2.5. Where t is the time interval (seconds), m is the weight of object (kg), Cp is the specific heat capacity (J/(kg °C)), ΔT is the temperature change (°C) and Q is the added or removed heat (Watts).

$$t = (m \times Cp \times \Delta T)/Q \tag{B.2.5}$$

Appendix C

Applicators Design

C.1 Applicator I

C.1.1 Design Parameters

Table C.1: Applicator I parameters

Parameters	Dimensions (mm)
l_p (Patch element length)	34.9
w_p (Patch element width)	44
f_l (Feed position from centre)	10.5
d_e (optical emitter diameter)	8
l_s (optical emitter/detector separation)	38
a_l (substrate length)	47.3
w_a (substrate width)	51
h_1 (substrate thickness)	1.587
h_2 (superstrate thickness)	1.587

C.1.2 Original Simulation Model Thermal Study

Superstrate thickness comparison with the original simulation model with 2 mm skin and 10 mm muscle thickness. Thermal distribution are illustrated in Figure C.1, where (a and c) are the 1.6 mm thick and (b,d) is the 3.2 mm superstrate thickness .The peak temperature profile presented in Figure C.2. The results clearly indicate the advantage of 1.6 mm superstrate over thicker dielectric material. The peak temperature in *yz*-plane

are equivalent in the skin-fat interface for both thickness. However in the *xz*-plane, the 1.6 mm superstrate was 4 °C lower in the skin layer and just 1.5 °C lower in the muscle.

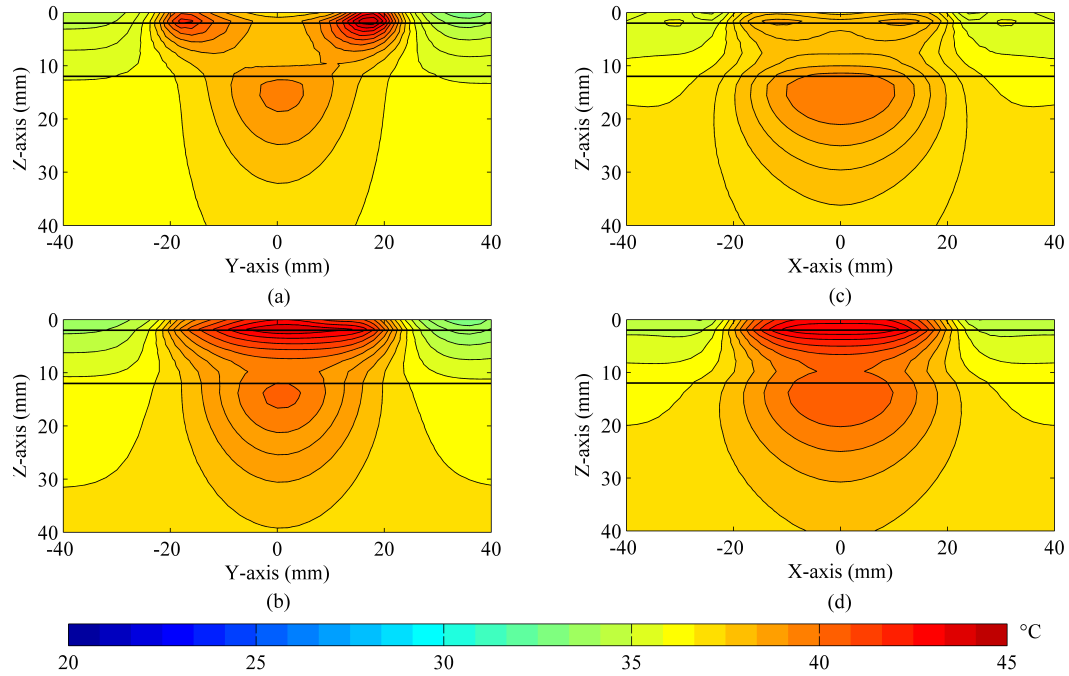

Figure C.1: Thermal distribution at of simulated patch antenna at different superstrate thickness. (a,b) *yz*-plane at 1.6, 3.2 mm thickness, (c,d) *xz*-plane at 1.6, 3.2 mm thickness

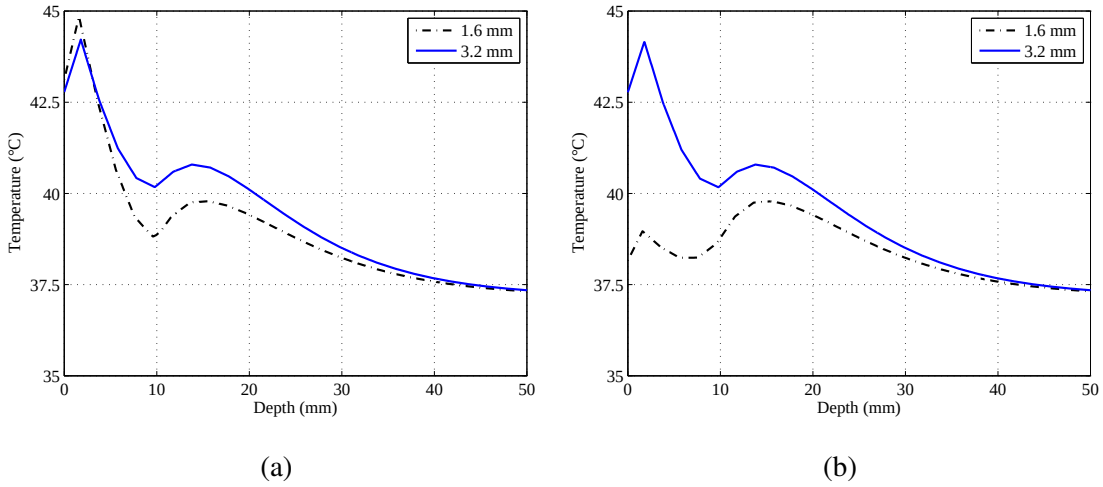

Figure C.2: Peak temperature at different superstrate thickness after 5-minutes of exposure. (a) across *yz*-plane, (b) across *xz*-plane

C.1.3 Phantom study

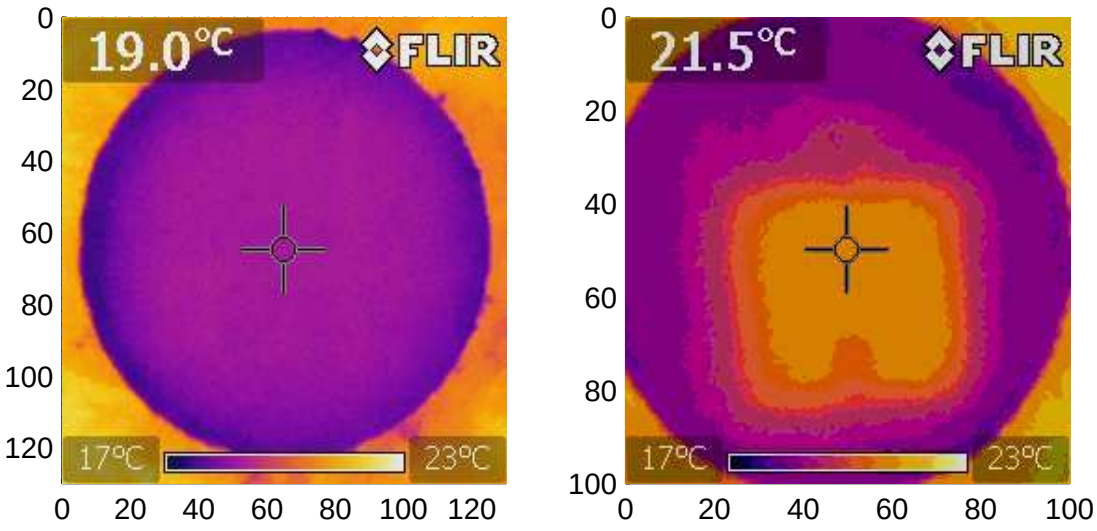

(a) (b)

Figure C.3: Measured Thermal distribution on phantom surface without heating, (a) Phantom tempreature, (b) Phantom temperature with applicator placed (passive heating)

C.2 Applicator II

C.2.1 Design Parameters

Table C.2: Applicator II parameters.

Parameters	Dimensions (mm)
D_o (Element external diameter)	29.6
D_i (Element internal diameter)	9.0
f_p (Feed position from centre)	8.50
l_o (Substrate/superstate diameter)	55.0
C_t (Exterior housing thickness)	7.35
D_l (LDF probe diameter)	6.0
D_n (NIRS optodes diameter)	10.0
N_s (NIRS optodes separation)	40.0
h_1 (Substrate thickness)	1.52
h_2 (Superstrate thickness)	2.0

C.2.2 Cooling Element

Figure C.4 illustrates the measured thermal distribution at the surface of Applicator II with active cooling. It can be seen, the cooling distribution is clearly non-uniform, although uniformity may also be a function of time, thermal resistance and area. As previously shown the heating pattern on the skin surface have an identical distribution, therefore positioning the TE module on the radiating edges may significantly reduce the superficial hotspots.

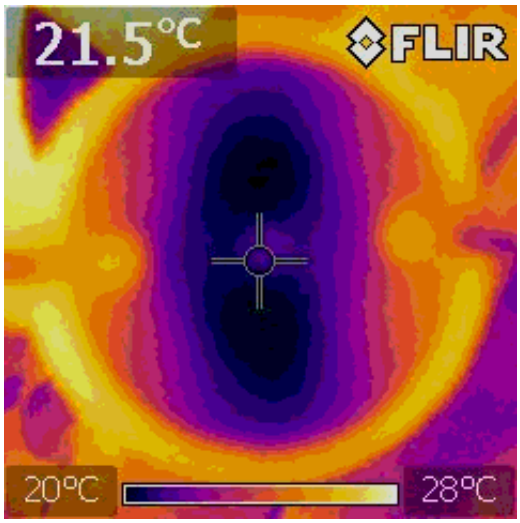

Figure C.4: Captured thermal image of Applicator II surface with active cooling

C.3 CP Applicator

C.3.1 Design Parameters

Table C.3: CP Applicator parameters

Parameters	Dimensions (mm)
w_n (Notch width)	5.0
l_n (Notch length)	4.2
D_z (Element External diameter)	29.4
D_u (Element Internal diameter)	8.0
f_s (Feed position from centre)	11
D_r (Element Internal diameter)	29.1
w_r (Notch width)	2.4
l_r (Notch Length)	3.3
w_s (Stub width)	3.4
l_s (Stub length)	2.1

C.3.2 In-vivo Passive Cooling

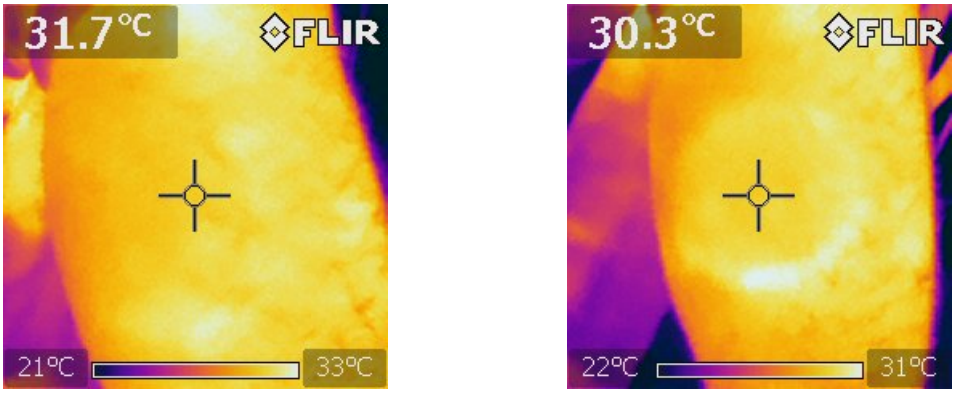

(a) (b)

Figure C.5: Captured skin thermal distribution of applicator passive cooling at: (a) original tissue without applicator, (b) after 10 minutes of thermal equilibrium of applicator placement without microwave or active cooling

Appendix D

Commercialisation of Hybrid System

This chapter covers the commercial aspect of the hybrid system. This includes various models of innovation, Intellectual property (IP), medical devices regulatory, market research and future plans.

D.1 Introduction

The purpose of the device is to assist physicians to diagnose the physiological responses of a patient when their muscle is thermally stimulated, which to date can only be achieved superficially on the skin. The developed device facilitates the investigation of thermoregulation in the muscle (1.5 cm below the skin surface). The device is based on a non-invasive novel microwave radiator (antenna) to induce non-ionising radiation for local warming, in a few centimetres square, in the muscle. Local warming causes the blood vessels to dilate for cooling down the heat; it is part of the human thermoregulation process. This thermal response, in the form of increase of blood flow, is monitored by the integrated near infrared spectroscopy (NIRS) probes. An in-house built integrated system prototype has been used to demonstrate that muscle thermal stimulation can be obtained and monitored. The measurement shows the device is capable of measuring the changes of blood haemoglobin levels in the muscle while suppressing the changes in the skin layer. Current commercially available devices in health care today are only able to monitor superficial thermal responses. This limits the efficacy of the diagnosis and cannot determine the state of the muscle tissue alone. The hybrid monitor has an innovative advantage which allows to be competing against other present devices but more significantly it is a possible new diagnosis segment.

Starting a business is a complicated process, and in most cases, the success rate is influenced by the factor that cannot be controlled. Commercialising new technology holds the highest amount risks but there is also a possibility of high amount prospect. Having established the technology, it is necessary to consider the individual and the commercial goals, which is presented in the route to marketing flowchart shown in Figure D.1 [165]. The personal goal is to develop and commercialise a medical device to assist in evolving the technology used in today's and future health care. While the initial commercial goal is to initiate collaboration with a research clinician to develop the device, and meet consumer needs. As with the majority of commercial product's research is the start of the key chain that leads to new inventions, which requires further

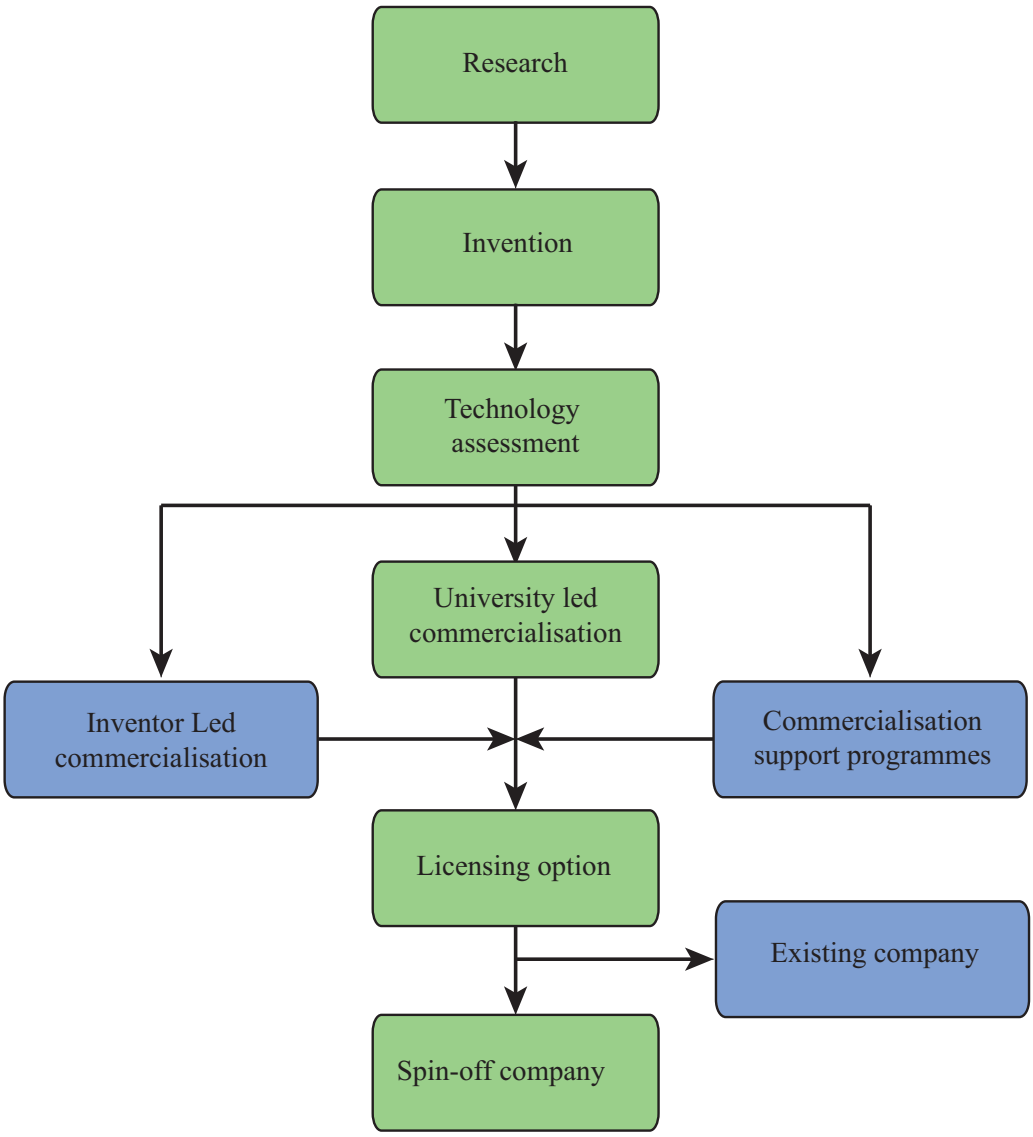

Figure D.1: Commercialisation path.

literature review, disclosure and market research. In this scenario, the research and the developed device are conducted as part of research degree in the university, leaning toward a university led commercialisation. As with most of the new inventions, IP protection is the initial step to commercialise a product. The invention is created in the higher education institutes, thus the inventors will possess the IPs, however, the inventors must also consider the revenue share with the institute when the product is successfully commercialised. Subsequently, a business model is necessary after identifying a patent, which include market research, segment sales activities, financial strategies and product development. Alternative paths outside the academia are led by the inventors directly or support/grant program where the IP is entirely owned by the

inventors or by the fund sponsors respectively. Typically new business does not have enough resources, licensing option is essential and must be consider carefully, which applies to excising company or university led spin-off companies.

D.2 Innovation and Technology Transfer

Innovation begins when a particular problem needs to be solved to satisfy customer needs. Creating an innovative technology is the foundation of a successful business that increases competitiveness and economic growth of the company [166]. Successful innovation requires both technical and consumer need to be fulfilled. This is achieved by balancing the requirement of the product, development and organization. In other words, it is the knowledge and the diffusion of the knowledge. There are four types of innovation to be considered [167]:

- Product Innovation: A new product which is significantly enhanced against current products.
- Process Innovation: Improvement in production method (Reduction in cost and time, increase quality).
- Marketing Innovation: Involve changes in product design, promotion and addressing customer needs to essentially boost sales.
- Organizational innovation: Organising the firm internally such as reduction in administrative costs and increase in work efficiency.

D.2.1 Innovation Model

Technology transfer is founded from research, knowledge and development activities. This procedure is initially considered as a sequential process as shown in Figure D.2.The linear technology transfer advances in a unidirectional manner where scientific theory creates innovation, which leads to development, followed by production (manufacturing) and finally to consumers [168]. This model was adopted at the beginning of 1950 and is commonly known as the market push strategy, where the suppliers drive the technology toward consumers based on a predicted demand. The push model lacks both feedback and loops between each stage, subsequently the delivered technology is limited by the original source where the demands are uncertain. Not until 1970 the

second model is emerged, which is known as the market pull strategy, this is based on the same linear concept but in the reverse order. In this scenario, consumer demands a product, which leads back to the research and initiates the linear cycle again. The downside of market pull is the lead time required to respond the market demands.

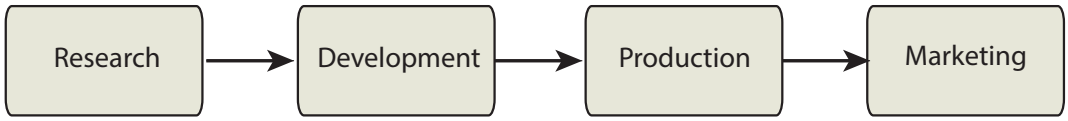

Figure D.2: Linear model of innovation.

To address the criticism of the linear model, a more realistic and complex model was developed by Stephen J. Kline in 1985 known as the Chain-Linked model as shown in Figure D.3 [169]. It can be seen from Figure D.3, research, and knowledge are often linked with each other, this is to address any raised doubts during the process. The knowledge and the science are different at each stage, such as pure science is required during the invention. However, in the design and development stage the science is based on analysis how each component of system interact with each other, while in production stage the research is needed to consider further improvement and cost reduction. Multiple feedbacks and loop are considered in the model to ensure the product serves market need by considering users 6 perspective for potential improvement of the product. There are many other innovation transfer models, including Network Model and open innovation [170] [171].

Innovation is a complicated, non-linear and iterative process. Industry tries to predict this process to increase profit and reduce risks. None of the innovation models are accurate, particularly in different industries, where requirements and product lines are diverse. In academia, information is transformed from a large-scale study to scientific knowledge to investigate the success and failures of the possible innovation for an increase in the prediction of success [170].

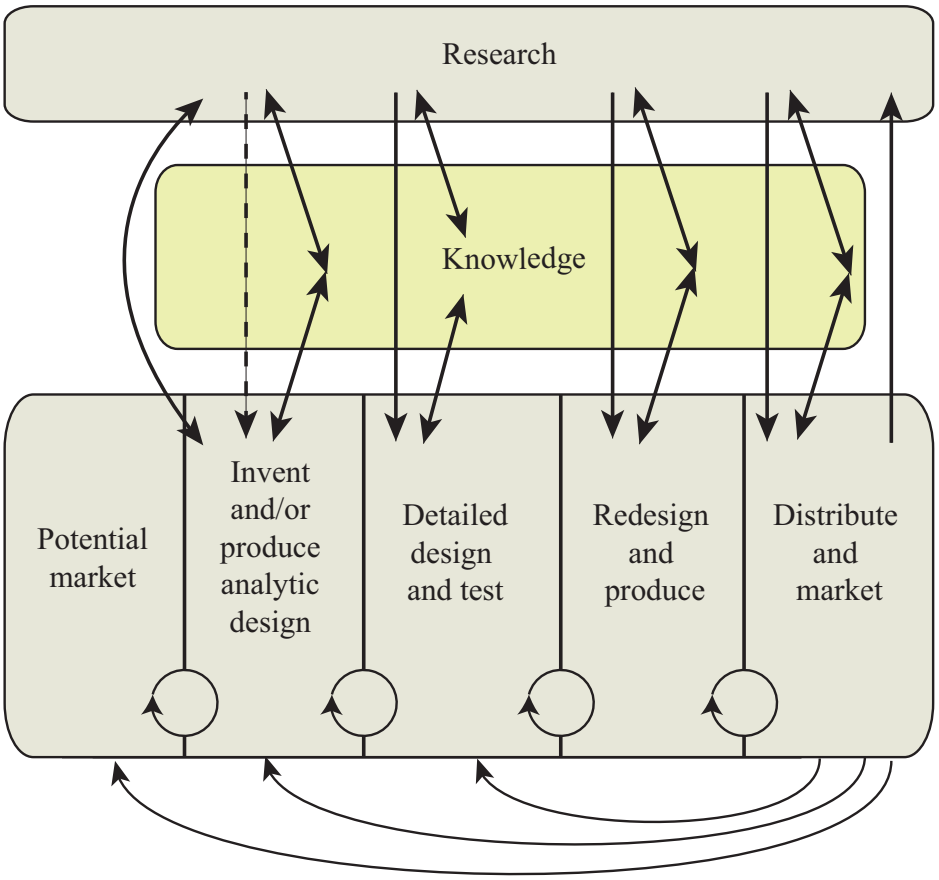

Figure D.3: Chain-linked model of innovation.

D.2.2 Diffusion of Innovation

Diffusion of innovation theory developed and published by Everett Rogers in 1962, the theory explains how innovation or idea diffuses to social groups (consumers) where it has been adopted and accepted by individuals in the group. The diffusion theory is most suitable for examining adoption of innovation in higher-education [172]. Adoption of new product does not occur concurrently within the social group, but it occurs in some individuals who choose to adopt early because they perceive the technology as innovative [173]. This shows individuals who adopt technology earlier than others have distinctive characteristics. During the promotion of the technology is important to understand these individual characteristics to boost the adoption of innovation. Roger's technology adoption curve shown in Figure D.4 including product life cycle, which consists of four essential stages to for evaluating corporate strategies:

- The introductory stage of commercialisation often starts with a narrow and focused user group that helps in identifying early problems with the product. This

would be the ideal starting scenario of the hybrid system.

- Growth stage is where customer stratification and loyalty are established, with continuous improvement and increase in distribution with larger companies.

- At the Maturity stage, a brand has now been built, require to improve customer service and considering other possibilities of the technology.

- Decline is the final stage of product life cycle, and it is impossible stop it. The options are either to exit or slow down the decline.

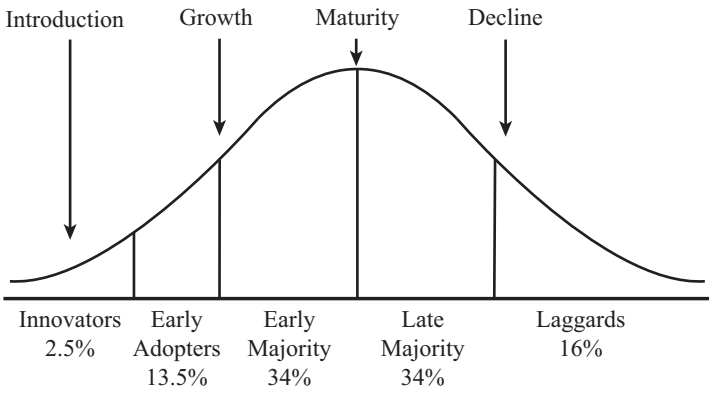

Figure D.4: Diffusion of innovation adoption curve.

Having established technology life-cycle, the next step is to understand the characteristics of each customer group, and they are five types of adopter shown Figure D.4.

- The inventors stage is the introductory stage representing only about 2.5% of individuals that are interested in the new idea, those individuals (usually technologists) are willing to take risks and further develop the product. This is would be the starting point for the hybrid system, by attracting research physicians to solve the desired customer problem.

- The early adopters representing 13.5% of population, those individuals are visionary who take the product on faith to solve a particular customer problem, and aware of need to change and comfortable with adopting new ideas.

- Early Majority covers 34% of adopters, those individuals known as pragmatists and require solid evidence before adopting new innovation. The product would be stable and reliable during this stage. To attract this group must provide publication or reports to show the success of the technology.

- Later majority also covers 34% of adopters, and considered as conservative and only adopt when the majority have adopted. To tackle this group by providing market statistics.

- Laggards represent 16% of the population, and they are the last individuals to adopt. This group is sceptic and difficult to take on board, however the strategy is to apply pressure.

D.3 Proof of Concept and Intellectual Property (IP)

This section briefly discusses the designed technology prototype and subsequent future stages including IP protection, product regulatory and quality system management.

D.3.1 Product Prototype

For successful commercialisation, it is essential to prove the claimed technology works, which will require a working prototype. Fortunately, the first prototype was designed and developed during the research degree and in working condition. Experimental trial has been conducted on a tissue mimicked material and directly on human calf. This was approved by UCL ethics to deploy on a maximum of five subjects. The prototype already considers a fail-safe mechanism to eliminate any hazards caused by the radiating microwave. The developed prototype will be used to demonstration to the potential early adopters. The prototype was initially intended as a research tool, with further modification it can be used for larger-scale study with a supported physician. The prototype has not been through any external testing or regulatory at the moment. However, it will be the next stage as it is a requirement before conducting a large case study. For future purposes there will be a fully documented design brief that includes operation manual and specification of the device, as this is an essential and a must step for a certified technology.

D.3.2 IP Protection

Successfully commercialising innovation in the medical device's domain, rely on the intellectual property right (IPR), including patent, copyright, trademark. Novelty and effectiveness are criteria to consider for innovations that are applicable for a patent. For novelty, the technology must be new, performs precisely as stated and beneficial product. In addition the idea must not be revealed to public including research publication, particularly before applying to a patent.

The combined hybrid system consisting of microwave, optical, cooling systems and the probe are unique and have not been investigated before. The particular concept of measuring thermal responses in the muscle tissue alone was not previously achieved unless an invasive approach is used. However, the patent will be on the design of the probe, rather than the optical or microwave system as they are already well established concepts. The design of the probe is where the integration of three systems, which operates simultaneously to measure thermal response in the muscle. The established prototype was used for human experimental trials; the obtained trial results was evaluated and further design tweaking is currently being implemented. The goal is to ensure the probe operate as intended to before applying for design patent. The invention must be documented with in depth technical description, drawing and including the computer program used. These are necessary steps along with evidence of results, and advantages of the technology compared to current commercial devices.

The implementation of the hybrid system is university-based commercialisation. Any applied patents are possessed by the authors while still registered in the university. A complication of IP ownership could arise if the research was partially funded by industry. However, in case of the hybrid system, there are no sponsors for the project and as a result the IP options are between the university and the authors. Furthermore, there is a revenue sharing scheme for the university led commercialisation that must be taken into account. Inventors at early stage with net profit less than £50,000 receives the largest share of 50% in contrast to 30% share when profit is greater. The share agreements for University College London are shown in Table D.1

Table D.1: University College London IPR revenue sharing arrangements

Net Income	Exploitation fee	Inventor(s)	UCL Central Funds	Department
<50k	30%	50%	10%	10%
>50k	30%	30%	30%	10%

D.3.3 Medical Device Compliance

Applying medical technology to clinics is a complicated and extensive procedure. To achieve this goal, one must have a comprehensive set of organisation skills. Moreover, small inexperience companies are expected to seek out for guidance from a qualified agency in handling the regulatory, quality management and commercialisation procedure. Alternatively, an early stage industrial collaboration would be favourable for some; further knowledge could be gained from clinical trials and commercialisation aspects. Design of medical devices requires considerations of the material, ergonomic and environmental implications such as minimising the microwave leakage from the hybrid probe to the surrounding. The initial intention is to obtain CE marking through a European commission (EC) Medical Device Directive; the regulatory will allow the product to be used in EU.

All medical devices must comply with the regulatory procedure, and they are classified according to the risk level, as demonstrated in Figure D.5(a). Majority of devices are categorised as Class I, which have the least regulative control as it possesses a low risk such as elastic bandages [174]. Intermediate regulatory controls are applied to class II devices; this is where the hybrid system fall into the category with medium risks. Meanwhile, Class III devices are only 10% of overall devices and pose the highest risks, and they are typically invasive such as pacemaker implants. Figure D.5(b) shows the section of medical device classification that is identifying the hybrid system; it can be seen class II is divided further into IIa and IIb. The developed system falls into the category of class IIb, which requires additional regulatory control, including quality assessment ISO 13485. The hybrid system is intended for diagnostic, which incorporates a low-power therapeutic characteristic that is necessary to produce changes in physiology.

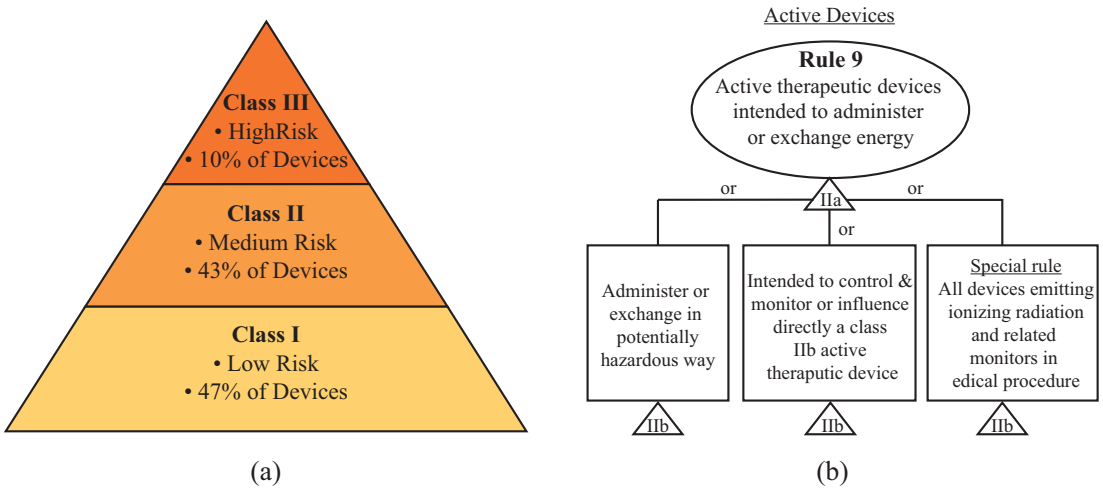

Figure D.5: Medical devices classification. (a) risk levels, (b) detailed classification

Quality management system (ISO 13485) is an addition to the regulative approval, where the inventors must demonstrate the abilities of providing devices that fulfils customer and CE compliance needs. To achieve this, numerous steps are required to comply with the medical regulatory as shown in Fig. 7. The Initial step requires some research and documentation starting with identifying the correct classification for the device as mentioned in Figure D.5(b). Risk management is an essential requirement to determine the safety of the device and is often is in congestion with ISO 13485 when higher level of regulation control is required. The device specification, clinical study evaluation and application are all to be documented and submitted accordingly. When the device is initially approved, the next procedure is inspection and declaration of conformity, upon successful compliance the product could be placed on the market.

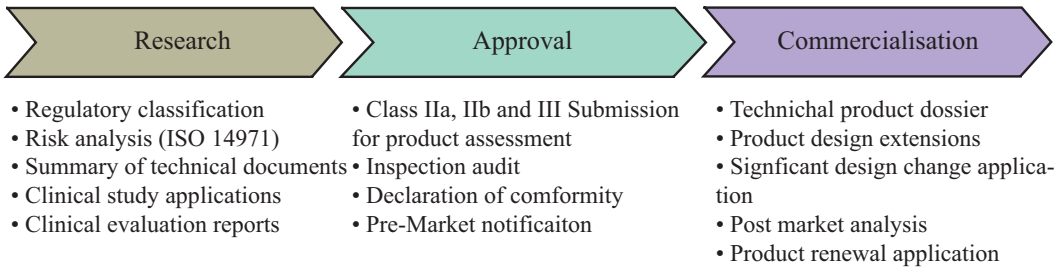

Figure D.6: Medical device regulatory and quality management system procedure.

D.4 Market Research

Commercialising a technology is more than just developing an innovative product, it is about understanding how the technology meets the market need. Having established the basic principles of innovation, IPR and regulatory it is important to implement a market research simultaneously to identify if the technology is already developed or patented, and if there is a market need for the product. All this would be discussed in the following section.

D.4.1 Medical Devices Industry

Technologies are constantly being implanted to improve the health of many individuals, to treat the variety of diseases and conditions. Medical device's sector grew by approximately 5.6% in 2011 and currently worth £214bn and will gain additional £64bn by 2016 according to the forecast [175]. This clearly indicates medical devices are attractive segment in the healthcare domain, with more than 500,000 products are commercialised [176]. The largest healthcare market expenditure is the US, whereas in UK, holds approximately 11% of EU and 3% of the global market based on statistics from 2009 [177]. The market share sector breakdown is shown in Figure D.7 [176]. Patient monitoring equipment and therapies are the second largest amount of transactions ap-

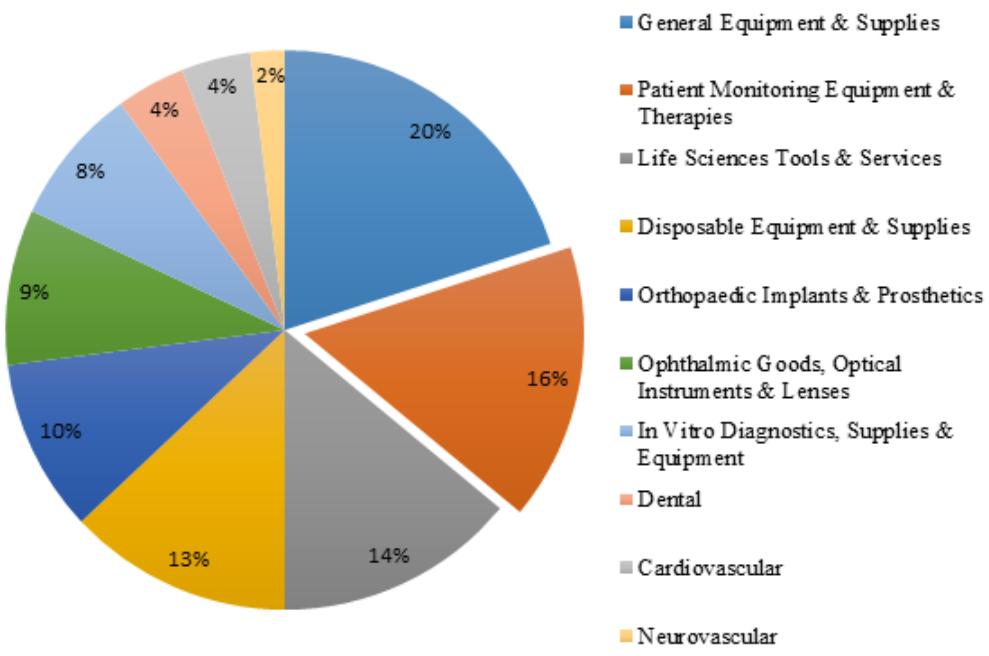

Figure D.7: Medical devices sub-sector breakdown in 2012.

proved. This sector includes many other medical devices, which can be narrowed down further to reach to electro-medical devices, where the hybrid system and other active diagnostic devices, including MRI and ultrasound.

D.4.2 Commercially Available Thermoregulation Monitors

There are two successful devices, which compromise of NIRS by Hamamatsu Photonics and laser Doppler flowmetry (LDF) by Moor instruments. These existing devices are already in use for various clinical diagnosis and research purposes. The NIRS monitor are typically used to monitor brain activities and muscle physiology in sports activities [178]. However, the measurement incorporates thermal responses from muscle, fat and skin layer inclusively. For that reason, NIRS system independently cannot be used to estimate muscle physiology alone, thus it must be used in conjunction with other devices to eliminate responses from skin and fat layer. Whereas the LDF monitor commonly used for burn assessment [179], flap monitoring [40] and Reynold's phenomena [180]. This device is reasonably priced, non-invasive and easily deployable. Moreover, the main disadvantage is the diagnosis limited to on skin layer only.

Having established the limitations of competitor's devices, the hybrid system has utilises the integrates NIRS probes which are capable of measuring the skin, fat and muscle physiological responses. However, it operates in conjunction to a microwave antenna that induces heat in the muscle. The heat is an essential process to produce change in blood volume. Furthermore, cooling system is incorporated to maintain temperature on the superficial layers, and produce changes in the muscle alone, in this manner the NIRS will only monitor the muscle haemodynamics. Studies shows measuring physiological response in the muscle can be performed by an invasive technique using radioactive tracer. This method is highly regulated and rarely applied in practice [181, 3]. Consequently the objective is to introduce a non-invasive device that's capable of monitoring muscle thermal response. This monitor is beneficial to physiotherapist and doctors in current common clinical difficulties, including free flap reconstruction where replanted flaps require deep tissue assessment of blood supply to evaluate tissue recovery and alert for flap failure [182]. The device can also address 14 other applications, including monitoring amputation level, vascular diseases and sport science [183].It has been established the need of a non-invasive muscle thermoregulation mon-

itor in the market. The next stage is to identify the early adopters to use and develop the device.

D.4.3 Market Needs

The objective is to maintain narrow market segment, and attempt to attract clinicians who can support and assist developing the device to solve a common problem. At the moment, we are consulting physicians from University College Hospital for collaboration to aid in the investigation and clinical trials. With this collaboration, it will be possible to assess the market need of the developed product, which may also divert the target segment. The hybrid system will be built around the early adopters, where profit will not be generated, rather only to improve customer need by taking the feedback on board. For the clinical trial, the aim is to develop a second prototype which would be a robust design and reduce the cost by eliminating extra unnecessary functionality. The current prototype would be used to demonstrate the concept to clinicians, and the final prototype will be used for trials. Clinical trials would be a step toward CE compliance, then device can be promoted to attract more customers.

In every commercial sector, there is a specific market drive that will attract additional customers. In the medical sector, there are two crucial factors, and they are economic and social market drives [177]. The economic drives, mainly about reducing the cost level but have a positive impact such as non-invasive treatments, which is a key feature of the hybrid system. Early diagnosis is another important factor, identifying a condition in early stages, will aid to improve quality of life, and also cost saving. The diagnosis of the hybrid system is the ability to study diseases or condition in deeper muscle, which allows for early prediction of flap failure during surgery. Social drivers, which have an important role in the success and failure of the device, this includes ageing population where a high-potential market demands to increase life expectancy. Furthermore, it's about safety, and this can be addressed by various regulatory certification and also additional safety interlock features such as implemented for the hybrid system.

D.4.4 Market Strategy

In the early phases of technology development are accompanied by frequent design changes until the requirements are fulfilled. A common commercialization pitfall is

launching a prototype directly into production; this is a typical problem applied to company to force production. The products will eventually cause problems during launch as quality assurance, functionality is not fully met, and production cost is generally higher. Resource management is essential in reducing production risks. This takes into account when considering mass production. Research prototypes are designed to work for study purposes without consideration of mass production, and robustness. There are often multiple design stages before reaching to the optimal design.

The development of first prototype was built for research purpose, as the development cost was not a deciding factor. The original prototype costs approximately £5,210 as shown in Table D.2. The hardware expenses can be reduced for the second prototype by eliminating unnecessary functionality while maintaining the core technology. The hardware cost can be deducted by approximately £810 from the first prototype which essentially will be used for clinical trials. Furthermore, manufacturing cost at this point is not considered as it will be designed mostly in department. The overall highest comes from clinical investigation approximately £3,820, which is a necessary process before obtaining CE marking, the cost of the trials depending on the device classification (risk level) [184]. The overall cost of second prototype would be around £8,160 in comparison to the £10,000 (Academic price) of the commercially available device by Moor Instrument. As mentioned earlier those devices are only able to study the thermoregulation on the superficial layer.

The device would have to be redesigned for manufacturing, when commencing to commercialisation stage. Cost reduction can be implemented by redesigning the architecture as prototypes are often based on off-the-shelf parts, which are more expansive. Mass production does reduce the overall costs, but the redesign to fit the core functionality can reduce further. However, this procedure requires organisation, planning time and considering component cost. On the other hand, Using of the shelf parts ensures highest quality and fastest time to commercialisation; this is still to be considered after implementation of second prototype. The software package used for both prototypes 16 requires an annual license of approximately £1,000. Developing custom software is crucial for cost reduction, also to provide a friendly and simple user interface.

A possible forecast can be drawn from second prototype to a commercial product. The hybrid device will have custom software to eliminate the excess of license cost,

Table D.2: Product cost comparison.

Cost division / Devices	Prototype 1 (research)	Prototype 2 (clinical trials)	Commercial device	Commercially available (LDF)
Hardware	£4,210	£3,400	£3,000	£10,000
Software (p.a)	£1,000	£1,000	NA	Included
Manufacturing	In-house	In-house	£500	NA
Clinical trials	NA	£3,820	NA	Included
Overhead	NA	NA	£1500	NA
Overall	£5,210	£8,160	£5,000	£10,000
Sale price	NA	NA	£6,250	£10,000
Profit	NA	NA	£1,250	NA

and designing the program to meet customer requirement. Large-scale production is not always necessary for starting companies, unless high demands, however, cost reduction can be achieved. The hardware cost of the commercial product could be in the region of £3,000, with consideration of design improvement gained from the earlier prototype. Manufacturing cost per unit would approximately be £500 and overhead of £1,500. The overhead expense covers all the ongoing company expenses, including CE compliance cost, wages and to finance equipments. Starting companies may have to take risks in lowering cost to cause's market penetration. The overall cost per unit is estimated to about £5,000. Unit sale price is about £6,250 and producing a 20% sales profit of about £1,250. The pricing is aggressive in comparison to competitors. However, this is essential to produce a push in the market and develop large customer community.

D.5 Summary and Future Plans

hybrid system has the potential to compete in the market, by solving a difficult problem in the clinical sector. The development and commercialisation of medical devices in medical segment is a complicated process, as there are many considerations to take into account. The essential steps are advancing through the medical trials, regulatory compliances and the quality management system. This establishes a robust device,

which attracts more customers. The route to successful marketing is achieved by evaluating customer feedback of the small adopters community (such as the physicians). The collaboration will be beneficial, and a must step to continue the innovation process. The market research shows the hybrid system have a unique advantages and open doors for many possible opportunities that is yet to be discovered. These advantages allows for better market penetration if priced correctly. In the market strategy, we put together the costs of each prototype and forecast the price of the actual commercial product.

There are few procedures are required to continue the commercialisation and development of the hybrid system, and they are:

- Establishing IP protection, as mentioned this is crucial step, and we are currently in touch with the university to commence this procedure.

- Applying for grant to continue research and development, this is the most important step. Currently, we require funds to develop new prototypes, apply for clinical trials and compliances. At this moment research grant is being applied. However, we will also consider business funding such as Invention for Innovation program (i4i). This program supports development and commercialisation of medical devices and allows for collaboration between industry and academia. A typical route of early stage development is Venture Capital, which needs to be considered carefully.

- The next procedure is maintaining contact with research clinicians and physician, to establish early collaboration and develop the product to fit customer needs.

- Alternatively industrial collaboration, by communicating with Moor Instruments, which we already have established contact

- Considering license options or agreements, to allow collaborative partners to commercialise the product, this is the scenario when resources are restricted.

- Further device development is required in clinical trials and cost reduction implementation for the commercialised the product.

- Spin-off Company from university commercialisation is an option to be considered upon the success of previous steps, at this stage business plan must be carefully done.

D.6 Award Acknowledgement

I would like to thank UCL Advances for the Enterprise Scholarship, which provided me the additional time and funds to navigate my attention from scientific studies to commercialisation. This was a fantastic opportunity which I have managed to familiarize myself with the procedures that undergoes from a research prototype to a commercial product. This was made possible thanks to the UCL advances short courses on marketing strategy. Often researchers and scientist do not consider marketing aspects, which makes it difficult to spot commercial opportunities. Our goal is to relish the research opportunities to help build a better world in a more effective and constructive way, and the experienced gained so far brings us a step closer to reality. I would certainly recommend this scholarship to other students, as it is an invaluable experience

Bibliography

[1] G. C. Goats, "Microwave diathermy.," *British journal of sports medicine*, vol. 24, pp. 212–8, Dec. 1990.

[2] C. Song, "Effect of local hyperthermia on blood flow and microenvironment: a review," *Cancer Research*, vol. 44, pp. 4721s–4730s, 1984.

[3] D. J. Wyper and D. R. McNiven, "The effect of microwave therapy upon muscle blood flow in man.," *British Journal of Sports Medicine*, vol. 10, pp. 19–21, Mar. 1976.

[4] K. V. Schuylenbergh and R. Puers, "Monitoring orthopaedic implants using active telemetry," *in Medicine and*, pp. 2672–2673, 1992.

[5] S. Salvador and E. Fear, "Exploring joint tissues with microwave imaging," *IEEE Transactions on Microwave Theory and Techniques*, vol. 58, no. 8, pp. 2307–2313, 2010.

[6] a.W. Guy, "History of Biological Effects and Medical Applications of Microwave Energy," *IEEE Transactions on Microwave Theory and Techniques*, vol. 32, pp. 1182–1200, Sept. 1984.

[7] A. V. Vorst, A. Rosen, and Y. Kotsuka, *RF/Microwave Interaction with Biological Tissues*. Wiley-IEEE Press, 1st ed., 2006.

[8] H. Moseley, *Non-ionizing Radiation: Microwaves, Ultraviolet Radiation and Lasers (Medical physics handbook)*. Institute of Physics Publishing, 1988.

[9] A. Guy, "Therapeutic applications of electromagnetic power," *Proceedings of the IEEE*, vol. 62, no. 1, pp. 55–75, 1974.

[10] R. P. Feldman J T, "The Edwin Smith Surgical Papyrus," *Child's nervous system*, vol. 15,, no. 6, pp. 281–284, 1999.

[11] A. Giombini, V. Giovannini, A. Di Cesare, P. Pacetti, N. Ichinoseki-Sekine, M. Shiraishi, H. Naito, and N. Maffulli, "Hyperthermia induced by microwave diathermy in the management of muscle and tendon injuries.," *British medical bulletin*, vol. 83, pp. 379–96, Jan. 2007.

[12] M. R. Horsman and J. Overgaard, "Hyperthermia: a potent enhancer of radiotherapy.," *Clinical oncology (Royal College of Radiologists (Great Britain))*, vol. 19, pp. 418–26, Aug. 2007.

[13] A. W. Guy, J. F. Lehmarm, J. B. Stonebridge, J. F. Lehmann, J. B. Stonebndge, C. G. Warren, B. J. Delateur, J. F. Lehmam, C. C. Johnson, C. H. Durney, and N. P. Plenk, "Evaluation of a Therapeutic Direct-Contact 915-MHz Microwave Applicator for Effective Deep-Tissue Heating in Humans," *IEEE Transactions on Microwave Theory and Techniques*, vol. 26, no. 8, pp. 556–563, 1978.

[14] P. R. Stauffer, F. Rossetto, M. Leoncini, and G. B. Gentilli, "Radiation patterns of dual concentric conductor microstrip antennas for superficial hyperthermia.," *IEEE transactions on bio-medical engineering*, vol. 45, pp. 605–13, May 1998.

[15] R. T. Held, V. Zderic, T. N. Nguyen, and S. Vaezy, "Annular phased-array high-intensity focused ultrasound device for image-guided therapy of uterine fibroids," *Ultrasonics, Ferroelectrics, and Frequency Control, IEEE Transactions on*, vol. 53, no. 2, pp. 335–348, 2006.

[16] A. Cheung and A. Neyzari, "Deep local hyperthermia for cancer therapy: external electromagnetic and ultrasound techniques," *Cancer research*, 1984.

[17] F. K. Storm and D. L. Morton, "Localized hyperthermia in the treatment of cancer.," *Nihon Gan Chiryo Gakkai shi*, vol. 17, pp. 250–81, Mar. 1982.

[18] S. Field and J. Hand, *An Introduction to the Practical Aspects of Clinical Hyperthermia*. Taylor & Francis, 1990.

[19] V. Bhatia, "Antennas and Other Electromagnetic Applicators in Biology and Medicine," *Proceedings of the IEEE*, vol. 80, no. 1, 1992.

[20] M. Klemm and J. Leendertz, "Microwave radar-based differential breast cancer imaging: imaging in homogeneous breast phantoms and low contrast scenarios," *IEEE Transactions on Antennas and Propagation*, vol. 58, no. 7, pp. 2337–2344, 2010.

[21] P. Meaney and M. Fanning, "A clinical prototype for active microwave imaging of the breast," *IEEE Transactions on Microwave Theory and Techniques*, vol. 48, no. 11, pp. 1841–1853, 2000.

[22] A. J. Fenn, G. L. Wolf, and R. M. Fogle, "An adaptive microwave phased array for targeted heating of deep tumours in intact breast: animal study results.," *International journal of hyperthermia*, vol. 15, no. 1, pp. 45–61, 1999.

[23] M. J. Burfeindt, E. Zastrow, S. C. Hagness, B. D. Van Veen, and J. E. Medow, "Microwave beamforming for non-invasive patient-specific hyperthermia treatment of pediatric brain cancer.," *Physics in medicine and biology*, vol. 56, pp. 2743–54, May 2011.

[24] N. Ichinoseki-Sekine, H. Naito, and N. Saga, "Effects of microwave hyperthermia at two different frequencies (434 and 2450 MHz) on human muscle temperature," *Journal of Sports*, vol. 7, pp. 191–3, Jan. 2008.

[25] G. Kantor, D. Witters, and J. Greiser, "The performance of a new direct contact applicator for microwave diathermy," *IEEE Transactions on Microwave Theory and Techniques*, vol. 26, no. 8, pp. 563 – 568, 1978.

[26] A. Guy, "Electromagnetic fields and relative heating patterns due to a rectangular aperture source in direct contact with bilayered biological tissue," *Microwave Theory and Techniques, IEEE Transactions on*, vol. 16, no. 2, pp. 214–223, 1971.

[27] K. I. L. Hamada, H. Yoshimura, "A New Feeding Technique for Temperature Distribution Control in Microwave Hyperthermia," *IEICE Trans. Electron*, vol. 3, no. 7, pp. 1318–1323, 1999.

[28] K. Saito, O. Nakayama, L. Hamada, and K. Ito, "Analysis of temperature distributions generated by square array applicator composed of coaxial-slot antennas for hyperthermia," *Electronics and Communications in Japan (Part II: Electronics)*, vol. 84, pp. 20–29, Nov. 2001.

[29] N. M. Reddy, V. Maithreyan, A. Vasanthan, I. S. Balakrishnan, B. K. Bhaskar, R. Jayaraman, V. Shanta, and S. Krishnamurthi, "Local RF capacitive hyperthermia: thermal profiles and tumour response.," *International journal of hyperthermia : the official journal of European Society for Hyperthermic Oncology, North American Hyperthermia Group*, vol. 3, no. 4, pp. 379–87.

[30] F. Storm, R. Elliott, W. Harrison, and D. Morton, "Clinical RF Hyperthermia by Magnetic-Loop Induction: A New Approach to Human Cancer Therapy," *Microwave Theory and Techniques, IEEE Transactions on*, vol. 30, no. 8, pp. 1149 – 1158.

[31] C. Chou, "Application of electromagnetic energy in cancer treatment," *IEEE Instrumentation and Measurement Society*, vol. 31, no. 4, pp. 547–551, 1988.

[32] M. Sancho, G. Martìnez, and C. Martìn, "Accurate dielectric modelling of shelled particles and cells," *Journal of electrostatics*, vol. 57, pp. 143–156, 2003.

[33] R. L. Magin and a. F. Peterson, "Noninvasive microwave phased arrays for local hyperthermia: a review.," *International journal of hyperthermia : the official journal of European Society for Hyperthermic Oncology, North American Hyperthermia Group*, vol. 5, no. 4, pp. 429–50, 1989.

[34] E. Bond and X. Li, "Microwave imaging via space-time beamforming for early detection of breast cancer," *IEEE Transactions on Antennas and Propagation*, vol. 51, no. 8, pp. 1690–1705, 2003.

[35] J. F.Lehmann, *Therapeutic Heat and Cold*. Lippincott Williams and Wilkins, 4th ed., 1990.

[36] R. W. Y. Habash, R. Bansal, D. Krewski, and T. Hafi, "Thermal Therapy , Part III : Ablation," *Crit Rev Biomed Eng*, vol. 35, pp. 37–121, 2007.

[37] P. Gebuhr, J. P. Jorgensen, B. Vollmer-Larsen, S. L. Nielsen, and B. Alsbjorn, "Estimation of amputation level with a laser Doppler flowmeter," *Journal of Bone & Joint Surgery, British Volume*, vol. 71-B, no. 3, pp. 514–517, 1989.

[38] A. Nicotra, M. Asahina, and C. J. Mathias, "Skin vasodilator response to local heating in human chronic spinal cord injury.," *European journal of neurology*, vol. 11, pp. 835–7, Dec. 2004.

[39] J. Yuen and Z. Feng, "Monitoring Free Flaps Using the Laser Doppler Flowmeter: Five-Year Experience," *Plastic and reconstructive surgery*, 2000.

[40] F. Hölzle, D. J. Loeffelbein, D. Nolte, and K.-D. Wolff, "Free flap monitoring using simultaneous non-invasive laser Doppler flowmetry and tissue spectrophotometry.," *Journal of cranio-maxillo-facial surgery : official publication of the European Association for Cranio-Maxillo-Facial Surgery*, vol. 34, pp. 25–33, Jan. 2006.

[41] L. Dubois, J.-P. Sozanski, V. Tessier, J.-C. Camart, J.-J. Fabre, J. Pribetich, and M. Chive, "Temperature control and thermal dosimetry by microwave radiometry in hyperthermia," 1996.

[42] M. Okoniewski, "A study of the handset antenna and human body interaction," *IEEE Transactions on Microwave Theory and Techniques*, vol. 44, no. I, 2002.

[43] F. Apollonio, "Theoretical analysis of voltage-gated membrane channels under GSM and DECT exposure," *Microwave Symposium Digest, 1997., IEEE MTT-S International*, vol. 1, pp. 103–106, 1997.

[44] A. V. Vorst and F. Duhamel, "1990-1 995 Advances in Investigating the Interaction of Microwave Fields with the Nervous Svstem," *IEEE Transactions on Instrumentation and Measurement*, vol. 44, no. 10, 1996.

[45] J. C. Lin and S. M. Michaelson, *Biological Effects and Health Implications of Radiofrequency Radiation*. Springer, 1987.

[46] D. H. Staelin, A. Morgenthaler, and J. A. Kong, *Electromagnetic Waves*. Prentice Hall, 1993.

[47] C. Polk and E. Postow, *Handbook of Biological Effects of Electromagnetic Fields*. CRC Press Inc, 1995.

[48] T. Liu, J. Fothergill, S. Dodd, and U. Nilsson, "Dielectric spectroscopy measurements on very low loss cross-linked polyethylene power cables," *Journal of Physics: Conference Series*, vol. 183, p. 012002, Aug. 2009.

[49] H. P. SCHWAN, "Electrical properties of tissue and cell suspensions.," *Advances in biological and medical physics*, vol. 5, pp. 147–209, Jan. 1957.

[50] P. Debye, *Polar Molecules*. Dover Publications inc, re issue e ed., 1929.

[51] B. Greenebaum and F. S. Barnes, *Bioengineering and Biophysical Aspects of Electromagnetic Fields (Handbook of Biological Effects of Electromagnetic Fields, Third Edition)*. CRC Press, 2006.

[52] S. Gabriel, R. W. Lau, and C. Gabriel, "The dielectric properties of biological tissues: III. Parametric models for the dielectric spectrum of tissues.," *Physics in medicine and biology*, vol. 41, pp. 2271–93, Nov. 1996.

[53] C. Gabriel, S. Gabriel, and E. Corthout, "The dielectric properties of biological tissues: I. Literature survey.," *Physics in medicine and biology*, vol. 41, pp. 2231–49, Nov. 1996.

[54] S. Gabriel and R. Lau, "The dielectric properties of biological tissues: II. Measurements in the frequency range 10 Hz to 20 GHz," *Physics in medicine and biology*, vol. 2251, 1996.

[55] Edward C. Jordan, *Electromagnetic Waves and Radiating Systems*. Prentice-Hall, 1950.

[56] R. Habash, *Bioeffects and Therapeutic Applications of Electromagnetic Energy*. CRC Press, 2007.

[57] G. Bit-Babik, C. K. Chou, A. Faraone, A. Gessner, M. Kanda, and Q. Balzano, "Estimation of the SAR in the human head and body due to radiofrequency radiation exposure from handheld mobile phones with hands-free accessories.," *Radiation research*, vol. 159, pp. 550–7, Apr. 2003.

[58] IEEE C95. 1-1992, "IEEE Standard for Safety Levels with Respect to Human Exposure to Radio Frequency Electromagnetic Fields, 3 kHz to 300 GHz," *Inc, New York, NY*, 1992.

[59] "ICNIRP statement on the "Guidelines for limiting exposure to time-varying electric, magnetic, and electromagnetic fields (up to 300 GHz)".," *ICNIRP Health physics*, vol. 97, pp. 257–8, Sept. 2009.

[60] G. Kantor and D. Witters, "A 2450 Mhz Slab-Loaded Direct Contact Applicator with Choke," *MTT-S International Microwave Symposium Digest*, vol. 80, pp. 355–357, 1980.

[61] D. Draper and K. Knight, *Therapeutic Modalities: The Art and Science: AND Clinical Activities Manual*. Lippincott Williams & Wilkins,US, 1st ed., 2007.

[62] M. Kutz, *Biomedical Engineering and Design Handbook, Volume 1: Volume I: Biomedical Engineering Fundamentals*. McGraw-Hill Professional, 2 edition ed., 2009.

[63] H. Pennes, "Analysis of tissue and arterial blood temperatures in the resting human forearm," *Journal of applied physiology*, vol. 1, no. 2, pp. 93–122, 1948.

[64] E. Zastrow, S. C. Hagness, and B. D. Van Veen, "3D computational study of non-invasive patient-specific microwave hyperthermia treatment of breast cancer.," *Physics in medicine and biology*, vol. 55, pp. 3611–29, July 2010.

[65] "Visible Human Project by National Library of Medicine (NLM)." URL: http://www.vr-laboratory.com/ (visited on 18/08/2014).

[66] S. K. S. H. MD and D. J. W. MD, *Radio Frequency Catheter Ablation of Cardiac Arrhythmias: Basic Concepts and Clinical Applications*. Wiley-Blackwell, 2002.

[67] M. Miller and G. Hutchins, "Development of anatomically realistic PET and PET/CT phantoms with rapid prototyping technology," *Nuclear Science Symposium*, pp. 4252–4257, 2007.

[68] K. J. M. Surry, H. J. B. Austin, A. Fenster, and T. M. Peters, "Poly(vinyl alcohol) cryogel phantoms for use in ultrasound and MR imaging.," *Physics in medicine and biology*, vol. 49, pp. 5529–46, Dec. 2004.

[69] Y. Yuan, C. Wyatt, P. Maccarini, P. Stauffer, O. Craciunescu, J. Macfall, M. Dewhirst, and S. K. Das, "A heterogeneous human tissue mimicking phantom for RF heating and MRI thermal monitoring verification.," *Physics in medicine and biology*, vol. 57, pp. 2021–37, Apr. 2012.

[70] M. Lazebnik, E. L. Madsen, G. R. Frank, and S. C. Hagness, "Tissue-mimicking phantom materials for narrowband and ultrawideband microwave applications.," *Physics in medicine and biology*, vol. 50, pp. 4245–4258, Sept. 2005.

[71] Y. Zhang, "The determination of the electromagnetic field and SAR pattern of an interstitial applicator in a dissipative dielectric medium," *IEEE Microwave Theory and Techniques Society*, vol. 36, no. 10, pp. 1438–1444, 1988.

[72] E. Porter, J. Fakhoury, R. Oprisor, M. Coates, and M. Popović, "Improved Tissue Phantoms for Experimental Validation of Microwave Breast Cancer Detection," in *Antennas and Propagation (EuCAP), 2010*, pp. 4–8.

[73] J. Zhou, D. Hara, and T. Kobayashi, "Development of ultra wideband electromagnetic phantoms for antennas and propagation studies," *Antennas and Propagation, 2006. EuCAP 2006.*, vol. 2006, no. October, 2006.

[74] M. G. Bini, A. Ignesti, L. Millanta, R. Olmi, N. Rubino, and R. Vanni, "The polyacrylamide as a phantom material for electromagnetic hyperthermia studies.," *IEEE transactions on bio-medical engineering*, vol. 31, pp. 317–22, Mar. 1984.

[75] K. Ito and H. Kawai, "Solid phantoms for evaluation of interactions between the human body and antennas," *IWAT 2005. IEEE International Workshop on Antenna Technology: Small Antennas and Novel Metamaterials, 2005.*, vol. 0, no. I, pp. 41–44, 2005.

[76] T. Iyama, T. Onishi, Y. Tarusawa, S. Uebayashi, and T. Nojima, "Novel Specific Absorption Rate (SAR) Measurement Method Using a Flat Solid Phantom,"

IEEE Transactions on Electromagnetic Compatibility, vol. 50, no. 1, pp. 43–51, 2008.

[77] D. Andreuccetti, M. Bini, and A. Ignesti, "Use of polyacrylamide as a tissue-equivalent material in the microwave range," *IEEE transactions on bio-medical engineering*, vol. 35, no. 4, pp. 275–277, 1988.

[78] M. Venkatesh and G. Raghavan, "An overview of dielectric properties measuring techniques," *General Assembly and Scientific Symposium, 2011*, 2005.

[79] "Agilent Basics of Measuring the Dielectric Properties of Materials." http://www3.imperial.ac.uk/pls/portallive/docs/1/11949698.PDF, 2006.

[80] J. B. Andersen, a. Baun, K. Harmark, L. Heinzl, P. Raskmark, and J. Overgaard, "A hyperthermia system using a new type of inductive applicator.," *IEEE transactions on bio-medical engineering*, vol. 31, pp. 21–7, Jan. 1984.

[81] H. I. Bassen and R. F. Coakley, "United States radiation safety and regulatory considerations for radiofrequency hyperthermia systems.," *The Journal of microwave power*, vol. 16, pp. 215–26, June 1981.

[82] J. W. Han, G. M. Van Leeuwen, S. Mizushina, J. B. Van de Kamer, K. Maruyama, T. Sugiura, D. V. Azzopardi, and a. D. Edwards, "Monitoring of deep brain temperature in infants using multi-frequency microwave radiometry and thermal modelling.," *Physics in medicine and biology*, vol. 46, pp. 1885–903, July 2001.

[83] L.W. Turne, *Electronics Engineer's Reference Book*. Newnes; 4th Revised edition edition, 4th ed., 1976.

[84] "Bio Med Inc - RADARMED 2500 CP." URL: http://www.biomedindia.net/electrotherapy-equipments.php, (visited on 04/05/2014).

[85] A. Giombini, V. Giovannini, A. Di Cesare, P. Pacetti, N. Ichinoseki-Sekine, M. Shiraishi, H. Naito, and N. Maffulli, "Hyperthermia induced by microwave

diathermy in the management of muscle and tendon injuries.," *British medical bulletin*, vol. 83, pp. 379–96, Jan. 2007.

[86] R. Huber, V. Treyer, J. Schuderer, T. Berthold, A. Buck, N. Kuster, H. P. Landolt, and P. Achermann, "Exposure to pulse-modulated radio frequency electromagnetic fields affects regional cerebral blood flow.," *The European journal of neuroscience*, vol. 21, pp. 1000–6, Feb. 2005.

[87] H.-R. Ahn and K. Lee, "Capacitive-loaded interstitial antennas for perfect matching and desirable SAR distributions.," *IEEE transactions on bio-medical engineering*, vol. 53, pp. 284–91, Feb. 2006.

[88] "BSD-500 Microwave Hyperthermia System." URL: http://www.bsdmedical.com/usa, (visited on 04/05/2014).

[89] "Emblation Microwave ISYS245 System." URL: http://www.emblationmicrowave.com/index.html (visited on 04/05/2014).

[90] W. Dooley, H. Vargas, and A. Fenn, "Randomized study of preoperative focused microwave phased array thermotherapy for early-stage invasive breast cancer," *Cancer Therapy*, vol. 6, pp. 395–408, 2008.

[91] F. Rossetto and P. R. Stauffer, "Effect of complex bolus-tissue load configurations on SAR distributions from dual concentric conductor applicators. Specific absorption rate.," *IEEE transactions on bio-medical engineering*, vol. 46, pp. 1310–9, Nov. 1999.

[92] P. F. Maccarini, H.-O. Rolfsnes, D. Neuman, and P. Stauffer, "Optimization of a dual concentric conductor antenna for superficial hyperthermia applications.," *Annual International Conference of the IEEE Engineering in Medicine and Biology Society.*, vol. 4, pp. 2518–21, Jan. 2004.

[93] S. Hava, R. Hunsperger, and H. Sequeira, "Monolithically Peltier-cooled laser diodes," *Journal of Lightwave Technology*, vol. 2, pp. 175–180, Apr. 1984.

[94] K.-y. Wang, "Thermal management of a medical device using thermoelectric

coolers," *Twentieth Annual IEEE Semiconductor Thermal Measurement and Management Symposium (IEEE Cat. No.04CH37545)*, pp. 122–124.

[95] S. Belavskaya, "Research of the possibility to use thermoelectric unit in device for reflexotherapy," in *Electron Devices and Materials, 2005. Proceedings. 6th Annual.*, pp. 5–6, 2005.

[96] S. Hede, N. Trivedi, Mekala, and N. Huilgol, "Thermometry studies of radio-frequency induced hyperthermia on hydrogel based neck phantoms.," *Journal of cancer research and therapeutics*, vol. 1, no. 3, pp. 162–7, 2005.

[97] D. C. Crawford, B. Hicks, and M. J. Thompson, "Which thermometer? Factors influencing best choice for intermittent clinical temperature assessment.," *Journal of medical engineering & technology*, vol. 30, no. 4, pp. 199–211, 2006.

[98] C. Yeager and S. Courts, "A review of cryogenic thermometry and common temperature sensors," *IEEE Sensors Journal*, vol. 1, no. 4, pp. 352–360, 2001.

[99] K. Arunachalam, P. Maccarini, T. Juang, C. Gaeta, and P. R. Stauffer, "Performance evaluation of a conformal thermal monitoring sheet sensor array for measurement of surface temperature distributions during superficial hyperthermia treatments.," *International journal of hyperthermia*, vol. 24, pp. 313–25, June 2008.

[100] Y. Leroy, B. Bocquet, and A. Mamouni, "Non-invasive microwave radiometry thermometry.," *Physiological measurement*, vol. 19, pp. 127–48, May 1998.

[101] K. R. Foster and E. a. Cheever, "Microwave radiometry in biomedicine: a reappraisal.," *Bioelectromagnetics*, vol. 13, pp. 567–79, Jan. 1992.

[102] A. Barrett, P. Myers, and N. Sadowsky, "Detection of breast cancer by microwave radiometry," *Radio Science*, 1977.

[103] G. F. Gabrielian ES, Khachatrian LA, Nalbandian SG, "Microwave method of determining cerebral blood flow," *Biull Eksp Biol Med*, vol. 103, no. 5, pp. 625–7.

[104] L. Dubois, J. Pribetich, J. J. Fabre, M. Chive, and Y. Moschetto, "Non-invasive microwave multifrequency radiometry used in microwave hyperthermia for bidimensional reconstruction of temperature patterns.," *International journal of hyperthermia : the official journal of European Society for Hyperthermic Oncology, North American Hyperthermia Group*, vol. 9, no. 3, pp. 415–31, 1993.

[105] S. Jacobsen, P. R. Stauffer, and D. G. Neuman, "Dual-mode antenna design for microwave heating and noninvasive thermometry of superficial tissue disease.," *IEEE transactions on bio-medical engineering*, vol. 47, pp. 1500–9, Nov. 2000.

[106] M. Cope and D. T. Delpy, "System for long-term measurement of cerebral blood and tissue oxygenation on newborn infants by near infra-red transillumination," *Medical and Biological Engineering and Computing*, vol. 26, no. 3, pp. 289–294, 1988.

[107] A. Lima and J. Bakker, "Near-infrared spectroscopy for monitoring peripheral tissue perfusion in critically ill patients.," *Rev Bras Ter Intensiva.*, vol. 23, pp. 341–351, Sept. 2011.

[108] S. J. Matcher, P. J. Kirkpatrick, K. Nahid, M. Cope, and D. T. Delpy, "Absolute quantification methods in tissue near-infrared spectroscopy," 1995.

[109] S.Susumu, T.Sumio, O.Takeo, and K.Yukio, "A Tissue oxygenation monitor using NIR spatially resolved spectroscopy," *Proceedings of SPIE, the International Society for Optical Engineering*, vol. 3597, no. January 1999, pp. 582–592, 199.

[110] A. Duncan, J. H. Meek, M. Clemence, C. E. Elwell, L. Tyszczuk, M. Cope, and D. T. Delpy, "Optical pathlength measurements on adult head, calf and forearm and the head of the newborn infant using phase resolved optical spectroscopy.," *Physics in medicine and biology*, vol. 40, pp. 295–304, Feb. 1995.

[111] J. C. Lin, *Electromagnetic Fields in Biological Systems Biological Effects of Electromagnetics*. CRC Press, 1 edition ed., 2011.

[112] J. Short and P. Turner, "Physical hyperthermia and cancer therapy," *Proceedings of the IEEE*, vol. 68, no. 1, pp. 133–142, 1980.

[113] T. Sunaga, H. Ikehira, S. Furukawa, M. Tamura, E. Yoshitome, T. Obata, H. Shinkai, S. Tanada, H. Murata, and Y. Sasaki, "Development of a dielectric equivalent gel for better impedance matching for human skin.," *Bioelectromagnetics*, vol. 24, pp. 214–7, Apr. 2003.

[114] H. R. Underwood, a. F. Peterson, and R. L. Magin, "Electric-field distribution near rectangular microstrip radiators for hyperthermia heating: theory versus experiment in water.," *IEEE transactions on bio-medical engineering*, vol. 39, pp. 146–53, Feb. 1992.

[115] R. Gupta and S. Singh, "Analysis of the SAR distributions in three-layered biomedia in direct contact with a water-loaded modified box-horn applicator," *IEEE Transactions on Microwave Theory and Techniques*, vol. 53, no. 9, pp. 2665–2671, 2005.

[116] I. Bahl and S. Stuchly, "Analysis of a microstrip covered with a lossy dielectric," *IEEE Transactions on Microwave Theory and Techniques*, vol. 28, no. 2, pp. 104–109, 1980.

[117] A. Bhattacharyya and T. Tralman, "Effects of dielectric superstrate on patch antennas," *Electronics Letters*, vol. 24, no. 6, pp. 356–358, 1988.

[118] H. Underwood and R. Magin, "Rectangular microstrip radiator for a multielement local hyperthermia applicator," in *Engineering in Medicine and Biology Society, 1988. Proceedings of the Annual International Conference of the IEEE*, pp. 864–865, 1988.

[119] E. Topsakal, "Antennas for medical applications: Ongoing research and future challenges," *Electromagnetics in Advanced Applications, 2009. ICEAA '09. International Conference on*, pp. 890–893, 2009.

[120] F. Kaymaram and L. Shafai, "Enhancement of microstrip antenna directivity using double-superstrate configurations," *Electrical and Computer Engineering, Canadian Journal of*, vol. 32, no. 2, 2007.

[121] W. Choi, Y. Cho, C. Pyo, and J. Choi, "A high-gain microstrip patch array antenna using a superstrate layer," *ETRI journal*, vol. 25, no. 5, pp. 407–411, 2003.

[122] M. F. Iskander and C. H. Durney, "An electromagnetic energy coupler for medical applications," *Proceedings of the IEEE*, vol. 67, no. 10, pp. 1463–1465, 1979.

[123] I. Bahl, S. Stuchly, and M. Stuchly, "A new microstrip radiator for medical applications," *IEEE Microwave Theory and Techniques Society*, vol. 28, no. 12, pp. 1464–1468, 1980.

[124] Y.-X. Du, X.-L. Xi, and W. Guo, "The Design and Simulation of Two-Armed Spiral Antenna for Microwave Hyperthermia," *2011 5th International Conference on Bioinformatics and Biomedical Engineering*, pp. 1–4, May 2011.

[125] M. a. Al-Joumayly, S. M. Aguilar, N. Behdad, and S. C. Hagness, "Dual-Band Miniaturized Patch Antennas for Microwave Breast Imaging.," *IEEE antennas and wireless propagation letters*, vol. 9, p. 268, Mar. 2010.

[126] V. Manfrini and P. Stauffer, "Dual concentric conductor arrays for microwave hyperthermia: theoretical study of design parameters," in *WESCON/'95. Conference record*, no. 1, 1995.

[127] D. Correia, H. P. Kok, M. de Greef, A. Bel, N. van Wieringen, and J. Crezee, "Body conformal antennas for superficial hyperthermia: the impact of bending contact flexible microstrip applicators on their electromagnetic behavior.," *IEEE transactions on bio-medical engineering*, vol. 56, pp. 2917–26, Dec. 2009.

[128] M. Schneider, "Microstrip lines for microwave integrated circuits," *Bell System Technical Journal*, 1969.

[129] K. F. Lee and W. Chen, *Advances in Microstrip and Printed Antennas*. Wiley-Blackwell, 1997.

[130] E. O. Hammerstad, "Equations for Microstrip Circuit Design," in *Microwave Conference, 5th European*, pp. 268–272, 1975.

[131] J. James and P. Hall, *Handbook of Microstrip Antennas [2 Vol set]: IEE Electromagnetic Waves*. Institution of Engineering and Technology, 1989.

[132] T. A. Milligan, *Modern Antenna Design*. Wiley, 2nd editio ed., 2005.

[133] J. C. Lin, *Electromagnetic Fields in Biological Systems*. CRC Press, 1st editio ed., 2012.

[134] A. Taflove and M. Brodwin, "Numerical solution of steady-state electromagnetic scattering problems using the time-dependent Maxwell's equations," *IEEE Transactions on Microwave Theory and Techniques*, no. 8, 1975.

[135] D. M. Sullivan, D. T. Borup, and O. P. Gandhi, "Use of the finite-difference time-domain method in calculating EM absorption in human tissues.," *IEEE transactions on bio-medical engineering*, vol. 34, pp. 148–57, Feb. 1987.

[136] A. Taflove, *Computational Electrodynamics: The Finite-Difference Time-Domain Method,*. Artech House, 3 edition ed., 2005.

[137] K. Yee, "Numerical solution of initial boundary value problems involving maxwell's equations in isotropic media," *Antennas and Propagation, IEEE Transactions on*, vol. 14, no. 3, pp. 302–307, 1966.

[138] G. Meunier, *The Finite Element Method for Electromagnetic Modeling*. ISTE Ltd., 1 edition ed., 2008.

[139] "Computer Simulation Technology Microwave Studio." URL: http://www.cst.com, (visited on 20/07/2014).

[140] T. Weiland, "A discretization model for the solution of Maxwell's equations for six-component fields," *Archiv fuer Elektronik und Uebertragungstechnik*, vol. 31, pp. 116–120, 1977.

[141] R. Pontalti, L. Cristoforetti, and L. Cescatti, "The frequency dependent FDTD method for multi-frequency results in microwave hyperthermia treatment simulation," *Physics in Medicine and Biology*, vol. 1283, 1993.

[142] P. Dimbylow, "FDTD calculations of the whole-body averaged SAR in an anatomically realistic voxel model of the human body from 1 MHz to 1 GHz," *Physics in medicine and biology*, vol. 479, 1997.

[143] M. Klemm, C. Fumeaux, D. Baumann, and I. J. Craddock, "Time-domain simulations of a 31-antenna array for breast cancer imaging," *2011 IEEE International Symposium on Antennas and Propagation (APSURSI)*, pp. 710–713, July 2011.

[144] S. Curto and P. McEvoy, "Compact patch antenna for electromagnetic interaction with human tissue at 434 MHz," *IEEE transactions on antennas and propagation*, vol. 57, no. 9, pp. 2564–2571, 2009.

[145] P. Dimbylow, "Finite difference calculations of current densities in a homogeneous model of a man exposed to extremely low frequency electric fields.," *Bioelectromagnetics*, vol. 8, pp. 355–75, Jan. 1987.

[146] P. J. Dimbylow and O. P. Gandhi, "Finite-difference time-domain calculations of SAR in a realistic heterogeneous model of the head for plane-wave exposure from 600 MHz to 3 GHz.," *Physics in medicine and biology*, vol. 36, pp. 1075–89, Aug. 1991.

[147] A. Christ, T. Samaras, A. Klingenböck, and N. Kuster, "Characterization of the electromagnetic near-field absorption in layered biological tissue in the frequency range from 30 MHz to 6,000 MHz.," *Physics in medicine and biology*, vol. 51, pp. 4951–65, Oct. 2006.

[148] G. Cerri, R. D. Leo, and G. Rosellini, "Evaluation of electromagnetic power deposition in a spherical multilayer head in the near field of a linear antenna," *Wireless Networks*, vol. 3, pp. 499–510, 1997.

[149] K. Nikita and M. Cavagnaro, "A study of uncertainties in modeling antenna performance and power absorption in the head of a cellular phone user," *IEEE Transactions on Microwave Theory and Techniques*, vol. 48, no. 12, pp. 2676–2685, 2000.

[150] H. Massoudi and C. Durney, "Electromagnetic absorption in multilayered cylindrical models of man," *IEEE Transactions on Microwave Theory and Techniques*, vol. 27, no. 10, 1979.

[151] S. Curto and M. Ammann, "Electromagnetic coupling mechanism in a layered human tissue model as reference for 434 MHz RF medical therapy applicators," *Antennas and Propagation Society*, pp. 3185–3188, 2007.

[152] C. Johnson and A. Guy, "Nonionizing electromagnetic wave effects in biological materials and systems," *Proceedings of the IEEE*, vol. 60, no. 6, 1972.

[153] O. Sipahioglu and S. Barringer, "Modeling the dielectric properties of ham as a function of temperature and composition," *Journal of Food Science*, vol. 68, no. 3, 2003.

[154] H. Chen, B. P. Marks, and R. Y. Murphy, "Modeling coupled heat and mass transfer for convection cooking of chicken patties," *Journal of Food Engineering*, vol. 42, pp. 139–146, Nov. 1999.

[155] Y. S. Wu and F. J. Rosenbaum, "Mode Chart for Microstrip Ring Resonators (Short Papers)," *IEEE Transactions on Microwave Theory and Techniques*, vol. 21, no. 7, pp. 487–489, 1973.

[156] J. Lehmann, J. Sfonebridge, and A. Guy, "A comparison of patterns of stray radiation from therapeutic microwave applicators measured near tissue-substitute models and human subjects," *Radio Science*, vol. 14, no. 6, pp. 271–283, 1979.

[157] M. I. Khattak, R. M. Edwards, O. A. Ojerinde, C. J. Panagamuwa, and M. Gul, "A Study of Perturbations in Linear and Circular Polarized Antennas in close proximity to the Human Body and Dielectric Liquid Filled Rectangular and a Cylindrical Phantom at 1.8 GHz," in *Antennas and Propagation Conference (LAPC), 2010 Loughborough*, no. November, pp. 409–412, 2010.

[158] C. Chou, A. Guy, and R. Johnson, "SAR in rats exposed in 2,450-MHz circularly polarized waveguides," *Bioelectromagnetics*, vol. 398, pp. 389–398, 1984.

[159] H. Kazuhiro and M. Haneishi, *Analysis, Design, and Measurement of Small and Low-Profile Antennas*. Artech House Publishers, 1st editio ed., 1991.

[160] J. James and P. Hall, *Handbook of Microstrip Antennas*. Stylus Publishing, LLC, 1989.

[161] J. Row and C. Ai, "Compact design of single-feed circularly polarised microstrip antenna," *Electronics Letters*, no. September, pp. 4–5, 2004.

[162] L. Shen, "The elliptical microstrip antenna with circular polarization," *IEEE transactions on antennas and propagation*, no. January, pp. 90–94, 1981.

[163] K. Tamakuma and H. Iwasaki, "A small size circularly polarized annular microstrip antenna," *Antennas and Propagation Society International Symposium*, pp. 716–719, 2003.

[164] M. Haneishi and S. Yoshida, "A Design Method of Circularly Polarized Rectangular Microstrip Antenna by One−Point Feed," *Electronics and Communications in Japan (Part I: Communications)*, vol. 64, no. 4, pp. 46–54, 1981.

[165] DCU Innovation and Enterprise Centre, *Commercialisation Handbook, An Introductory Guide for Researchers*. 2001.

[166] M. E. Porter, *Competitive Advantage*. Free Press, 2004.

[167] *Oslo Manual: The Measurement of Scientific and Technological Activities Guidelines for Collecting and Interpreting Technological Innovation Data*. Paris: OECD, 3rd editio ed., 2005.

[168] R. Rothwell, "Towards the Fifth-generation Innovation Process," *International Marketing Review*, vol. 11, no. 1, pp. 7–31, 1994.

[169] S. Kline and N. Rosenberg, "An overview of innovation," *The Positive Sum Strategy: Harnessing Technology for Economic Growth*, pp. 286–290, 1986.

[170] P. Trott, *Innovation Management and New Product Development*. Pearson Education, 2008.

[171] N. D. du Preez and L. Louw, "A framework for managing the innovation process," in *2008 Portland International Conference on Management of Engineering & Technology*, pp. 546–558, IEEE, July 2008.

[172] B. Medlin, *The factors that may influence a faculty member's decision to adopt electronic technologies in instruction*. PhD thesis, Virginia Polytechnic Institute and State University, 2001.

[173] E. M. Rogers, "Diffusion of Innovations," *New York: Free Press*, 1962.

[174] "Learn if a Medical Device Has Been Cleared by FDA for Marketing." http://www.fda.gov/medicaldevices/resourcesforyou/consumers/ucm142523.htm, 2009.

[175] "Medical Equipment and Supplies Report 2013." http://www.kurmannpartners.com/fileadmin/user_upload/MR-MedTech/2013_Medical_Equipment_Supplies_final.pdf, 2013.

[176] "The European Medical Technology Industry in Figures." http://www.eucomed.org/uploads/Modules/Publications, 2013.

[177] "Commercialising Medical Devices A Guide for UK Based Small Companies." http://www.quotec.co.uk/attachments/article/37/Commercialising Medical Devices.pdf, 2010.

[178] M. Wolf, M. Ferrari, and V. Quaresima, "Progress of near-infrared spectroscopy and topography for brain and muscle clinical applications.," *Journal of biomedical optics*, vol. 12, no. 6, p. 062104, 2007.

[179] K. Waxman, N. Lefcourt, and B. Achauer, "Heated laser Doppler flow measurements to determine depth of burn injury," *The American journal of surgery*, vol. 157, no. June, pp. 541–543, 1989.

[180] A. L. Herrick and S. Clark, "Quantifying digital vascular disease in patients with primary Raynaud's phenomenon and systemic sclerosis," *Annals of the Rheumatic Diseases*, vol. 57, pp. 70–78, Feb. 1998.

[181] J. Micheels, B. Aisbjorn, and B. Sorensen, "Laser doppler flowmetry. A new non-invasive measurement of microcirculation in intensive care?," *Resuscitation*, vol. 12, pp. 31–39, 1984.

[182] A. Cornejo, T. Rodriguez, M. Steigelman, S. Stephenson, D. Sahar, S. M. Cohn, J. E. Michalek, and H. T. Wang, "The use of visible light spectroscopy to measure tissue oxygenation in free flap reconstruction.," *Journal of reconstructive microsurgery*, vol. 27, pp. 397–402, Oct. 2011.

[183] P. Gebuhr, J. P. Jorgensen, B. Vollmer-Larsen, S. L. Nielsen and B. Alsbjorn, "Estimation of amputation level with a laser Doppler flowmeter," *Journal of Bone and Joint Surgery*, vol. 71, no. 3, pp. 514–517, 1989.

[184] "Clinical trials for medical devices." URL: http://www.mhra.gov.uk/Howweregulate/Devices/Clinicaltrials/#3 (visited on 27/01/2014).